



HAL
open science

L'émergence des galaxies passives massives à $z \approx 3$

Chiara d'Eugenio

► **To cite this version:**

Chiara d'Eugenio. L'émergence des galaxies passives massives à $z \approx 3$. Other [cond-mat.other]. Université Paris Cité, 2020. English. NNT : 2020UNIP7200 . tel-03343697

HAL Id: tel-03343697

<https://theses.hal.science/tel-03343697>

Submitted on 14 Sep 2021

HAL is a multi-disciplinary open access archive for the deposit and dissemination of scientific research documents, whether they are published or not. The documents may come from teaching and research institutions in France or abroad, or from public or private research centers.

L'archive ouverte pluridisciplinaire **HAL**, est destinée au dépôt et à la diffusion de documents scientifiques de niveau recherche, publiés ou non, émanant des établissements d'enseignement et de recherche français ou étrangers, des laboratoires publics ou privés.

Université de Paris

École doctorale Astronomie et Astrophysique d'Île-de-France ED127

Laboratoire AIM, Service d'Astrophysique CEA-Saclay

The emergence of massive quiescent galaxies at $z \sim 3$

Par

Chiara D'Eugenio

Thèse de doctorat de Astronomie et Astrophysique

Dirigée par Emanuele Daddi

Présentée et soutenue publiquement le 18 Décembre 2020

devant un jury composé de :

Isabelle Grenier	Professeur	DAP CEA-Saclay (LEPCHE)	Président
Bianca Poggianti	Professeur	INAF OAPD	Rapporteur
Stephane Arnouts	Astronome	LAM Marseille	Rapporteur
Henry J. McCracken	Astronome	IAP	Examineur
Francesco Valentino	Professeur	DAWN Center Copenhagen	Examineur
Emanuele Daddi	Astronome	DAP CEA-Saclay (LCEG)	Directeur de thèse



Except where otherwise noted, this work is licensed under
<https://creativecommons.org/licenses/by-nd/3.0/fr/>

L'émergence des galaxies passives massives à $z \sim 3$

Chiara D'EUGENIO

The emergence of massive quiescent galaxies at $z \sim 3$

Résumé court: Cette thèse a pour objectif la compréhension de la nature des galaxies rouges lointaines dans l'univers jeune, dans le cadre de la recherche des galaxies massives passives ou "mortes". Dans l'univers local, les galaxies passives sont parmi les plus massives, compte tenu de tous les types de galaxies. Elles se caractérisent par des populations stellaires extrêmement vieilles, distribuées selon une structure interne homologue de sphéroïde, raison pour laquelle elles sont souvent appelées elliptiques. Elles se caractérisent aussi par des taux de formation stellaire (SFR) faibles par rapport à la population moyenne des galaxies à formation d'étoiles de même masse stellaire, qui forment la Séquence Principale (aussi dit 'Main Sequence', MS). L'étude détaillée de leurs couleurs et de leurs spectres a permis d'évaluer l'âge de leurs étoiles et, d'une manière similaire à des fossiles cosmiques, elles ont permis de dater la formation de ces galaxies et de la placer à $z \sim 2$, quand l'univers avait 25% de son âge actuel. Toutefois, des galaxies passives ont été découvertes déjà massives et déjà "éteintes" à cette époque là. L'existence des galaxies à la fin de leur évolution dans un univers jeune a posé de nombreuses questions sur leur formation, sans qu'une réponse univoque ait été trouvée. Sa compréhension nécessite d'établir un lien clair entre leur masse et les mécanismes qui peuvent empêcher la formation des étoiles à toutes les époques cosmiques. Cela reste un sujet de recherche très actif. À $z \sim 2$, ces galaxies sont composées d'étoiles de 1-2 milliards d'années, enfermées dans des structures 10-100 fois plus denses, car leurs rayons de demi-lumière typiques sont en moyen 3-5 fois plus petits que dans l'univers local.

L'un des défis les plus considérables dans l'astrophysique observationnelle est de comprendre la nature des objets rouges lointains, car ils peuvent être des galaxies passives sans jeunes étoiles bleues et massives, ou également des galaxies à forte formation stellaire mais fortement obscurcies par la poussière, dont la distribution spectrale d'énergie (SED) peut ressembler à celle des galaxies passives. Cette thèse s'attaque au problème avec un échantillon de 10 candidats galaxies passive dans l'univers lointain, sélectionnés dans le champ COSMOS entre $2.4 < z < 3.3$. Je me suis occupée de la

réduction et de l'analyse des spectres sans fente WFC3/G141 dans le proche infrarouge, provenant du télescope spatial Hubble (HST). La confirmation spectroscopique de leur décalage vers le rouge a été possible pour la totalité de l'échantillon. Dans leur référentiel au repos, leurs spectres ultraviolets et optiques, ainsi que leur photométrie à large bande de l'ultraviolet au proche infrarouge, indiquent qu'ils sont des galaxies qui forment peu d'étoiles, bien que très jeunes. Ceci est un signe que le dernier épisode de formation stellaire a eu lieu récemment. Cet échantillon est, à ce jour, l'un des plus larges et robustes échantillons de galaxies passives disponible à ces époques cosmiques (D'Eugenio et al. 2021, soumis à A&A).

Des raies d'absorption de Balmer très intenses indiquent la présence d'étoiles jeunes, de type A, qui survivent environ quelques centaines de millions d'années. Pour mieux quantifier leur fréquence par rapport aux autres galaxies passives massives connues dans l'univers plus proche, j'ai créé un spectre moyen ("stacked") qui a permis de maximiser le rapport signal-sur-bruit et confirmer un âge stellaire moyen de ~ 300 millions d'années, avec des raies d'absorption de Balmer typiques des galaxies connues comme "post-starburst". On a ainsi pu étendre la classification de galaxie "post-starburst" ("suivant à une flambée d'étoiles") à la majorité des galaxies passives massives à $z \sim 3$ sélectionnées par les méthodes les plus utilisées de la littérature. Cet aspect marque leur convergence à leur époque de passivisation. La présence d'une faible raie d'émission de l'oxygène ionisé ($[\text{O II}]\lambda 3727$) suggère que l'évolution rapide de l'âge stellaire par rapport aux autres galaxies passives à distances intermédiaires n'est pas suivie par une augmentation du taux de formation stellaire par unité de masse (taux de formation stellaire spécifique, ou SSFR) ou, d'une façon équivalente, par une augmentation de la fraction de gaz disponible (D'Eugenio et al. 2020, ApJ Lettres). Malgré les données HST ne permettant pas d'avoir informations sur des autres indicateurs de SFR comme H_β , H_α , $[\text{NII}]$ and $[\text{OIII}]$, l'émission radio médiane à 3 GHz permet d'exclure la présence de galaxies à haut taux de formation stellaire, qui peuvent contaminer l'échantillon. Cette émission radio pourrait suggérer une évolution importante de l'activité du trou noir central par rapport aux autres galaxies passives à $z \sim 1.5$, par des processus non-thermiques qui maintiennent ces galaxies éteintes.

Cependant, des données millimétriques profondes (ALMA/NOEMA) sont nécessaires pour mesurer le SFR résiduel obscurci par la poussière de chaque galaxie, compte tenu des limites supérieures peu profondes fournies par les données disponibles dans l'infrarouge lointain. La détection de 30% de l'échantillon aux hautes énergies (2-10keV) suggère un taux d'accrétion de matière sur le trou noir central dans ces jeunes galaxies passives renforcé par rapport aux galaxies à formation d'étoiles de même masse stellaire à la même époque, mais aussi par rapport à des autres galaxies passives plus proches. Une morphologie généralisée compacte et sphéroïdale, couplée à des âges stellaires pondérées en masse très jeunes, suggère que les mécanismes responsables de la transformation morphologique pourraient précéder

ou même accompagner l'arrêt de la formation stellaire, d'une façon similaire aux galaxies à formation d'étoiles compactes observées à haut décalage vers le rouge.

Mots clefs : evolution des galaxies, formation des galaxies, galaxies passives, galaxies elliptiques, galaxies massives, galaxies compactes, post-starbursts, formation stellaire, AGN, trous noirs supermassifs, spectre infrarouge proche, HST WCF3, spectroscopie sans fente.

Abstract

Chiara D'EUGENIO

The emergence of massive quiescent galaxies at $z \sim 3$

This thesis investigates the nature of distant red galaxies in the early universe in search for massive quenched galaxies (QGs). In the local universe, QGs are the most massive among all galaxy types, having extremely old stellar populations, self-similar structures and extremely low star-formation rates (SFRs) at fixed stellar mass if compared to the typical relation describing the normal mode of star-formation in galaxies, the so-called Main Sequence. Archaeological information from their spectra in the nearby universe placed their formation at $z \geq 2$, however such quenched galaxies were later found to be already in place at such early epochs. They were found with suppressed SFRs and evolved stellar populations (1-2 Gyr) but with smaller sizes (by a factor of 3-5) and higher stellar densities (by a factor of 10-100). Tracing the emergence of the massive quiescent galaxy population has since then been an increasingly hotter research topic, since it required understanding the interplay between mass assembly, star formation and quenching, interplay which is still highly debated today. One of the major challenges of observational astrophysics is disentangling the nature of faint distant red objects, as they can be passively evolving systems lacking blue short-lived massive stars; or dusty star-forming galaxies whose high level of dust reddening can often mimic the spectral energy distribution (SED) and colors of quiescent objects.

This thesis addresses this issue by characterizing a sample of QG candidates in the distant universe ($z \sim 3$). I reduced and analyzed the Hubble Space Telescope WFC3/G141 near-Infrared grism spectra of 10 QG candidates at $2.4 < z < 3.3$ in the COSMOS field. Successful spectroscopic confirmation was accomplished for the entire sample. Their rest-frame nearUV-optical spectra, combined with their broadband UV to NIR photometry, point towards their quiescent nature, albeit the galaxies being consistent with having had their star-formation shut down very recently. Such sample constitutes one of the widest and most robust samples of quiescent galaxies available to date in the distant universe (D'Eugenio et al 2021, submitted to A&A).

The strong Balmer absorption lines, which flag the presence of young A-type stars, were better quantified through the creation of an high signal-to-noise average spectrum, confirming a mean age of ~ 300 Myr and the presence

of post-starburst features. Such confirmation allowed us to extend the post-starburst classification to the majority of classically selected quiescent galaxies at $z \sim 3$, marking their convergence to the quenching epoch. The presence of a weak [O II] $\lambda 3727$ emission line suggests that the rapid age evolution with respect to intermediate redshift analogs is not followed by an increase in specific star formation rate or, equivalently, by an increase in gas fraction (D'Eugenio et al. 2020, ApJ Letters). Despite HST data do not provide spectral coverage for H_β , H_α , [NII] and [OIII], median stack emission from 3GHz data helps excluding the presence of strong star-forming interlopers and might be indicative of a substantial evolution in radio-mode AGN activity with respect to $z \sim 1.5$. However, we caution that deep mm (ALMA/NOEMA) data are needed to individually assess the level of residual dust-obscured star formation given the shallow upper-limits from the FIR. Individual X-ray detections (30% of the sample) point towards an enhanced black hole accretion rate in recently quenched objects with respect to either similarly massive star forming galaxies at the same epoch or QGs at lower redshifts. The widespread compact, bulge-dominated morphologies, coupled with the young mass-weighted ages, suggest that the mechanisms responsible for structural and morphological transformation might be preceding quiescence, similarly to what seen in compact star forming galaxies at high- z .

Keywords: galaxy formation, galaxy evolution, quiescent galaxies, elliptical galaxies, massive galaxies, compact galaxies, post-starbursts, star formation, galaxy quenching, AGN, supermassive black holes, near-infrared spectra, HST WCF3, slitless spectroscopy.

Summary

Chiara D'EUGENIO

The emergence of massive quiescent galaxies at $z \sim 3$

The work presented in this thesis is devoted to the understanding of the processes that regulate some of the earliest episodes of quenching affecting massive galaxies. The population of early-type galaxies in the local universe comprises the most massive galaxies observed ($\log(M_*/M_\odot) > 11$). These are primarily pressure-supported spheroids with not enough cold gas reservoirs to host substantial star formation, composed of Gyr-old, metal rich stars. The most massive quenched galaxies were found to host the oldest stars, placing the formation of their stellar populations at $z > 2$. With the advent of near-IR spectrographs, populations of already assembled massive quenched galaxies were found to be in place at $z \sim 1.5 - 2$ with much more compact morphologies (rest-frame optical sizes about a factor of 3-5 smaller with respect to low redshift). A major challenge has been, therefore, that of tracing the assembly and growth of the so-called red-sequence through cosmic time by identifying the first evidences of quenched galaxies to the highest redshifts in order to find more clues on their structural transformation and on the mechanisms which had the highest impact in halting their star formation. Spectroscopic studies performed at $z > 1$ revealed an increasing age spread among massive quenched objects, driven by an increasing fraction of newly quiescent galaxies with respect to the "old" population (> 1 Gyr). At $z \sim 2$ this fraction starts to account for roughly half of the quenched population at $\log(M_*/M_\odot) > 11$. Spectroscopic confirmations of massive quiescent galaxies now extend up to $z \sim 4$ but the statistics remains limited to very few objects. Several major barriers are in fact still present for this kind of studies, such as the long integration times required to acquire the spectra of faint objects and their rapidly dropping number densities at $z > 2$, which make large, deep fields needed. This thesis work increased the statistics on quiescent galaxies at $z \sim 3$ and started building a comprehensive view of their properties bridging the relatively well studied epochs to the current frontiers at $z \sim 3.5 - 4$. Here I exhibit the value of HST when it comes to perform spectroscopic confirmation of $\log(M_*/M_\odot) > 10.8$ quiescent galaxies at $2.4 < z < 3.2$, thanks to its continuous spectral coverage along the Balmer/4000 Å break. Spectroscopic confirmation was achieved for the full sample confirming the quality of the photometric redshift originally used for the sample selection, as well as the accuracy of z_{phot} from more recent catalogs. To test the quiescence of our

targets, I compared their grism spectroscopy and UV-to-NIR broad-band photometry to various templates of composite stellar populations built with different prescriptions of star formation histories. This first test was able to reject star forming solutions for the entire sample. The emission of newly born, massive stars can however be strongly suppressed if substantial amounts of obscuration by dust is taking place. Dust absorbs UV radiation and re-emits most of the absorbed energy in the form of a grey body spectrum in the far-infrared. For this reason, I constrained the level of obscured SFR on the basis of mid-IR, far-IR and radio wavelengths by exploiting the most recent deblended photometry available in the literature. Such deblending improved source detection in observations with large PSFs such as those from Spitzer, Herschel and Scuba2 with respect to previously available blindly extracted catalogs. If the UV-to-NIR emission classify our galaxies as quiescent, mid-IR detections make the interpretation of four of our galaxies less straightforward. Three of such mid-IR sources have counterparts in the X-rays with flux densities consistent with being AGN powered. The mean-stack radio peak flux of our undetected sources at 3 GHz (9 out of 10) places their average obscured SFR strictly on a sub-MS level ($<50 M_{\odot}\text{yr}^{-1}$). However, the IR-based or radio-based upper-limits on the *individual* obscured SFRs are shallow at these epochs ($<120\text{-}190 M_{\odot}\text{yr}^{-1}$). This makes the use of deep mm data compelling to conclusively discern between AGN activity and residual star formation on a galaxy-by-galaxy basis.

The work shown in this thesis contains the stacked spectrum of our sample which, to date, is one of the highest quality of its class. The average spectrum shows strong Balmer absorption lines typical of post-starburst systems. Both the spectrum fitting technique and the adoption of the D_B and D_n4000 spectral indices to measure the strength of the Balmer absorption lines suggest a recent shut down of star formation. This holds on a galaxy-by-galaxy basis by including the available photometry and marginalizing over different attenuation curves and SFHs. Our galaxies were forming the bulk of their stars at high rates ($1800\text{-}3000 M_{\odot}\text{yr}^{-1}$, consistent with formation redshifts around $z\sim 3.5$) around 300-800 Myr prior to observation. Both the spectrum fitting and the spectral indices agree in marking a significant reduction in age compared to $z\sim 1.5$ massive analogs. These findings let us spectroscopically confirm the post-starburst properties already suggested by the UVJ color selection, implying that the magnitude cut necessary for spectral acquisition at high- z biases observations towards objects which had undergone a fast suppression of their SFR. However, we were also able to conclude that $\sim 60\text{-}70\%$ of the massive quiescent population at these epochs is likely in the same evolutionary stage by comparing the mass to light ratio distribution of our sample and that of parent sample from which they were drawn.

Additionally, we performed an indirect estimate of the average gas fraction of our galaxies: the weak [OII] emission line present in the stacked spectrum is consistent with a residual dust-corrected SFR of $7 \pm 3 M_{\odot}\text{yr}^{-1}$ which,

adopting the latest estimates of the star formation efficiency of $z \sim 1.8$ massive QGs, translates into a $\sim 9 \pm 4\%$ average gas fraction. This disfavors the continuation at high- z of the increase in gas fraction (or alternatively sSFR) with redshift reported by previous works from $z=0$ to $z=1.8$. However, given the degenerate origin of the [OII] emission, mm data are required to independently test this finding.

Recently, observations and cosmological simulations appeared to broadly agree on the number density of quiescent galaxies at $z \sim 3$ but it is unclear whether a population of passive objects exists as early as $z \sim 5$ in significant numbers. Increased consensus among simulations has also been reached when it comes to ascribe quenching in massive galaxies to AGN feedback. However, the agreement of simulations with different implementations of feedback to observed number densities appears to be redshift dependent. This is likely due to the fact that AGN feedback is not the only process that can halt or reduce star formation in high- z galaxies (such as for example cosmological starvation, the development of a stable virial shock in massive dark matter halos or compaction accompanied by fast gas consumption). As for the information contained in our data, the mid-IR and X-ray individual detections and the radio-stack shallow detection are consistent with a 30% incidence of luminous AGN and a widespread radio-mode feedback a factor of 4 stronger than in similarly massive QGs at intermediate redshifts, respectively. The BH mass growth appears to be substantially enhanced with respect both to $z \sim 2$ quiescent analogs ($\times 30$) and to coeval star forming galaxies at a fixed stellar mass ($\times 100$). This is in agreement with the recent results on the stacked emission of photometrically selected populations of QGs at $2.25 < z < 3.50$.

Lastly, I discussed the similarities between our $\sim 10^{11} M_{\odot}$ quiescent systems at $z \sim 2.8$ and compact star forming galaxies at $z \sim 2$ in terms of colors, sizes, structure and possibly SFRs. The many similarities with the most compact star forming galaxies at high- z make the question of identifying "contaminants" less clear-cut in the sense that they are likely part of the very same population of newly quenched systems at slightly different stages of their evolution, as already suggested by the finding of a pair at $z \sim 3.7$ consisting of a QG and an obscured compact star forming galaxy (Schreiber et al., 2018a). As a final remark, current estimates of number densities of $z > 4$ massive QGs are consistent with old ones (age > 1 Gyr) being 20% of QGs at $z \sim 3$. At the same time, however, the region where their descendants should lie in the UVJ diagram at $z \sim 2.8$ notoriously harbors star-forming contaminants. So, did any of the quenched objects found in at $z \sim 4$ and potential candidates at $z \sim 5$ evolve passively until $z \sim 3$? Or did they experience major star formation fluctuations? HST NIR spectroscopy can effectively differentiate old objects ($\Delta t \sim 1.3$ Gyr from $z=5.5$ to $z=2.8$) from dusty post-starbursts or star-forming contaminants. If no such object is found (or found in lower numbers compared to the expected number density from the latest observations), it implies that their apparent "post-starburstiness" at high- z might

be due to fluctuations in SFR and that the first episodes of passivization did not lead to a definitive shut down of star-formation. To verify this hypothesis we have selected 3 galaxies in COSMOS selected on the basis of their rest-frame UVJ colors, at $\log(M_*/M_\odot) > 10.9$ and $2.7 < z_{\text{phot}} < 3.3$ in the region preferentially populated by old galaxies and away from the region known to host star-forming contaminants. We removed galaxies with combined FIR+mm detections and Xray (2-10 keV) detections to avoid star-forming interlopers or AGN. Although we were confident about the passive nature of the proposed sources, whether they would eventually result in contaminants would strengthen the idea that post-starbursts make up nearly all the QG population. I proposed to use HST/WFC3 F160W+G141 to spectroscopically confirm the reddest and faintest passive galaxy candidates ever targeted exploiting the wide 1.1-1.7 μm spectral coverage to use the ratio between the Balmer Break index (D_B) and 4000A Break index (D_{4000}) as a resolution-unaffected and dust-unbiased spectral diagnostic between post-starburst and old spectra. Even though the proposal was not awarded time, its ranking in the first quintile confirms the intriguing consequences of such scenario which is testable with the available facilities.

Résumé

Chiara D'EUGENIO

The emergence of massive quiescent galaxies at $z \sim 3$

Le travail présenté dans cette thèse est finalisé à la compréhension des processus qui gouvernent les premiers épisodes de suppression de formation stellaire dans des galaxies massives. La population des galaxies de type "précoce" (dites "early-type") dans l'univers local est formée par les galaxies plus massives observées ($\log(M_*/M_\odot) > 11$). Elles sont principalement des sphéroïdes, dont la structure est une conséquence des orbites stellaires désordonnées. Elles sont pauvres en gaz froid pour soutenir une formation stellaire significative et sont aussi composées par des étoiles de plusieurs milliards d'années et d'haute métallicité. Les plus massives entre ces galaxies ont aussi les populations stellaires plus vieilles, ce qui a permis de repousser l'époque de leur formation à $z > 2$. Avec l'avènement des spectrographes qui travaillent dans le proche infrarouge, des populations de galaxies aussi massives que dans l'univers local et déjà éteintes ont été découvertes à $z \sim 1.5 - 2$. Cependant elles montrent une morphologie plus compacte (3-5 fois plus compacte que dans l'univers proche, dans leur référentiel au repos optique). L'un des défis les plus considérables dans l'astrophysique observationnelle est de reconstruire le développement de la "Sequence rouge" des galaxies passives au fil du temps cosmique. À cette fin, il faut identifier les premières galaxies éteintes aux plus hauts décalages vers le rouge pour mieux comprendre le lien entre leur transformation structurelle et les mécanismes qui ont causé la terminaison de leur formation stellaire.

Des études spectroscopiques à $z > 1$ ont révélé une différenciation d'âge stellaire parmi les galaxies massives de type précoce provoquée par une augmentation de la fraction des nouvelles galaxies éteintes par rapport aux galaxies vieilles (avec des étoiles plus vieilles que 1 milliard d'années). À $z \sim 2$ cette fraction représente environ la moitié de la population des galaxies passives avec $\log(M_*/M_\odot) > 11$. La confirmation spectroscopique de l'existence des galaxies massives éteintes s'étend à ce jour à $z \sim 4$ mais les contraintes statistiques sont encore plutôt limitées. Les obstacles plus difficiles qui gênent ce type d'études sont les temps d'intégration très longs nécessaires pour acquérir des spectres de bonne qualité et la rareté de ces galaxies dont la densité numérique plonge d'un facteur 10 de $z=2$ à $z=3$. Pour ce motif, des champs très larges et très profonds sont nécessaires. Avec 10 galaxies

dans ce travail de thèse, on a presque doublé le nombre de galaxies passives à $z > 2.5$ et on a commencé à établir une vue d'ensemble qui comble des époques relativement mieux explorées avec les frontières actuelles à $z \sim 3.5 - 4$. Dans ce travail, je montre la valeur du télescope spatial Hubble (HST) pour la confirmation spectroscopique du décalage vers le rouge des galaxies passive avec $\log(M_*/M_\odot) > 10.8$ à $2.4 < z < 3.2$, grâce à sa couverture spectrale continue autour de la région spectrale du Balmer/4000 Å break. La confirmation spectroscopique a été possible pour la totalité de l'échantillon, en confirmant aussi la qualité des décalages vers le rouge photométriques utilisées pour la sélection, ainsi que celle des données des catalogues plus récents. La vérification de leur quiescence a été réalisée en comparant leurs spectres et leurs données photométriques (en couvrant une région spectrale de l'ultraviolet (UV) au proche infrarouge (NIR)) avec plusieurs modèles de populations stellaires composites, obtenues avec des différentes histoires de formation stellaire. Ce premier test a permis d'exclure des solutions à formation d'étoiles pour l'échantillon entier. Cependant, l'émission par des nouvelles étoiles massives peut être fortement obscurcie si des grandes quantités de poussière les entourent. Dans leur référentiel au repos, les grains de poussière, en fait, absorbent les photons UV produits par les étoiles massives et ils re-émettent l'énergie absorbée dans l'infrarouge. Pour cette raison, j'ai mesuré leur taux de formation stellaire obscurci sur la base des données dans l'infrarouge moyen et lointain, ainsi que dans le domaine radio, en utilisant les derniers catalogues photométriques disponibles. Ces catalogues permettent de attribuer d'une façon plus correcte le signal au sources en cas d'observations à basse résolution spatiale (comme celles de Spitzer, Herschel et Scuba2) par rapport au catalogues précédents. Si l'émission de l'UV au NIR classe nos galaxies comme quiescentes, des détections dans l'infrarouge moyen compliquent l'interprétation physique de quatre objets. Trois d'entre eux montrent des contreparties aux rayons X (2-10keV), ayant des densités de flux compatibles avec l'hypothèse d'être causées par des AGN. La limite supérieure à l'émission radio médiane à 3 GHz des sources non détectées (9 sur 10) impose une limite de $50 M_\odot \text{yr}^{-1}$ sur le taux de formation stellaire obscurci, donc un facteur 6 plus faible que dans des galaxies de séquence principale ayant la même masse stellaire et à la même époque. Toutefois, les limites supérieures établies pour les objets individuels ne sont pas assez strictes ($< 120-190 M_\odot \text{yr}^{-1}$). Pour cette raison, c'est évident la nécessité des données millimétriques profonds pour distinguer entre AGN et formation stellaire résiduelle pour chaque objet.

Dans cette thèse on montre aussi le spectre moyen de ces galaxies que, à ce jour, est l'un à plus haute qualité dans les domaine des galaxies passives lointaines. Ce spectre montre des raies d'absorption de Balmer typiques des galaxies "post-starburst" ("suivant à une flambée d'étoiles"). Le deux techniques (le "spectrum fitting" et la mesure des indices spectraux D_B et D_n4000) suggère une suppression très récente de la formation stellaire, aussi dans les objets individuels. Nos galaxies sont compatibles avec des âges

entre 300-800 million d'années et avec un taux de formation stellaire de 1800-3000 $M_{\odot}\text{yr}^{-1}$ au maximum de leur activité, ayant à $z\sim 3.5$ leur époque de formation. Ces résultats montrent une réduction marquée de l'âge stellaire de ce type de galaxies par rapport aux galaxies similaires à $z\sim 1.5$. On a ainsi pu étendre la classification de leur état évolutif de "post-starburst" au 60-70% des galaxies passives massives à $z \sim 3$ sélectionnées par les méthodes les plus utilisées de la littérature en comparant leur distribution de rapport masse-luminosité avec celle de l'échantillon parent.

Par ailleurs, on a estimé d'une façon indirecte la fraction de gaz moyenne de nos galaxies: la luminosité d'une faible raie d'émission de l'oxygène ionisé ($[\text{O II}]\lambda 3727$) est compatible avec un taux de formation stellaire corrigé par l'effet de la poussière de $7 \pm 3 M_{\odot}\text{yr}^{-1}$ que, en supposant que nos galaxies aient la même efficacité de formation stellaire des galaxies passives massives à $z \sim 1.8$ (pour lesquelles on a les mesures plus robustes à ce jour), se traduit en une fraction moyenne de gaz froid de $\sim 9 \pm 4\%$. Ce résultat défavorise le scénario d'une augmentation progressive de la fraction de gaz (ou du taux de formation stellaire spécifique) à haut décalage vers le rouge aussi forte que ce qu'a été observé jusqu'à $z\sim 1.8$. Par contre, compte tenu des plusieurs processus qui peuvent produire une raie de $[\text{O II}]$ en émission, des données millimétriques supplémentaires sont requis au fin de tester ce résultat d'une façon indépendante.

Récemment, les observations et les simulations cosmologiques ont trouvé des résultats similaires pour ce qui concerne la densité numérique des galaxies quiescentes à $z\sim 4$ mais il n'est pas évident qu'une population significative de ces galaxies existe déjà à $z\sim 5$. Les différentes simulations attribuent un rôle clé au trou noir supermassif central ("AGN feedback") dans la formation des galaxies passives lointaines. Cependant, l'accord entre des simulations avec différentes mises en oeuvre du AGN feedback et les observations dépend fortement du décalage vers le rouge auquel on fait référence. Cela est dû au fait que l'AGN feedback n'est pas le seul processus qui peut inhiber la formation stellaire dans les galaxies lointaines (on a aussi, par exemple, le processus appelé "cosmological starvation", le développement d'un choc viriel stable dans les halos de matière noire ou la compaction accompagné par une consommation de gaz très intense). Pour ce qui concerne nos données, les détections individuelles dans le moyen infrarouge, au rayons X et l'émission radio médiane à 3 GHz sont compatibles avec une fréquence de 30% des AGN lumineux et avec un feedback radio non-thermique (jets) généralisé plus fort d'un facteur 4 par rapport aux galaxies passives ayant masse similaire à $z\sim 1.8$, respectivement. La croissance en masse du trou noir central est renforcé par rapport aux galaxies similaires ($\times 30$) à $z \sim 2$ ainsi qu'aux galaxies à formation d'étoiles de même masse stellaire à la même époque ($\times 100$). Ce résultat est en accord avec l'émission moyenne détectée dans les galaxies passives massive sélectionnées sur base photométrique à $2.25 < z < 3.50$.

Dans la dernière partie de la thèse, j'ai présenté les similarités en couleurs,

tailles, structures et peut-être SFRs entre nos $\sim 10^{11} M_{\odot}$ galaxies quiescentes à $z \sim 2.8$ et les galaxies à formation d'étoiles compactes connues à $z \sim 2$. Les nombreuses similitudes avec les galaxies à formation d'étoiles plus compactes compliquent l'identification et l'interprétation des "contaminants", car il est possible qu'ils appartiennent à la même population de galaxies à différents stades de leur évolution, comme suggéré par la paire à $z \sim 3.7$ composé d'une galaxie passive et une à formation d'étoiles compacte obscurcie. En conclusion, les estimations actuelles de la densité numérique des galaxies passives à $z > 4$ sont compatibles avec une population vieille (âge > 1 milliard d'années) à $z \sim 3$ qui représente 20% de la totalité des objets éteints mais, par contre, on sait que la région dans l'UVJ diagram où elles devraient se trouver est fréquemment contaminée par des galaxies à formation d'étoiles riches en poussière ou plus proches. Donc, est-ce que les galaxies éteintes observées à plus haut décalage vers le rouge évoluent passivement jusqu'à $z \sim 3$ où pas? Est-ce qu'elles reprennent à former des étoiles? La spectroscopie infrarouge de HST peut distinguer entre des objets vieux ($\Delta t \sim 1.3$ Gyr from $z = 5.5$ to $z = 2.8$) et des galaxies jeunes obscurcies. Si on trouve des galaxies vieilles avec une densité numérique mineure par rapport aux prévisions basées sur les observations à z_4 , on peut penser que l'arrêt de la formation stellaire a été plus complexe que prévu. Au fin de vérifier cette hypothèse, on a sélectionné 3 galaxies dans le champ COSMOS, sélectionnées sur la base de leurs couleurs UVJ dans leur référentiel au repos, ayant $\log(M_*/M_{\odot}) > 10.9$ et $2.7 < z_{\text{phot}} < 3.3$. On a exclu tous les objets ayant des détections dans l'infrarouge lointain, millimétrique et X (2-10 keV) pour exclure des galaxies à formation d'étoiles ou des AGN. Si on trouve que ces candidats sont en effet des contaminants, ça renforcerait l'idée que les premiers épisodes de suppression de formation stellaire n'avaient pas été définitifs. J'ai proposé l'utilisation de HST pour tester la nature des galaxies les plus rouges et faibles jamais observées en utilisant le rapport entre l'indice de Balmer (D_B) et l'indice du 4000Å Break (D_{n4000}) en tant que diagnostic peu affecté par la résolution spectrale ou par le rougissement provoqué par la poussière. Même si la proposition n'a pas été sélectionnée pour être observée, son classement dans le premier quintile confirme l'importance des conséquences d'un scénario vérifiable avec des instruments déjà à disposition.

Contents

Abstract	v
1 Introductory remarks	1
1.1 Brief cosmological overview	1
1.2 Galaxies	3
1.3 Quenched galaxies and their evolution with redshift	7
1.3.1 The low-mass end	9
1.3.2 The high-mass end	9
Their formation in simulations	10
Observed properties of massive quiescent galaxies at high redshift	11
1.4 Thesis motivation	15
1.4.1 Investigating the nature of high-z photometric candidates	15
1.4.2 Understanding what drives the transition towards qui- escence	18
2 Target identification and observations	21
2.1 The COSMOS field	21
2.2 Sample selection	24
2.3 Slitless spectroscopy with HST: characteristics and observations	25
2.3.1 Observation strategy	27
2.4 Data reduction	28
2.5 Spectroscopic confirmation	32
2.5.1 Fitting setup	32
2.5.2 Redshift identification	33
2.5.3 Performance of photometric redshifts	37
3 Testing their quiescence	41
3.1 Addition of photometry	41
3.1.1 Zero-point calibrations	42
3.1.2 Dust attenuation laws	44
3.2 Quiescence of individual targets	48
3.2.1 What can be learnt from UV-to-NIR data	48
3.2.2 Further constraints from multiwavelength data sets . .	49
IR and X-rays	50
Radio	51

4	Recently quenched galaxies, recently formed	55
4.1	Stacked spectrum	55
4.1.1	Spectral fit	56
4.1.2	Strength of spectral breaks	58
4.2	How common are post-starbursts at $z \sim 3$?	60
4.3	Analysis of individual targets	62
4.4	Discussion	63
5	The emergence of massive quiescent galaxies at $z \sim 3$	73
5.1	Insights on the residual gas fraction from [OII]	73
5.2	Tracing AGN feedback	77
5.2.1	Radio perspective	78
5.2.2	X-ray perspective	78
5.3	Comparison with compact star forming galaxies	82
6	Conclusions and future perspectives	85
6.1	Did any galaxy evolve quiescently from $z > 5$ to 3?	87
6.2	Probing residual gas reservoirs with ALMA archival images	89
6.3	Using quiescent galaxies as signposts for groups and proto-clusters	91
6.4	Using JWST to study early stellar and chemical evolution	93
A	IR and radio cutouts	97
B	Contribution to other papers as co-author	109
C	Accepted proposals	113
D	First author papers	121

Chapter 1

Introductory remarks

The work contained in this manuscript is held in the framework of galaxy evolution and deals with the specific subject of the suppression of star-formation in massive galaxies in the early universe. In particular, the whole thesis is focused on a sample of distant quiescent galaxy candidates and their properties. The results of the analysis performed on such sample led to a letter published on ApJ (D'Eugenio et al., 2020) and in a paper (D'Eugenio et al. 2021) which, at the time of writing, has been submitted to A&A and is under revision. The structure of the manuscript itself is intended to guide the reader through the steps that led to the aforementioned papers and to provide an homogeneous view of the work through the various chapters. In particular, chapter 2 and 3 contain the work I performed on the data reduction and the test on the quiescent nature of our target galaxies, respectively. In chapter 4, I report the main result of the letter which is the direct identification of post-starburst absorption features enabled by the creation of a stacked spectrum -one of the highest quality spectra available of its class at these redshifts- whose properties can be considered widespread among the massive quiescent population in the early universe. In the same chapter, I also introduce the results of a similar analysis but performed on a galaxy-by-galaxy basis and discuss the evolutionary stage of $z \sim 3$ quiescent galaxies in the context of the current literature (as appearing in the submitted paper). Chapter 5, instead, contains the results and discussion enclosed in the paper, where I explore the incidence of AGN feedback on our sample in light of their young stellar populations and overall bulge-dominated morphologies. In the same chapter, I also discuss the similarities with compact star forming galaxies known to exist at high redshift. In the present chapter, after a brief overview of the cosmological context which this thesis relies upon, the key aspects about the formation and evolution of quiescent systems will be presented in sections 1.2 and 1.3. The open questions which motivated this thesis work are summarized in section 1.4.

1.1 Brief cosmological overview

The interpretation of galaxy evolution, and of the universe as we see it, has to deal with the very basic assumption of a cosmological model. The one that

is generally adopted at the time of writing is the Λ CDM standard cosmology, which models the universe as a geometrically flat ($\Omega_{\text{tot}} = 1$) homogeneous, isotropic fluid, in accelerated expansion. Its components are matter, radiation and dark energy. Specifically, matter is further composed of a $\sim 16\%$ of ordinary baryons (protons, neutrons and electrons, as customary) and an $\sim 84\%$ in the form of dark matter, which interacts only through gravitation. Dark matter is believed to be cold, i.e. non-relativistic at the time of decoupling of matter from radiation, in order to avoid free-streaming effects and favor the assembly of small-scale density perturbations observed in the Cosmic Microwave Background (CMB). However, its exact nature remains unknown. Dark energy, which is thought to sustain said expansion, appears to be constrained in the current understanding of the cosmological equation of state as $w(z) = -1$ interpreted as a vacuum energy, constant in time. The exact value of w is still under debate.

Despite lacking a conclusive physical description of what the dark components are, this model has the advantage of characterizing a wide-range of phenomena with the relatively low number of six parameters. These phenomena include structure formation, the accelerating expansion, primordial nucleosynthesis, the fluctuations in the CMB, galaxy clustering and the Large Scale Structure.

The density parameters have been measured with remarkable precision by several surveys, the most accurate to date being the Planck mission which measures the angular power spectra of temperature and polarization anisotropies in the CMB and yields $\Omega_{\text{m}} = 0.315 \pm 0.007$, $\Omega_{\Lambda} = 0.685 \pm 0.007$ (Planck Collaboration et al., 2020). The increasing accuracy of precision cosmology has lead, however, in 2019 to conclude that independent probes at low-redshift¹ and high-redshift² do not agree on the same value of the Hubble constant H_0 (which not only sets the expansion rate of the universe but also its present age). For example, the best SH0ES and H0LiCOW results find $H_0 = 73.5 \pm 1.4 \text{ km s}^{-1} \text{ Mpc}^{-1}$ and $H_0 = 73.3 \pm 1.8 \text{ km s}^{-1} \text{ Mpc}^{-1}$ respectively (Riess et al., 2019; Wong et al., 2020) in 4.2 and 3.3 σ tension with the early Universe prediction from Planck ($H_0 = 67.4 \pm 0.5 \text{ km s}^{-1} \text{ Mpc}^{-1}$). Thus far, it is unclear whether systematics in the different methods adopted are at the base of such discrepancy or whether there is an underlying new physical property of the universe to be understood. From a strictly pragmatic point of view however, until the advent of further diriment probes, it is necessary to find an agreement and make measurements within the same reference frame. This agreement is the *concordance* cosmological model mentioned above with the density parameters set as $\Omega_{\text{m}} = 0.27$, $\Omega_{\Lambda} = 0.73$. The Hubble constant is set to $H_0 = 70 \text{ km s}^{-1} \text{ Mpc}^{-1}$, which implies an age of the universe of 13.8 Gyr.

¹E.g. improved Cepheids distances with the SH0ES survey, (Riess et al. 2016), Type Ia SNe, galaxy clustering with the DES survey, “time-delay distance” methods using variable background quasars with strong gravitational lensing in the H0LiCOW survey.

²Big Bang nucleosynthesis, Baryon Acoustic Oscillations, CMB (e.g. Abbott et al., 2018).

In this framework, dark matter sets the dominant gravitational field and, by being the first to collapse, governs the mass assembly of the observable universe (Peebles, 1982). Galaxies are therefore the manifestations of the evolutionary stage of the universe at each time-frame of observation and, in particular, of the complex baryonic interactions happening at small scales under the large-scale effect of gravity (Blumenthal et al., 1984).

The most general picture sees the virialization and collapse of the dark matter halos followed, after matter-radiation decoupling, by the cooling and condensation of pristine gas clouds into the first galaxies along the large scale structure filaments (White and Rees, 1978). Additionally a central supermassive black hole (SMBH) grows more or less in lockstep and becomes visible as an active galactic nucleus (AGN) when it is accreting material. As the gas gets consumed by star formation, some is returned into the interstellar medium (ISM) through stellar mass loss and supernovae (SNe), some gets ejected by AGN jets and SNe superbubbles. When this happens, the cold, metal-enriched gas is injected into the circum galactic medium (CGM, generally in pressure equilibrium at temperatures of $10^5 - 10^6$ K) and is subject to shear, ablation and thermal conduction. The ejected material will mix with the surrounding diffuse gas (in terms of temperature and metallicity) and will return back to the galaxy or will be dispersed into the CGM depending on the cloud's mass and speed. These stellar and AGN feedback processes heavily impact the evolution of the galaxy. They can trigger gas compression and star formation locally but, on the long run, they can effectively contribute to the depletion of cold gas reservoirs favoring the quenching of star formation. Lastly, galaxies are influenced by whether they reside in the field, in groups or clusters. The different peculiar velocities and gas dynamics set the mechanisms leading to structural and morphological transformation and, ultimately, to additional pathways for quenching. The interplay of these processes, internal and external, is not the same for every type of galaxy. This complexity is manifested and enclosed in the diversity of galaxies in the universe as it appears today (Fig.1.1). Understanding the detailed evolution for each and every type of galaxy is the ultimate driver of extragalactic astrophysics.

1.2 Galaxies

As will become clear in what follows, the many ways of classifying galaxies all seem to converge to two main groups: living galaxies and dead ones. Starting from the meticulous classification of galaxies as they appear in the local universe and following backwards in time the bulk evolution of star forming ones, it is possible to think about the field of galaxy evolution as an exceptional collective effort to understand what leads to fatal star formation suppression and to pinpoint how early in the cosmic history the first evidences of quenching start to appear.

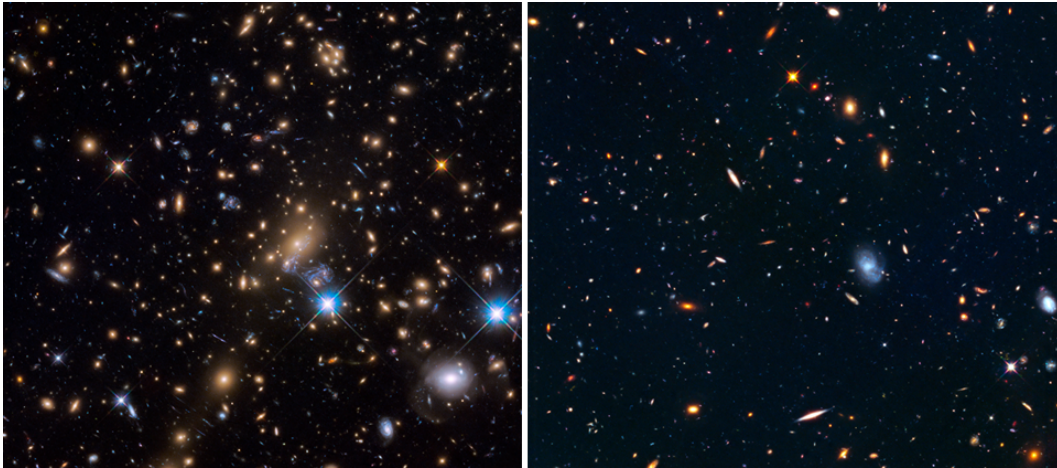


FIGURE 1.1: Left: MACS J1149 galaxy cluster. Right: adjacent parallel field. From the Hubble Frontier Fields program. Image credit: NASA, ESA, and J. Lotz, M. Mountain, A. Koekemoer, and the HFF Team (STScI)

The initial classification took into account direct observables as morphology, structure, dynamics and stellar content:

- *Early-type* galaxies (ETGs) are pressure-supported spheroids, composed primarily of several Gyr-old, metal rich stars, with not enough cold gas to sustain star formation (Renzini, 2006). They obey to tight scaling relations such as the color-magnitude relation in which they form the so-called "red sequence" (Baum, 1959; de Vaucouleurs, 1961; Strateva et al., 2001; Bell et al., 2004), the Faber-Jackson relation³ (Faber and Jackson, 1976), the mass-size relation (Shen et al., 2003) the mass-metallicity relation (Tremonti et al., 2004; Gallazzi et al., 2005); the fundamental plane⁴ (Djorgovski and Davis, 1987; Dressler et al., 1987).

Their stellar surface brightness profiles can be fit with a Sérsic function with index $n=4$, known as the de Vaucouleurs profile (de Vaucouleurs, 1948), indicating a centrally peaked profile with faint but extended wings. This class corresponds to ellipticals and S0s in the original Hubble scheme (Hubble, 1926). Their gas reservoir is mostly in the form of a hot diffuse plasma emitting through thermal bremsstrahlung and permeating the surrounding space to scales of tens of kpc.

- *Late type* galaxies (LTGs), such as spirals, are instead characterized by a thin disk (supported by rotation) with spiral arms, a central bulge and sometimes a bar. The relative contribution of the disk and the bulge

³A power-law relation between the total luminosity and the central velocity dispersion.

⁴Which relates the effective radius, the average surface brightness within the effective radius and the central velocity dispersion in a three-dimensional plane. The existence of the fundamental plane highlights how their structure is relatively self-similar, indicating some degree of consistency in their formation.

to the total galaxy surface brightness can vary significantly among the whole population. In general, it does so as a function of stellar mass, in the sense that more massive galaxies have larger bulge-to-disk ratios (Abramson et al., 2014; Tacchella et al., 2015; Cappellari, 2016). In terms of surface brightness profiles the disk component has typically an exponential profile (Sérsic profile with $n=1$), while the bulge is more similar to ETGs. Irregular galaxies are then a peculiar class of gas rich, star forming galaxies characterized by disturbed morphologies, likely as a result of interactions.

These two classes form the well known bimodality in the color-magnitude relation, which holds up to $z=3$ (Franzetti et al., 2007; Brammer et al., 2009; Whitaker et al., 2011).

Two of the most relevant discoveries in galaxy evolution were the identification of the connection between star formation rate (SFR) and cold gas surface densities through the Schmidt-Kennicutt relation (Schmidt, 1959; Kennicutt, 1998), for which the amount of star formation is proportional to the availability of dense neutral and molecular gas; and the realisation that the SFR of galaxies is tightly connected to their stellar mass at least up to $z\sim 4$ (see Fig. 1.2, Brinchmann et al., 2004; Noeske et al., 2007; Elbaz et al., 2007; Daddi et al., 2007; Whitaker et al., 2012b; Schreiber et al., 2015). The so-called main sequence (MS) of star formation divides galaxies into starbursts, normal star-forming galaxies, intermediate "green valley" ones and quiescent galaxies⁵. The slope and scatter of the MS hold over an extensive redshift range, whereas the normalisation drops by a factor of 20-30 from $z=3$ to $z=0$.

Broadly speaking, the sSFR (SFR/M_*) correlates with galaxy morphology, structure, dynamics, stellar populations and gas content so that their complexity decreases from extreme systems, such as starbursts, all the way down to passive spheroids. In the measure that when one refers to the original classification between ETGs and LTGs it is already accounting for this difference in residual activity.

This means that it is possible, at all times, to broadly classify the whole galaxy population according to the ability of a system to form stars: star forming galaxies whose stellar mass growth is generally smooth, self-regulated by gas inflows, outflows, and consumption; starbursts, associated at low- z to violent processes such as mergers⁶; quiescent galaxies in which the star formation is strongly suppressed with respect to the MS population and therefore can be

⁵Formally, one should distinguish between *passive* and *quiescent* according to a certain threshold in sSFR (usually $\log(\text{sSFR}) \ll -11 \text{ yr}^{-1}$) or colors in order to account for different stages of quenching. As the sSFR of galaxies globally increases with redshift, hereafter these terms will be used interchangeably to refer to quenched systems.

⁶These funnel large amounts of gas into compact cores triggering strong star formation (e.g. sub-millimeter galaxies) and short depletion times. Whether this enhanced star formation rate is due to more gas mass or higher star formation efficiency is still a matter of debate.

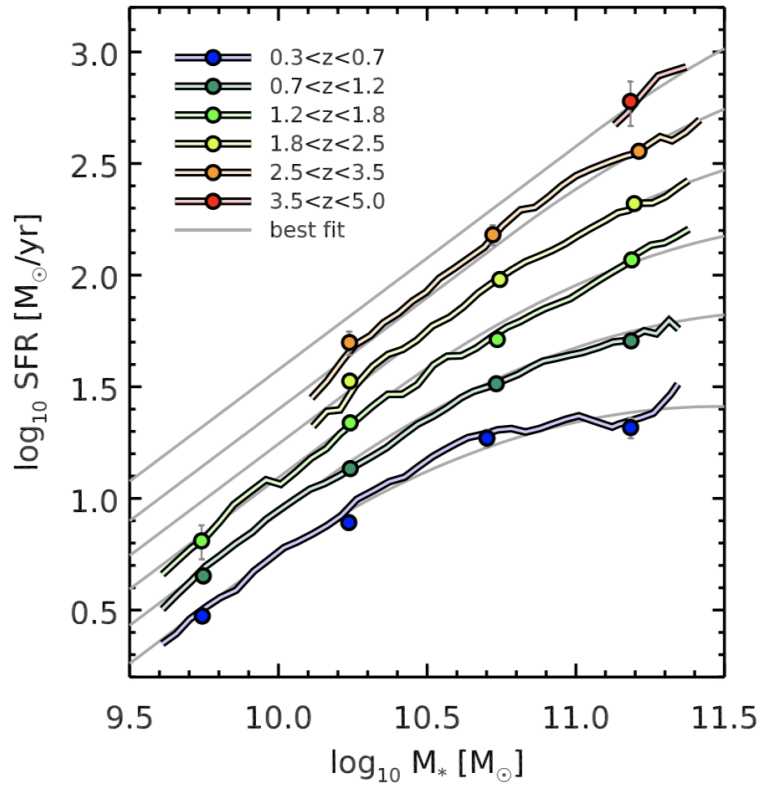


FIGURE 1.2: From Schreiber et al., 2015. Evolution of the main sequence of star formation with redshift. The origin of the MS bending at the high-mass end at low- z is debated. It is likely driven by intermediate-SFR galaxies being a mixed population of blue galaxies becoming quiescent (Martín-Navarro, van de Ven, and Yıldırım, 2019) and passive galaxies undergoing episodes of rejuvenation (Mancini et al., 2019).

considered "remnants" of galaxies' lifecycle. This thesis work is focused on the latter.

1.3 Quenched galaxies and their evolution with redshift

Altogether, quenched or quiescent galaxies (QGs) contain 75% of the total stellar mass budget of the present-day universe. Moreover, the majority of massive galaxies ($\log(M_*/M_\odot) > 10.5$) appear to be quenched, with QGs outnumbering star-forming galaxies by a factor of 10 at $\log(M_*/M_\odot) > 11.5$ (Baldry et al., 2004). Understanding the build up of the red sequence represents to date one of the long standing puzzles in galaxy evolution, literally and figuratively.

A key finding was the segregation of the SFR in terms of stellar mass and environment: galaxies above $\log(M_*/M_\odot) > 11$ are more likely to be quiescent irrespective of whether they reside in the field or in overdensities; lower-mass QGs are preferentially found in dense groups or clusters (see Fig.1.3, taken from Peng et al., 2010). This establishes that the composition of the red sequence itself, despite the relatively high degree of uniformity compared to LTGs, is heterogeneous.

The relatively good knowledge of the physics regulating stellar evolution has allowed to interpret the colors and the integrated spectra of massive quiescent galaxies in terms of stellar populations⁷ which revealed a correlation between their stellar mass and the look-back time of their main star-formation episode (known as "archeological downsizing", Gallazzi et al., 2005; Thomas et al., 2005; Fontanot et al., 2009; Thomas et al., 2010; Citro et al., 2016). The most massive ones are also composed by the oldest stellar populations: local cluster QGs appear to have formed at $z \gtrsim 3$ followed by field QGs ~ 1 Gyr later (Thomas et al., 2005).

Such results based on fossil record studies have then been reinforced by the first identifications of QGs at increasing redshifts (Dunlop et al., 1996; Franx et al., 2003; Cimatti et al., 2004; Daddi et al., 2005) granted by near-infrared (NIR) sensitive detectors which sample the rest-frame optical at $z \geq 1.5$. In this regard, ground-based 8-10m class telescopes and space based facilities as the Hubble Space Telescope (HST) have been fundamental in a complementary way: the former thanks to large collective areas and high-resolution spectrographs; the latter thanks to significantly lower background and absence of strong, variable atmospheric components, either in emission or in absorption. These advances were essential to show that the assembly (and quenching) of massive systems took place at $z > 1-1.5$ with little evolution

⁷Starting from the pioneering works of Tinsley 1972; Tinsley 1978; Tinsley 1980 all the way to the most recent fitting techniques (e.g. Kriek et al., 2009; Conroy, 2013; Schreiber et al., 2018b; Leja et al., 2019; Carnall et al., 2019).

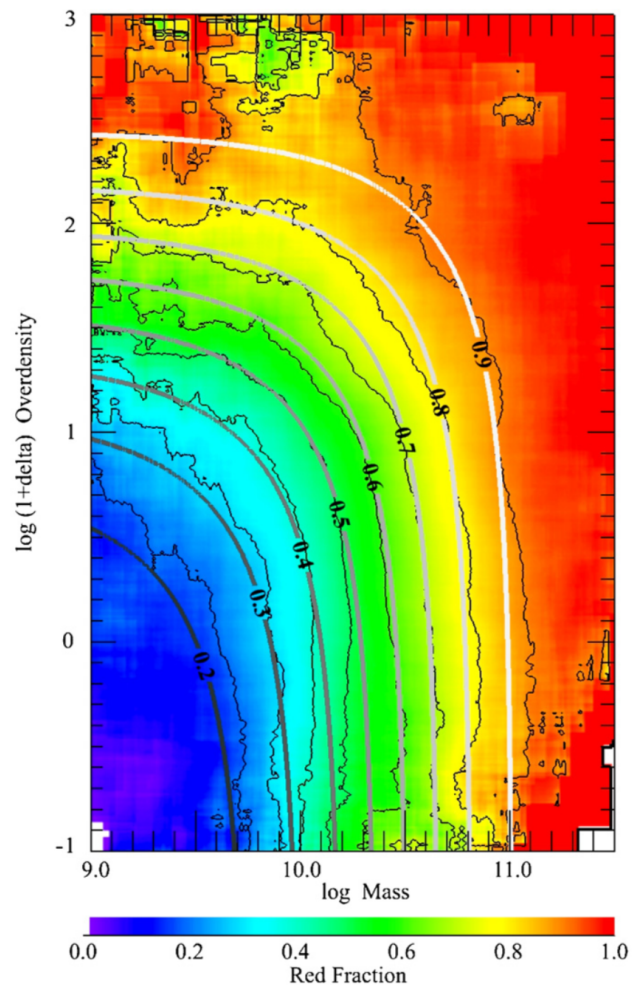


FIGURE 1.3: Red fraction in SDSS as a function of stellar mass and environment. from Peng et al., 2010

of the high-mass end of the luminosity/stellar mass functions, especially compared to the progressive rise of the low-mass end (Fontana et al., 2004; Cimatti, Daddi, and Renzini, 2006; Arnouts et al., 2007; Drory et al., 2009; Pozzetti et al., 2010; van Dokkum et al., 2014; Gargiulo et al., 2016; Davidzon et al., 2017; Kawinwanichakij et al., 2020).

1.3.1 The low-mass end

The growth of the lower-mass end of the red sequence can be thought of as the result of the generalized progressive passivisation of the star-forming population through gas consumption, cluster related processes and cosmic starvation in lower density halos, mostly at $z < 1.5$ (e.g. Saracco, Longhetti, and Gargiulo, 2011; Carollo et al., 2013). The drastic change of the low-mass end of the quiescent stellar mass function, in fact, appears to be going hand-in-hand with the simultaneous progressive decline of gas fraction and SFR normalization in MS galaxies, resulting in the exponential decay of the global star formation rate density at $z < 1.5$ (e.g. Madau and Dickinson, 2014; Sargent et al., 2014; Schreiber et al., 2015). Incidentally these are the epochs when the most massive galaxy clusters at $z < 1.5$ virialize, impacting the replenishment of cold gas for further star formation, as hydrodynamical simulations seem to suggest (Dekel, Sari, and Ceverino, 2009). Observationally, lower mass disk QGs at $z < 1$ (old or recently quenched) have been linked to ram pressure stripping, starvation, strangulation or harassment events of star-forming galaxies when in cluster environments (e.g. Emsellem et al., 2011; Carollo et al., 2013; Wild et al., 2016; Maltby et al., 2018a; Matharu et al., 2019; Kawinwanichakij et al., 2020) and to disk fading (Rizzo, Fraternali, and Iorio, 2018) or mergers (Querejeta et al., 2015) when in groups or in the field. This continuous injection of galaxies into the red sequence (known as "progenitor bias") is believed to partly drive the observed size growth of QGs at low redshift (Valentinuzzi et al., 2010; Carollo et al., 2013; Poggianti et al., 2013).

1.3.2 The high-mass end

On the other hand, understanding how massive galaxies quenched in an epoch when galaxies were generally gas rich and prodigiously star-forming ($2 < z < 4$, Daddi et al., 2010; Tacconi et al., 2010; Genzel et al., 2010; Madau and Dickinson, 2014) is itself non trivial and has given birth to a vast literature in recent years.

Their formation in simulations

The progressive discovery of populations of massive quenched galaxies already in place at high- z (Dunlop et al., 1996; Franx et al., 2003; Cimatti et al., 2004; Daddi et al., 2005; Kriek et al., 2009; Gobat et al., 2012; Glazebrook et al., 2017a) posed challenges to hierarchical models of structure formation given that the number of the most massive galaxies observed seemed to be too numerous compared to the haloes that should have hosted them (e.g. Steinhardt et al., 2016). In fact, hydrodynamical simulations and semi-analytical models (SAM) have struggled to reproduce the comoving number densities of massive, passively evolving galaxies at $z > 2-3$, falling short by roughly an order of magnitude (Wellons et al., 2015; Nelson et al., 2015; Steinhardt et al., 2016; Davé, Thompson, and Hopkins, 2016; Cecchi et al., 2019; Schreiber et al., 2018b). Over the years, however, improved simulations and observational constraints on both the halo mass function (HMF) and stellar mass function (SMF) have eased such discrepancy showing that the slope of the high-mass end of the SMF at $z > 3$ agrees with that of the HMF within the uncertainties (see Fig.1.4, taken from Davidzon et al., 2017). The paucity of galaxies at the high-mass end of the SMF compared to the HMF at $z < 3$ seen in Fig.1.4 requires suitable quenching mechanisms to hamper the conversion of baryons into stars (e.g. Granato et al., 2004; De Lucia et al., 2006; Raseria and Teyssier, 2006; Fontanot et al., 2009). One of the most effective mechanisms invoked in SAMs and hydrodynamical simulations to shut down star formation in massive galaxies is AGN feedback (De Lucia and Blaizot, 2007; Henriques et al., 2017; Girelli et al., 2020). This should be active at least as early as the redshift of the most distant quenched galaxies observed (Moster et al., 2010). Moreover, simulations based primarily on AGN feedback should closely reproduce the abundance of quenched objects at all redshifts. However, the agreement of simulations with observed data appears to be redshift dependent. Some simulations perform better at $z \lesssim 2$ (e.g. SIMBA, Illustris TNG300) while others better reproduce the tentative estimations at $z \sim 5$ (EAGLE). This is likely due to the fact that AGN feedback is far from being the only process that can halt or reduce star formation in high- z galaxies, meaning that many different channels of quenching exist, contributing at different timescales as well as spatial scales (an overview can be found in Sec. 1.4.2).

The most recent estimates of the number density of QGs extend to $z \sim 4-5$ by making use of photometric samples (e.g. Straatman et al., 2014; Merlin et al., 2019; Santini et al., 2020) as well as spectroscopically confirmed ones (Glazebrook et al., 2017a; Schreiber et al., 2018b; Valentino et al., 2020; Forrest et al., 2020a; Forrest et al., 2020b). On the other hand, cosmological simulations progressively increased in volume, spatial and mass resolution, as well as improving feedback schemes and subgrid physics regulating star formation (Illustris: Vogelsberger et al. 2014a; Vogelsberger et al. 2014b; Genel et al. 2014; Nelson et al. 2015; Illustris TNG: Pillepich et al. 2018; Nelson et al. 2019; EAGLE: Schaye et al. 2015; SIMBA: Davé et al. 2019). These advances

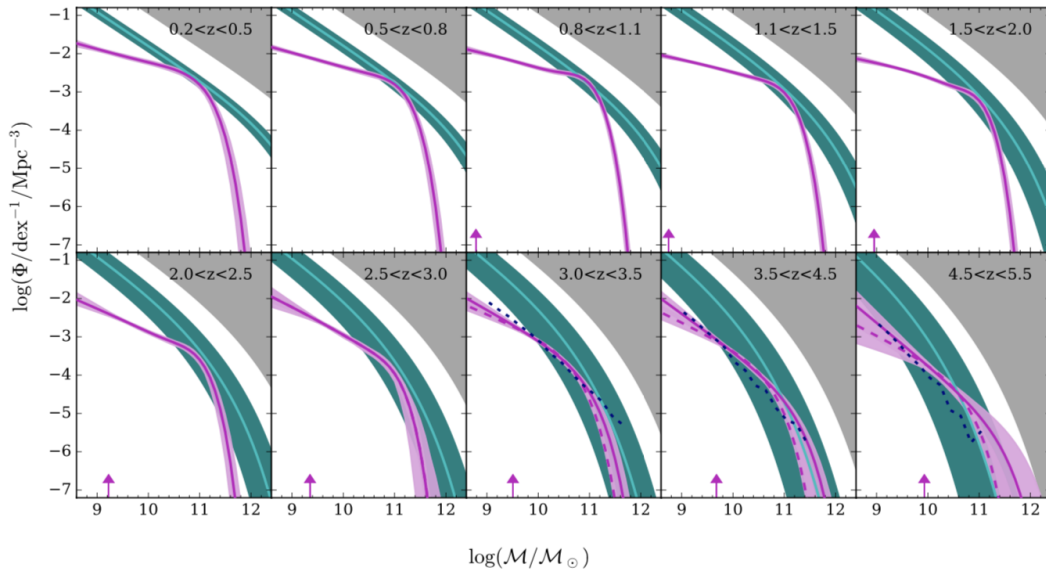


FIGURE 1.4: From Davidzon et al. 2017. Evolution of the total galaxy stellar mass function (magenta curve) and of the theoretical halo mass function (green curve). To ease the visualisation, the halo mass function as been normalized in mass by a factor 0.018 which corresponds to the stellar to halo mass ratio at $z=0$ at $M=M^*$.

led the empirical and theoretical approaches to broadly agree on the number density of quiescent galaxies at $z\sim 3$ (Merlin et al., 2019; Valentino et al., 2020) but it is unclear whether such an agreement continues to $z\sim 4$ and whether a population of passive objects exists as early as $z\sim 5$ in significant numbers (see Fig. 1.5). It should be noted, again, that such an agreement between observations and simulations is not firmly established. Systematics like the exact details on sample selection (such as the cut on the sSFR of QGs), the correction for completeness and the choice of the radius on which stellar masses and SFRs are computed in simulations, are crucial to determine whether such an agreement is robust. The effect of the latter can be seen in the difference of 1 dex at $z\sim 3$ between the number densities computed from Illustris TNG100 in Fig. 1.5 (dashed vs. solid blue lines). Moreover, in Valentino et al. 2020 it can be seen that observational samples can disagree by up to 1 dex due to differences in selection criteria. Also for example, at the time of writing, Forrest et al. 2020a claim that even Illustris TNG300 falls short at representing the observed numbers of QGs at $z\sim 4$.

Observed properties of massive quiescent galaxies at high redshift

Another fundamental advance brought by observational discoveries is the possibility of reconstructing the evolution of internal properties of QGs, such as their structure and the age of their stellar content. Detailed imaging revealed that at $z\sim 2$ they were on average 5 times smaller than at present

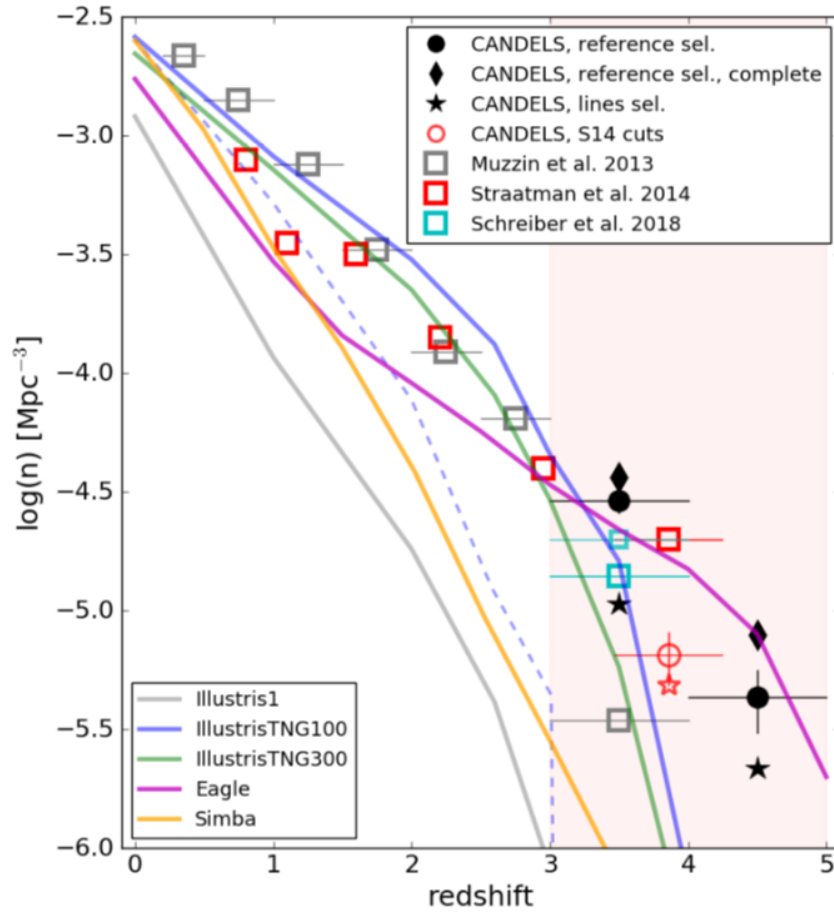


FIGURE 1.5: From Merlin et al. 2019. Number density of passive galaxies as a function of redshift. Observations from Muzzin et al. (2013b), Straatman et al. (2014), and Schreiber et al. (2018b) are shown with symbols whereas predictions from hydrodynamical simulations ($M_*/M_\odot > 5 \times 10^9$) are marked with curves. Illustris-1 (Vogelsberger et al., 2014a), Illustris-TNG100 and Illustris-TNG300 (Pillepich et al., 2018), Eagle (Schaye et al., 2015), and Simba (Davé et al., 2019). Photometric candidates at $3 < z < 5$ are marked by black symbols.

(effective radii $R_e = 1\text{--}2$ kpc) and a factor of ~ 100 more compact (Daddi et al., 2005; Trujillo et al., 2007; van Dokkum et al., 2008; Cimatti et al., 2008; Cassata et al., 2010; van der Wel et al., 2014). All-in-all, this means that the origin of the QG population at $\log(M_*/M_\odot) \geq 11$ as we see it today, is itself twofold: descendants of rapidly quenched high- z QGs can either survive as compact old remnants ("red nuggets" Trujillo et al., 2009; Poggianti et al., 2013) or grow in size through dry satellite accretion to become brightest central galaxies (BCGs) at the center of clusters' potential well (Naab, Johansson, and Ostriker, 2009; Hopkins et al., 2009; Poggianti et al., 2013; van der Wel et al., 2014). Regarding the age evolution of their stellar components, the boundedness of the age of the Universe can be leveraged to investigate the demographics of the quiescent population across cosmic time as it keeps emerging. In fact, as the population becomes younger and younger at increasing redshift, the discerning power of rest-frame optical spectra at mapping the early star formation of massive quiescent galaxies surpasses the one at low redshift. This is because around $z \gtrsim 2$ the Universe starts to be young enough to make stellar age differences of ~ 1 Gyr, down to few hundred Myr, visible thanks to the rapid appearance of Balmer absorption lines in stellar populations of ages < 1 Gyr, when A-type stars enter the Turn-Off (therefore increasingly dominating the integrated stellar spectra through the so-called "frosting effect" (Trager et al., 2000)). In particular, extensive information on their stellar ages has been collected, tracing the progressive youngening of $\log(M_*/M_\odot) > 11$ QGs with look-back time and revealing an increasing spread in stellar age and dust extinction with bulk values around 1–2 Gyr and $A_V = 0\text{--}1.0$ mag at $z \sim 2$, respectively. This is apparently happening while keeping high metallicities relatively close to local scaling relations and velocity dispersions about a factor of two higher than local values ($\sigma = 300\text{--}500$ km s $^{-1}$) (Toft et al., 2012; Onodera et al., 2012; van de Sande et al., 2013; Belli, Newman, and Ellis, 2015; Kriek et al., 2016; Belli, Newman, and Ellis, 2017; Estrada-Carpenter et al., 2019; Estrada-Carpenter et al., 2020; Stockmann et al., 2020).

In other words, for a substantial fraction of otherwise mature massive QGs, the frosting effect of recently formed stars is much stronger at these epochs than in the present day universe at fixed stellar mass. This is indirectly highlighting the increasing weight in mass at high- z of the latest episodes of star formation (Salvador-Rusiñol et al., 2019). This increased age spread is marking a change in the relative fraction of young vs. old QGs (age > 1 Gyr) in the build-up of the massive red sequence. Although spectroscopic confirmation is always required to reject low-redshift interlopers, number densities from photometric and spectroscopic samples appear to be in broad agreement (Whitaker et al., 2010; Whitaker et al., 2013). At the same time, the population of elliptical galaxies known at lower redshift to host recently formed A-type stars on top of a much more massive and older stellar component, the so-called "E+A" or "k+a" galaxies, (e.g. Dressler and Gunn, 1983; Zabludoff et al., 1996; Hammer et al., 1997; Dressler et al., 1999; Balogh et al., 1999; Goto et al.,

2003) has inspired the classification of many recently quenched massive QGs at $z > 1$ as post-starbursts (PSB). While for E+A or k+a galaxies there was a relatively strict selection on the absorption strength of $H\delta$, D_n4000 and on the absence of nebular emission lines such as [OII],[OIII], $H\alpha$ (e.g. $EW(OII) < 3-5 \text{ \AA}$ in emission, $EW(H\delta) > 3 \text{ \AA}$ in absorption, Goto, 2007; Poggianti et al., 2009); these conditions have been relaxed at high- z due to the decreased age of the universe (hence the consequent youngening of the underlying stellar continuum) and due to possible residual star formation after the supposedly abrupt truncation (Pawlik et al., 2018, for a review). Many works refer to galaxies with spectral fitting-derived ages $< 1 \text{ Gyr}$ (induced by the strong Balmer absorption features of A-type stars) as "A-type" PSBs, when not directly as PSBs (Wild et al., 2009; Whitaker et al., 2012a; Bezanson et al., 2013; Belli, Newman, and Ellis, 2015; Wild et al., 2016; Bezanson et al., 2019; Belli, Newman, and Ellis, 2019a). Detectable emission lines have however pros and cons: the inclusion of objects with weak [OII] or [OIII] emission in the sample selection allows, in principle, to investigate the presence of any residual star formation or AGN activity (i.e. stellar mass vs black hole mass growth) and any causal connection between the two. Indeed high fractions ($\sim 36-50\%$) of AGN were found among PSBs with emission lines (e.g. Wild et al., 2007; Yesuf et al., 2014) which favor the scenario in which AGN activity plays a role in inducing the rapid transition from star formation to passivity. However, weak emission lines plus strong Balmer absorption lines could also arise in case of an highly obscured on-going starburst: O, B stars would be completely dust enshrouded while only relatively old A-type stars in external regions would show up in the optical. This configuration has been found in IR luminous galaxies undergoing interactions or within a merger sequence (Poggianti and Wu, 2000; Calabrò et al., 2019a), reason for which FIR photometry is needed to properly assess the obscured SFR.

When considering the growth of the red sequence, the observed fraction of PSBs among massive QGs remains low $< 1-3\%$ from $z=0$ to $z \sim 0.5$ (Tran et al., 2003) and fastens between $z \sim 1-2$ to $\sim 20\%-50\%$, with percentage variations mirroring different selection criteria (Le Borgne et al., 2006; Whitaker et al., 2013; Wild et al., 2016). The mounting fraction of massive QGs with evidence of recent quenching already accounts for half of the population at $z \sim 2$, when their number densities start to match (Arnouts et al., 2007; Whitaker et al., 2012b). This is further supported by the growth rate of $\log(M_*/M_\odot) \geq 10.8$ PSBs of less than 1 Gyr at $z \sim 2$, which accounts for half that of the whole quiescent population (Belli, Newman, and Ellis, 2019b).

In short, the increased spread in stellar ages in massive high- z QGs and the increasing number density of PSBs are both pointing at an epoch when their relative contribution to the quiescent population is reversed, posing interesting questions on the global SFH of QGs in light of the most distant spectroscopic confirmations. This point will be addressed in the last chapter of this thesis.

1.4 Thesis motivation

1.4.1 Investigating the nature of high- z photometric candidates

Until recently, large samples of QGs had been constructed up to $z \sim 2.5$ in COSMOS and the CANDELS fields exploiting large telescopes (e.g. Bezanson et al., 2013; Belli, Newman, and Ellis, 2015; Onodera et al., 2015; Kriek et al., 2016; Belli, Newman, and Ellis, 2019a; Stockmann et al., 2020) or HST in combination with strong lensing (Whitaker et al., 2012b; Whitaker et al., 2013; Newman et al., 2018). After the discovery of quenched galaxies at $z \gtrsim 3$ ignited by the high number of candidates in photometric samples (Straatman et al., 2014; Merlin et al., 2018; Santini et al., 2019), the identification and spectroscopic verification of compact massive QGs at higher redshift has been accelerating (Gobat et al., 2012; Glazebrook et al., 2017b; Schreiber et al., 2018b; Valentino et al., 2020; Forrest et al., 2020a; Forrest et al., 2020b). However, the extremely long integration times required to observe these galaxies still represent a barrier when trying to increase the statistics and characterise in detail the physical properties of the whole population. This is particularly the case when trying to infer robust age estimates and when looking for possible progenitors.

One of the critical steps to identify quiescent galaxy candidates is selecting galaxies with sufficiently red colors. The two most used techniques are the BzK criterion in the observed-frame (Daddi et al., 2004) and the UVJ criterion in the rest-frame (Wuyts et al., 2007; Williams et al., 2009). The BzK criterion (see Figure 1.6) singles out as passively evolving objects those that satisfy the following condition:

$$BzK \equiv (z - K)_{AB} - (B - z)_{AB} < -0.2 \cap (z - K)_{AB} > 2.5$$

which traces the spectral range in which either the Balmer break or the 4000 \AA falls between the observed z and K filters, with sufficient emission detected also in the B band. This method does not require any model-dependent SED fitting but its maximum efficiency is limited to $1.4 < z < 2.5$. After $z > 2.5$ the Lyman limit starts to approach the observed B band while the z magnitude becomes progressively fainter.

The UVJ criterion (which stems from the early works of Pozzetti and Manucci 2000 and Labbé et al. 2005), on the other hand, requires the knowledge of a photometric redshift in order to compute rest-frame colors but has the advantage of being applicable up to the highest redshifts (provided that a clear distinction between the star-forming and passive population is still in place). It selects quiescent systems in the following locus:

$$(U - V)_{\text{rest}} > 1.3, (V - J)_{\text{rest}} < 1.5 \text{ at all redshifts}$$

$$(U - V)_{\text{rest}} > (V - J)_{\text{rest}} \times 0.88 + 0.59 \text{ at } 1.0 < z < 4.0$$

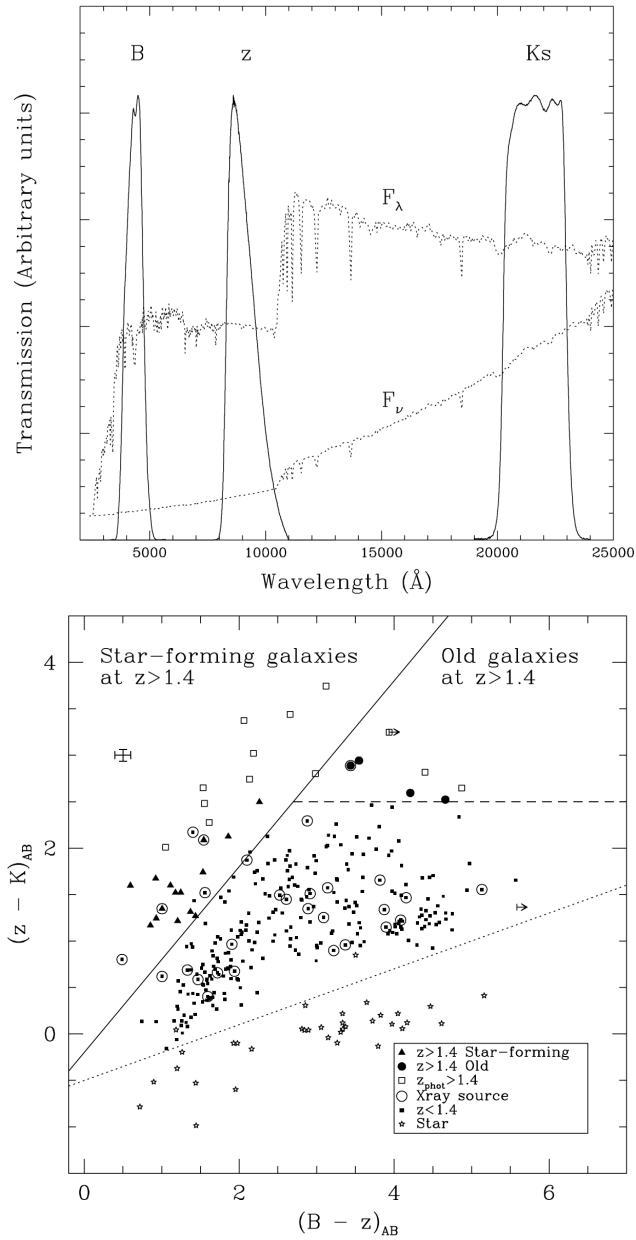


FIGURE 1.6: The transmission curves of the BzK filters (top panel) and the BzK diagram used to select $z > 1.4$ galaxies (bottom panel), both from Daddi et al. 2004. The top panel also shows the SED of a galaxy at $z=1.729$ for reference.

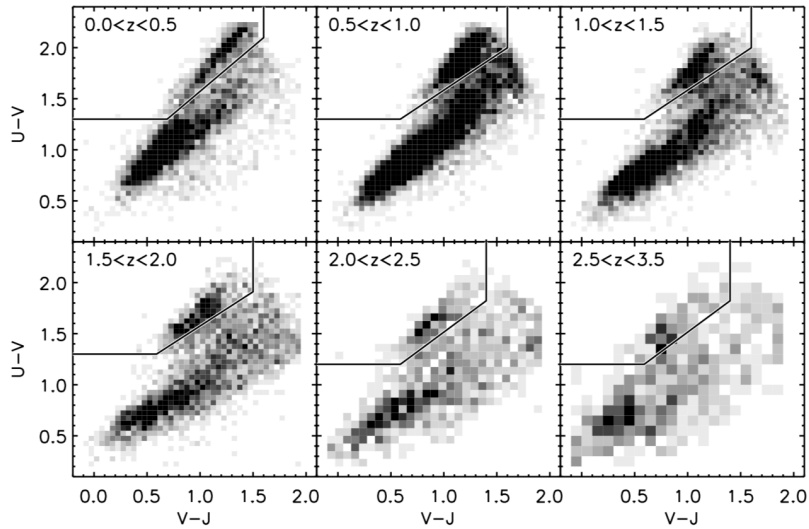


FIGURE 1.7: From Whitaker et al. 2011. The UVJ selection in Whitaker et al. 2011 differs from that of Muzzin et al. 2013b in that the quiescent boundaries are adjusted to include bluer objects at increasing redshifts.

(Muzzin et al., 2013b) which contains quiescent galaxies in a more or less steady track as they become redder with cosmic time, ending in a tight sequence at $z=0$. Dust extinction has the effect of shifting galaxies along a diagonal of fixed slope, making this technique relatively robust against the age-dust degeneracy (see Fig. 1.7).

Attempts at mapping the UVJ diagram in terms of age, dust extinction and sSFR to derive a color-age calibration using spectroscopically confirmed samples have been performed up to $z \sim 1.5-2$ (Belli, Newman, and Ellis, 2015; Belli, Newman, and Ellis, 2019b) and lead to identify where recently quenched galaxies lie (see Fig. 1.8). At higher redshift, the lack of sizable samples of quiescent galaxies has hindered the verification of such calibration, especially at redder UVJ colors. In particular, complex dust geometries can scatter objects in the passive UVJ region, especially in the region generally associated to old passive galaxies due to strong dust attenuation in red star-forming galaxies (Lemaux et al., 2017; Forrest et al., 2020b). In general, the extensive use of the UVJ color selection at all redshifts effectively shows that the quiescent population shifts to bluer colors at high- z (bounded by the age of the universe) while also suffering from increasing contamination by star-forming galaxies given the increased scatter in the blue cloud (see Fig. 1.7, Whitaker et al., 2011; Muzzin et al., 2013b; Lemaux et al., 2017). This makes the UVJ selection prone to contamination, estimated to be around 20% at $3 < z < 4$ (Schreiber et al., 2018b).

The need for sufficient S/N for spectroscopic confirmation is typically shifting the selection towards the most luminous objects falling in the region below the standard quiescent boundary (down to $(U-V) \sim 1$ and $(V-J) \sim 0.3$) where young PSBs and transitioning objects can be found (e.g. Schreiber

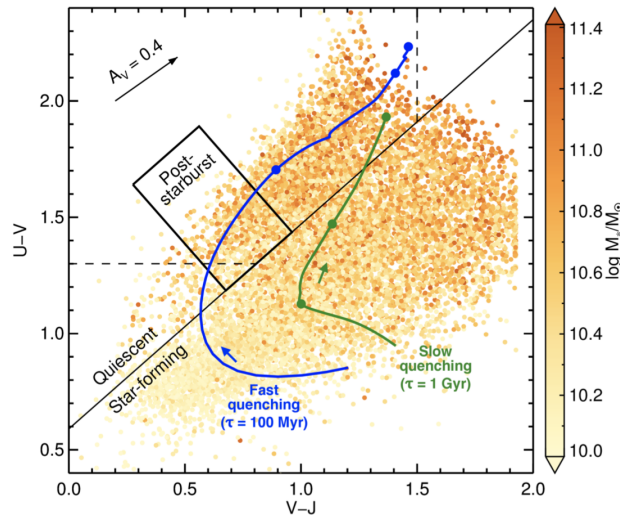


FIGURE 1.8: From Belli, Newman, and Ellis 2019b

et al., 2018b; Valentino et al., 2020). However, compact dusty star-forming galaxies are known to also populate the same locus (Barro et al., 2013; Barro et al., 2014; Marsan et al., 2015). This, together with the current lack of testing for the robustness of the color-age calibration at high- z , makes spectroscopic confirmation compelling when studying high- z QGs. Ancillary FIR imaging is also mandatory in order to probe the presence of obscured star formation. This thesis work is particularly devoted to this: the spectroscopic confirmation of a statistical sample of QGs candidates, the assessment of the degree of their SFR suppression and the characterisation of their quiescence stage. This was done in an attempt to get clues of the properties of massive QGs at an epoch when quiescent and star-forming galaxies appear to be broadly converging.

1.4.2 Understanding what drives the transition towards quiescence

While we do not specifically tackle with direct observations the identification of progenitors, it is worth mentioning few of the channels of formation and fast quenching that have been proposed so far in the literature. The extreme stellar densities suggested by compact quiescent systems at $z \sim 2$ (Franx et al., 2003; Daddi et al., 2005; van Dokkum et al., 2008; Newman et al., 2012) suggest intense bursts of star formation triggered by the rapid collapse of a large amount of gas occurred at $z > 4$. This could be resulting, for example, from starbursting cores plunging down into quiescence after a dissipative gas-rich merger (Cimatti et al., 2008; Elbaz et al., 2018; Gómez-Guijarro et al., 2018; Gómez-Guijarro et al., 2019; Puglisi et al., 2019) or more “secular-like”

evolution followed by violent disk instabilities in high-redshift dusty star-forming galaxies, quickly accreting and consuming gas, leaving compact passive remnants (e.g. Dekel, Sari, and Ceverino 2009; Barro et al. 2013; Toft et al. 2014a; Zolotov et al. 2015; Valentino et al. 2020).

The relative roles of strong AGN-driven outflows expelling large gas reservoirs from a galaxy ("quasar-mode AGN feedback", e.g. Silk and Rees 1998; Bower et al. 2006; Croton et al. 2006; Hopkins et al. 2008; Cattaneo et al. 2009) and strangulation by virial shock heating in dark matter (DM) overdensities is still to be clarified: recent simulations show, for example, that the quiescent population up to $z \sim 2$ can be reproduced simply shutting off cold gas infall, leaving existing gas to be consumed by star formation (Gabor and Davé, 2012; Davé et al., 2017). The shortcoming of this latter scenario is that such infalling streams have yet to be observationally established.

Interestingly, it appears that the absence of cold gas is not even a necessary condition for a galaxy to be quenched, as mounting evidence show the presence of quiescent galaxies with a suppressed star formation efficiency (e.g., Davis et al. 2014a; Alatalo et al. 2014; French et al. 2015; Schreiber et al. 2016; Suess et al. 2017; Lin et al. 2017; Gobat et al. 2018), defined as the star formation rate per unit gas mass ($SFE=SFR/M_{\text{gas}}$)

Despite the major achievements accomplished so far in this field, it remains unknown whether there is a dominant process among these channels that causes quenching (Man and Belli, 2018). As previously mentioned, the termination of star formation in the most massive galaxies at high redshift must have been particularly rapid. Many simulations ascribe fast quenching to powerful injection of energy into the ISM such as AGN feedback. However, though closely related, quenching and feedback are not necessarily synonyms. Also, generally speaking, any process that works against the presence of unstable cold molecular gas ($T < 10^2 \text{K}$) in a galaxy is contributing to its quenching. I summarize below the main processes known to affect galaxies. Currently, there is no consensus on the exact interplay of such mechanisms.

Starting from the largest scales, cosmological starvation models (Feldmann and Mayer, 2015) predict that, after a first period of gas accretion and exponential growth of the SFR, the gas and DM accretion rates onto their haloes first stall and subsequently decrease, leaving the galaxy to exhaust its remaining reservoirs. This scenario predicts that galaxies in a still collapsing large-scale structure have larger sSFRs than central galaxies embedded in a relaxed, virialized environment. Also, it predicts recently quenched, high- z galaxies to have on average fewer satellites at large distances than star-forming galaxies of the same stellar mass. This model relies on the presence of some maintenance mode to prevent further star formation from stellar evolution driven mass loss.

Another channel that prevents cold gas from accreting onto a galaxy is the

development of a stable virial shock in sufficiently massive haloes (generally $\sim 10^{12} M_{\odot}$ at $z < 1.5$, even if the threshold is somewhat arbitrary and model dependent). This mass threshold is thought to increase at high- z up to $\sim 5 \times 10^{13} M_{\odot}$ at $z = 3-4$, where the so-called "cold accretion" is thought to take place in a hot diffused shock-heated gas (e.g. Dekel and Birnboim, 2006; Cattaneo et al., 2006). After the shock, however, the hot halo gas should cool and become available for star formation. To prevent this process, additional gas heating is necessary. The two channels that could have a role are jet-powered radio-mode feedback from radiatively inefficient accretion onto a SMBH (Best et al., 2005; Croton et al., 2006) or gravitational heating from infalling satellites releasing potential energy in the diffuse medium through ram pressure or dynamical friction (Dekel and Birnboim, 2006; Khochfar and Ostriker, 2008; Johansson, Naab, and Ostriker, 2009; Johansson, Naab, and Ostriker, 2012).

Additionally, the star formation efficiency of a galaxy can be impacted by its internal structure. The shear induced by the presence of a pressure-supported stellar bulge could prevent any available gas from becoming unstable and fragment into star forming clumps. This is often referred to as "morphological quenching" (Martig et al., 2009). This phenomenon is thought to act as a maintenance mode when the SFR and the gas mass of a galaxy have already significantly decreased ($< 10\%$ - 20% with respect to the initial value).

Another very popular scenario combines fast gas consumption with expulsion: major mergers or violent disk instabilities can compress the gas into massive compact cores and trigger starburst events which rapidly consume the gas of the system (Dekel and Silk, 1986; Murray, Quataert, and Thompson, 2005). Quasar activity is ignited by these processes, launching powerful outflows into the CGM and depleting the host galaxy from its reservoirs (Sanders et al., 1988; Di Matteo, Springel, and Hernquist, 2005; Hopkins et al., 2006; McCarthy et al., 2011). However, at high z the link between merging and quasar activity is not clear (Schawinski et al., 2011; Kocevski et al., 2012) except at the highest quasar luminosities (Treister et al., 2012), neither is clear the link between quasar activity and star formation (Goulding et al., 2014).

Chapter 2

Target identification and observations

To understand what causes quenching at an epoch when the star formation rate density of the Universe was close to its maximum one of the most promising ways is to trace the earliest appearance of galaxies with a suppressed star formation activity. However the higher the redshift, the lower the number density of massive quiescent systems. In particular, as shown in Fig. 1.5, the number density of massive QGs drops rapidly with redshift. At $z \sim 3$, photometric samples such as in Straatman et al. (2014) point at a drop by roughly a factor of 10 with respect to $z \sim 2$. At the redshift of our interest, the "candidate" number density being of the order of $10^{-4.5} \text{ Mpc}^{-3}$, less in case of contamination by low redshift interlopers or misclassifications. In terms of surface densities, it is indicating $\lesssim 10^2 \text{ deg}^{-2}$ demonstrating the need of large fields to both identify candidates in significant numbers and reduce the impact of cosmic variance. The COSMOS field is up for the task, being also equipped with deep multi-wavelength photometric coverage, necessary to robustly assess the colors and SEDs of faint galaxies for target selection.

After an overview of the COSMOS field properties, I will describe the key characteristics of slitless spectroscopy with a particular focus on the Wide Field Camera 3 (WFC3) G141 disperser. A description of the sample selection and of the observations will follow. Afterwards, I will describe the main parts of my work which consisted in the data reduction and analysis of the acquired data. In section 2.5.1, I will describe the setup for the spectral fitting and the results obtained in terms of spectroscopic confirmation. The methods used to assess the level of quiescence of the galaxies in our sample will be shown in the following chapter.

2.1 The COSMOS field

The Cosmic Evolution Survey (COSMOS, Scoville et al. 2007) is a large program designed to study the evolution of galaxy physical properties, star formation and BH activity with cosmic time within the LSS. The survey covers a $\approx 2 \text{ deg}^2$ field centered at RA= +150.11917 and DEC= +2.20583 degrees (J2000). The position near the celestial equator was chosen primarily

to guarantee visibility from all major astronomical facilities while ensuring a region devoid of stars, bright X-ray, UV and radio sources. Also, the region was selected for its low galactic extinction ($\langle E_{B-V} \rangle \sim 0.02$ mag) to reduce dust contamination and background when observing faint distant sources.

The field has been extensively studied over the years and imaging from the X-rays to the radio domain is available at different depths. In particular, the latest publicly available observed-frame data consist of:

- X-ray: Chandra coverage for a total depth of 2.2×10^{-16} erg cm⁻² s⁻¹ in the soft band (0.5-2 keV) and 1.5×10^{-15} erg cm⁻² s⁻¹ in the hard band (2-10 keV). The original 1.8 Ms Chandra COSMOS Survey program (C-COSMOS Elvis et al., 2009) was incorporated in the latest COSMOS-Legacy survey (Civano et al., 2016) reaching a total of 4.6Ms. The central 1.5 deg² area is covered by an effective exposure of 160 Ks with an external shallower region at 80 Ks reaching a total area of 2.2 deg². The Chandra COSMOS Legacy survey contains 4016 X-ray sources, 97% of which have optical and NIR counterparts available in Marchesi et al. (2016).
XMM-Newton observations are also available as part of the XMM-COSMOS program which consists of 55 pointings for a total exposure of ~ 1.5 Ms reaching a flux limit of $\sim 1.7 \times 10^{-15}$ erg cm⁻² s⁻¹ and $\sim 9.3 \times 10^{-15}$ erg cm⁻² s⁻¹ over 1.92 deg² in the soft and hard band respectively (Cappelluti et al., 2009).
- Ultraviolet-Optical: near-UV (~ 2310 Å) and far-UV (~ 1530 Å) imaging from GALEX down to $m_{AB}=25.5$ were used in the latest¹ COSMOS2015 data release (Zamojski et al., 2007; Laigle et al., 2016). PSF-homogenised imaging in the optical regime was obtained through a wide set of broad-, intermediate- and narrow-band filters, the deepest of which are: u^* (CFHT/MegaCam) and BVi^+z^{++} (Subaru/Suprime-Cam) from the COSMOS-20 survey (Capak et al., 2007; Taniguchi et al., 2007; Taniguchi et al., 2015) reaching a 3σ depth of $m_{AB}=25.9-27$ in 3" apertures;
- Near-IR: the NIR mapping of COSMOS in $YJHK_s$ is one of the deepest available, yet the coverage is not homogeneous. The field can be divided into the UltraVISTA area (1.8deg², McCracken et al. (2012)) and a WIRCam-only area which provides H and K_s coverage outside UltraVISTA (limiting $K_s = 23.4$ at 3σ in a 3" aperture, McCracken et al. (2010)). The UltraVISTA region can be further divided into a Deep region reaching $H=24.3$ and $K_s = 24.0$ AB mag (both 3σ) over the full area and into 4 additional UltraDeep stripes (0.8 deg² in total) with a gain of 0.2-0.7 mag in the 3σ limiting AB magnitude depending on the filter. Ultradeep H and K_s reach down to 3σ $H=24.6$ and $K_s = 24.7$ AB mag respectively.

¹At the time of writing.

The latest COSMOS2015 catalog improves the previous 30-band Muzzin et al. (2013a) catalog with the addition of deeper B and $YJHK_s$ images over a larger area (1.62 vs. 2 deg²) and the use of the z^{++} filter to increase the catalog completeness for bluer objects;

- Mid-IR: deep images were taken with Spitzer/IRAC at 3.6, 4.5, 5.8 and 8.0 μm (channels 1, 2, 3 and 4 respectively) during the SPLASH (PI: P. Capak) and S-COSMOS (Sanders et al., 2007) programs. The magnitude limits (3σ depth, 3" aperture) are 25.5 AB mag for channels 1 and 2, and 23 AB mag for channels 3 and 4. At longer wavelengths, Spitzer/MIPS has observed COSMOS at 24 μm resulting in the blindly extracted source catalog of Le Floch et al. (2009) (80 μJy sensitivity). Recent improvements in source detection and deblending have been performed by Jin et al. (2018) and included in the "Super-deblended" FIR catalog;
- Far-IR and sub-mm: Observations in the far-IR were obtained with Herschel/PACS (100 and 160 μm Poglitsch et al., 2010) and Herschel/SPIRE (250, 350, 500 μm Griffin et al., 2010) during the PACS Evolutionary Probe (PEP Lutz et al., 2011) and the Herschel Multi-tiered Extragalactic Survey (HerMES, Oliver et al., 2012) programs. Sub-mm and mm imaging is also available: at 850 μm with SCUBA2 from the S2CLS program (Cowie et al., 2017; Geach et al., 2017), at 1.1 mm with ASTE/AzTEC (Aretxaga et al. 2011) over a sub-area of 0.72 deg² and at 1.2 mm with MAMBO (Bertoldi et al., 2007). These data are highly affected by blending and confusion due to the PSF of observations whose FWHM is increasing significantly with wavelength, ranging for example from $\sim 6''$ at 24 μm to 7-12" at 100 and 160 μm to 36.7" at 500 μm ;
- Radio: COSMOS has been extensively observed at 20 and 10 cm with the VLA as part of the 1.4 GHz Deep Project (Schinnerer et al., 2010) and the VLA-COSMOS 3 GHz Large Project (Smolčić et al., 2017) respectively. The former has a uniform rms sensitivity of $\sim 10\text{-}15 \mu\text{Jy beam}^{-1}$ over the 2 square degrees with an angular resolution of 1.5" thanks to the previous VLA-COSMOS 1.4 GHz Large Project data, improving the sensitivity in the central square degree down to ~ 7 (12) $\mu\text{Jy beam}^{-1}$ at a resolution of 1.5" (2.5"); the latter reaches a 3GHz rms = 2.3 $\mu\text{Jy beam}^{-1}$ at a $\sim 0.75''$ resolution over the whole field;

COSMOS has been observed with HST in the optical and near-IR by several programs, providing additional imaging and grism spectroscopic coverage (mostly F814W, F125W, F160W and G102, G141 respectively). The deepest area is indeed CANDELS (Koekemoer et al., 2011), counting 88 orbits allocated in Cycles 19 and 20 focused on a 0.05 deg² central region of the field (WFC3+ACS in parallel). There are additional 68 G141 pointings plus 12 G102 pointings allocated during Cycles 18 and 19 to the 3D-HST/CANDELS

project (Momcheva et al., 2016) with two-orbit WFC3 visits (G141 in combination with F140W shallow imaging as direct exposures).

2.2 Sample selection

The sample selection for our HST Cycle 25 observations was performed on the McCracken et al. (2010) catalog, extracting sources with $K_{\text{tot}} < 22.5$. At this stage, only sources satisfying the observed-frame BzK criterion were kept. However, objects formally classified as star-forming BzK but having a signal-to-noise ratio $S/N < 5$ in the B and z bands were retained. Their classification as star-forming, in fact, is degenerate with quiescent galaxies at lower masses or increasing redshift (since QGs become fainter in such bands). The photometric redshifts necessary for the UVJ color selection were derived via EAZY (Brammer, van Dokkum, and Coppi, 2008). These were calibrated for high-z sources using the calibration methods in Onodera et al. (2012) and Strazzullo et al. (2015). Briefly, the calibration on high-z z_{phot} retrieval is done estimating systematic photometric offsets on the McCracken et al., 2010 photometry between the default EAZY templates and the best-fit values obtained running EAZY on a training sample after having fixed the redshift to the known spectroscopic value. For each band, the median offset between the observed galaxy flux and the flux of the best-fitting templates is applied to each passband, iterating until convergence. For source identification at $z \sim 3$, the calibration of Strazzullo et al., 2015 was used, adopting the sample of 34 passive galaxies at $1.3 < z_{\text{spec}} < 2.1$ observed with VLT/VIMOS which later appeared in Gobat et al. (2017) and the sample of 18 passive galaxies at $1.4 < z_{\text{spec}} < 1.9$ of Onodera et al. (2012) observed with Subaru/MOIRCS as spectroscopically confirmed training sets.

Such calibrated z_{phot} were used to select galaxies within $2.5 \leq z_{\text{phot}} \leq 3.5$ and to remove objects whose UVJ colors were inconsistent with passive evolution. A first test on the quiescent nature of the candidates was performed by means of SED fitting. FAST (Kriek et al., 2009) was used to fit the observed SEDs with constant and delayed exponentially declining SFHs and optical dust attenuation free to vary up to $A_V = 5$ mag (assuming a Calzetti et al. (2000) attenuation law). The SED fits were repeated adopting only purely quiescent templates to identify the sources with the highest probabilities of being quiescent. All sources with optical-NIR broadband photometry consistent with star-forming solutions were rejected. A further cut was applied on all objects with Spitzer/MIPS $24\mu\text{m}$ $S/N > 4$ detections in Le Floch et al. (2009) catalog to reduce contamination by dusty star-forming galaxies. The only exceptions were galaxies with high-confidence passive SEDs since their $24\mu\text{m}$ emission might be produced by a central dusty AGN torus.

Among the most massive bona fide passive candidates, 10 galaxies were targeted for HST WFC3/IR G141 near-IR² observations: 9 with $H_{\text{AB}} < 22$

²Rest-frame near-UV/optical.

($M_* > 1.1 \cdot 10^{11} M_\odot$) and 1 robust candidate with $H_{AB}=22.9$ ($M_* = 8 \cdot 10^{10} M_\odot$) as the highest- z candidate. Hereafter stellar masses are quoted for a Salpeter (1955) IMF unless otherwise specified.

2.3 Slitless spectroscopy with HST: characteristics and observations

Ground-based observations have already confirmed the existence of quiescent galaxies at $z \sim 4$ (Schreiber et al., 2018b; Valentino et al., 2020; Forrest et al., 2020a). However, in the framework high- z galaxy evolution, their statistical power is mostly modulated by the time-expensiveness of such campaigns. Being a space-based facility, HST skips OH sky emission lines and related background that affect ground-based observations. At $z \sim 3$, this ensures extended and continuous spectral coverage on the Balmer/4000 Å breaks while reducing the integration times necessary to have sufficient S/N per resolution element. This means that HST represents an efficient trade-off between spectral resolution and statistics for high- z studies. I would like to recall here the properties and strengths of HST slitless spectroscopy used in this work.

The HST WFC3 features two independent imaging channels: the UV/Visible channel (UVIS) and the near-IR channel (IR). The latter is optimized to cover the spectral range from $0.8 \mu\text{m}$ to $1.7 \mu\text{m}$ thanks to a Teledyne HgCdTe detector array, whose central 1014×1014 pixels are used for imaging. A channel-selection mirror directs on-axis light from the HST optical telescope assembly (OTA) to the IR channel as can be seen in Fig. 2.1. HST IR channel has a native pixel scale of $\approx 0.13''/\text{pixel}$ and a field of view (FOV) of $136'' \times 123''$, namely 4.65 arcmin^2 . It is worth mentioning that the advantage of an IR detector over a CCD detector is to allow the non-destructive accumulation of signal to reduce read-out noise and recognize pixels affected by cosmic rays (CRs) in different reads. This is achieved during observations with a scheme of short exposures ("ramps") that will be featured also in future facilities such as JWST/NIRSpec.

Slitless spectroscopy uses a dispersive and transmissive element (the grism) to produce a dispersed image of the sky. This technique lacks a physical aperture, therefore the observed two-dimensional spectrum can be understood as the intrinsic spectrum of the source processed by the dispersing element, convolved with the source's spatial profile. An example of this can be seen in Fig. 2.2. This implies that the physical extent of the source along the dispersion direction will introduce "self-contamination" which will limit the achievable spectral resolution. The IR channel features 2 dispersive elements (G102 and G141) together with several sets of wide- and medium-band filters. The spectral range of interest to observe $z \sim 3$ targets is covered by the G141 grism (from 1.1 to $1.7 \mu\text{m}$ with maximum transmission

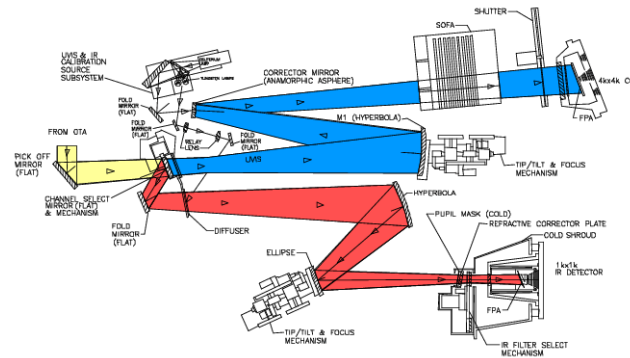


FIGURE 2.1: Setup of the WFC3 instrument. The red path shows the structure of the IR channel, as opposed to the UVIS channel (blue).

at $1.45 \mu\text{m}$). The G141 mean dispersion in the first spectral order is $46.5 \text{ \AA pixel}^{-1}$ yielding a maximum resolution of $R \sim 130$ at $1.6 \mu\text{m}$ and varying by a few percent across the FOV. However, given the dependence of the spectral resolution on the size of the source along the dispersion axis, direct and grism observations are done in pair, usually selecting an imaging filter whose response closely follows the grism one. This is done also for the sake of sources' astrometric registration and recovery of the absolute wavelength scale. In our case, F160W was coupled to the G141 disperser since it enabled a good spectral coverage on the tip of the spectral breaks, maximizing the S/N of H-band imaging.

The lack of a physical slit also means that grism spectroscopy is particularly appropriate for faint sources since it has the advantage of eliminating flux losses due to narrow slits. Additionally, it is possible to simultaneously acquire the spectra of nearly all the sources falling in the FOV, making this technique attractive for future surveys such as JWST or WFIRST. An example of this can be seen in Fig. 2.5 which shows two of the reduced frames containing our highest z source (located at the center). A limitation in this regard is represented by contamination of the spectral traces by neighboring sources: since no prior selection of targets can be done, many spectral orders (zeroth, first, second etc.) are typically visible in the FOV. This introduces a non-zero probability that the spectral traces of sources at distances of several hundred pixels will overlap with the one of interest. In principle, for single targets this can be eliminated (or at least mitigated) by the careful selection of the ORIENT angle before observation. Moreover, observations of field galaxies are greatly favored because of reduced over-crowding. This enables the search for serendipitous spectral breaks. Several of them were found in our grism exposures and will be addressed in the last chapter of this thesis. Finally, spectral extraction is often performed following the optimal weighting technique introduced by Horne (1986) and Robertson (1986). This is aimed at maximizing the S/N ratio of spectra by attributing lower weights to pixels that contain only a small fraction of the object's flux.

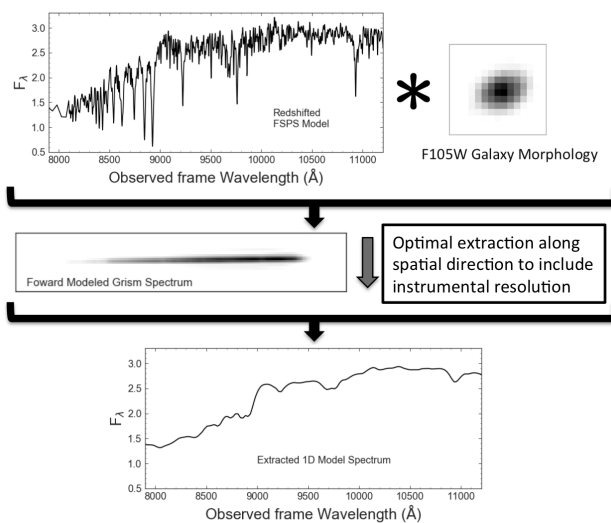


FIGURE 2.2: From Estrada-Carpenter et al. (2019). In slitless spectroscopy the source spatial extension along the dispersion axis serves as a slit aperture, determining the final spectral resolution. It can be thought of as if the intrinsic spectrum of each pixel gets convolved with the H-band spatial profile of the source (F160W in our case) and the G141 grism resolution (top row) producing the two-dimensional spectrum shown in the middle row. Optimal extraction is then necessary to obtain a 1D spectrum and reduce further self-contamination due to any source asymmetry in the external regions.

2.3.1 Observation strategy

A total of 17 orbits were allocated for program GO 15229 (PI: E. Daddi). Observations took place from January 11th 2018 until December 2nd 2018. Each visit consisted of 1 to 3 orbits according to each target H_{AB} magnitude. The overall schedule can be found in Table 2.1. For each target the first orbit was split into a direct F160W exposure (for a total of 984 s) and a grism G141 exposure (for a total of 1498 s), adopting the WFC3-IR-DITHER-LINE-3PT dither pattern to improve the sampling of the PSF. For targets with 2 orbits, the second orbit was also split in two, with total direct exposure 73 s and 2496 s in grism mode adopting WFC3-IR-DITHER-BLOB dither pattern. The third orbit for id361413 was a repetition of the second one. The ORIENT was carefully chosen at this stage for each target as to avoid any contamination from neighboring sources.

TABLE 2.1: Coordinates and orbit details for the targeted galaxies. IDs are quoted as in the Laigle et al. (2016) catalog which will be used for the rest of the analysis.

ID _{Laigle}	RA	DEC	N _{orbits}	total int. time (s)	
				F160W	G141
135730	10:01:39.9790	+01:29:34.49	1	983.8	1497.7
707962	09:59:32.5170	+02:22:21.99	1	983.8	1497.7
503898	10:01:31.8594	+02:03:58.79	1	983.8	1497.7
137182	10:00:57.3452	+01:29:39.46	1	983.8	1497.7
252568	09:57:48.5727	+01:39:57.82	2	1056.7	3993.9
977680	10:00:12.6549	+02:47:23.47	2	1056.7	3993.9
575436	10:00:43.7668	+02:10:28.71	2	1056.7	3993.9
478302	09:59:1.3123	+02:01:34.15	2	1056.7	3993.9
447058	09:59:11.7700	+01:58:32.96	2	1056.7	3993.9
361413	10:02:0.9700	+01:50:24.30	3	1129.7	6490.1

2.4 Data reduction

I performed the data reduction of direct F160W and grism G141 exposures exploiting the pipeline *grizli*³, version number *0.7.0-34-g91c9412* developed by G. Brammer. The pipeline is structured in a series of nested Python modules which allow end-to-end processing of WFC3/IR data, starting from their retrieval from the HST MAST web archive to their spectral fitting.⁴ Since the pipeline was under development, I applied each module/section step by step in order to check whether the data quality was satisfactory. In the following, I will describe the main steps of the data reduction. After introducing sub-pixel shifts (few percent of a pixel along the x-axis) for relative alignment between each direct and grism exposures, absolute astrometric registration was performed providing the pipeline with COSMOS ACS I-band reference catalogs of RA/DEC positions of sources brighter with $I_{AB} < 27$ mag within a radius of 5' from each target.

Extraction of WFC3/IR slitless spectra depends on an accurate determination of the diffuse background light that is observed in all grism exposures. The two-dimensional structure in the background is caused primarily by overlapping grism spectral orders, vignetted in different position in the FOV and by the spectrum of the diffuse background. To subtract this structure, *grizli* exploits the Master sky images from Brammer, Ryan, and Pirzkal, 2015 applying a grey correction using the F160W flat-field for the G141 grism.

³<https://github.com/gbrammer/grizli>

⁴The spectral fitting in this work was carried out using *czspecfit*, a custom IDL routine used in previous works within our collaboration (e.g. Gobat et al., 2012; Gobat et al., 2017), in order to not introduce further uncertainties when comparing results.

Residuals are generally of the order of 0.5-1% of the overall background level. The source of such residuals is still unclear, plausibly they are due to spectra slightly below the detection limit. However, these are further removed subtracting the column-average of the sky pixels in the grism exposures. During this phase the pipeline also runs Astrodrizzle to reject dead or hot pixels, cosmic rays, persistence and other artifacts combining the dithered exposures. The final drizzling parameters were kept as default. An example of the reduced and combined direct and grism exposures is shown in Fig. 2.5.

SExtractor (Bertin and Arnouts, 1996) is applied to the drizzled and combined direct exposure to create a segmentation map. This identifies all the detected sources above the detection threshold and uses their positions and flux densities (integrated over the pixels in each segmentation area) to model the spectral trace of each object on each of the grism exposures. This is done in order to generate model contaminants to be subtracted from the target's cutout. The spatial region impacted by contamination is calculated based on the extent of the segmentation region of the contaminant itself. The spectral orders to include in the model contaminant are instead determined on the basis of the object brightness. At this stage, the detector's FOV is parsed and modelled assuming simple linear continua for all objects in the field (brighter than 25 mag). The pipeline then refines the modelling of the brightest objects ([16, 24] mag) with a second order polynomial fit, fitting spectra directly after subtracting off the models for contaminants. The reduced and decontaminated 2D spectra of our targets are presented in Fig. 2.6 together with their relative F160W cutouts.

The 1D spectra were eventually optimally extracted by the pipeline following Horne (1986). Each pixel in the cross-dispersion direction of the 2D spectrum is weighted according to the fraction of the source's flux expected to fall in that pixel (assuming a uniform spatial profile) and to the pixel variance. The final adopted scale of the extracted spectra is 0.8 in units of the native dispersion of the G141 spectrograph.

Their flux calibration was later checked by comparing the average flux density around the spectral break to the one obtained for the aperture-corrected total H-band magnitude in Laigle et al., 2016. For id135730 and id707962 a correction of almost a factor of 2 was necessary. We ascribe this effect to a combination of signal in the very extended wings lost by the segmentation map (due to high Sérsic indices) further downweighted by optimal extraction and possible aperture effects in the photometry. However, most of the analysis performed in the rest of the work is not directly dependent on the relative calibration between spectroscopy and photometry. When necessary, as in the creation of the stacked spectrum, spectroscopy and photometry were matched in flux (Sect.4.1). The final set of spectra with their relative SEDs can be found in Fig. 3.1.

As a sanity check with respect to noise correlation introduced by the drizzling procedure, the distribution of the noise taken in multiple regions in each 2D cutout was fitted with a gaussian of varying mean and standard

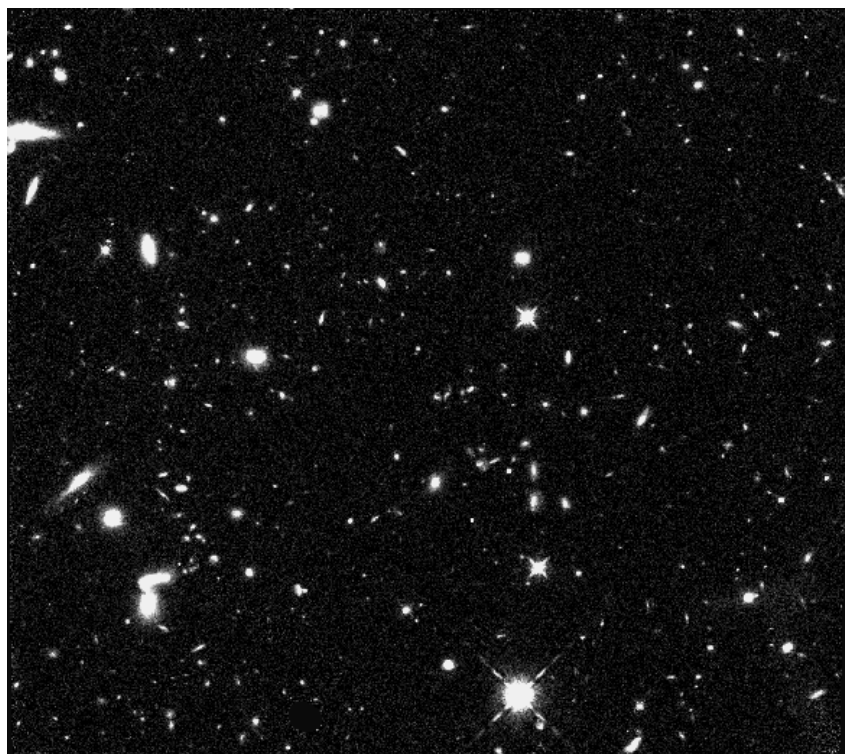


FIGURE 2.3: F160W

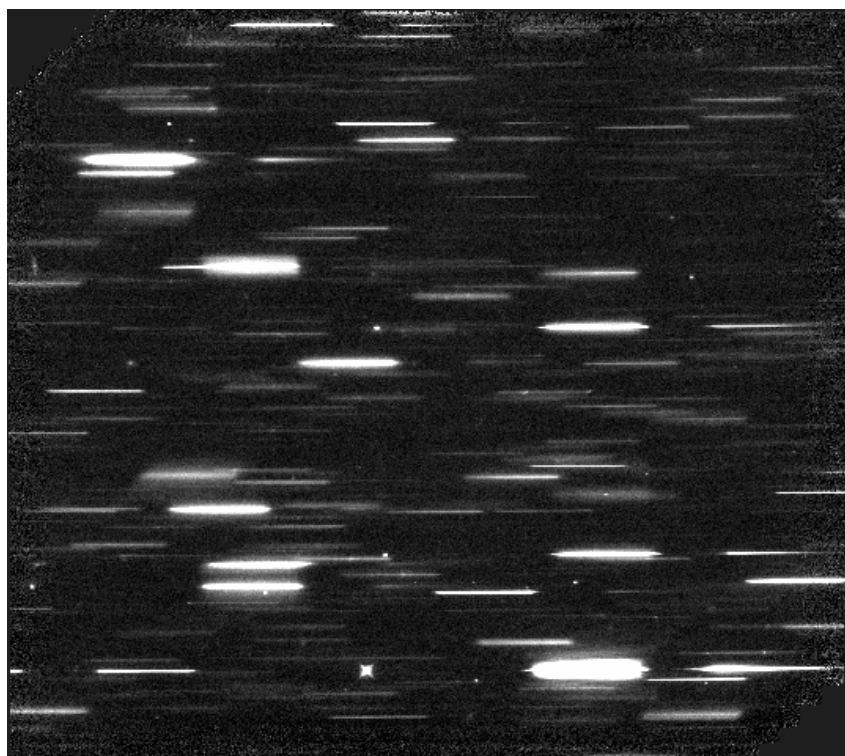


FIGURE 2.4: G141

FIGURE 2.5: Examples of a direct F160W exposure (top) and a grism G141 exposure (bottom).

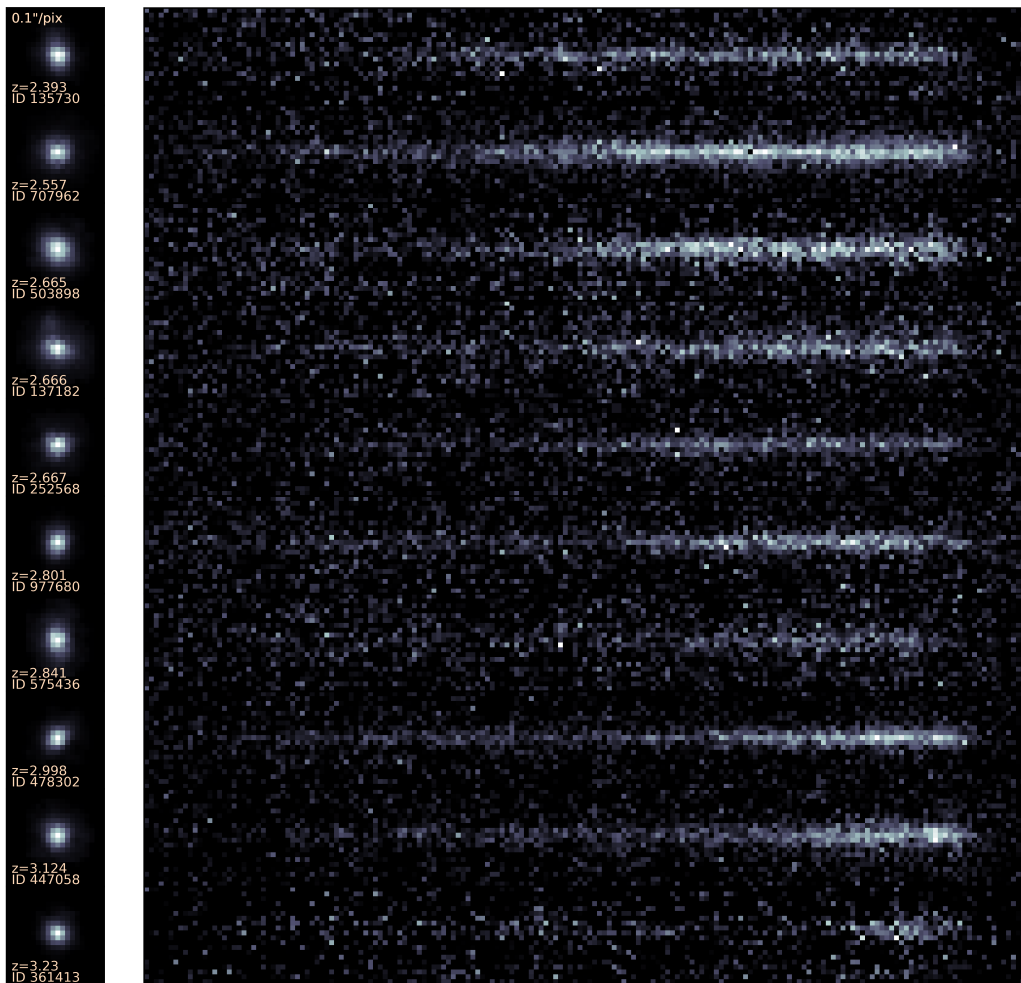


FIGURE 2.6: F160W imaging cutouts (left) and 2D G141 spectra (right). Redshift increases from top to bottom. The color scale is in linear scale.

deviation and compared to a gaussian centered on 0 and with dispersion 1. In all cases the observed distribution was centered on zero, with a dispersion ranging between 0.8-0.9 and therefore judged acceptable. A similar test was performed after spectral fitting on the residuals normalized by the noise vector across the 1D spectra. Again the the observed dispersion was under unity.

Some of the direct exposures show the presence of persistence from hot pixels, showing up as bright pixels along the dither pattern. Despite the fact that this did not affect the grism exposures, a second reduction was later performed with a more recent version of *grizli* in order to fix this issue in view of the morphological analysis (see Appendix B).

As can be seen from the 1D spectra in Fig. 2.7– 2.9 a bump at $\lambda_{\text{obs}} < 12500 \text{ \AA}$ seems to be present in some of the sources, albeit at low S/N (1.5–3). This could be caused by noise patterns across the grism exposures. When masking this spectral region, the redshift determination proved to be robust, thanks to the presence of strong absorption features at $\lambda_{\text{obs}} > 14500 \text{ \AA}$. As for the age-dust degeneracy, the addition of photometry together with the lower weight of these low S/N pixels in the fitting process make their impact minimum, if any.

2.5 Spectroscopic confirmation

In the sections that follow I will describe the model grid that I used to fit the extracted spectra and the results of the spectroscopic confirmation.

2.5.1 Fitting setup

The 1D spectra were fitted with a custom IDL routine originally developed by R. Gobat. It compares the 1D spectra with composite stellar population templates by χ^2 -minimization. Such templates were generated on the fly by combining a grid of Bruzual and Charlot (2003) (hereafter BC03) simple stellar population (SSP) models with a set of parametric SFHs: a constant, an exponentially declining, a delayed exponentially declining and truncated SFH. In the latter, the initial SFR drops to zero after a time τ_{tr} from the onset of star formation. In standard τ -models however, τ is the e-folding timescale of the SFH. The ratios of t/τ and t/τ_{tr} , when above unity, approximate the description of an SSP.

The line spread function derived by the routine collapsing the spatial profile of the source on the dispersion direction (necessary to broaden the stellar templates), produced a spectral broadening larger than the one shown by the observed absorption lines. The source of this mismatch is still unclear. Therefore, the adopted templates were smoothed to the G141 resolution adopting a FWHM computed fitting the stacked absorption lines of each galaxy with the IRAF task *splot*, resulting in relatively good agreement after

TABLE 2.2: Grid of parameters used for the spectral and for the optical-to-NIR SED fitting.

parameter [units]	min	max	step
z	0.01	5	0.01 (then 0.001)
age [Gyr]	0.1	$\text{age}_H(z)$	0.1
τ [Gyr]	0.001	1	0.1
A_V [mag]	0	8	0.1
Z_\odot			0.4, 1, 2.5
δ attenuation curve (Noll et al. 2009)			-0.7, -0.4, 0 (Calzetti)
IMF			Salpeter 1955
Stellar population templates			Bruzual & Charlot 2003

eye inspection.

The variety in SFHs was chosen in order to allow for both passive and dusty star-forming solutions. While searching for the best fitting redshift, the routine fits the observed spectra simultaneously with a set of emission lines complexes using standard line ratios (Anders and Fritze-v. Alvensleben, 2003) and the SFR– $H\alpha$ calibration of Kennicutt, 1998 where the SFR is taken from the model SFH. For redshift identification, the Calzetti et al., 2000 attenuation law was adopted and the stellar metallicity was left free to vary from $0.4 Z_\odot$ to $2.5 Z_\odot$. In Table 2.2 I list the grid of parameters used for the fit. The additional attenuation laws reported in the table will be included in the analysis starting from the next chapter.

2.5.2 Redshift identification

In order to reduce the computational cost, I divided the spectral fit into two steps. The first pass was done using a low resolution redshift grid ($dz = 0.01$) from $z=0.01$ to $z=5.0$. The age was constrained to be lower than the present age of the universe. The 1σ confidence range around the best fitting redshift was computed by means of the χ^2 difference following Avni, 1976. Once the most probable peaks were identified, I narrowed down the redshift grid to an interval of $\Delta z \sim 0.2$ spanned at $dz = 0.001$ centered on these peaks. This time we limited the template library to the age of the Universe at the lowest most probable redshift. This approach led to the redshift probability distributions showed in the upper panels of Fig. 2.7–2.9.

Seven of our sources showed unambiguous redshift solutions at a 3σ confidence already during the low resolution pass ($dz=0.01$). Two show a secondary peak within the same confidence level and one (id503898) lacks a marked spectral break. Nine galaxies out of ten are consistent with single solutions at 1σ . Despite the low resolution of G141 spectroscopy, redshift

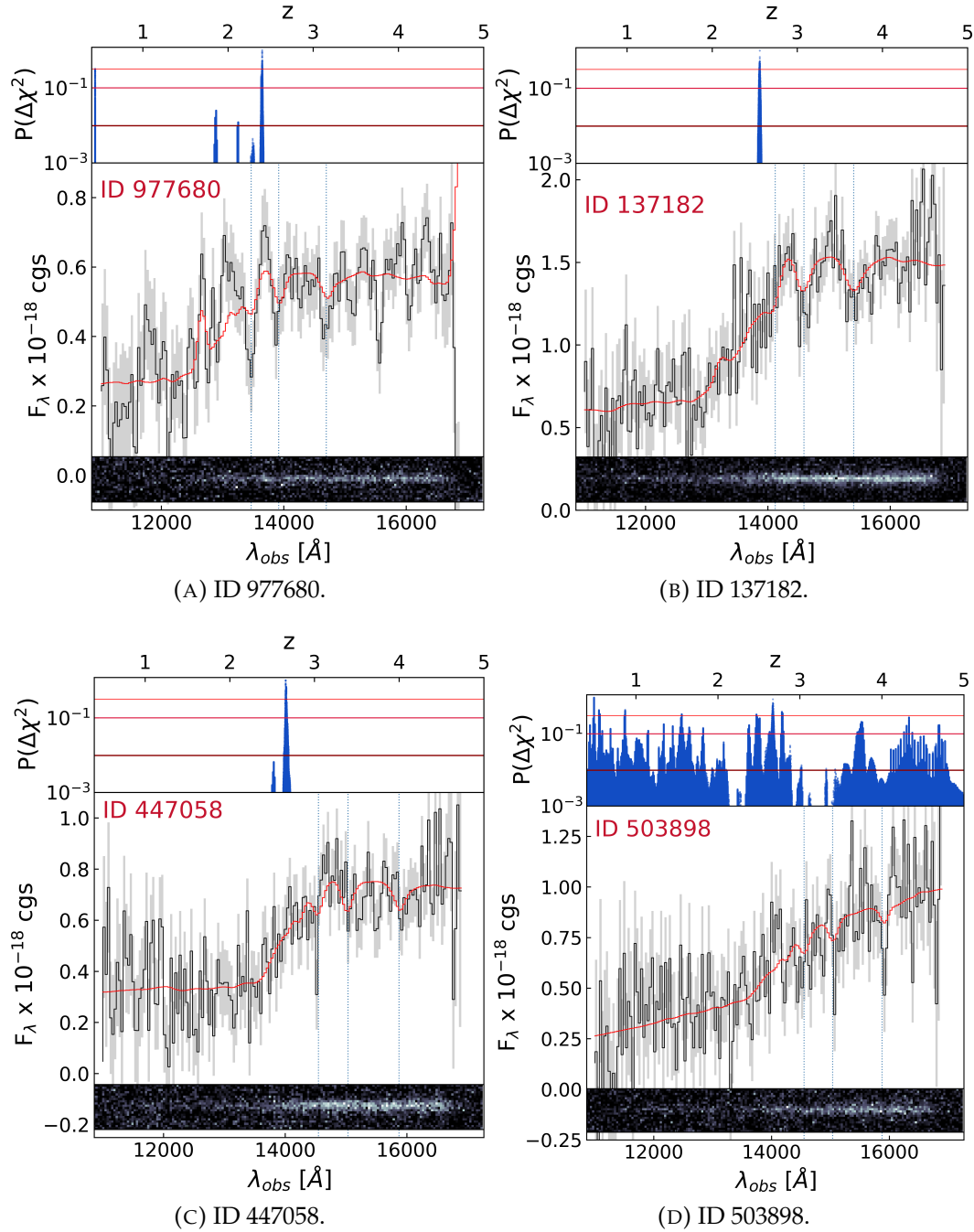


FIGURE 2.7: Upper panels: redshift probability distribution for each target. Solid lines from light- to dark-red mark 1-, 2-, 3- σ confidence levels respectively. Middle panels: optimally extracted 1D grism spectra (black) and best-fitting solutions (red) of our targets. The noise vector is showed in grey in each panel. Bottom panels: corresponding G141 2D spectra. The color scale is in linear scale. Galaxies are shown in order of increasing redshift.

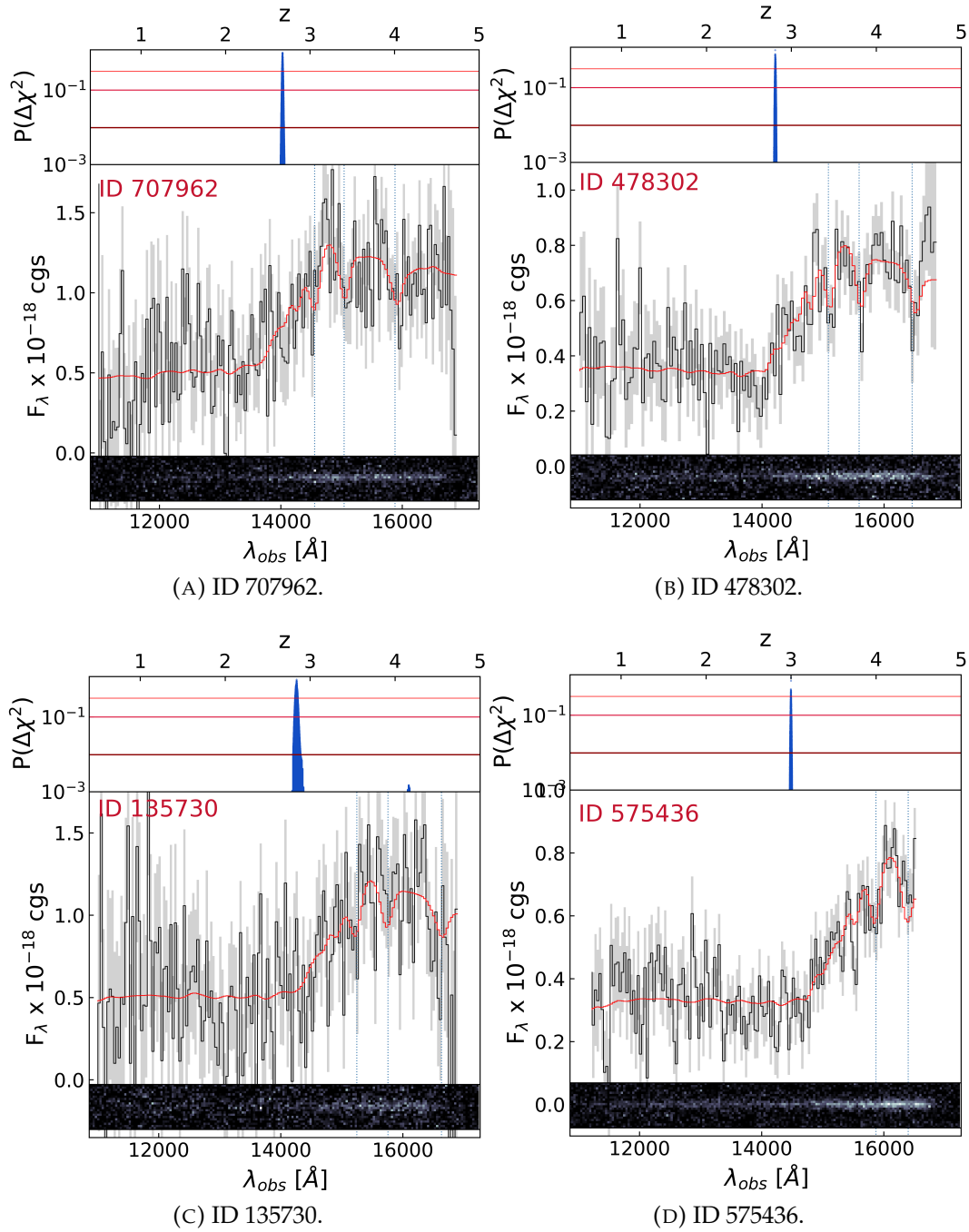


FIGURE 2.8: Continued.

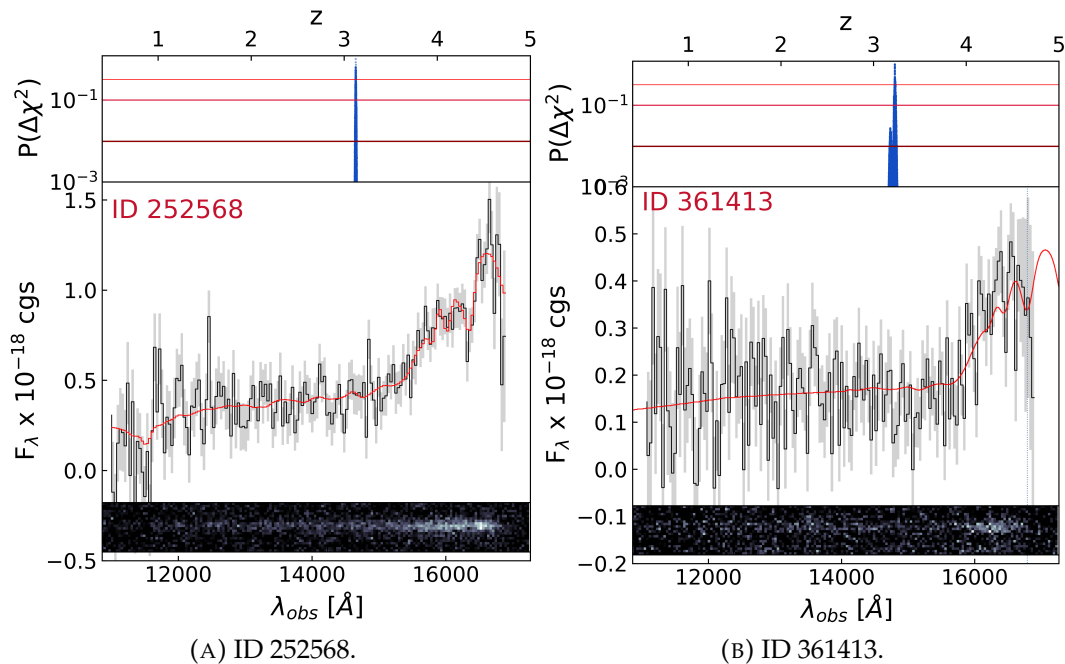


FIGURE 2.9: Continued

identification is made possible thanks to the presence of prominent spectral breaks and strong absorption lines for most of the targets (see Fig. 2.7– 2.9). For the highest redshift sources, namely id252568, id575436 and id361413, MgI and MgII 2640 – 2850 Å absorption lines also enter the spectrograph, albeit with relatively low S/N. Notably, id503898 lacks absorption features as strong as for the rest of the sample. This makes it consistent with multiple redshift solutions ($0.4 < z < 3.5$) within 1σ confidence. I attempted at narrowing down the redshift interval for this source in several ways: 1) I checked the consistency of the lowest redshift solutions with the available COSMOS2015 photometry placing $z > 1.5$ as a lower-limit⁵; 2) secondly I parsed the $1 < z < 3.5$ redshift range at high-resolution ($dz=0.001$). This attempt yields $z = 2.673^{+0.124}_{-0.204}$ consistent with the original best fitting solution within the uncertainties. The new 1σ confidence range appears to be relatively narrow, as a result of identifying a solution with a significantly lower χ^2 when refining the sampling. However, the error bars loosen relatively quickly at 2σ ($z = 2.673^{+0.133}_{-1.528}$) and extend to the arbitrarily chosen constraints at 3σ ($z = 2.673^{+0.764}_{-1.673}$); 3) being this object a bright hard X-ray emitter, we attempted at detecting the Fe K α line at 6.4 keV which, if placed at $z > 2$, would fall in the Chandra soft band. With a total of 70 counts however, the S/N of the X-ray spectrum is not sufficient to significantly detect the line (C. Vignali, private communication); 4) as can be seen from its cutout in Fig. 2.6, the H-band image shows the presence of two components.

⁵If id503898 were to be placed at $z < 1$, one would expect its SED to drop in H band onward, which is not observed: its SED rises in flux from J to H band.

The 2D spectrum appears to be slightly asymmetrical, with an excess flux along the dispersion axis at the level of the secondary component, hinting at it being either a companion galaxy or an object at a somewhat higher redshift in close projection. After deblending the two sources with SExtractor, the separate extraction of each spectrum did not improve the redshift determination of the main component significantly. The S/N of the secondary component does not allow to determine its redshift. The final spectroscopic confirmation of this source was obtained performing the combined fit of its photometry and grism spectrum across the $1 < z < 3.5$ redshift range at high-resolution ($dz=0.001$). This test confirms the previously derived best fit solution and reduces the error bars on z_{spec} at all confidence levels. At 1σ it yields $z = 2.674_{-0.009}^{+0.005}$, whereas at 3σ it yields $z = 2.674_{-0.026}^{+0.021}$ showing the stability of the best fit solution compared to the information derived from spectroscopy only (see Fig. A.1). In the rest of the analysis I will refer to the former confidence level as done for the rest of the sources.

Id977680 shows some excess flux at 11870 \AA . The secondary peak in the redshift probability distribution is placed at $z=2.3$, where the fitting routine is attempting at reproducing the two most prominent absorption lines with $H\delta$ and $H\gamma$ instead of $H\epsilon$ and $H\delta$ favored by the best fitting template. This redshift is not low enough to explain the excess flux with a $[\text{OII}]\lambda 3727$ emission line. Such line would have to be placed at $z=2.18$ yet it would not match any of the absorption features present in the spectrum. We therefore interpret such excess flux as a spurious feature. For the lowest S/N galaxies patterns generated by correlated noise can be quite severe and in some cases mistaken for absorption or emission lines. Additionally, the FWHM with which to smooth the stellar templates can be larger than what the observed spectrum suggests, also because a Gaussian profile is not fully representative of the intrinsic Sérsic profile of the source. I attempted at smoothing the templates with a smaller FWHM (roughly half of the initial one, in order to match the number of pixels in the brightest regions of the imaging cutout and to mimic the effect of a centrally peaked profile) however the best-fitting redshift does not change significantly, while the redshift uncertainties are reduced by $\sim 50\%$. This suggests that the observed features, narrower than the stellar absorption features according to the best-fitting redshift, are likely a result of correlated noise.

2.5.3 Performance of photometric redshifts

Robust spectroscopic confirmation was achieved for the full sample. I then compared the resulting z_{spec} with the calibrated photometric redshifts used for the sample selection to assess the quality of the latter (Fig. 2.10). The quoted normalized median absolute deviation of the adopted photo- z s⁶ was $\sigma_{\text{NMAD}} = 0.025$ estimated on the spectroscopically confirmed sample at

⁶ $\sigma_{\text{NMAD}} = 1.48 \cdot \text{median}(|z_{\text{phot}} - z_{\text{spec}}| / (1 + z_{\text{spec}}))$, Hoaglin et al. 1983

$z \sim 1.5$, reducing to 0.018 once galaxies with less reliable z_{spec} were excluded. As clarified in Strazzullo et al. 2015, the accuracy is maximum for bright objects (such as those used for spectroscopic confirmation) and decreases for fainter ones (either less massive sources or at higher z). In order to take this into account, in Fig. 2.10 I show the error bars computed using the z_{phot} accuracy estimated by the authors for faint objects, as a function of the K band magnitude in McCracken et al., 2010. For objects between $K=[20.8, 22]$ -such as in our case- the expected uncertainty is $\sim 0.040(1+z)$. The z_{phot} used for the selection of our sample largely agree with the z_{spec} derived here, with a small systematic underestimation of 0.04%. I also included the performance of photometric redshifts from Muzzin et al., 2013b. Note that id135730 and id137182 are outside the UltraVISTA area and therefore not present in this latter catalog. The nominal σ_{NMAD} I derived here by comparison with our spectroscopic sample are 0.057 and 0.033 for the two catalogs respectively. Applying the same calibration to the Muzzin et al. 2013b photometry at $z \sim 1.5$ (instead of McCracken et al. 2010), the accuracy improved to $\Delta z / (1+z) = 0.015$, especially at $z \geq 1.8$, comparable to that obtained in Muzzin et al. 2013b, as can be expected given the deeper photometry in the Muzzin et al. 2013b with respect to McCracken et al. 2010 catalogs (see Strazzullo et al. 2015).

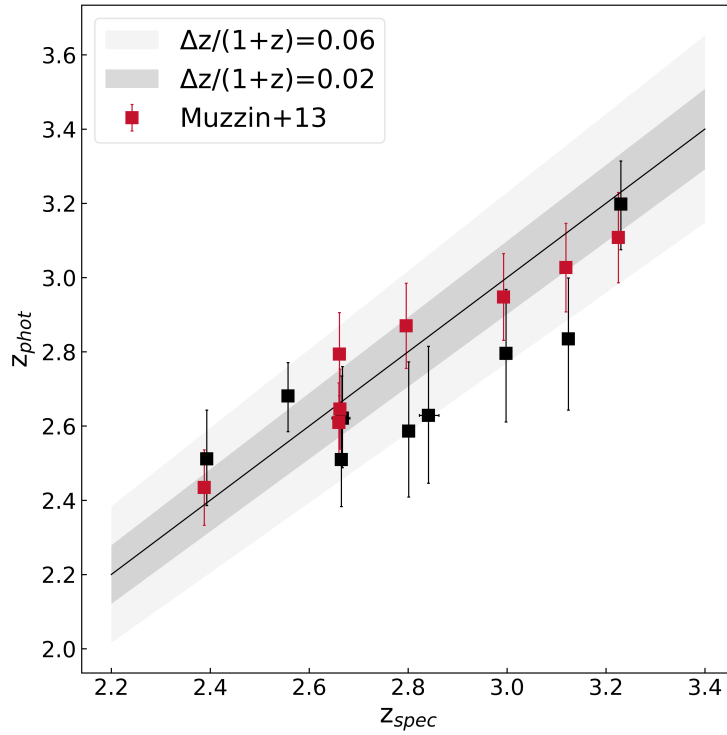


FIGURE 2.10: Comparison between calibrated z_{phot} s and spectroscopic redshifts. Black squares mark the original calibrated z_{phot} s used for the selection. Red squares mark z_{phot} s from Muzzin et al. (2013b). The black solid line and relative shaded area mark the 1:1 relation and the nominal dispersions between the original calibrated z_{phot} s and the newly derived z_{spec} (see text). The errorbars reflect the estimated σ_{NMAD} for sources of the given K mag magnitude in the original photometric catalog. Redshifts from Muzzin et al. have been shifted horizontally by -0.005 for clarity.

Chapter 3

Testing their quiescence

This chapter is devoted to the assessment of the level of star formation present in our sources, namely in the classification as star forming objects or quiescent ones. The scheme behind this part of the work is as follows: first I checked what information could be extracted from the grism spectra alone; then I combined the spectra with COSMOS2015 photometry and repeated the test. Afterwards, I checked for any possible detections in the recently released FIR catalog of Jin et al. 2018, which provides more realistic detections with respect to the blindly extracted catalog of Le Floch et al., 2009 originally used for the selection.

In Section 3.1, I introduce the method adopted to combine photometry and spectroscopy and later investigate the possible systematics affecting the consistency between the two data sets used. In Section 3.2, I show the diagnostic used to infer the nature of the targets and present what can be learnt from X-ray, mid- to far-IR and radio constraints. The detailed analysis of the ages and dust extinction values yielded by the combined UV-to-NIR fits will be the subject of the following chapter.

3.1 Addition of photometry

In order to characterize the physical properties of the galaxies, the information from HST grism spectroscopy was combined with COSMOS2015 total fluxes from CFHT/u* to IRAC/5.8 μ m (Laigle et al., 2016). The 3" diameter aperture magnitudes were converted to total magnitudes adopting their eq. (9) and (10). IRAC/8 μ m was excluded from the fit due to higher chances of AGN contamination. A lower limit of 0.05 mag was used for the photometric errors in all the bands. The two data sets (spectroscopy and photometry) were fit separately and later merged by adding the χ^2 matrices of the two fits. This procedure allows to find the solution that best fits both data sets, minimizing the impact of residual mismatches in normalization between the spectrum and the photometric SED. The same range of model parameters that was used for the spectroscopic confirmation is used here. The redshift however was fixed to the 1σ range around the best fitting z_{spec} . Contrary to what was done for the spectroscopic confirmation, the metallicity was fixed to the solar value at this stage according to the normalization and

scatter of the local ETG mass-metallicity relation (Thomas et al., 2010). This assumption is reinforced by recent clues from HST/G102 grism spectra of $1 < z < 1.8$ QGs as part of the CLEAR survey, which suggest that massive quenched galaxies were enriched to approximately solar metallicity already at $z \sim 3$ (Estrada-Carpenter et al., 2019). The metallicity was then let free to vary when testing directly the quiescence of the targets (Sect. 3.2). The resulting best fitting templates are shown in Fig. 3.1.

3.1.1 Zero-point calibrations

When comparing the consistency of the best fitting spectroscopic solutions for mass-weighted ages and dust extinction values with the best fitting combined ones, we found discrepant results. In particular, inspecting the spectroscopic χ^2 matrix for each target, in most cases the solution corresponding to the combined best fit had a $\Delta\chi^2$ inconsistent by more than 3σ with the spectroscopic best fit. It should be noted that the approach of *a posteriori* combining the χ^2 matrices has the caveat of finding a compromise solution between the NUV and the NIR emission. These rest-frame spectral ranges generally correspond to two different stellar components: while the NUV samples the presence of young stars, the NIR samples the oldest populations present in the galaxy (hence the bulk of the stellar mass). Therefore, this approach is limited by construction when it comes to finding more complex SFHs. However, before invoking more exotic SFHs to explain the inconsistencies within the results, I checked the effect of the assumptions made on the data sets and on the setup used to fit them.

In particular, from Fig. 3.2, it can be seen that the SED fits to total fluxes resulted in relatively high reduced χ^2 (χ_R^2), considering the few degrees of freedom of the fitting procedure. The χ_R^2 from spectroscopy on the other hand appear to be close to unity. To identify the source of the problem, I checked the means of the distributions of the normalized residuals in each photometric band, finding systematic shifts in B , V , i^+ , z^{++} (marginally), J , H , IRAC/ $3.6\mu\text{m}$, IRAC/ $4.5\mu\text{m}$ (see Fig. 3.3, red histograms).

As noted in Capozzi et al., 2016, the procedure of re-calibrating photometric zero-points (ZPs) to optimize photometric redshift retrieval (commonly performed when building photometric catalogs) can impact the results of SED fitting. These tweaks can introduce systematics in several bands, since the re-calibrations are often based on specific samples at a specific redshift. In the case of COSMOS2015 these were tailored on various samples of spectroscopically confirmed QGs at $z < 2.5$ (Onodera et al., 2012; Krogager et al., 2014; Stockmann et al., 2020), among a much larger number of star-forming galaxies. In addition to this, the templates used to derive such adjustments can also have a role in introducing systematics. In light of this, I tested whether removing photometric corrections, mostly calibrated on lower- z sources, was at the base of the aforementioned relatively high χ^2 .

Indeed, the offsets that we find in our data suggest that model fluxes tend

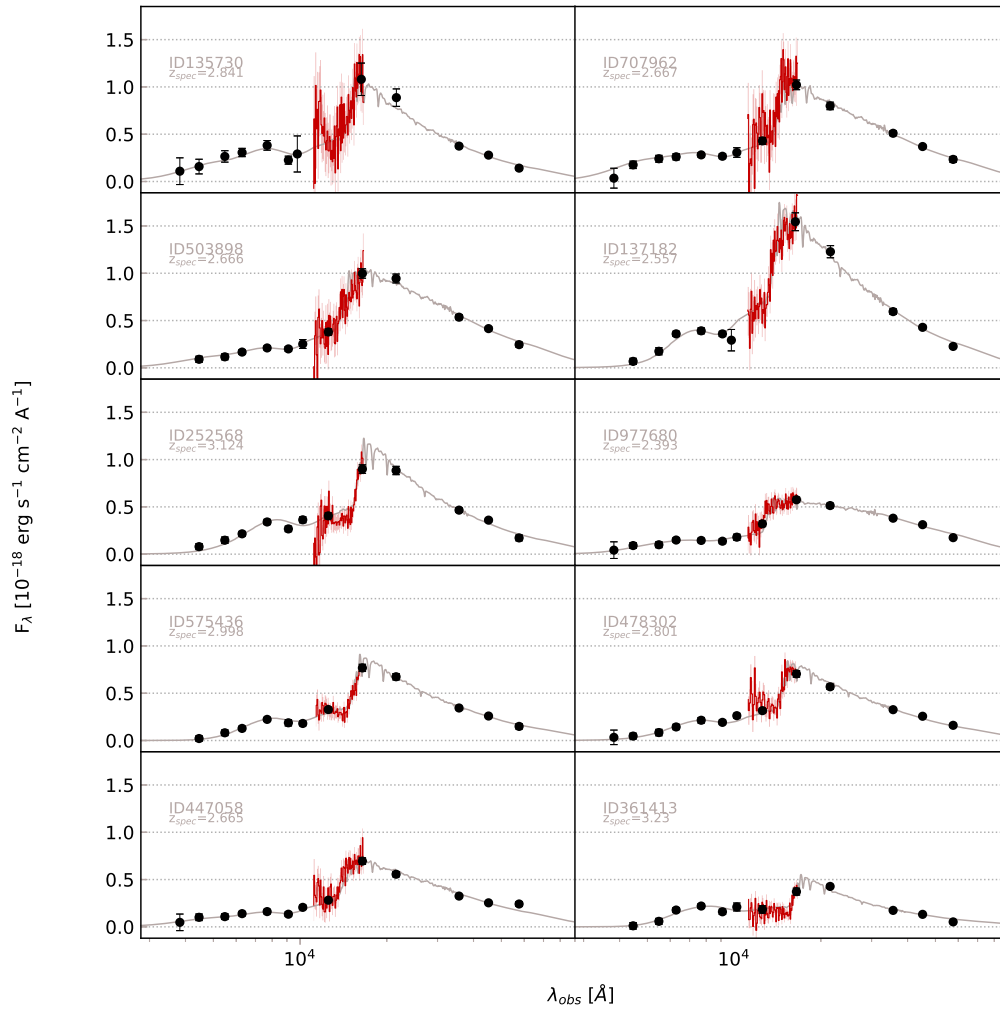


FIGURE 3.1: Photometry from Laigle et al., 2016 catalog (black dots). Grey curves show the best fitting templates smoothed to the G141 resolution. The observed-frame grism spectra are superimposed, rebinned for clarity.

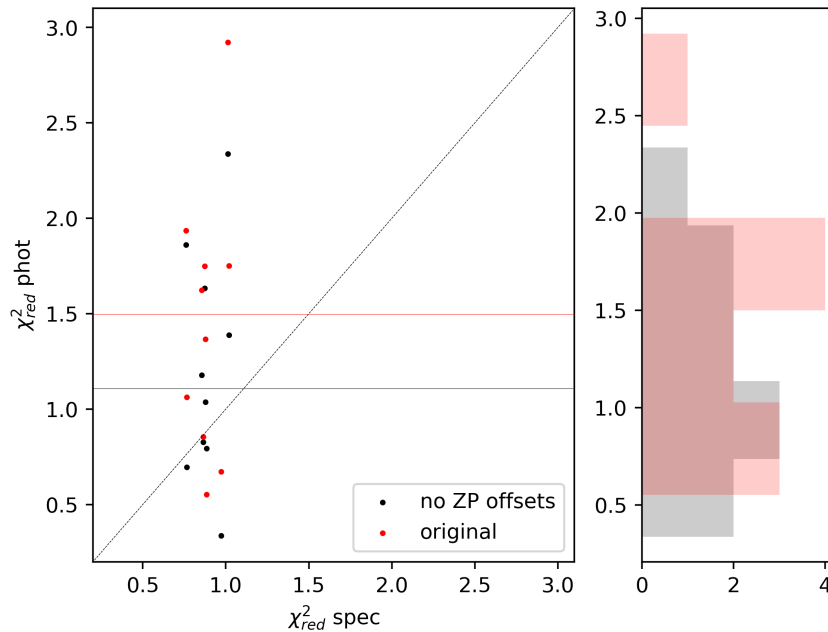


FIGURE 3.2: Distributions of photometric reduced χ^2 before (red dots) and after removing the ZPs re-calibration (black dots). Median values are marked by red and black solid lines respectively.

to overestimate observed fluxes when COSMOS2015 ZP corrections subtract flux to the observed signal and viceversa (see Fig.3.4). However, when dropping ZP corrections most of the wavelength-dependent systematics disappear and models are in agreement with the originally observed fluxes. This can be seen in both Fig.3.2 and Fig.3.3, where the sample median χ_R^2 reaches down to 1.1. A high χ_R^2 could be also flagging systematically low photometric errors. A common practice in such a case is to rescale photometric errors to reach a $\chi_R^2 \sim 1$. However, given the behaviour highlighted in Fig.3.3 and Fig.3.2 and since there is no reason to believe that photometric errors are underestimated in COSMOS2015, such rescaling appears unnecessary. We thus conclude that the ZP re-calibrations derived in Laigle et al., 2016 are no longer needed when it comes to $z \sim 3$ quiescent galaxies.

Lastly, a high χ_R^2 could be caused by broad residual distributions produced, for example, by the presence of some outliers in the sample. Visual inspections of imaging cutouts relative to each object in each band does not reveal peculiarities.

For these reason, the rest of the analysis has been performed on the original COSMOS2015 photometry, namely without making use of any ZP correction.

3.1.2 Dust attenuation laws

At this point, any further inconsistency between the spectroscopic and the combined best fit solutions could be ascribed either to an unsuitable attenuation law or to a complex underlying SFH.

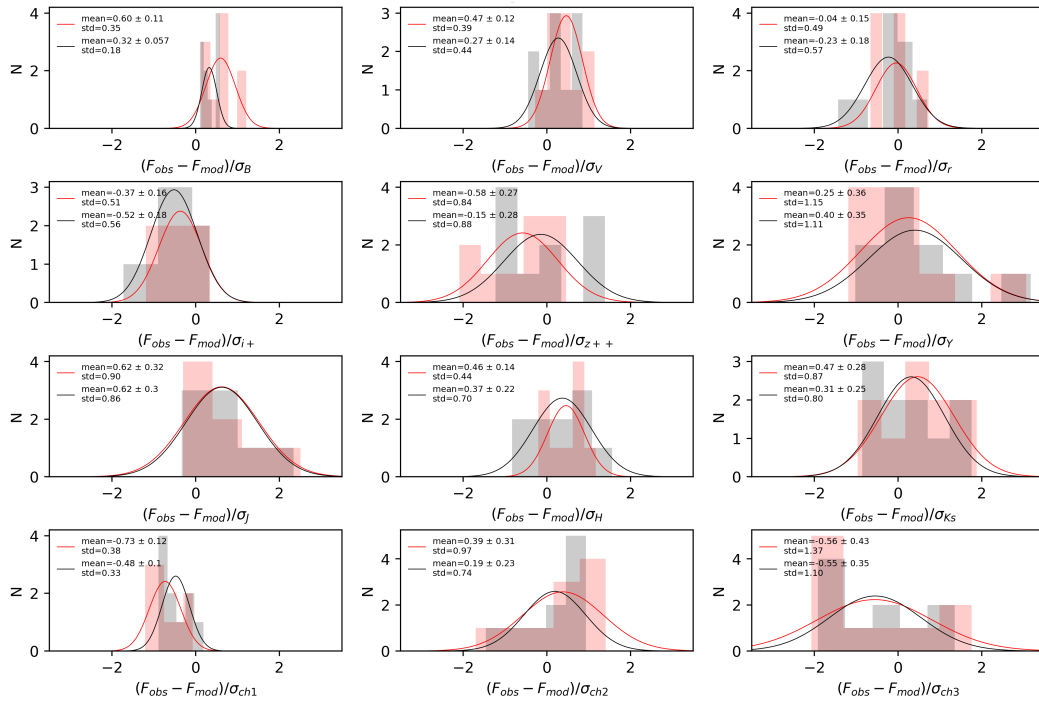


FIGURE 3.3: Normalized residuals distribution of target galaxies in each photometric band. Red and black histograms show residuals adopting re-calibrated and original ZPs respectively. Solid red and black curves show gaussian fits to such distributions. Their means, standard mean errors and standard deviations are listed in each panel.

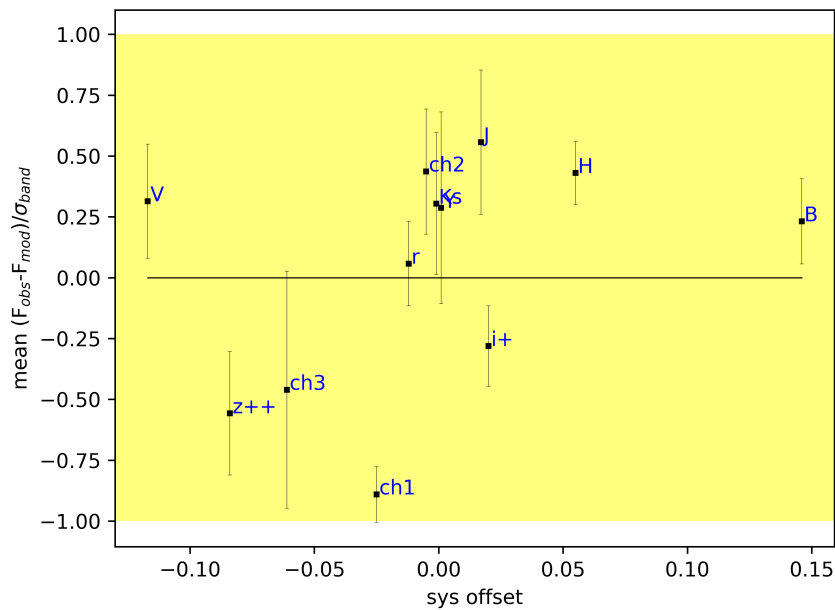


FIGURE 3.4: Mean residuals of photometric bands as a function of the systematic offset to be applied to correct photometric ZPs. A correlation seems to be present, with increasing residuals for increasing corrections. Error bars mark the standard error on the mean shown in Fig. 3.3. The yellow band shows the 1σ range of the normalized residuals.

To test the role of dust attenuation recipes, we included in the fitting library alternative attenuation curves in addition to Calzetti et al., 2000 for starbursts. For example, Kriek and Conroy, 2013 and Salim, Boquien, and Lee, 2018 advocate for the use of a steeper attenuation law when it comes to $z > 1$ star-forming galaxies (the former) and local SDSS quiescent galaxies (the latter). The slope of the curve is generally dependent on the grain size distribution and geometry, with steeper curves associated to differential attenuation according to the age of stellar populations. I adopted the methodology proposed in Salim, Boquien, and Lee, 2018, following from Noll et al., 2009, where the Calzetti curve is multiplied by a power-law term with exponent δ which sets the slope of the curve itself. Negative δ values imply a steeper slope in A_λ/A_V than Calzetti at rest-frame $\lambda < 5500 \text{ \AA}$. In this formalism, the Calzetti law has $\delta=0$ by definition, whereas $\delta=-0.4$ is similar to the small magellanic cloud (SMC) curve. The curve is further modified by introducing the so-called 2175\AA bump (Fitzpatrick and Massa, 1986), modeled as a Drude profile D_λ , with fixed central wavelength and width (FWHM=350) and varying amplitude. Since I linked the bump strength to δ according to the linear relation found by Kriek and Conroy, 2013 (see their eq.3), the law was constrained mainly by one parameter, its slope, which was left free to vary between 0, -0.4 and -0.7. This latter value was introduced to test the expected behavior of local quiescent galaxies as shown in Salim, Boquien, and Lee, 2018.

Therefore, from this point onwards, I fitted both spectroscopy and photometry with the three different attenuation laws defined above. One in particular, the curve with $\delta = -0.4$, appears to reduce the dispersion of the χ^2_R distribution for the photometry and maximizes the consistency of the combined solution with the spectroscopic one as can be seen in Fig. 3.5. In fact, it systematically yields the lowest $\Delta\chi^2 \sim 2.6$ which makes the two data sets consistent within 2σ . When testing the overall goodness of fit in terms of the slope, $\delta = -0.4$ is the best fit solution preferred by the majority of the targets. Five galaxies out of nine tend to reject $\delta = -0.7$ at a 5% level (but not at 1%). Given the overall similar goodness of fit (especially between Calzetti and $\delta = -0.4$) it was not possible to reject one of them consistently for the entire sample. Therefore, during the rest of the analysis, I let δ vary marginalizing over it when deriving physical parameters.

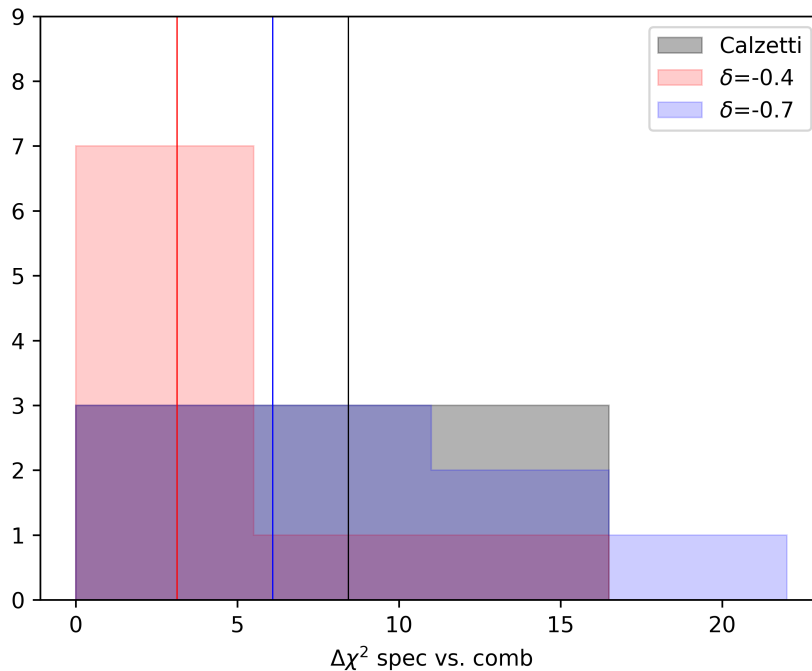


FIGURE 3.5: Chi squared difference between the best fitting spectroscopic solution and the best fitting combined solution selected from the spectral χ^2 matrix. Black, red and blue histograms show the distribution of such differences when varying extinction law. Vertical lines mark median values of the distributions. It can be seen that $\delta = -0.4$ is the one that reduces the median offset, bringing the solutions of the two fits consistent within 2σ .

3.2 Quiescence of individual targets

3.2.1 What can be learnt from UV-to-NIR data

I tested the quiescent/dusty star-forming nature of each galaxy by comparing the goodness-of-fit of the best fitting constant star-forming template with a free dust extinction parameter, with that of a solution defined as passive by constraining the best fitting SFH as follows: $t_{50} \geq 0.3$ Gyr, $A_V < 0.8$ mag and $t/\tau \geq 3$ where t is the lookback time at the onset of star formation and τ is the timescale of the SFH. Such ratio corresponds to a drop in SFR of about a factor of 20 with respect to the initial value for an exponentially declining SFH. To classify a galaxy as quiescent, the consistency of the CSF solution has to show a probability of < 0.01 , as inferred from their χ^2 difference. This simple parameterization is able to discern on a zero-order level the consistency of both the spectrum and the photometry with a heavily dust attenuated star forming component, whether it fits better than the passive solution and the confidence level of its consistency. The test was performed fixing the redshift to z_{spec} . I first tested the spectra alone and then I repeated the test on the combined solutions. The two objects for which the spectra have a larger probability of being consistent with a star-forming solution are id503898 (with a shallow spectral break) and id977680, as shown in Fig. 3.6. The addition of

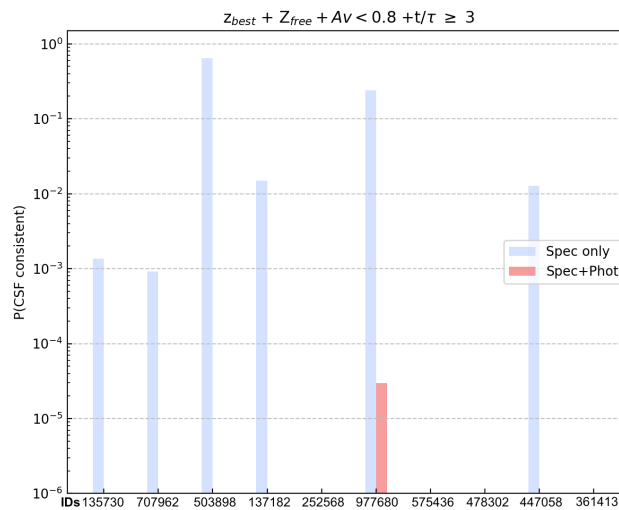


FIGURE 3.6: Probability of constant star forming solutions (here CSF) relative to that of passive solutions. Blue bars mark the results from spectroscopy only. Red bars show the probabilities from the combined fit.

photometry, however, rejects SF solutions for all our sources. This suggests that once the redshift of the target can be constrained to a sufficient accuracy, photometry can help rejecting a SFH in those cases where spectroscopy alone is not able to robustly distinguish between the two. This is made possible thanks to the wider wavelength coverage and overall quality provided by

the photometry.

I verified that letting z_{spec} vary within its 1σ confidence range does not impact the probabilities significantly. Letting the metallicity of the templates vary (adopting $0.4 Z_{\odot}$, Z_{\odot} and $2.5 Z_{\odot}$) has a similarly negligible effect. The result of id503898 can be explained by the lack of prominent (emission or absorption) lines which reduces the power of the test when considering the spectrum alone. At the best fitting redshift, however, the photometric points are inconsistent with a constant star forming solution.

The second object showing the largest consistency with a star forming template is id977680. Despite the addition of photometry rejects star forming solutions, one should be aware that this object lies in a region of the UVJ diagram where contamination is expected to be more frequent (due to the scatter of the blue cloud). Moreover, its best fitting combined mass-weighted age and A_V are still pointing towards a very young and dust reddened stellar content ($t_{50} = 0.3^{+0.3}_{-0.1}$ Gyr and $A_V = 1.6^{+0.1}_{-0.3}$ mag, respectively). The nature of very young sources with MIPS and Chandra detections will be further addressed in the following sections. I anticipate here that we consider id977680 a likely AGN host. We conclude with reasonable confidence that all of our galaxies can be classified as passive on the basis of their UV-to-NIR emission.

3.2.2 Further constraints from multiwavelength data sets

I took advantage of individual detections in the recently released mid-IR to radio Super-deblended Jin et al., 2018 catalog and in the Chandra COSMOS-Legacy Survey catalog (Civano et al., 2016) to estimate the levels of obscured star formation or nuclear activity.

The prior-extraction method used in Jin et al., 2018 fits the PSF of MIPS $24 \mu\text{m}$, VLA 1.4 and 3GHz images at the positions of known K_S -selected (plus radio 3GHz selected) sources. This procedure improves faint sources identification in the mid-IR (Spitzer/MIPS), far-IR (*Herschel*/PACS, *Herschel*/SPIRE) and sub-mm (JCMT/SCUBA2, ASTE/AzTEC, IRAM/MAMBO) wavelengths, where the large PSF makes source identification prone to blending and confusion. This represents a substantial advance with respect to the blindly-extracted catalog of Le Floch et al., 2009 by significantly reducing flux errors (by roughly a factor of two) while also improving source deblending.

Five of our galaxies figure as detections at MIPS $24 \mu\text{m}$ in the Super-deblended catalog (id135730, id503898, id977680, id478302, id447058, see Table 4.1) but are not significantly detected in the FIR: none of them shows a combined FIR+mm (100–1200 μm) S/N higher than 5. Id135730 formally counts multiple detections in Spitzer/MIPS and *Herschel*/PACS bands but it is flagged as unreliable since it lies in a region of COSMOS affected by incomplete prior coverage, non resolved blending and underestimated flux uncertainties. Visual inspection of its MIR and FIR cutouts did not reveal any detection at the source position (see Appendix A).

At the mean redshift of this sample, observed-frame $24\mu\text{m}$ emission corresponds approximately to a rest-frame $6\mu\text{m}$. Emission at such wavelengths can arise from a range of processes: from star-formation (Polycyclic Aromatic Hydrocarbons (PAH) emission lines and/or warm dust continuum); from a dusty torus obscuring a central AGN; from warm diffuse cirrus clouds heated by old stellar populations or from circumstellar dust around Asymptotic Giant Branch (AGB) stars (Draine and Li, 2007; Béthermin et al., 2015; Fumagalli et al., 2014).

Unfortunately, the $\sim 6''$ FWHM of Spitzer/MIPS PSF is much larger than the typical projected size of our galaxies ($< 1''$), hence it is not possible to distinguish whether the emission is extended or centrally concentrated.

Assuming that the remainder four detections are powered from star formation, I computed for each target the individual SFR expected for an average MS galaxy emitting at the observed flux density. I corrected the flux densities by a factor of 1.7, as noted in Jin et al., 2018 and adopted conversions from Magdis et al., 2012. These conversions were driven from template SEDs of MS galaxies whose variation as a function of z is mainly driven by the strength of the mean radiation field $\langle U \rangle$ evolving up to $z \sim 2.5$ as $(1+z)^{1.15}$ and flattening at $z > 2.5$ as observed for the sSFR evolution. At fixed redshift, MS galaxies appear to share uniform radiation fields (traced by $L_{\text{IR}}/M_{\text{dust}}$) and similar SED shapes. Such templates also assume a fraction of dust mass into PAH of $q_{\text{PAH}} = 2.5\%$ for $z > 1.5$ MS galaxies. The results can be found in Table 4.1.

It appears that the $24\mu\text{m}$ -derived SFR range between ≈ 300 and $900 M_{\odot}\text{yr}^{-1}$, the same order of magnitude of $z \sim 3 \log(M_*/M_{\odot}) \sim 11$ MS galaxies albeit somewhat higher, inconsistent with remaining undetected in the FIR. Such star-forming galaxies, in fact, typically show FIR Herschel flux densities around a few to 10 mJy (Schreiber et al., 2015; Elbaz et al., 2018) which would show up in *Herschel*/SPIRE. As for the sources that remain individually undetected at $24\mu\text{m}$, the 3σ upper limits are too shallow to reject milder (but substantial) SFRs. Stacking the rest of the sample at $24\mu\text{m}$ results in 0.036 ± 0.018 mJy which, again, translates into a shallow upper limit of $< 200 M_{\odot}\text{yr}^{-1}$. I would like to stress here that the current available 3σ depth of Super-deblended data from Spitzer/MIPS, *Herschel*/SPIRE, *Herschel*/PACS in COSMOS is not sufficient to securely reject *sub-MS* levels of obscured star-formation on a galaxy-by-galaxy basis.

IR and X-rays

Id977680, id478302 and id503898 have counterparts in the hard X-ray domain with rest-frame luminosities of the order of $\log L_X(2-10\text{keV}) \sim 43.7, 44.3$ and 44.3 respectively, assuming a photon index $\Gamma = 1.4$ (e.g. Gilli et al. 2007).

I tested whether or not their $24\mu\text{m}$ signal could be consistent with being powered by an accreting black hole converting the observed-frame $24\mu\text{m}$ flux

densities to unobscured rest-frame X-ray (2-10keV) luminosities, adopting the relation of Fiore et al., 2009 (see their eq. 1). This relation assumes that the 2–10 keV luminosity, computed directly from the observed fluxes without any correction for intervening absorption, can be considered representative of the intrinsic AGN X-ray luminosity. The relation has a scatter of 0.2 dex. In addition, some outliers are expected in case of significant X-ray absorption. For these three sources, their expected $L(2-10\text{keV})_{24\mu\text{m}}$ are in agreement with the observed ones. Therefore, although I could not reject the scenario in which some level of star formation would contribute to the rest-frame $6\mu\text{m}$ emission, I concluded that our data can be fully explained by an AGN obscured by a dusty absorber.

Interestingly, id447058 shows a 0.1 mJy $24\mu\text{m}$ detection at 10σ significance which is not matched by an X-ray detection. Given that its spectrum and photometry are both pointing towards a passive nature, we tend to favor the hypothesis for which strong obscuration might be playing a role in hiding X-ray photons from the central engine.

Id977680, id478302 and id447058 appear to tentatively show SPIRE/250- and $350\mu\text{m}$ signal at the source position. For the latter two the contamination by nearby projected FIR bright sources due to poor spatial resolution is evident. For id977680 the Jin et al., 2018 catalog formally provides non-detections at 100 and $160\mu\text{m}$ and no deblending at longer wavelengths. In postage stamps, the SPIRE/250 μm signal appears to show emission centered on the source position in the middle between two other $24\mu\text{m}$ bright sources. Jin et al., 2018 attribute the 250- and $350\mu\text{m}$ signal to the severe blending of these two sources within the SPIRE large PSF, larger than the distance of these sources from our target ($\approx 10''$).

Radio

Star formation is traceable not only in the FIR where most of the UV photons are re-emitted after having been absorbed in dust-enshrouded star-forming regions. It is also traceable at radio wavelengths, where non-thermal processes dominate, like synchrotron emission from SNe bubbles or shocks. In particular, for MS galaxies a tight correlation exists between their stellar mass and the ratio of their total IR luminosity (integrated from 8 to $1000\mu\text{m}$) over their radio luminosity. This is the so-called IR-Radio correlation, which allows one to use the radio luminosity of a galaxy as a dust-unbiased tracer of its obscured SFR. In our case, assuming that radio emission is given by star formation only, we derived individual 3σ upper limits on the obscured SFR from the 3GHz flux densities using the IR-Radio correlation of Delvecchio et al. 2020. This particular version of the relation has multiple advantages: 1) it has been derived from a large mass-selected sample of star-forming galaxies in COSMOS with careful removal of AGN candidates, 2) has explored in detail the dependency on M_* and z up to $z=4$, simultaneously, with unprecedented accuracy.

Id135730 is securely detected at 3GHz. Given the unphysically high SFR estimated for it, the origin of its radio emission is to be ascribed to AGN radio jets. For the rest of the sample, the inferred upper limits ($<150 M_{\odot}\text{yr}^{-1}$), again, do not conclusively exclude the presence of sub-MS levels of star formation on a galaxy-by-galaxy basis. Finally, mean-stacking 3GHz undetected sources yields a peak flux density of $S_{3\text{GHz}}=2.72\pm 0.93\mu\text{Jy}$ (see Fig. 3.7), which assuming a spectral index of $\alpha=-0.75$, translates into a rest-frame $L(1.4\text{ GHz}) \sim 2\times 10^{23}\text{ W/Hz}$, 4 times higher than what observed in $z\sim 1.8$ massive quiescent galaxies (Gobat et al., 2018). Such a detection is formally consistent with $50\text{-}60 M_{\odot}\text{yr}^{-1}$ of obscured star formation (assuming the IR-radio correlation at $\log(M_{\star}/M_{\odot})\sim 11$ at $z\sim 3$, Delvecchio et al. 2020). I would like to recall here that stacking in the radio has the advantage of avoiding confusion and blending issues affecting Herschel PACS and SPIRE observations. The higher resolution and sensitivity of VLA 3GHz observations (PSF $\approx 0.75''$ at 3GHz vs. $18\text{-}24''$ of Herschel/SPIRE bands) reduces possible clustering by star forming satellite which would contaminate to the SFR measure.

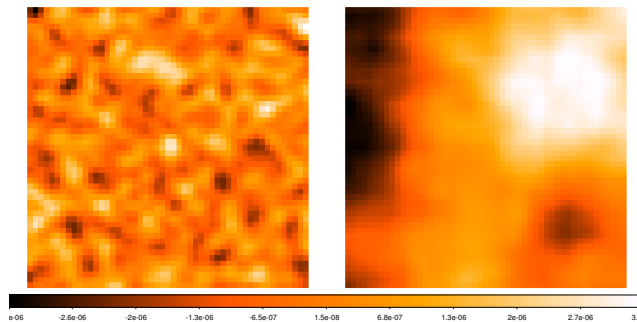


FIGURE 3.7: Image (left) and rms (right) maps resulting from mean-stacking undetected galaxies at 3GHz. The cutouts have a size of $10''$.

In summary, three of our four $24\mu\text{m}$ detected objects have X-ray counterparts. Their $\sim 6\mu\text{m}$ rest-frame luminosities are consistent with being AGN powered within the uncertainties (e.g. $\log(L_{X,24\mu}) = 44.26 \pm 0.36$ vs. $\log(L_{X,obs}) = 43.89$ for id503898). The remaining $24\mu\text{m}$ source (id447058) is non detected in X-ray and might host obscured star formation or an obscured AGN. Individual SFR upper limits were derived assuming our galaxies are MS galaxies using Magdis et al. 2012 templates. Individual SFR estimates range between ≈ 300 and $900 M_{\odot}\text{yr}^{-1}$. These values are typical of the upper end of the $z\sim 3$ $\log(M_{\star}/M_{\odot})\sim 11$ MS, inconsistent with FIR non-detections. Such MS galaxies, in fact, typically show FIR *Herschel* flux densities around a few to 10 mJy (Schreiber et al., 2015; Liu et al., 2018; Jin et al., 2018) which would be detected in *Herschel*/SPIRE. As for the sources that remain individually undetected at $24\mu\text{m}$, the 3σ upper limits are too shallow to reject milder (but substantial) star formation. Stacking the rest of the sample at $24\mu\text{m}$ results in $0.036 \pm 0.018\text{ mJy}$ which translates into a shallow upper limit of $<200 M_{\odot}\text{yr}^{-1}$. Hence, we concluded that the available 3σ depth of the

Super-deblended data from Spitzer/MIPS, *Herschel*/SPIRE, *Herschel*/PACS in COSMOS is not sufficient to securely reject *sub-MS* levels of obscured star-formation on a galaxy-by-galaxy basis. Individual 3GHz upper limits constrain the SFR to be below 120-190 $M_{\odot} \text{ yr}^{-1}$. Once again, still not deep enough to exclude mild (sub-MS) but substantial star formation. Finally, mean-stacking 3GHz undetected sources yields a peak flux density of $S_{3\text{GHz}} = 2.72 \pm 0.93 \mu\text{Jy}$. As will be explored in the following chapters, this is plausibly suggesting a higher radio-mode feedback at fixed stellar mass closer to the quenching epoch. However, such a detection is also formally consistent with 50 $M_{\odot} \text{ yr}^{-1}$ of obscured star formation (assuming the IR-radio correlation at $\log(M_{*} / M_{\odot}) \sim 11$ at $z \sim 3$, Delvecchio et al. 2020). This SFR is about 5-6 times lower than the coeval MS at a similar mass.

As we shall see in the following chapter, our spectra show strong Balmer absorption lines plus a weak [OII] emission revealed by the stacked spectrum. We tend to interpret such combination of features as the ones of a recently quenched population of galaxies with residual unobscured star formation. I also stress here, however, that the very same combination has been found locally in dusty galaxies hosting strong obscured star formation (Poggianti and Wu, 2000, e(a) galaxies). Whether or not our galaxies host, in fact, $\approx 50 M_{\odot} \text{ yr}^{-1}$ of obscured star formation can only be probed by means of deep mm observations (ALMA or NOEMA), which would reveal the amount of residual cold gas reservoirs by constraining the Rayleigh-Jeans tail of cold dust emission. Increasing the sampling of the FIR SED would also allow for a less degenerate simultaneous modelling of the stellar component, a hot AGN torus component and a cold ISM component with state-of-the-art tools such as BEAGLE (Chevallard and Charlot, 2016), CIGALE (Boquien et al., 2019) or MAGPHYS (da Cunha, Charlot, and Elbaz, 2008) to cite a few. In conclusion, given the spectroscopic and the photometric constraints (including IR, X-ray and radio wavelengths) we interpret our sources as quiescent. However, as it will be discussed in the following chapters, the very young mass-weighted ages and high dust extinction values for some of our targets (usually the same that we believe to be AGN hosts) do not make things easier and leave the classification on a galaxy-by-galaxy basis somewhat ambiguous. Extended spectral coverage (e.g. covering $H\alpha$ and [NII]) could be of help on this matter to distinguish between star formation and liner activity through, for example, BPT diagrams.

Chapter 4

Recently quenched galaxies, recently formed

This chapter explores the current evolutionary stage of our sample galaxies. This is done by estimating ages (mass-weighted and light-weighted) and measuring spectral indices. I will first show the stacked spectrum whose wavelength coverage and overall quality enabled us to extend the use of spectral indices out to $z \sim 3$ for the first time. The early investigation of its properties let us quantify spectroscopically how far back in time their major quenching phase took place. Being our quiescent galaxies very young, we investigated how much of the parent population of massive quiescent galaxies at the same redshift is consistent with the properties of our sample. The results of such work were published in D'Eugenio et al., 2020. Here I will describe such work and I will later show the work done on the individual sources as well. The analysis and discussion performed here on the single targets are contained in D'Eugenio et al., 2021 submitted (at the time of writing) to A&A and currently under revision.

4.1 Stacked spectrum

One of the first steps done to broadly characterize our sample was to exploit its size in order to maximize the signal-to-noise of the spectral features. To this end, I created an average spectrum of the 9 galaxies¹ first identified as quiescent, adopting the following procedure: I scaled the wavelength vector of each galaxy to the mean redshift of the sample ($z_m=2.808$) and interpolated their fluxes and error spectra on a 5\AA rest-frame grid, increasing the error in each new pixel by the square root of the width ratio between the old and the new spectral bin, to account for the introduced noise correlation. Each error spectrum was interpolated in quadrature. Each spectrum was normalized to its average flux between $\lambda_{rest}=3800\text{-}3900\text{\AA}$, in order to select a wavelength range covered for all galaxies. I then created a stacked spectrum as the inverse variance weighted mean of the individual fluxes in each wavelength bin. The final error spectrum was computed as the error on the flux-weighted

¹When the work on the stacked spectrum was performed, the redshift identification for id503898 was still too uncertain to include it in the analysis.

mean in each pixel. A jackknife resampling yielded consistent results. The z_{spec} uncertainty of the whole sample is $dz \sim 0.006$ at 68% confidence. This, however, does not affect the final spectral resolution, being three times smaller than the broadening introduced by the spatial extent of the galaxies. This redshift uncertainty results in the apparent wavelength offset seen for $H\delta$ and, possibly, for $H\gamma$, both of them however within the noise. The average spectrum was rescaled to match the average broadband photometry of the sample at $\lambda_{rest} = 3800\text{--}3900 \text{ \AA}$, in turn obtained by stacking the individual galaxy best fit SEDs (as done for the spectra). The average spectrum can be found in Fig. 4.1. It shows clear Balmer absorption lines from $H\eta$ to $H\gamma$, a weak [O II] (unresolved) doublet at 3727 \AA in emission and the FeI absorption line. With a mean S/N ~ 13 per pixel at 4000 \AA this is one of the highest S/N spectra available for high- z QGs and the first spanning a large continuous spectral range around the key spectral break. I would like to stress here that the spectral feature in absorption at $\sim 4580 \text{ \AA}$ is driven by id977680 which is dominating the weighted average at these wavelengths. This feature is, most likely, caused by correlated noise fluctuations since there is no known major absorption line at 4580 \AA restframe. Since we were interested in the average emission at the level of the break and $H\delta$, I checked that our results were not biased towards galaxies particularly dominating the average spectrum. I created a penalized spectrum by assigning lower weights to those galaxies contributing more than 50% to the weighted average. Fitting such average spectrum gives consistent results in terms of ages and dust extinction.

4.1.1 Spectral fit

In general, a major source of uncertainty when retrieving the mass-weighted age of stellar populations is the choice of the SFH used to interpret the observed data. This is because 1) the true intrinsic SFH is unknown; 2) there is a degeneracy introduced by the similar effect that age and dust reddening have on the integrated stellar spectrum of a galaxy² and 3) there is an extra degeneracy in the fitting process caused by the slow evolution of the spectral features of stellar populations older than 1.5-2 Gyr. In this regard, many efforts have been done in the last decade to develop codes in which the SFH is not approximated with simple parametric functions in an attempt of removing any bias in the SFH reconstruction. This is generally done either by increasing the flexibility of the SFH itself (through the addition of more degrees of freedom, e.g. Schreiber et al., 2018b; Carnall et al., 2019; Belli, Newman, and Ellis, 2019b), or by removing the dependence on parametric functions (e.g. Cappellari and Emsellem, 2004; Cid Fernandes et al., 2005; Cappellari, 2017; Leja et al., 2019). In this latter approach the SFH is described as a linear combination of simple stellar population components (SSPs), each of which has a different contribution to the observed integrated spectrum. Recent works suggest, however, that when it comes to estimating the age

²The adoption of solar metallicity templates was motivated in Sect. 2.5.1

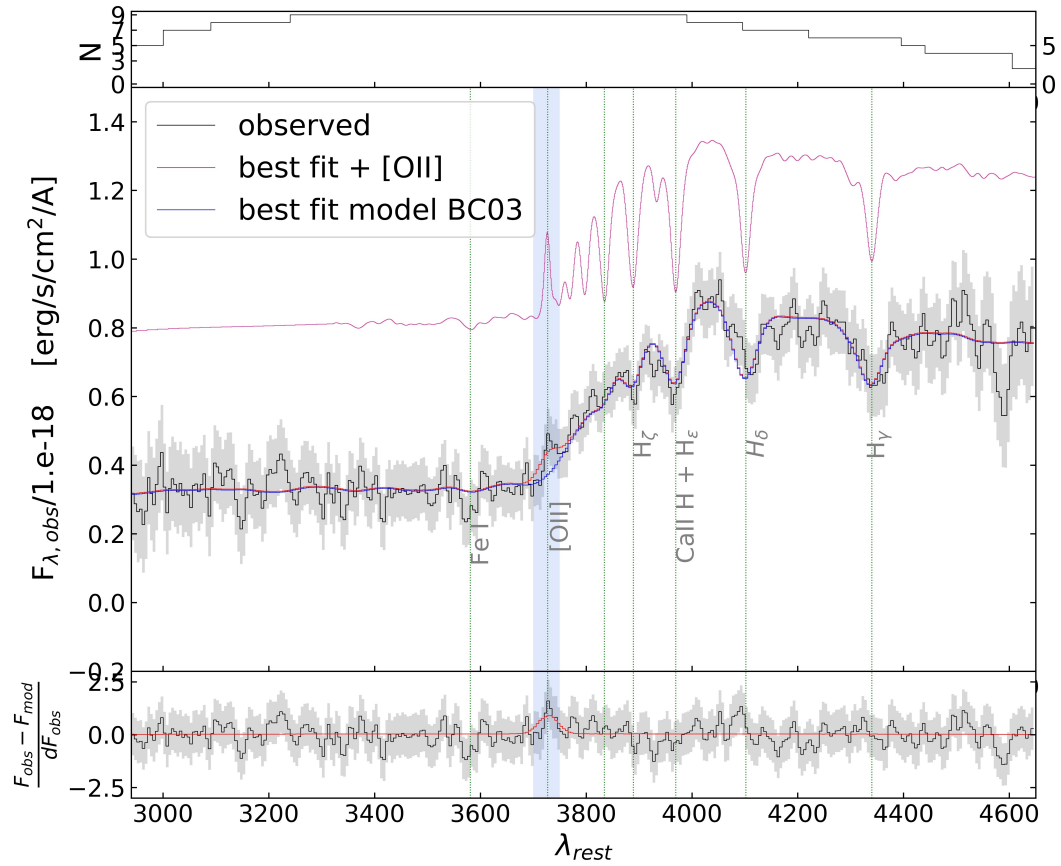


FIGURE 4.1: Top: Number of galaxies contributing to each spectral bin. Middle: Stack of 9 quiescent galaxies' spectra. Blue curve: best-fit model from the BC03 library. Red curve: Gaussian fit to the residual, added to the blue continuum. Pink curve: best-fit BC03 template smoothed for a $\sigma_v \sim 200 \text{ km s}^{-1}$, shifted in flux for clarity. Vertical dotted lines mark the identified absorption features. Bottom: Fit residuals normalized to the error spectrum.

and optical dust extinction at $z > 1.5$, relatively simple parameterisations of the SFH perform similarly as more flexible ones and, all in all, behave in a relatively stable way (Belli, Newman, and Ellis, 2019b; Valentino et al., 2020). This happens, because, at high redshift the discerning power of rest-frame optical spectra at mapping the SFH greatly increases. Stellar ages are, in fact, bounded by the age of the universe at the epoch of observation. Additionally, the rapid transition ($\sim 10^2$ Myr up to 1 Gyr) in the optical regime from metal (e.g. CaII H&K) to Balmer absorption lines in stellar populations younger than 1 Gyr increases the accuracy of light-weighted age estimates. Such a transition is due to the integrated emission around $\sim 3800 \text{ \AA}$ being dominated by the spectrum of A-type stars, which evolve on timescales of few hundreds of Myr.

As for the spectral fitting performed here, I marginalized over the different SFHs adopted in this thesis as to render the best fitting values and their uncertainties slightly more robust against the choice of the specific function adopted. The mass-weighted ages are intended here as the lookback time relative to observation at which the galaxy formed half of its stellar mass, t_{50} . The fit for the stacked spectrum was carried out limiting the age grid to the age of the universe at z_m (~ 2.3 Gyr) and using the average FWHM derived for the individual targets as the spectral broadening. The fit to the stacked spectrum yields $t_{50} = 0.30^{+0.20}_{-0.05}$ Gyr and $A_V = 0.6^{+0.6}_{-0.4}$ mag as average values for our sample. The 1σ uncertainties were estimated marginalizing over these two quantities, taking into account the various parameterizations used for the SFHs. These values are induced by the presence of strong Balmer absorption features but, as it will be shown later, even when adding the photometric information to individual galaxies, the best fitting mass-weighted ages remain very young. This is suggestive of the bulk of the mass of our galaxies being formed very recently, possibly around $z_{\text{form}} \sim 3.5$, when our galaxies would have been actively forming stars. More importantly the young ages inferred here are implying that the quiescence was reached only very recently.

4.1.2 Strength of spectral breaks

A more direct approach to measure how recent was the last episode of star formation is to quantify the light-weighted contribution of short-lived massive stars with respect to long-lived lower-mass stars. Balmer absorption lines reach their maximum strength in A-type stars with a spectral break at 3646 \AA . Stars of lower mass and lower effective temperature produce metal absorption lines (CaII H & K, Fe, Mg) which result in a sharp spectral break at 4000 \AA . Moreover, the underlying continuum changes shape with time, progressively losing emission in the NUV/blue spectral range while flattening in the NIR. Their different evolutionary speed and fractional contribution to the optical light at fixed mass make it possible, therefore, to trace the evolutionary stage of a galaxy. This information is quantifiable by

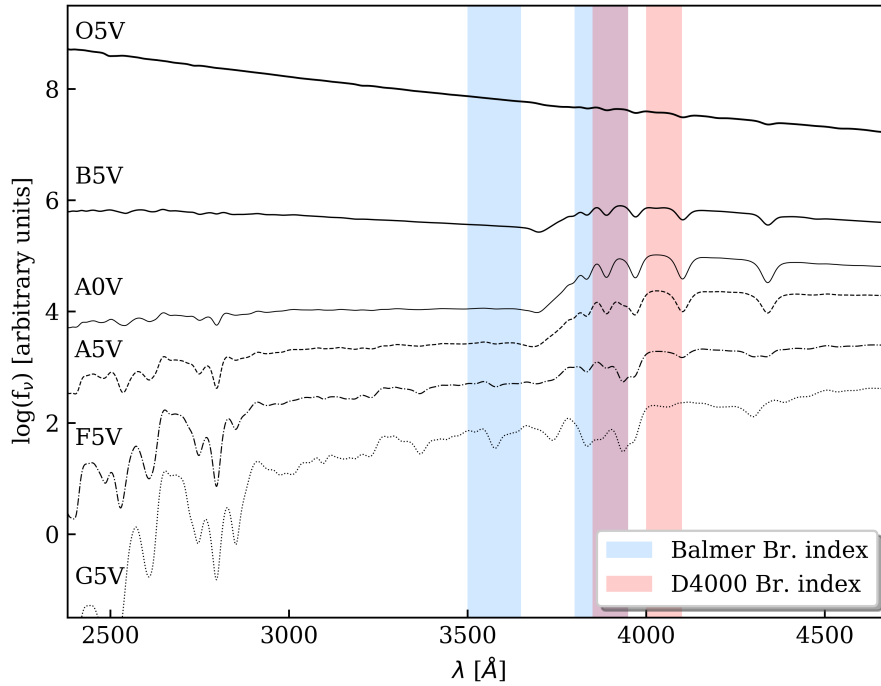


FIGURE 4.2: Flux densities of UVBLUE stellar templates smoothed to the HST resolution. The spectral class of the stars decreases from top to bottom. The bandwidths corresponding to the Balmer Break index (D_B) and D_n4000 are highlighted by blue and pink vertical bands respectively. The two indices together measure the change in the shape of the spectral break caused by the light-weighted contribution of massive stars to the integrated spectrum of a galaxy.

the relative strength of the Balmer versus 4000 Å breaks. Here I measured it through the D_B definition (Kriek et al., 2006) and the D_n4000 definition (Balogh et al., 1999) respectively, as well as computing the ratio between the two. The two indices are defined as follows:

$$D = \frac{\langle F^+ \rangle}{\langle F^- \rangle} = \frac{(\lambda_2^- - \lambda_1^-) \int_{\lambda_1^+}^{\lambda_2^+} F_\nu d\lambda}{(\lambda_2^+ - \lambda_1^+) \int_{\lambda_1^-}^{\lambda_2^-} F_\nu d\lambda}$$

where

$$(\lambda_2^+, \lambda_1^+, \lambda_2^-, \lambda_1^-) = \begin{cases} (4100, 4000, 3950, 3850) & \text{for } D_n4000 \\ (3950, 3800, 3650, 3500) & \text{for } D_B \end{cases}$$

and can be visualized in Figure 4.2.

The behaviour of the two indices with age can be found in Fig. 4.6 (left panels). In the top panel, lighter shaded curves show the variation with increasing duration of star-formation. The ratio is shown in the lower panel as a function of age of composite templates, built with a short truncated SFH. The ratio of the two indices is only mildly dependent on dust reddening since the two breaks share a similar wavelength range. Also, the two indices are fairly robust against low resolution. As can be seen, D_B varies more strongly than D_n4000 during the first 1 Gyr or so, reaching its maximum around 0.3-0.5 Gyr. Eventually, their ratio drops below 1 once the light-weighted contribution from A-type stars fades away. Constant star-formation results instead in a ratio of the two indices around ~ 1.1 rather constant with time. The simultaneous use of these two indices appears to be able to trace the phase transition when young, post-starburst stellar populations dominate the integrated emission and eventually disappear. Their behavior shows the light-weighted age difference between our stacked spectrum (red star in the lower panel of Fig. 4.3) and the stacked spectrum of 34 similarly massive spectroscopically confirmed quiescent galaxies at $z \sim 1.5$ from Gobat et al. 2017 (green star).

I also measured the $H_{\delta A}$ spectral index on the stacked spectrum as in Worthey and Ottaviani, 1997. Since the spectral resolution of HST is worse than in the original Lick system, the $H_{\delta A}$ was measured on the best-fitting, original STELIB-resolution, BC03 model smoothed to the Lick resolution and adding the broadening due to a 200 km s^{-1} stellar velocity dispersion corresponding to our $\langle M_* \rangle$ to account for the high stellar mass of our average galaxy. The D_n4000 and D_B instead are not affected much by resolution. The indices result in $D_n4000 = 1.38 \pm 0.05$, $D_B = 2.20 \pm 0.07$ and $H_{\delta A} = 10.1^{+0.0}_{-0.6} \text{ \AA}$ marking the very recent onset of quiescence. The error on $H_{\delta A}$ was computed measuring the index maximum variation on the templates within the uncertainties on t_{50} and A_V , accounting for the negative correlation between these two. The weakness of the D_n4000 compared to the strength of the Balmer Break and of $H_{\delta A}$ classifies the spectrum as post-starburst-like dominated by A-type stars. The indices can be found in Fig. 4.3. For display purposes only, the figure also shows $H_{\delta A}$ measured on the stacked spectrum at the resolution of the G141 as an empty red star. As can be seen, the index measured on the observed spectrum directly is affected by the low spectral resolution and, therefore, it is not comparable with previous literature results based on the Lick system.

4.2 How common are post-starbursts at $z \sim 3$?

At this point, we investigated whether such post-starburst features could be widespread among the population of massive quiescent galaxies at a similar redshift. To this end, we verified whether our spectroscopic sample was representative of the parent photometric sample and quantified the impact of the selection bias introduced by the H-band selection at $2.5 \leq z \leq 3.5$. A

Kolmogorov–Smirnov test revealed that the probability of the two samples being drawn from the same M/L distribution is only 3%, confirming the selection bias. However, removing 30% of the highest M/L objects from the parent sample yields $p = 0.5$, leaving our HST sample consistent with the remaining 70%. Moreover, the median M/L ratios of the two samples become identical once the highest M/L objects, 40% of the parent sample, are removed. We also computed the lowest M/L that a non post-starburst galaxy would have relative to that of our average galaxy ($\Delta M/L$). A non post-starburst was defined here as a stellar population characterized by $D_B/D_n4000 < 1$. This implies a cut at

$$M/L_{old} \geq M/L_{HST} + \Delta M/L$$

which includes at most 30% of the non-spectroscopically confirmed sample. We thus concluded that at least 60-70% of passive galaxies at $z \sim 3$ are post-starburst. I would like to stress here that the remaining faint and red galaxies could be a mixed population of post-starbursts with higher dust extinction, old galaxies, redshift interlopers, star forming interlopers or AGN. Hence, we concluded that the typical passive galaxy at $z \sim 3$ is a post-starburst. This conclusion is corroborated by the global fast rise of the passive stellar mass function over $2.5 < z < 4$ (Muzzin et al., 2013b; Davidzon et al., 2017) consistent with a ~ 1 dex increase of the number density, implying that a large proportion of the massive passive population in place at $z \sim 3$ must have been recently quenched. Although I did not attempt at computing the number density implied by our objects, the fractions that we find are qualitatively consistent with the overall growth of the fraction of massive young quiescent galaxies reported at lower redshifts (e.g. Whitaker et al., 2013; Wild et al., 2016), as will be discussed later on in this chapter. Moreover, when selecting galaxies at $2.5 < z < 3.5$ at $\log(M_*/M_\odot) > 10.9$ in the Muzzin et al. 2013b catalog and excluding obvious FIR sources in Jin et al. 2018 catalog ($\text{SNR}_{IR} < 5$), ~ 30 sources with UVJ colors are compatible with being in the old region, i.e. $(U-V) + (V-J) > 2.8$. This appears to be consistent with 30-40% of massive PEGs at $z=3$ being old, as expected from the estimated number density at $z \sim 4$ ($\approx 1 \times 10^{-5} \text{ Mpc}^{-3}$) which is itself uncertain at the moment (see Fig. 1.5). In addition, from Fig. 4.4 and from the strong Balmer lines in the published spectra, it appears that all $z \geq 3$ spectroscopically confirmed passive galaxies from the literature are sharing our global spectral properties and UVJ colors (Schreiber et al., 2018b; Valentino et al., 2020; Forrest et al., 2020a). A crucial question at this point is whether or not old systems were in place at $z \sim 3$ and whether their fraction with respect to the total population is

consistent with the number densities of recently quenched objects at higher z .

4.3 Analysis of individual targets

Before discussing what can be learnt from our sample with respect to the literature, I report below the results of the analysis carried out on the individual HST targets, where I included the photometric information.

Fig.4.5 shows the resulting t_{50} and A_V extracted from the grism spectra (blue points) compared to those derived including COSMOS2015 photometry (red points). Light to dark shading marks 3-, 2- and 1σ confidence levels respectively, obtained following Avni, 1976 with two interesting parameters. The degeneracy between t_{50} and A_V appears to be strongly mitigated by the addition of the photometry once the redshift is constrained with sufficient accuracy to the spectroscopic value. The bulk of our targets are consistent with having formed half of their stellar mass relatively recently, systematically having $t_{50} < 1$ Gyr. In some cases, as for id977680 and id478302, the best fitting combination suggests the presence of dust enshrouded young stellar populations. Incidentally these two galaxies are also detected in X-rays and $24 \mu\text{m}$, as discussed in the previous chapter (Sect. 3.2). Their t/τ ratio can be viewed as an indication of the SFR suppression with respect to the peak level under the assumption of a τ -model. Their nominal best-fitting t/τ are 6 and 11.1 respectively. Their 1σ uncertainties however extend down to 1.1 and 2 respectively. This is suggesting that these galaxies could host a current level of SFR which is suppressed by at least a factor of 3 with respect to their initial value.

I would like to stress here that the age difference between the stacked spectrum and the average from individual sources is mainly driven by the fact that the analysis on the former does not include the information from a stacked SED.

Motivated by performance of the spectral indices on the stacked spectrum, I tested their yield on the individual galaxies as well. In Fig.4.6 (upper right) I show the two indices computed on our targets. The grey dashed line highlights the transition where their ratio equals 1. The mean error in each side band was divided by the square root of the number of pixels within it. For id361413, whose rest-frame spectrum does not cover the entire wavelength range required to compute the D_n4000 red sideband, I used the average flux density as the mean of the best-fitting template in the same range. The error was computed as the mean of the noise spectrum taken on the last 10 spectral bins. I flagged this galaxy with a red diamond. The blue star shows the indices computed on id503898 which has the least robust redshift. The red star marks the values obtained on the average spectrum. As it can be seen, the S/N of our spectra result in large errorbars. However, the indices, together with their uncertainties, all lie well above the 1:1 relation, thus independently confirming the presence of young stellar populations

in all of our targets. This supports the results of the spectral modeling, highlighting how some of the most massive QGs at $z \sim 3$ appear to be only recently quenched. An overview of the physical parameters derived for our sample can be found in Table 4.1.

4.4 Discussion

Despite the overall stability of the spectral fitting mentioned above, one should keep in mind that age estimates still rely on the spectral fitting scheme adopted, on the assumptions made in the choice of template libraries and ultimately on the shape of the SFH used. Keeping such caveats in mind, we can start making meaningful statements on the ages of our QGs through relative comparisons of the mass-weighted ages within our sample.

The bulk of our targets is consistent with having suppressed their star-formation very recently, no earlier than 300-800 Myr prior to observation. The median value being 0.5 Gyr with a dispersion of 0.2 Gyr. Two outliers are present, id977680 and id478302, showing younger ages than the bulk of the sample, 0.25 and 0.1 Gyr respectively. Despite the fact that for id977680 the D_B/D_n4000 ratio appears to be the strongest, the S/N of our spectra prevents us from identifying significant differences among our galaxies. Moreover, the downward trend of the D_B/D_n4000 ratio at $t_{50} \leq 0.1$ Gyr precludes the possibility of testing the age inferred from the spectral fit, such as for id478302. These two sources have counterparts both at $24\mu\text{m}$ and in the X-rays (2-10keV) which, given also the 3σ upper limits on the SFR placed by the radio 3GHz non-detections, we attribute to the presence of an AGN (see Sect.3.2). If sub-MS star formation is present in these sources, they could represent transitioning objects in which the AGN is playing a substantial role in suppressing the star formation.

Globally, our mass-weighted ages are rather short. A reason for this could be the choice of adopting smooth star formation histories to model simultaneously the rest-frame UV/optical spectra and the broad-band NIR photometry. Should a recent burst of star formation have taken place on top of an older, more massive stellar population the best-fitting model to both data sets would be a compromise solution between the two components. Interestingly, however, the coupling of $H\delta_A$ and D_n4000 appears to be lying on the evolutionary track of a single burst stellar population, contrary to what happens for K+A galaxies. Moreover, such short t_{50s} (and quenching times) have been reported by several independent works, using either parametric (Schreiber et al., 2018b; Valentino et al., 2020) or non-parametric SFHs (Forrest et al., 2020b; Saracco et al., 2020; Marsan et al., 2020), pointing at such feature to be not directly caused by our particular fitting method. Lastly, the surprisingly short t_{50s} of id478302 and id977680 (0.1 and 0.25 Gyr, respectively) could be due to residual star formation as mentioned above. Their SFRs are lower than the current lower limits constrainable by the photometry

id	z_{spec}	t_{50} [Gyr]	A_V [mag]	δ	DB	D_n4000	$f_{24\mu m}$ [mJy]	$\log L_{X_{obs}}$	$\log L_{X_{24\mu m}}$	S_{3GHz} [mJy]	$SFR_{24\mu m}$ [$M_{\odot} yr^{-1}$]	SFR_{3GHz}
135730	$2.841^{+0.021}_{-0.018}$	$0.5^{+0.2}_{-0.2}$	$0.2^{+0.3}_{-0.1}$	[-0.7,0]	2.22 ± 0.51	1.47 ± 0.23	-	< 43.6	-	0.576 ± 0.03	867	~ 12930
707962	$2.667^{+0.015}_{-0.002}$	$0.5^{+0.0}_{-0.1}$	$0.7^{+0.1}_{-0.0}$	[-0.4,0]	2.07 ± 0.41	1.61 ± 0.20	0.032 ± 0.023	< 43.6	43.50	0.005 ± 0.003	<261	<183
503898	$2.673^{+0.124}_{-0.204}$	$0.7^{+0.3}_{-0.2}$	$0.6^{+0.3}_{-0.2}$	[-0.7,0]	2.02 ± 0.35	1.27 ± 0.17	0.111 ± 0.011	44.26 ± 0.36	43.89	0.004 ± 0.003	419	<183
137182	$2.557^{+0.005}_{-0.005}$	$0.8^{+0.0}_{-0.1}$	$0.1^{+0.1}_{-0.0}$	[-0.4,0]	2.02 ± 0.22	1.34 ± 0.10	-	< 43.16	-	-	-	-
252568	$3.124^{+0.003}_{-0.003}$	$0.4^{+0.2}_{-0.1}$	$0.4^{+0.2}_{-0.2}$	[-0.7,0]	2.39 ± 0.19	1.37 ± 0.11	0.041 ± 0.018	< 43.6	43.73	0.011 ± 0.004	<540	<307
977680	$2.393^{+0.011}_{-0.000}$	$0.3^{+0.3}_{-0.0}$	$1.6^{+0.1}_{-0.0}$	[0]	2.25 ± 0.51	1.15 ± 0.15	0.146 ± 0.020	43.73 ± 0.29	43.87	0.005 ± 0.003	289	<155
575436	$2.998^{+0.002}_{-0.003}$	$0.7^{+0.0}_{-0.0}$	$0.1^{+0.0}_{-0.0}$	[-0.7,-0.4]	2.23 ± 0.2	1.41 ± 0.09	0.000 ± 0.018	< 43.6	43.42	0.002 ± 0.002	<394	<144
478302	$2.801^{+0.005}_{-0.002}$	$0.1^{+0.1}_{-0.0}$	$1.0^{+0.0}_{-0.1}$	[-0.4]	2.02 ± 0.27	1.34 ± 0.12	0.100 ± 0.021	44.34 ± 0.32	43.91	0.002 ± 0.003	508	<197
447058	$2.665^{+0.003}_{-0.007}$	$0.4^{+0.2}_{-0.2}$	$0.8^{+0.2}_{-0.2}$	[-0.4]	2.18 ± 0.29	1.39 ± 0.12	0.171 ± 0.017	< 43.6	44.02	0.000 ± 0.002	644	<122
361413	$3.23^{+0.007}_{-0.006}$	$0.4^{+0.1}_{-0.1}$	$0.1^{+0.1}_{-0.0}$	[-0.7,-0.4]	3.15 ± 0.48	1.21 ± 0.09	0.000 ± 0.024	< 43.6	43.60	0.003 ± 0.003	<967	<242

TABLE 4.1: Best fit values and their 1σ uncertainties. Observed 24μ m and 3GHz flux densities. Upper limits are given at 3σ . Those for the observed bolometric X-ray luminosities were derived median-stacking all undetected sources. Id137182 is absent from Jin et al., 2018 catalog due to absence of K_s or VLA priors.

at our disposal ($\sim 300 M_{\odot} \text{yr}^{-1}$). Assuming an exponentially declining SFH and our best-fit t_{50} , our galaxies are consistent with having been forming half of their stellar mass around $z_{\text{form}} \sim 3.5$ at high SFR $\sim 1800 - 3000 M_{\odot} \text{yr}^{-1}$, similarly to what reported in Valentino et al., 2020 but shifted at a later epoch. It should be noted, however, that such simple representations of the SFHs are unlikely to be representative of the *peak* SFR if the intrinsic SFH was more complex, such as in the case of multiple phases in the star formation (Barro et al., 2016b) or in the case of mergers (which imply a degeneracy with mass assembly, hence in lower SFRs split between the progenitors).

Interestingly, the current color selection of high- z QGs preferentially selects bright blue UVJ quiescent objects where "dust-poor" PSBs often lie. In some cases, it extends to a bluer region outside the standard quiescent boundaries where compact transitioning galaxies are thought to lie along their fast drop in SFR (Belli, Newman, and Ellis, 2019b; Schreiber et al., 2018b; Valentino et al., 2020; Forrest et al., 2020a). This implies that high- z quiescent galaxies are selected more or less in the same evolutionary phase, namely after O and B stars exited the Turn Off and before the same happens for A-type stars. This appears to be manifesting through similar distributions of (mass-weighted) ages among the highest- z samples (perhaps unsurprisingly, see Fig. 4.7). This also means that the magnitude cut necessary for spectral acquisition is biasing the selection of high- z QGs against dusty PSBs or galaxies more slowly transitioning into quiescence. Moreover, considering the cosmic time between $z=2.8$ and $z=1.8$, the mass-weighted ages of our targets appear to be consistent with passively evolving into old QGs at intermediate redshifts (Whitaker et al., 2013). This is not the case for higher- z massive QGs, confirming that the high- z selection is directly probing the continuous injection of new compact quiescent galaxies into the passive population.

The enhanced fraction of PSBs (60%-70%, D'Eugenio et al., 2020; Lustig et al., 2021) among photometrically selected $\log(M_*/M_{\odot}) \geq 11$ QGs at $z \sim 3$, appears to be linked to the progressive migration of the red-sequence towards bluer colors with increasing redshift. PSBs represent an increasing fraction of the whole QGs population with redshift (Wild et al., 2016). Particularly so also because the transition from Balmer to CaII absorption lines is fast compared to the overall lifetime of a galaxy at low redshift. At the epochs spanned in this work, instead, such a phase naturally represents a much larger fraction of a galaxy lifetime. Our galaxies were selected to be massive and are all consistent with having formed the bulk of their stellar mass within the last 0.8 Gyr. High mass PSBs have been associated locally ($z < 0.05$) to fast dissipative events at high z , which might be followed by minor rejuvenation events from smaller gas rich companions (Pawlik et al., 2018). At $z < 0.2$, Kaviraj et al. (2007) report on 20%-60% mass fractions formed in recently quenched E+A galaxies at $\log(M_*/M_{\odot}) \sim 11$. In this mass regime, they linked strong star formation likely triggered by merger events to a fast drop in SFR due to AGN feedback increasing in quenching efficiency with the stellar mass of the host galaxy. At $0.5 < z < 1.3$, fully quiescent galaxies in

the same mass range are consistent with a <20% of stellar mass formed in the last 1 Gyr of evolution, whereas similarly massive $\log(M_*/M_\odot) \sim 10.8$ -11 spectrophotometrically confirmed PSB galaxies show SFHs consistent with having formed between 40% and 70% of their mass in the same time span (Wild et al., 2020). At $0.48 < z < 1.2$, massive K+A galaxies appear to be generally bulge-dominated but the connection between mergers and recent quenching is not clear (Vergani et al., 2010). The median bulge dominated compact morphologies of our galaxies (see next chapter) and their extremely young ages suggest that, regardless of the specific mechanisms involved, the channels responsible for fast quenching and structural transformation are strongly affecting the majority of the massive quiescent population at these epochs.

As mentioned in Belli, Newman, and Ellis, 2019b, the growth rate of $\log(M_*/M_\odot) \geq 10.8$ PSBs at $z \sim 2$ appears to account for nearly half of the quiescent population. This translates into a fast increase in the number density of young quiescent galaxies starting already at $z \sim 1.5 - 2$ (Whitaker et al., 2011; Whitaker et al., 2013) and reversing their relative contributions to the red sequence with respect to old galaxies at $z \sim 3$. At the time being, the exact degree to which such "post-starburstiness" is diffused all over the passive UVJ region can be addressed only with very expensive targeted HST observations. The enhanced sensitivity of JWST will be able to map the full distribution of PSBs along and across the UVJ diagram to the highest redshifts. These could potentially help in clarifying the distribution of dust attenuation among spectroscopically confirmed extremely red-objects and in turn provide insights on the global star formation history of high- z QGs. It is also worth highlighting the value of such a pilot sample, and of potential future HST campaigns, in order to test and possibly extend the calibration of the age-UVJ color relation of Belli, Newman, and Ellis, 2019b with accurate spectroscopic confirmations to the highest redshifts.

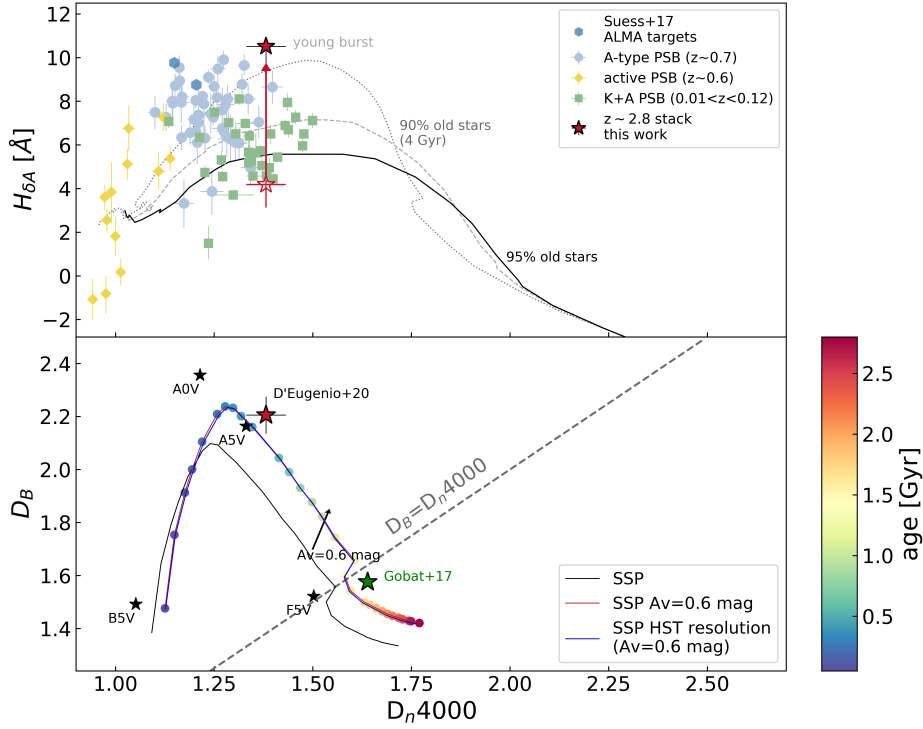


FIGURE 4.3: *Top*: comparison between the average D_n4000 and $H_{\delta A}$ of this sample and $z \sim 0.7$ A-type $\log(M_*/M_\odot) \sim 10^{11.1}$ post-starburst galaxies (light blue dots) from Suess et al., 2017. Green squares: K+A $z < 0.12$ $\log(M_*/M_\odot) \sim 10^{10.6}$ post-starbursts from French et al., 2015. Yellow diamonds: $z \sim 0.6$ $\log(M_*/M_\odot) \sim 10^{10.5-11.5}$ post-starbursts from Sell et al. 2014 dubbed "active" as they show a prominent UV continuum, [OII] and [OIII] emission lines with inferred SFR_{IR} of order of $\sim 500 M_\odot \text{yr}^{-1}$ (with a Salpeter IMF). Open red star: $H_{\delta A}$ computed on the stacked spectrum, hence at the resolution of the G141 spectrograph. This point was reported for display purposes only, to show the index sensitivity to low resolution. Filled red star: $H_{\delta A}$ measured on the best-fitting, STELIB-resolution BC03 template, smoothed to the Lick resolution and with a 200 km s^{-1} velocity dispersion to account for the high stellar mass of our average galaxy. Tracks with different amounts of old stars (age $> 4 \text{ Gyr}$) from Suess et al., 2017 are shown, going from a single burst of star formation (no old stars, dotted line) to 90% and 95% of old stars (grey solid lines), where only 10% and 5% of stellar mass was formed in the most recent burst of star formation, respectively. *Bottom*: strength of the Balmer and 4000 Å break indices as a function of the SSP age. Red star: and green stars represent the indices measured on our stack spectrum and on the average spectrum of similarly massive QGs at $z \sim 1.5$ (Gobat et al., 2017), respectively. The errorbars of the green star are smaller than the marker size. Black stars mark the indices computed on theoretical stellar spectra smoothed to HST resolution (Rodríguez-Merino et al., 2005).

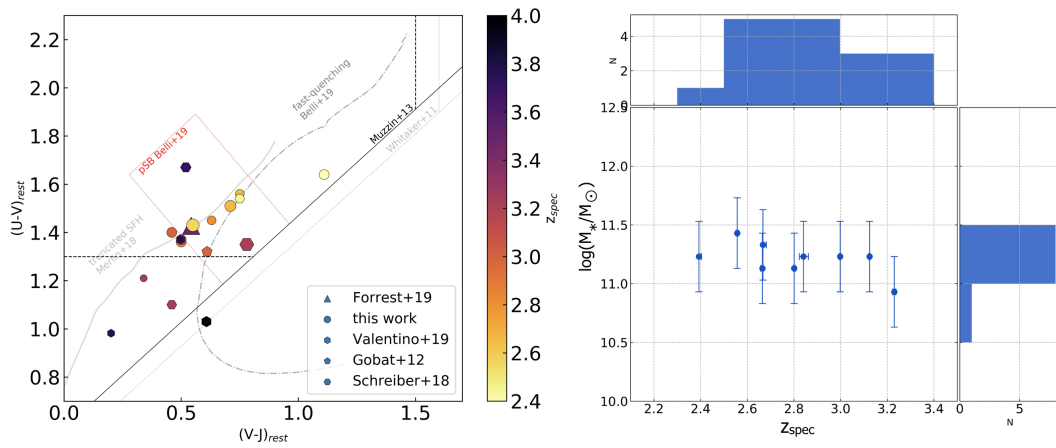


FIGURE 4.4: Left: UVJ colors of high-redshift ($z > 2.5$) quiescent galaxies color coded for their spectroscopic redshift. Solid and dotted-dashed tracks show the color evolution for fast-evolving SFHs, from Merlin et al., 2018 and Belli, Newman, and Ellis, 2019b respectively. The red box shows the post-starburst region as defined in Belli, Newman, and Ellis, 2019b. Marker sizes are proportional to stellar mass. Right: stellar mass and redshift distributions of the sample.

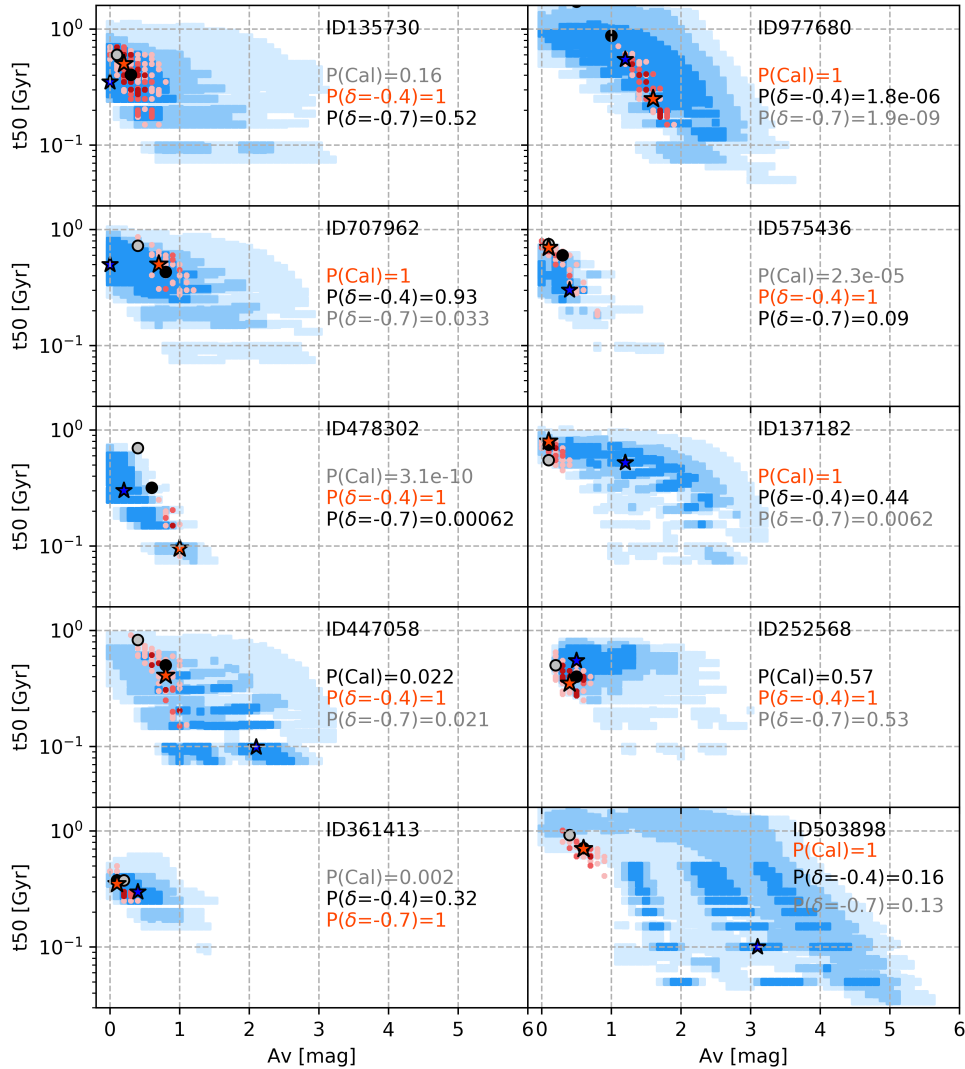


FIGURE 4.5: Mass-weighted ages and dust extinction values for our targets. Blue squares mark the confidence regions (3 to 1 σ going from light to dark points) extracted from the spectra only. Red points show the solutions of the combined fit. Blue and red stars in each panel mark the best fit solution from spectroscopic fit and the combined fit respectively. The probability of consistency of each extinction law with respect to the best fitting one are reported for each galaxy. Black and grey dots show the best fitting combined solution at fixed extinction law, their color coding follows that of probabilities.

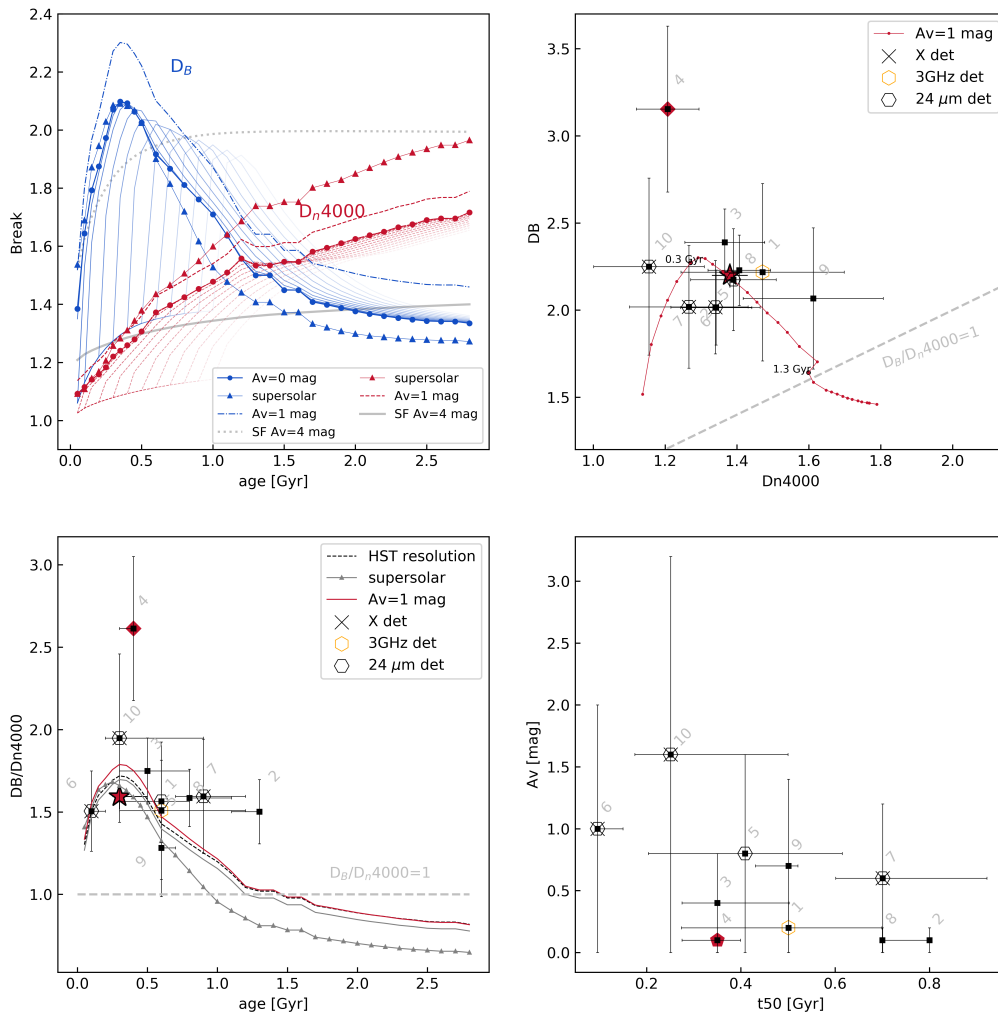


FIGURE 4.6: *Upper left*: variation of the Balmer and 4000 Å breaks for CSPs as a function of their age using BC03 templates at solar metallicity. Lighter curves mark the evolution for a truncated SFH with increasing duration of star formation. Dotted and solid gray curves show the behavior of a constant SFH for the two breaks respectively. *Upper right*: individual values of D_B and D_n4000 for our targets. The red track shows their evolution with age and is attenuated by 1 mag. The gray dashed line marks the 1:1 relation. *Lower left*: variation of the index ratio as a function of age for an SSP-like template. The effect of smoothing templates to the HST resolution is shown by a black dashed curve. The effect of a $A_V=1$ mag attenuation is shown instead by a red curve. The full transition between a Balmer-dominated and a 4000Å -dominated spectrum is flagged when $D_B/D_n4000=1$ (grey dashed line), which happens around 1.3 Gyr of passive evolution. *Lower right*: best-fit values for the dust attenuation and mass-weighted age from the combined fit.

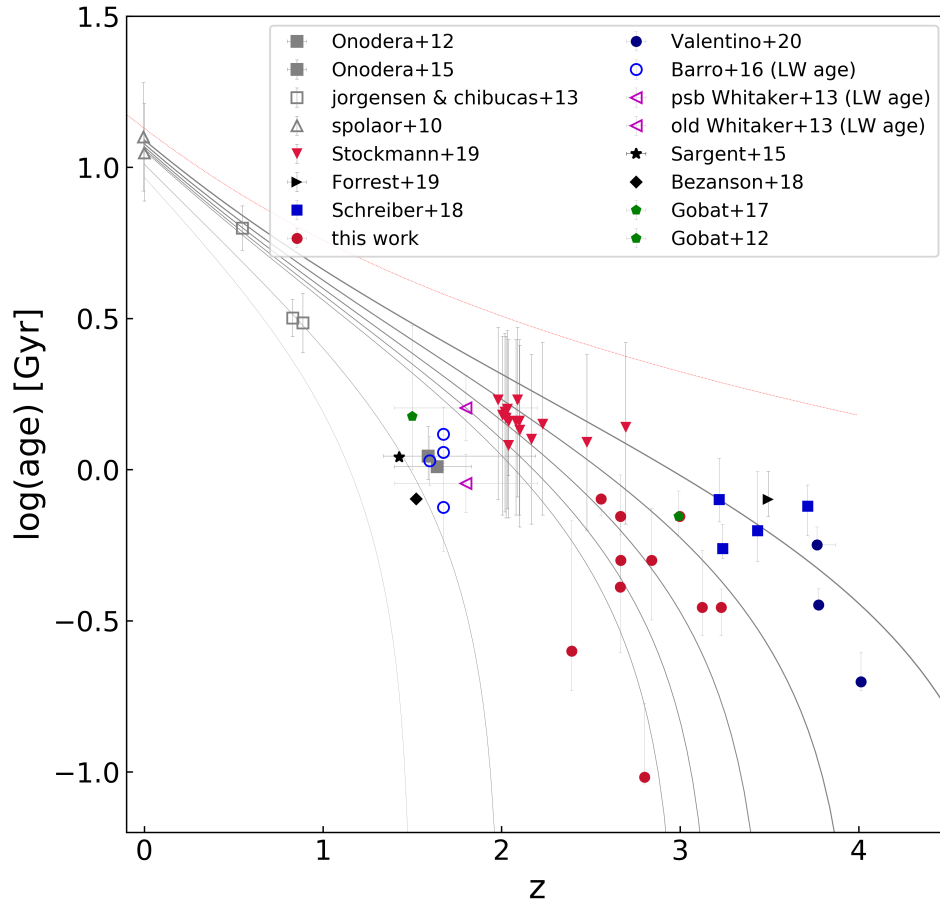


FIGURE 4.7: Age evolution with redshift in $\log(M_*/M_\odot) > 10.5$ quiescent galaxies. Adapted from Onodera et al., 2015. For $z > 2.5$ QGs we show their mass-weighted ages (t_{50s}). Gray solid lines show, from thin to thick, the age of simple stellar populations made at a z_{form} from 1.5 to 5.

Chapter 5

The emergence of massive quiescent galaxies at $z \sim 3$

In the previous chapters I showed how HST observations are able to probe the (H-band) brightest end of the massive QG population providing access to clear spectral breaks in the majority of the objects. Our data suggest that a substantial fraction of the massive quiescent population at $z \sim 3$ is approaching the quenching epoch, becoming intrinsically young and with spectra of post-starburst galaxies. In other words, with relatively few HST orbits it is possible to perform spectroscopic confirmation of QGs up to $z \sim 3.2$ and start quantifying the incidence of newly-quenched objects within the population.

In section 5.1 of this chapter, I will show the attempts done to constrain the average gas fraction of our QGs (D'Eugenio et al., 2020). In section 5.2, I will show evidences for an enhanced black hole activity with respect to similarly massive star forming galaxies in the same redshift range and to lower redshift QGs, while in section 5.3 I will show similarities with known compact star forming galaxies (D'Eugenio et al. 2021, arXiv:2012.02767).

5.1 Insights on the residual gas fraction from [OII]

Given the tight anticorrelation between the age of a stellar population and the specific SFR ($sSFR = SFR / \langle M_* \rangle$) of its host galaxy, expected in the case of a smooth declining intrinsic SFH (as opposed to a simple stellar population or a complex SFH), we investigated whether the observed age decrease at fixed M_* from intermediate redshift samples to $z \sim 2.8$ translates into a higher $sSFR$. To this end, I used as a reference the sample of 34 spectroscopically confirmed $M_* \sim 10^{11}$ QGs $z \sim 1.5$ observed at high-spectral resolution with VIMOS/VLT by Gobat et al., 2017 (hereafter G17). The authors constrain both the unobscured SFR by means of the [OII] emission line in their stacked UV/optical spectrum and the obscured SFR from a stacked FIR SED of an independent sample of similarly selected QGs. Here, I exploited the weak [OII] emission line detected in our stacked spectrum (see Sect. 4.1), under the assumption that it is entirely powered by photoionisation from hot O, B stars, i.e. star formation.

I used MPFIT to model the residuals of the fit to the stacked spectrum using a single Gaussian centered and fixed at 3727 \AA with a width matched to the data spectral resolution, measuring $F_{[\text{O II}]} = (3.1 \pm 0.7) \times 10^{-18} \text{ erg s}^{-1} \text{ cm}^{-2}$. The observed [O II] flux was dereddened adopting the best fit dust attenuation ($A_V = 0.6 \text{ mag}$) using a value of $f = 0.83$ for the ratio between stellar and nebular extinction (Kashino et al., 2013) as in G17 in order to perform a consistent relative comparison. Following Kennicutt 1998 I obtained an $\text{SFR} = 7 \pm 3 M_{\odot} \text{ yr}^{-1}$ which is a factor of ~ 60 below the main sequence (MS) level at $2.5 < z < 3.5$ (Schreiber et al., 2015). This is in agreement with estimates for intermediate redshift quiescent galaxies of the dereddened [O II] luminosity ($\text{SFR}_{[\text{O II}]} = 4.5 M_{\odot} \text{ yr}^{-1}$, G17), which is in turn consistent with their FIR luminosity ($\text{SFR}_{\text{IR}} = 4.8_{-1.3}^{+1.8} M_{\odot} \text{ yr}^{-1}$, Gobat et al., 2018, hereafter G18). Therefore, the age evolution implied by the continua of $z \sim 1.5$ and $z \sim 3$ similarly massive quiescent galaxies, appears to occur at a constant sSFR, mimicking the behavior of a simple stellar population rather than that of a smoothly declining SFH. This is also suggested by the equivalent width (EW) of the line which is $2.1 \pm 0.6 \text{ \AA}$ rest-frame. This value is almost half that obtained by G17 due to a higher UV continuum produced by ~ 1 Gyr younger stars. Afterwards, I checked whether residual star formation was partially filling the observed absorption lines, possibly affecting the age determination. I subtracted from the stacked spectrum the continuum associated to a 100 Myr-old stellar population forming stars at a constant rate and with $A_V = 0.6 \text{ mag}$. The continuum of such component was normalized in order to match the observed [OII] flux. I then repeated the spectral fit deriving $t_{50} = 0.30_{-0.05}^{+0.20} \text{ Gyr}$ and $A_V = 0.9_{-0.5}^{+0.4} \text{ mag}$. Letting the age and extinction of the star-forming component vary (100-300 Myr and 0.6-1.5 mag, respectively) leaves t_{50} unchanged while increasing A_V up to 1.0 mag. The flux at $\lambda > 4400 \text{ \AA}$ varies around the 95% of the original flux, suggesting that the CSF component does not account for more than 1-2% of $\langle M_{\star} \rangle$ as also confirmed by the mass produced in a $\Delta t \sim 300 \text{ Myr}$ at a constant SFR of $10 M_{\odot} \text{ yr}^{-1}$, namely the upper limit inferred here. We thus conclude that the presence of the youngest stellar population does not impact our results on t_{50} and A_V significantly. The sSFR of our sample, $(4.35 \pm 2.47) \times 10^{-11} \text{ yr}^{-1}$ is consistent with the available estimates at $z \sim 1.5-1.8$ (Sargent et al., 2015; Bezanson et al., 2019) and with the sSFR for the 4 quiescent galaxies in Schreiber et al., 2018b for which the $\text{sSFR}_{[\text{O II}]}$ is available and that display either a spectral break or absence of emission lines.

To check that the average spectrum is not dominated by emission from luminous unobscured AGN, I removed from the stack the two X-ray detected sources ($L_{X_{2-10\text{keV}}} = 10^{44.3}$ and $10^{43.7} \text{ erg s}^{-1}$)¹, getting $F_{[\text{O II}]_{\text{noX}}} = (3.53 \pm 0.90) \times 10^{-18} \text{ erg s}^{-1} \text{ cm}^{-2}$ consistent within the uncertainties. Stacking the available X-ray data in COSMOS for the undetected sources results in $L_{X_{2-10\text{keV}}} < 10^{43.6} \text{ erg s}^{-1}$ as a 3σ upper limit. If part of the [O II] luminosity

¹I recall that id503898 was not included in the stacked spectrum.

were caused by low AGN activity or shocks, the intrinsic SFR would be even lower, strengthening the conclusion that the young spectral age does not directly map into a higher sSFR. Using the UV-extended Maraston et al., 2009 models the best-fitting template yields a similar $t_{50} \sim 0.3$ Gyr but produces a slightly worse χ^2 and a less solid [O II] detection, with a flux that is 60% the one measured with BC03 templates, at 2.9σ confidence.

It is interesting to place our $z \sim 3$ results in the overall evolutionary context of passive galaxies. In order to be able to compare to the available literature I expressed, for convenience, the SFR constraints in terms of the available gas fraction through the relation $f_{mol} = sSFR/SFE$, where SFE is the star formation efficiency ($SFE = SFR/M_{gas}$). I caution that this is just an alternative way to look at the SFR result, as we are using the same single constraint: I will use both quantities interchangeably in the following and notably in Fig. 5.1. I assumed the same SFE derived in G18 ($5 \times 10^{-10} \text{ yr}^{-1}$) which is the most representative measure of the SFE of QGs to date, since it is derived from a stacked FIR SED of $977 M_* \sim 10^{-11}$ QGs at $1.4 < z < 2.5$ after correcting for clustering of satellite galaxies. In such work, the authors claim that the SFE of intermediate z QGs is lower than that of typical star forming galaxies by $\times 2-3$. Such reduced SFE appears to be also frequently observed in post-starburst galaxies (Suess et al., 2017; French et al., 2015). Our SFR thus converts into $M_{mol} = (1.5 \pm 0.6) \times 10^{10} M_{\odot}$, hence $f_{mol} \sim 9 \pm 4\%$. I compared this value to CO or dust-continuum-based gas fractions and upper limits (converted to Salpeter) for quiescent and post-starburst galaxies: Davis et al., 2014b and Saintonge et al., 2011 for local massive passively evolving galaxies; Sargent et al., 2015, Bezanson et al., 2019, Spilker et al., 2018, Zavala et al., 2019, Rudnick et al., 2017, Suess et al., 2017, Hayashi et al., 2018, Gobat et al., 2018 for intermediate- z QGs; Schreiber et al., 2018b and Valentino et al., 2020 for $z \sim 3-4$ galaxies. Despite the uncertainties, our data at $z \sim 3$ seems to disfavor the continuation of the steep $(1+z)^{4-5}$ trend inferred from $z = 0$ to $1.5-2$ in G18, suggesting a flattening in the M_{mol}/M_* evolution (or equivalently, of the sSFR).

The published $SFR_{[O II]}$ for $z > 3$ galaxies with a clear spectral break in Schreiber et al., 2018b and Valentino et al., 2020 also seem to support this trend.

Taken at face value, our data thus suggest that a substantial fraction of the massive QG is progressively youngening over $1.5 < z < 3-4$ with a more or less constant f_{mol} (or equivalently, sSFR). However, the precise measurement of the cold molecular gas mass still suffers from the uncertainty on the origin and intrinsic luminosity of the [OII] emission line: if weak nebular lines often flag a relatively recent shut down of star formation, they have also been linked to galaxies hosting substantial amounts of obscured star formation, contaminating the rest-frame colors commonly used for the sample selection (Poggianti and Wu, 2000; Lemaux et al., 2017).

In short, the combined spectral (rest-frame NUV/Optical) and photometric

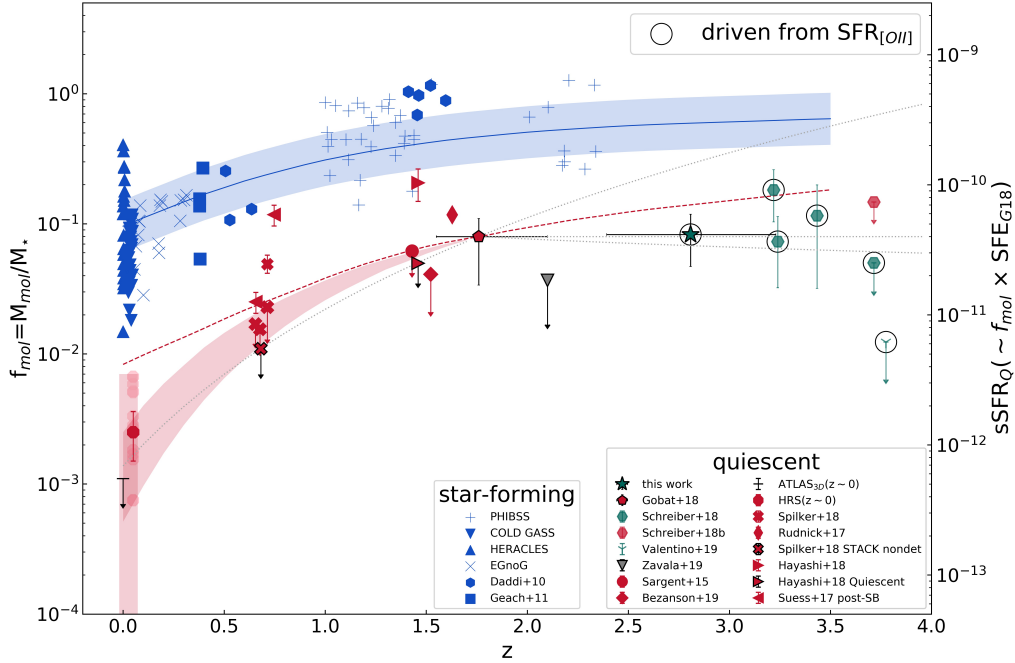


FIGURE 5.1: Evolution of f_{mol} or equivalently the $sSFR_Q$ of quiescent galaxies ($sSFR_Q \sim f_{mol} \times SFE_{G18}$) with redshift, adapted from Gobat et al., 2018. Red symbols mark quiescent galaxies, old and post-starbursts, with CO or dust-continuum measures, whereas circled green symbols mark estimates from $SFR_{[O II]}$ alone, converted to f_{mol} adopting G18 SFE. Black contours mark stacked samples, where horizontal error bars show the spread in redshift of individual targets. Blue symbols mark the gas fraction of low-, intermediate-, and high- z ($z > 1$) MS galaxies. The blue curve and shaded area mark the evolution of an average $5 \times 10^{10} M_{\odot}$ MS galaxy and its 0.2 dex scatter (Sargent et al., 2014). The red dotted curve shows the same relation, offset by a factor of 6 and for a stellar mass of $\log(M^*(z) + \Delta M)$, where ΔM is the offset between the median mass of G18 sample and the M^* of the passive stellar mass function at $\langle z \rangle \sim 1.8$. The pink shaded area shows the trend derived in G18. Grey lines are extrapolations of the low redshift trend assuming a gas fraction rise as $(1+z)^\alpha$, with $\alpha \sim 4-5$, as fast as in G18; $\alpha = 2.2$ as for MS galaxies; $\alpha = 0$ for no evolution; and $\alpha = -0.5$ representative of a negative evolution.

(rest-frame UV-to-NIR) emission rejects the presence of catastrophic photometric errors and strongly favors the quiescence of our targets. On the other hand, our targets are consistent with very young mass-weighted ages, which makes their final interpretation less clear as observing NUV/Optical spectral breaks does not exclude the presence of substantial dust attenuation. Multiwavelength data were used to further test the results obtained from HST spectroscopy: since the upper-limits on the obscured SFR placed by the latest deblended MIR and FIR photometry (Jin et al., 2018) are too shallow to exclude sub-MS SFRs in undetected galaxies, we relied on the mean-stacked shallow detection in the radio regime at 3GHz to constrain the potential average obscured SFR to be below $50 M_{\odot}\text{yr}^{-1}$ (D'Eugenio et al., 2020), hence 6 times lower the coeval MS, at most. Converting *individual* 3GHz 3σ upper-limits into SFRs results in $<120\text{-}190 M_{\odot}\text{yr}^{-1}$, which are not conclusive to exclude substantial obscured star formation on a galaxy-by-galaxy basis.

It should be noted, on the other hand, that the connection between MIR or radio detections and star formation is not straightforward either. The origin of the mid-IR emission is in principle degenerate since it can arise from multiple phenomena such as a dusty AGN torus, warm dust heated by star-formation, the presence of hot circumstellar dust around AGB stars and/or the presence of diffuse cirrus clouds heated by old stellar populations (Fumagalli et al., 2014). In particular, 30-40% of our galaxies show-up in MIPS $24\mu\text{m}$ images with $5\text{-}10\sigma$ detections in Jin et al., 2018 catalog. Their individual $24\mu\text{m}$ flux densities were converted to hard X-ray luminosities, compared to Chandra X-ray detections and judged consistent with being AGN-powered. Radio emission could also be driven by radio-mode AGN activity. These targets could potentially represent examples of rapidly transitioning galaxies which underwent a sharp truncation of their star formation, possibly through AGN feedback. I explore the incidence of AGN on our target galaxies in the context of the literature in the next section.

All-in-all, dedicated mm observations are necessary to conclusively assess the level of cold gas and residual star formation.

5.2 Tracing AGN feedback

Here I investigate the incidence and strength of BH feedback on newly quiescent galaxies, in the framework of SMBH-galaxy coevolution. In particular, given the arguments presented in section 3.2.2 one can use the rest-frame 1.4 GHz luminosity averaged over the entire sample to study the strength of mechanical feedback induced by AGN radio jets on our QGs, and use the fraction of X-ray detections and their rest-frame hard X-ray luminosities to constrain the rate of black hole mass growth.

5.2.1 Radio perspective

The mean stacked peak flux density of $S_{3\text{GHz}} = 2.72 \pm 0.93 \mu\text{Jy}$ reported in D'Eugenio et al., 2020 is here translated into a K-corrected rest-frame luminosity of $L(1.4 \text{ GHz}) \sim 2 \cdot 10^{23} \text{ W/Hz}$ and interpreted as arising from low-luminosity AGN activity. Under the assumption that $z \sim 2.8$ quiescent galaxies share a similar far-IR-radio global SED as lower- z analogs (Gobat et al., 2018), the flux density expected from star-formation corresponds to $L_{\text{mod}} = 1.2 \cdot 10^{22} \text{ W/Hz}$. This implies an excess signal of $L_{\text{mod}} = 1.8 \cdot 10^{23} \text{ W/Hz}$, namely a factor of ~ 18 higher. This is a factor of 3-4 higher than the excess found in $z \sim 1.8$ similarly massive QGs (Gobat et al., 2018). The low statistics implied by our sample size prevents us from making meaningful considerations on the overall duty cycle of AGN activity. It is worth mentioning, however, that the 0.66 duty cycle estimated in G18 from $z=1.4$ to $z=2.5$ implied a burst duration of 1.2 Gyr which is 1.6 times larger than our observational window (the cosmic time spanned by our sample is 0.72 Gyr). This, together with the ensemble radio detection, might imply that we are sampling an epoch when low-level AGN activity is almost always on in newly quiescent galaxies, with a stronger mechanical feedback from AGN-driven jets with respect to what inferred for lower- z massive analogs.

5.2.2 X-ray perspective

L_X can be viewed as a tracer of the typical rate of black hole growth in a given galaxy sample. Recent stacked analysis of quiescent galaxies in COSMOS constrain the average level of rest-frame hard X-ray emission to be $L_X = 2 \times 10^{43} \text{ erg s}^{-1}$ (Carraro et al., 2020, hereafter C20)². While our non-detections are consistent with C20, our mean rest-frame $L(2\text{-}10\text{keV})$ is higher by a factor of 3 (see Fig. 5.2).

Assuming Lusso et al., 2012 bolometric corrections and a $M_{\text{BH}} = M_*/500$ conversion as in Häring and Rix, 2004, we computed Eddington ratios for each target, defined as the bolometric X-ray luminosity (or its 3σ upper limit) divided by the maximum X-ray luminosity at which a galaxy of a given stellar mass can sustain spherical accretion onto the central BH before radiation pressure starts to dominate (the so-called Eddington luminosity). We obtain Eddington ratios of $\lambda_{\text{EDD}} \sim 2 - 11\%$ for detected sources and 3σ upper limits lower than 1% for all the undetected ones. When repeating the test using $24\mu\text{m}$ -derived $L(2\text{-}10\text{keV})$, we obtain λ_{EDD} which are a factor of 2 higher on average.

Such λ_{EDD} translate into Black Hole Accretion Rates (BHAR)³ which are largely in agreement with C20 at $z \sim 3$. Dividing the mean $\langle \text{BHAR} \rangle$ by the average $\langle \text{SFR}_{[\text{OII}]} \rangle$ estimated in D'Eugenio et al., 2020 I obtain an increase

²Our stellar masses were converted to a Chabrier IMF for consistency.

³ $\text{BHAR}(M_*, z) = (1-\epsilon) \cdot L_{2-10\text{keV}} \cdot \text{kbol}(M_*, z) / (\epsilon c^2) = \lambda_{\text{EDD}} \cdot L_{\text{EDD}} \cdot 10^{-45.8} M_{\odot} \text{ yr}^{-1}$, where the efficiency of mass conversion is $\epsilon = 0.1$

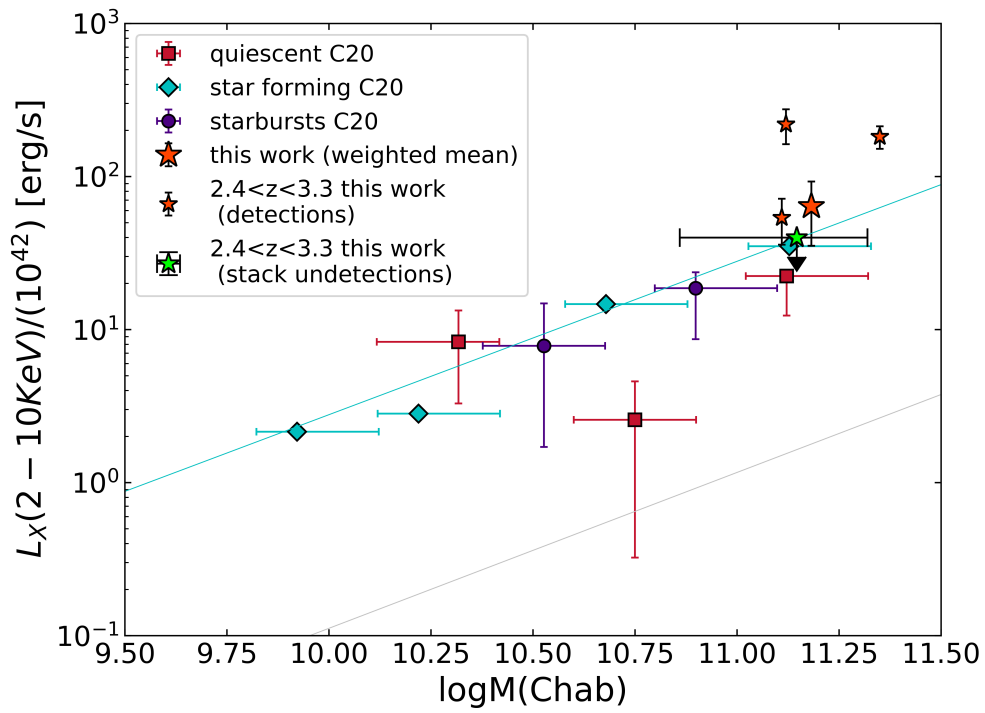


FIGURE 5.2: X-ray luminosity in the 2-10 keV band as a function of stellar mass for quiescent (red squares), star forming (cyan diamonds) and starburst galaxies (violet circles) at $2.25 < z < 3.50$. Adapted from Carraro et al. 2020.

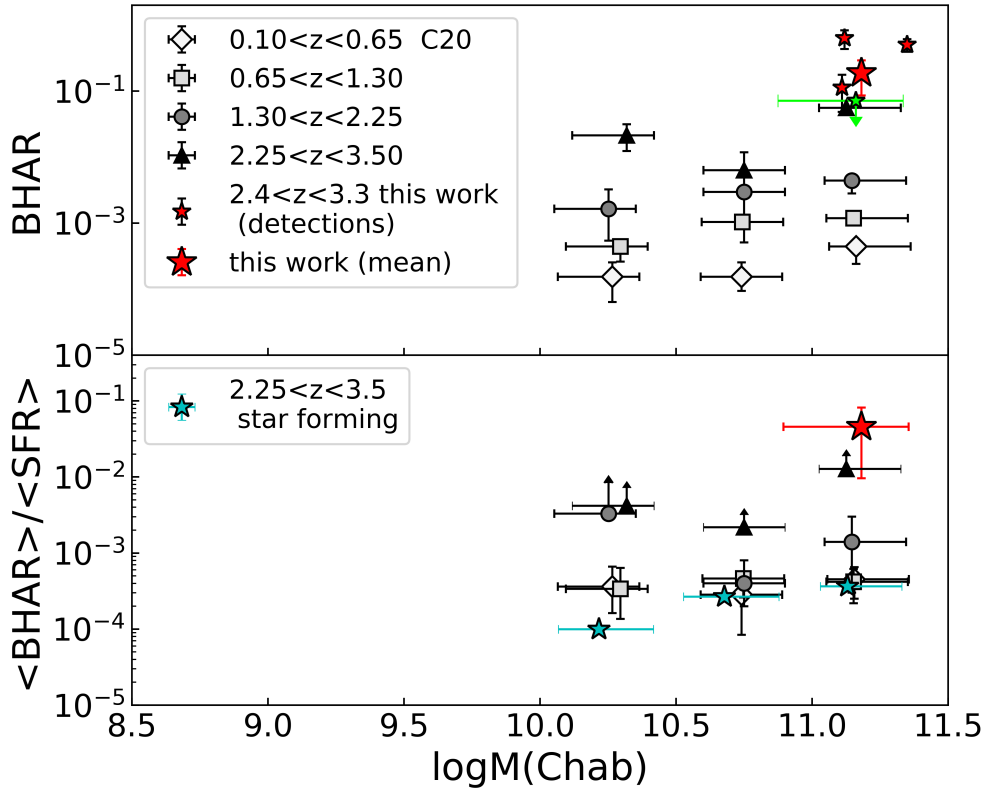


FIGURE 5.3: BHAR (top) and BHAR per unit star formation rate (bottom) as a function of stellar mass for quiescent galaxies in COSMOS. Different symbols mark different redshift bins. Cyan stars mark main sequence galaxies in the same range studied in this work. Errorbars on the average BHAR reflect the dispersion of the weighted mean on the rest frame L(2-10keV) of the sample. The average $\text{SFR}_{[\text{OII}]}$ was converted to a Chabrier IMF. Adapted from Carraro et al., 2020.

by a factor of ~ 30 with respect to $1.3 < z < 2.25$ QGs at the same mass, consistent with the lower limit for massive $2.3 < z < 3.5$ QGs inferred from the same paper. L_X increases by a factor of 2 with respect to star-forming galaxies at the same mass and redshift range, whereas the [OII]-derived dereddened SFR lies around ~ 60 times below the high- z MS. This translates into $\langle \text{BHAR} \rangle / \langle \text{SFR} \rangle$ being a factor of ~ 100 higher than the high-mass end of the MS at $z \sim 3$. This supports the idea that, while the stellar mass growth of the host galaxy has already come to an end, the BH mass growth in high- z QGs takes longer to fade away, as already pointed out in C20.

The stochastic nature of detectable AGN activity implies that it is usually only observed in a small fraction of galaxies at a given time. Aird, Coil,

and Georgakakis, 2019 report that high- z massive QGs exhibit enhanced AGN fractions compared to low- z SF galaxies hosting an equivalent SFR, suggesting that AGN activity in QGs might be fuelled and sustained by stellar-mass loss rather than the availability of cold gas. Their fraction of highly-accreting QGs ($\lambda_{\text{sBHAR}} > 0.1$, i.e. at more than 10% the Eddington limit) reaches 2-3% around $z \sim 3$. The fraction of normally accreting AGN ($\lambda_{\text{sBHAR}} > 0.01$) reaches 20-30% in the quiescent population with SFRs of order of $0.5-1 M_{\odot} \text{yr}^{-1}$. Schreiber et al., 2018b find 18% of X-ray detections among $3.2 < z < 3.7$ massive UVJ-quiescent galaxies, plus an additional 30% in the young-quiescent (lower-left) region of the UVJ diagram. Several of their young-quiescent SEDs show similarities with our id478302 and id447058 in terms of SED shape and possibly young age. Olsen et al., 2013 report a $19\% \pm 9\%$ luminous AGN fraction in a mass-complete sample of massive UVJ selected quiescent galaxies at $1.5 < z < 2.5$, with a total low-luminosity AGN fraction up to 70%-100%, advocating in favor of episodic AGN activity to maintain low SFRs in quiescent galaxies. Our sample likely contains a 30% fraction of luminous AGN, with a possibly compton thick source (40% assuming id503898 as an high- z quiescent source). I caution that we currently do not know in which direction the magnitude cut in the selection will affect the AGN fraction.

As also noted in Aird, Coil, and Georgakakis, 2019, stellar mass-loss and AGN feedback tend to be disfavored mechanisms to cause relatively high-accretion rates and high AGN fractions in sub-MS and quiescent galaxies: the former could sustain the accretion onto the central BH by providing a relatively stable supply of low-angular momentum gas but is expected to result in relatively low accretion rates. Moreover, stellar mass loss is most efficient soon after star formation (2-5 Myr) and declines exponentially afterwards, making its contribution likely not sufficient to explain the highest λ_{EDD} measured for some of our objects (unless non-negligible SF is occurring). The latter assumes that the gas supply, once used by the galaxy to sustain SF, is now instead accreted by the central SMBH. However, even the shortest ages shown by our stellar populations would imply a stability of the radiatively efficient AGN feedback of order of hundreds of Myr, whereas radiatively efficient accretion is expected to be stable on time-scales of 0.1 Myr. One other mechanism proposed by the same authors could be the build-up of a compact bulge, which would increase the stellar density of the host galaxy, hence increasing the rate at which the AGN is triggered by infalling gas, as also supported by observations (Barro et al., 2013). Indeed, Fig.5.4 shows that our likely-AGN hosts are among the most compact ones in the sample but also show the lowest sersic indices ($n=1.6-2.6$) and tentatively the lowest mass-weighted ages. This might be possibly suggesting a connection between recent star-formation (or transition towards quiescence) and the presence of AGN feedback. No clear trend with morphology seems to be detectable when using the D_B/D_{n4000} ratio.

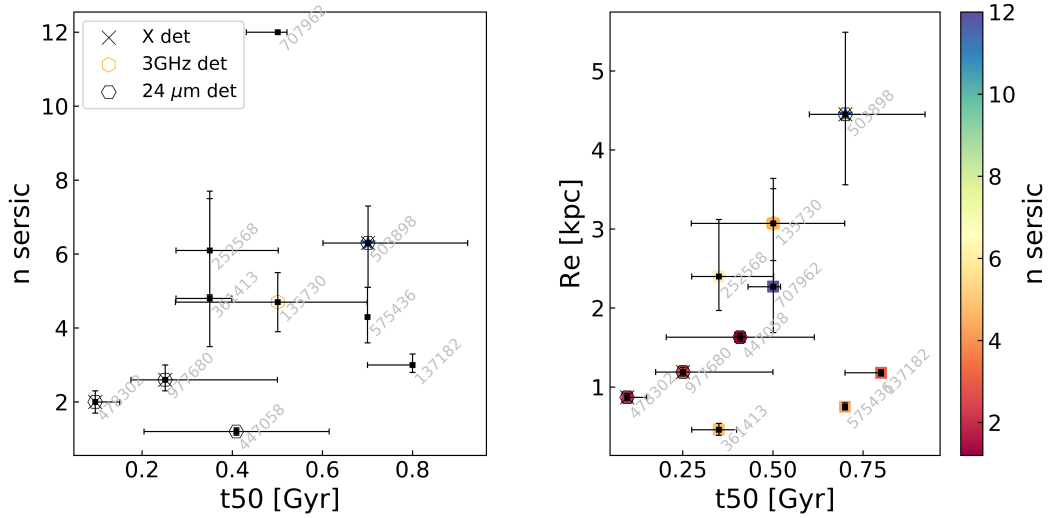


FIGURE 5.4: Comparison between our mass-weighted ages and the morphological parameters derived in Lustig et al., 2021, namely seric index n and effective radius R_e at 5000 \AA rest-frame.

5.3 Comparison with compact star forming galaxies

In light of the fast-track quenching routes proposed in the literature (Belli, Newman, and Ellis, 2019a; Merlin et al., 2018), it is interesting to compare our galaxies to known compact star forming galaxies (CSF) at similar stellar masses and redshifts. These, in fact, are known to share similar structural properties and colors, affecting the selection and identification of high- z quiescent systems. For example, Barro et al., 2014 analyze a sample of 45 relatively massive ($\log(M_*/M_\odot) > 10$, Chabrier IMF) compact star-forming galaxies at $2 < z < 3$ in the GOODS-South field. They were selected by imposing high stellar mass surface densities ($\log(M_*/r^{1.5}) > 10.45 M_\odot \text{ kpc}^{-1.5}$) and relatively high sSFRs ($\text{sSFR} > 1.8 \cdot 10^{-10} \text{ yr}^{-1}$, a factor of 4 higher than the estimated average value in D'Eugenio et al., 2020). SFRs were derived from total LIR (IR+UV) for MIR- and/or FIR-detected objects, whereas they relied on UV-based SFRs from observed-frame optical/NIR SED fitting otherwise. In particular it is worth noting that 31%, 56% and 87% of their sources are undetected in MIPS, PACS and SPIRE respectively. Most notably, 30% of their sample enter the UVJ quiescent region preferentially where H-band bright PSBs galaxies are located. Also their SED fitting results in sSFRs consistent with being lower than the typical MS values, with SFRs generally below $50 M_\odot \text{ yr}^{-1}$. Incidentally, they also exploited HST/G141 grism spectra for 36/45 objects to characterise their rest-frame 4000 \AA stellar populations. Strong absorption lines (Balmer and Gband) plus [OII] and [OIII] emission lines appear to be spread among the whole sample, albeit clear spectral breaks

are available for less than half. After degrading the spectral resolution and combining their spectra with the available broad band photometry, their best-fitting simple SFHs are consistent with short e-folding timescales τ , with the distribution of t/τ peaking at ~ 2.6 , whereas quiescent galaxies often result in $t/\tau \geq 6$ (Fontana et al. 2009) as it is indeed the case for the majority our HST targets⁴. Their passive-UVJ CSFs result in ages ranging from 0.3 to 1.1 Gyr (i.e. post-starburst populations) consistent with formation redshifts up to 3.5-4.2. Remarkably, the passive-UVJ CSF in their sample show the most compact structures, consistent in terms of sersic indices (relatively broad distribution centered on $n \sim 3$) and axis ratios (centered around $q \sim 0.75$) with our median values ($n \approx 4.5$, $q \approx 0.73$, Lustig et al., 2021). However they have slightly lower stellar masses (mostly between $10.5 < \log(M_*/M_\odot) < 10.8$ as opposed to our $\log(M_*/M_\odot) \approx 11.2$, converting to a Chabrier IMF), rest-frame optical sizes ($R_{e,CSF} \sim 0.5$ kpc vs $R_{e,QG} \sim 1.4$ kpc) and redshifts (median at $z=2.5$ vs. $z=2.8$).

We interpret these similarities in terms of an evolutionary link between our already compact, bulge-dominated newly quiescent galaxies and plausibly $z \sim 4$ CSFs where rapid structural transformation has already come to an end. In other words, given the remarkable number of similarities between Barro et al., 2014 passive-UVJ, FIR-undetected CSFs and our PSBs, we tend to interpret them as the very same class of newly quenched objects, at slightly different stages of their quenching. A plot of the size evolution with redshift of both quiescent and star forming populations can be found in Lustig et al. 2021. As can be seen in their Figure 8, at $2.5 < z < 3.5$ star forming galaxies are typically a factor of 2-2.5 larger than the quiescent population, at $\log(M_*/M_\odot) \sim 11$. Compact star forming galaxies are however typically selected to overlap with quiescent galaxies on the mass-size plane (Barro et al., 2014, Figure 1, bottom right panel). As discussed in Lustig et al. 2021, a link between a high Sérsic index and star formation rate suppression in massive compact galaxies was reported by Barro et al. 2017 who suggest an inside-out formation phase for MS disks, followed by strong core growth and Sérsic index increase (the so-called "compaction"), likely as a result of a gas-rich major merger or disk instabilities. This continues up to a threshold after which star formation is shut down. One could also wonder whether or not Barro et al. red nuggets would be detected as star-forming at all in COSMOS, given similar UVJ colors, rest-frame 4000 Å spectra, FIR non-detections and a MIPS/24μm depth a factor of 2 shallower than the one in the GOODS-S field. Spectroscopic confirmation and the identification of strong Balmer Breaks are then crucial to assess which of these has supposedly completed its transition towards the quiescence.

I would like to stress, nonetheless, that no direct link between such classes of objects has been firmly established and that more data, especially at the highest masses are required. For example, the lack of FIR detections in UVJ-quiescent CSFs in Barro et al., 2014 might be related to their stellar masses

⁴Note that t here refers to the time from the onset of star formation.

being lower than $\log(M_*/ M_\odot) \sim 11$, hence with a lower SFR.

Our galaxies have been quenched no earlier than ~ 300 -800 Myr prior to observation and already show bulge dominated morphologies as shown by their H-band steep surface brightness profiles and small effective radii (see Fig.5.4 with values taken from Lustig et al., 2021). Rapid structural transformation seems to be linked to fast-quenching and produce massive PSB galaxies at $z > 1$ (Whitaker et al., 2012a; Dekel and Burkert, 2014; Barro et al., 2016b; Maltby et al., 2018b; Bezanson et al., 2019): a central (sub)kpc starbursting region traceable by ALMA through dust continuum (Barro et al., 2016a) and high-J CO transitions (Puglisi et al., 2019) establishes the dense compact core of the final remnant, rapidly depleting the available gas reservoirs of the host through stellar mass growth (Toft et al., 2014b) and BH growth (Bournaud et al., 2011). Examples of such events appear to be present already within the MS (Elbaz et al., 2018; Puglisi et al., 2019) and could likely be the analogs of the seeds of passivization at high- z .

Chapter 6

Conclusions and future perspectives

In the previous chapters I presented the results obtained during the last three years of work, which were mostly devoted to understand the nature of a sample of distant red galaxies in the early universe. The identification and detailed characterization of massive quiescent galaxies at the earliest epochs of cosmic history has fuelled decades of research in galaxy evolution and is now more active than ever. The exact phenomena that contributed to rapidly shut down star formation in compact galaxies when the star formation rate density of the universe was growing and galaxies were richer in gas than at present are still hotly debated. The discovery of quiescent galaxies ~ 2 - 2.5 Gyr after the Big Bang has ignited the systematic search of red candidates which now extends remarkably to 1 Gyr earlier. The greatest barrier to their spectroscopic confirmation, however, remains the long integration times with near-IR spectrographs, which makes the build up of relevant spectroscopic samples hard to obtain.

In this work, I showed how HST observations efficiently provide full continuous spectral coverage along the Balmer/4000 Å region for $\log(M_*/M_\odot) > 10.8$ quiescent galaxies at $2.4 < z < 3.2$ bridging the relatively well studied epochs to the current frontiers at $z \sim 3.5 - 4$.

In particular, robust spectroscopic confirmation was achieved for the full sample, confirming the quality of the photometric redshift originally used for the sample selection, as well as the accuracy of z_{phot} from more recent catalogs (chapter 2). Thanks to the size of the sample, one of the largest available to date, it was possible to investigate the photometric re-calibrations of zero points proposed in Laigle et al., 2016. Such re-calibrations were derived mostly on samples of star forming galaxies at $z < 1$, adding sets of spectroscopically confirmed quiescent at $z < 2.5$ and extending to $z \sim 4$ with samples of star forming galaxies. The rest-frame NUV/optical spectra, combined with their corresponding UV-to-NIR photometry, suggest that when it comes to quiescent galaxies at $z \sim 3$ their use appears to be no longer motivated.

Also, I showed that our galaxies are preferentially fitted by an attenuation curve steeper than Calzetti, possibly suggesting different dust properties with respect to lower- z analogs or galaxies with higher sSFR (chapter 3).

I tested the quiescence of our targets starting with their rest-frame UV-to-NIR

emission using both the newly acquired grism spectroscopy and UV-to-NIR broad-band photometry. I extended to mid-IR, far-IR and radio wavelengths by exploiting recently released super-deblended photometry in order to gain realistic constraints on their possible level of obscured SFR, which are rare at these redshifts. If the UV-to-NIR emission classify our galaxies as quiescent, mid-IR detections make their interpretation less straightforward. The majority of such mid-IR sources have counterparts in the X-rays with flux densities consistent with being AGN powered. The mean-stack radio peak flux of our undetected sources at 3GHz places their global SFR strictly on a sub-MS level ($<50 M_{\odot}\text{yr}^{-1}$). However, I caution that the IR-based or radio-based upper-limits on the *individual* obscured SFRs are shallow at these epochs ($<120\text{-}190 M_{\odot}\text{yr}^{-1}$) making deep mm data necessary to conclusively discern between AGN activity and residual star formation on a galaxy-by-galaxy basis.

I then created the stacked spectrum of our sample which, to date, is one of the highest quality of its class, showing strong Balmer absorption lines typical of post-starburst systems. The associated average mass-weighted age and dust attenuation ($t_{50} = 0.30^{+0.20}_{-0.05}$ Gyr and $A_V = 0.6^{+0.6}_{-0.4}$ mag) imply a recent shut down of star formation. Such recent quenching was confirmed individually, object-by-object, by including the available photometry and marginalizing over different attenuation curves and SFHs. The analysis suggests that our galaxies were forming the bulk of their stars at high rates ($1800\text{-}3000 M_{\odot}\text{yr}^{-1}$) until 300-800 Myr prior to observation (chapter 4).

I measured, for the first time at these redshifts, the average strength of $H\delta_A$ and compared it to the D_n4000 index, showing that our galaxies formally classify as "post-starburst", just exiting from their major star formation epoch. All-in-all, both the spectrum fitting and the spectral indices agree in marking a significant reduction in age compared to $z \sim 1.5$ massive analogs. These findings let us spectroscopically confirm the PSB properties already suggested by the UVJ color selection, implying that the bulk of classically selected, massive, quiescent galaxies at these epochs is likely in the same evolutionary stage and that the magnitude cut necessary for spectral acquisition at high- z biases observations towards objects which had undergone a fast suppression of their SFR. These results were corroborated by subsequent publications which reached similar conclusions, independently from our work (Forrest et al., 2020b; Saracco et al., 2020; Marsan et al., 2020). Given the low resolution of our grism spectra, I quantified the global strength of their Balmer absorption lines for the first time at these redshifts and compared it to the one of the 4000 Å break by means of the D_B/D_n4000 ratio which is systematically higher than 1. This criterion gave consistent results when applied either on the stacked spectrum or on single galaxies. This criterion was also the technique at the basis of a JWST NIRSpec/PRISM (IFU mode) proposal, aimed at starting a systematic investigation of the nature of faint, red photometrically-quiescent galaxies at $z \sim 3$. Such galaxies, in fact, could either be the passively evolving descendants of massive quiescent galaxies

observed at $z \sim 4$ or, rather interestingly, dusty post-starbursts, if not dusty star-forming interlopers.

Furthermore, I presented one of the first attempts at constraining the gas fraction of high- z quiescent galaxies (chapter 5). The weak [OII] emission line present in the stacked spectrum is consistent with a residual dust-corrected SFR of $7 \pm 3 M_{\odot} \text{yr}^{-1}$ which, adopting the latest estimates of the SFE of $z \sim 1.8$ massive QGs, translates into a $\sim 9 \pm 4\%$ average gas fraction. This nominally disfavors the continuation at high- z of the increase in gas fraction (or alternatively sSFR) with redshift reported by previous works from $z=0$ to $z=1.8$. However, given the degenerate origin of the [OII] emission, mm data are required to independently test this finding. In the same chapter, I showed that the mid-IR and X-ray individual detections and the radio-stack shallow detection are consistent with a 30% incidence of luminous AGN and a widespread radio-mode feedback a factor of 4 stronger than in similarly massive QGs at intermediate redshifts, respectively. The BH mass growth appears to be substantially enhanced with respect both to $z \sim 2$ quiescent analogs ($\times 30$) and to coeval star forming galaxies at a fixed stellar mass ($\times 100$). This is in agreement with the recent results of Carraro et al., 2020 on the stacked emission of photometrically selected populations of QGs at $2.25 < z < 3.50$. This result was allowed by the sample size which, I recall, is one of the largest available.

Lastly, I discussed the similarities between our $\sim 10^{11} M_{\odot}$ quiescent systems at $z \sim 2.8$ and compact star forming galaxies at $z \sim 2$ in terms of colors, sizes, structure and possibly SFRs. If spectroscopic confirmation is necessary to detect clear spectral breaks or absorption lines, the many similarities with the most compact star forming galaxies at high- z make the question of identifying "contaminants" less clear-cut in the sense that they are likely part of the very same population of newly quenched systems at slightly different stages of their evolution, as already suggested by the finding of a pair at $z \sim 3.7$ consisting of a QG and an obscured compact star forming galaxy (Schreiber et al., 2018a). However, the direct evolutionary connection between these two classes is still to be established.

In the following section I would like to report on one of the most relevant questions that stemmed out of the conclusions summarized above. Specifically, it was at the core of an HST cycle 28 proposal which was not awarded time but which was ranked in the first quintile.

6.1 Did any galaxy evolve quiescently from $z>5$ to 3?

In chapters 3 and 4, I showed that massive and bright QGs at high- z host young stellar populations and are consistent with formation redshifts around $z \sim 3.5$. Our targets were selected for being bright ($H < 22$) and with blue UVJ

colors compared to the population of quiescent galaxies at lower redshifts. Despite this, their colors and M/L ratios are consistent with being representative of $\sim 60\text{-}70\%$ of the overall massive population at these epochs. This seems to be in conflict with the increasing number of works pushing back in time the first evidences of quenching. Recently, in fact, several works reported on the spectroscopic confirmation of quiescent galaxies at $z\sim 3\text{-}4$ and even higher, constraining the quenching epoch to be as early as $z\sim 4.5\text{-}5$ (Schreiber et al., 2018b; Valentino et al., 2020; Forrest et al., 2020a; Forrest et al., 2020b). Additionally, newly released photometric catalogs (Merlin et al., 2019; Girelli, Bolzonella, and Cimatti, 2019; Carnall et al., 2020) provide further ground for potential quiescent candidates at $z>4$. Hence, it appears that two contradictory lines of evidence are starting to emerge: one which keeps discovering quiescent objects at increasing redshifts and one which constrains their numbers to be necessarily low. As shown in Fig.1.5, the current estimates of number densities of $z>4$ massive QGs are consistent with being a minor fraction of QGs at $z\sim 3$ but, at the same time, the region where their descendants should lie in the UVJ diagram at $z\sim 2.8$ is notoriously affected by contamination (e.g. from very dusty objects or by low- z interlopers). As mentioned in chapter 4, the latest spectroscopic confirmations tend to be all selected in the same blue region of the UVJ diagram, including ours. This region is where transitioning or recently quiescent objects are found before they evolve along a much longer track which brings them in the reddest portion of the diagram as their stellar populations age passively. So, given the large fraction of objects consistent with PSB M/L and colors inferred here and the increasing scatter of the star forming population, should we expect to find the descendants of $z=4$ quiescent galaxies in significant numbers at $z\sim 2.8$? Do they keep evolving passively or do they experience major star formation rate fluctuations, implying a less trivial average SFH and a less straightforward path across the UVJ diagram? If yes, can we say something about their evolution from the comparison of stellar properties and dust attenuation? If $z\gtrsim 5$ quenched objects kept evolving passively, they should be lying in the region of the UVJ diagram with $(U-V)+(V-J)\gtrsim 3$ by the time they reach $2.5<z<3$ and HST NIR spectroscopy can effectively differentiate old objects ($\Delta t\sim 1.3$ Gyr from $z=5.5$ to $z=2.8$) from dusty post-starbursts or star-forming contaminants. If no such object is found (or found in lower numbers compared to the expected number density from the latest observations), it implies that their apparent "post-starburstiness" at high- z might be due to fluctuations in SFR ($\dot{\Sigma}$) and that the first episodes of passivization did not lead to a definitive shut down of star-formation.

Constraining the diversity of the quiescent population at high- z (by comparing the total fraction of old vs. post-starburst systems) may have potential strong implications for the understanding of the global SFH of massive objects in an alternative, less-model dependent way with respect to spectrum-fitting SFH reconstruction techniques. We have identified 3 galaxies in COSMOS from Muzzin et al., 2013a, selected on the basis of their rest-frame

UVJ colors, at $\log(M_*/M_\odot) > 10.9$ and $2.7 < z_{\text{phot}} < 3.3$. We conservatively selected galaxies lying in the region preferentially populated by old galaxies (corresponding to $(U-V)+(V-J) \gtrsim 3$, e.g. Belli, Newman, and Ellis, 2019b) and away from the edge of the passive region ($\Delta(U-V) = +0.2$, see Fig. 6.1), which notoriously harbors star-forming contaminants or low redshift interlopers (e.g. Forrest et al., 2020b). We removed galaxies with combined FIR+mm detections (100–1200 μm) in the Super-Deblended Jin et al. 2018 catalog ($S/N_{\text{IR}} < 5$) to avoid star-forming interlopers. None of our sources is detected in Xrays (2–10 keV). Although we were confident about the passive nature of the proposed sources, whether they would eventually result in contaminants would strengthen the idea that PSBs make up nearly all the QG population and that the descendants of QGs confirmed at $z \sim 4$ might be lying elsewhere, perhaps as bulges in larger star forming galaxies. We proposed to use HST/WFC3 F160W+G141 to spectroscopically confirm the reddest passive galaxy candidates ever targeted (see Fig. 6.1), exploiting the wide 1.1–1.7 μm spectral coverage to use the ratio between the Balmer Break index (D_B) and 4000A Break index (D_n4000) as a resolution-unaffected and dust-unbiased spectral diagnostic between post-starburst and old spectra (age > 1 Gyr, see Fig. 4.6).

In the following sections I would like to briefly report few more ideas that seemed to us a natural consequence of this thesis work. Some of them are admittedly at an early stage and possibly naive but we believe they are ideas worth exploring in the next future.

6.2 Probing residual gas reservoirs with ALMA archival images

As mentioned previously in the thesis, the most robust estimate of the star formation efficiency and gas content of intermediate redshift quiescent galaxies ($f_{\text{gas}} \sim 5\text{--}10\%$) is based on a stacked FIR SED of 977 $1.1 \times 10^{11} M_\odot$ QGs at $z \sim 1.8$ by Gobat et al., 2018 using 24 μm , 100–500 μm and 0.85–1.1 mm among other wavelengths. However, results on the dust or cold gas content of much smaller samples of quiescent galaxies at similar redshifts are somehow contradictory, possibly reflecting different selection criteria or conversion factors (Sargent et al., 2015; Spilker et al., 2018; Bezanson et al., 2019; Zavala et al., 2019). The data used by Gobat et al. to sample the peak and Rayleigh-Jeans tail of the dust emission suffer from a large PSF which introduces confusion (Herschel/PACS and SPIRE, JCMT/SCUBA2, ASTE/AzTEC). Despite satellites and clustering from star forming galaxies were taken into account in their work, their exact treatment can still be a source of systematics. Specifically, the original sample counted 2154 objects, half of which was excluded to reduce clustering effects from close pairs. Higher resolution imaging such as ALMA will clarify whether their result is to be confirmed. These objects

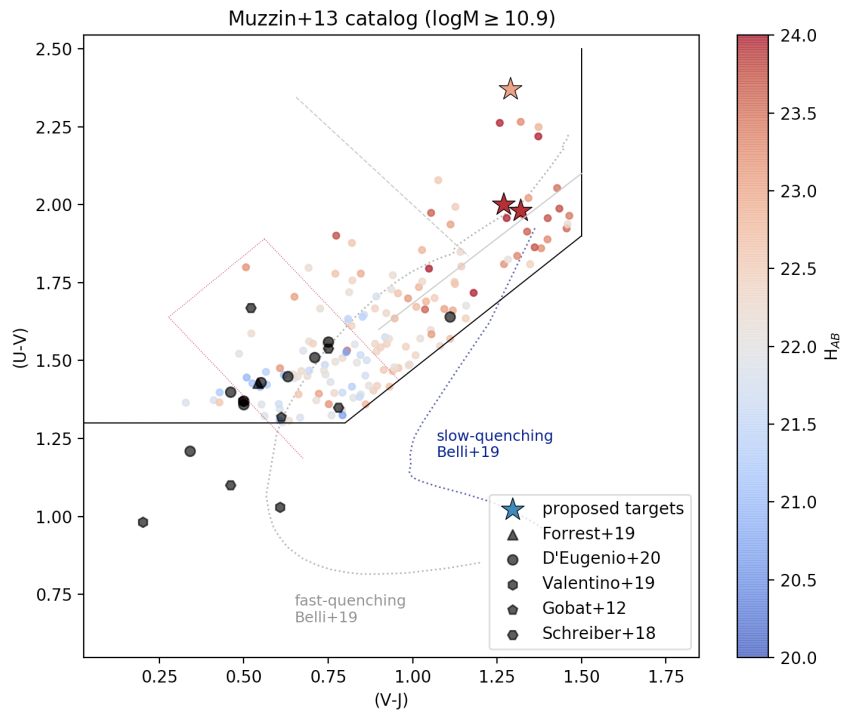


FIGURE 6.1: Distribution of the proposed targets at $\log(M_*/M_\odot) \geq 10.9$ across the passive region of the UVJ diagram (stars). Color coding follows H-band total AB magnitudes. Black markers show the position of all the spectroscopically confirmed quiescent galaxies published in the literature at $z > 2.4$. The area close to the diagonal border is notoriously affected by contamination from star-forming interlopers, our attempt at avoiding this region is represented by the grey solid diagonal line. The dashed diagonal line corresponds to $(U-V) + (V-J) = 3$ to conservatively exclude post-starbursts since they tend to have bluer colors. Fast and slow quenching tracks from Belli et al. 2019 are superimposed.

remain individually undetected in ALMA archival (sub)mm images. We plan to stack such pointings since, assuming the SED found by Gobat et al., we expect a $S/N=5.3$ detection of dust continuum given by the increase in the number of objects available (in collaboration with D. Liu).

6.3 Using quiescent galaxies as signposts for groups and proto-clusters

Massive quenched galaxies can be used as tracers of dense environments (Gobat et al. 2013, Strazzullo et al. 2015, Castignani et al. 2019). Their detection (via spectroscopic confirmation) and the investigation of their clustering over wide areas (e.g. with WFIRST) can potentially boost group identification at $2.5 < z < 3.2$ adding statistical power to the exploration of the role of environment and dark matter halo assembly in causing quenching (Dekel & Birnboim 2006). In particular, it would be interesting to understand if early QGs reside indeed in overdensities and whether there is a link between them and the reversal of the star-formation rate-density relation taking place at high- z . The HST exposures analyzed in this thesis revealed the presence of several additional spectral breaks, potentially hosted by quiescent galaxies or, more intriguingly, by star forming or transitioning objects. Their spectroscopic confirmation and detailed analysis have not been concluded yet. Incidentally, preliminary results using wPPM¹ in collaboration with G. Castignani suggest that some of these galaxies with additional breaks in the same HST exposure might reside in overdense regions independently of the photometric catalog used for the test. The radio stack could be also pointing in the same direction indicating widespread radio-mode feedback. The investigation of their dust properties and spatial clustering will probe whether quiescent galaxies at $z \sim 3$ actually reside in overdensities together with star-forming objects. Even more intriguingly, the famous case of the pair at $z \sim 3.7$ of a QGs and a compact dusty sub-MS star-forming galaxy of Schreiber et al., 2018a might not be an isolated case considering the increasing number of H-band dropouts found to be in overdensities around $z \sim 3-3.5$ (Franco et al., 2018; Zhou et al., 2020). Dedicated ALMA mm observations of QGs would be crucial not only in view of a possible dust continuum detection itself but also, in case of a significant detection, to check any spatial offset between the optical and the ALMA component.

¹Castignani et al., 2014; Castignani et al., 2019

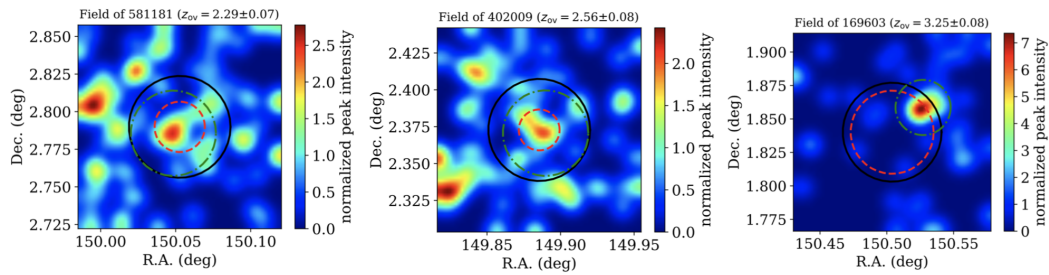


FIGURE 6.2: Gaussian density maps for some of our objects that are consistent with being in an overdensity at their respective redshifts (consistent results were obtained adopting either Laigle et al. 2016 catalog or Ilbert et al. 2009 catalog). The green circle it is centered on the overdensity peak and marks its radius.

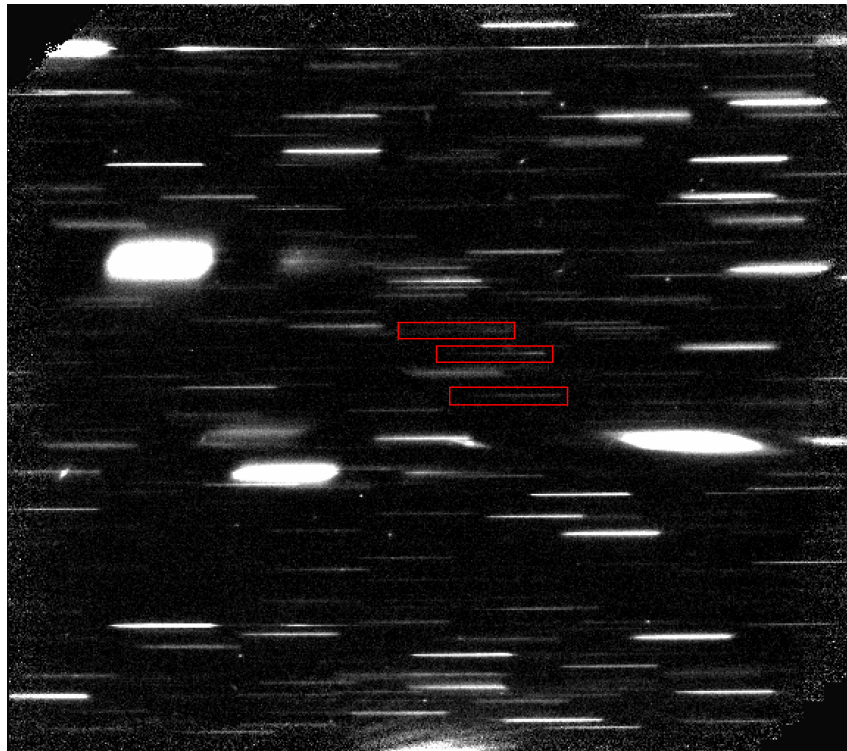


FIGURE 6.3: Example of the distribution in additional breaks found for 3-4 of our galaxies. Field of view of id252568.

6.4 Using JWST to study early stellar and chemical evolution

With the advent of JWST, the improved spectral resolution, high sensitivity and wide wavelength coverage of NIRSpec G140 and G235 will allow a number of studies to be performed on high- z QGs: the improved imaging sensitivity could allow to detect low-surface brightness emission which might be missed by current HST data, potentially flagging recent interactions. The wavelength coverage of NIRSpec spectrographs will probe the presence of emission lines such as $H\alpha$, [NII], [OIII] which could, in principle, be used in BPT diagrams to distinguish between residual star formation and LINER activity. The improved S/N of their spectra will allow the use of full-spectrum fitting to decompose their spectra into simple stellar populations, providing additional constraints to test the robustness of parametric and non-parametric techniques at inferring the mass-weighted ages of high- z quiescent galaxies. Furthermore, accessing to MgUV, D4000, Fe and Mg lines will lead to a better understanding of the chemical enrichment history of such objects, also in terms of α -element enhancement, which has to shed light on metal-poor quiescent galaxies reported so far in the literature (Kriek et al., 2016; Toft et al., 2017; Morishita et al., 2018). Also, similarly to what was done in Gobat et al., 2017, any age or metallicity gradient in their stellar populations observed in the 2D grism spectra could help constraining the mechanisms by which such compact objects formed.

List of Abbreviations

ACS	A dvanced C amera for S urveys
AGN	A ctive G alactic N ucleus
ALMA	A tacama L arge M illimeter/ S ubmillimeter A rray
ASTE	A tacama S ubmillimeter T elescope E xperiment
CANDELS	C osmic A ssembly N ear- I nfrared D eep E xtragalactic L egacy S urvey
CFHT	C anada F rance H awaii T elescope
CGM	C ircumgalactic M edium
CLEAR	C ANDELS L yman- α E mission at R eionization survey
COSMOS	C OSMOlogical E volution S urvey
ETG	E arly T ype G alaxy
EW	E quivalent W idth
FOV	F ield O f at V iew
FWHM	F ull W idth at H alf M aximum
HST	H ubble S pace T elescope
ID	I Dentification number
IMF	I nitial M ass F unction
IR	I nfrared
IRAC	I nfrared A rray C amera
ISM	I nterstellar M edium
JWST	J ames W ebb S pace T elescope
LTG	L ate T ype G alaxy
M/L	M ass to L ight ratio
MAMBO	M Ax- P lanck M illimeter B Olometer
MIPS	M ulti- B and I maging P hotometer for S pitzer
MS	M ain S equences
NEWFIRM	N OAO E xremely W ide- F ield I nfrared I Mager
NMBS	N EWFIRM M edium- B and S urvey
NOAO	N ational O ptical A stronomy O bservatory
NOEMA	N ORthern E xtended M illimeter A rray
PAH	P olycyclic A romatic H ydrocarbons
PACS	P hotoconductor A rray C amera and S pectrometer
PSB	P ost- S tarburst
PSF	P oint S pread F unction
QG	Q uiet G alaxy
S/N	S ignal to N oise
SB	S tarburst
SCUBA2	S ubmillimetre C ommon- U ser B olometer A rray 2
SDSS	S loan D igital S ky S urvey

SED	Spectral Energy Distribution
SF	Star Formation/Forming
SFE	Star Formation Efficiency
SFH	Star Formation History
SFR	Star Formation Rate
sSFR	Specific Star Formation Rate
SMC	Small Magellanic Cloud
SN	Supernova
SPIRE	Spectral and Photometric Imaging REceiver
UltraVISTA	Ultra-deep Survey with the VISTA telescope
UV	Ultraviolet
VIMOS	Visible Multi Object Spectrograph
VLA	Very Large Array
VLT	Very Large Telescope
WFC3	Wide Field Camera-3

Appendix A

IR and radio cutouts

I insert here the cutouts of our sources from the IR to the radio domain and their SED fits where super-deblending is available. Upper panel: multiband cutouts of our targets. The green text marks the instrument, the observed wavelength in units of μm and the size of the field of view. Lower panel: fits to the SEDs of our galaxies. The SEDs are fitted with a starburst-like dust continuum component (green curve; Magdis et al. 2012), a stellar component (blue curve; Bruzual & Charlot 2003) and an AGN torus component (red curve, Mullaney et al. 2011). The fits were fixed to the grism redshifts derived above. Points with $S/N > 2$ were considered detections in the fit. Upper limits are 2σ upper limits ($\text{flux} + 2 \times \text{dflux}$). Courtesy of S. Jin.

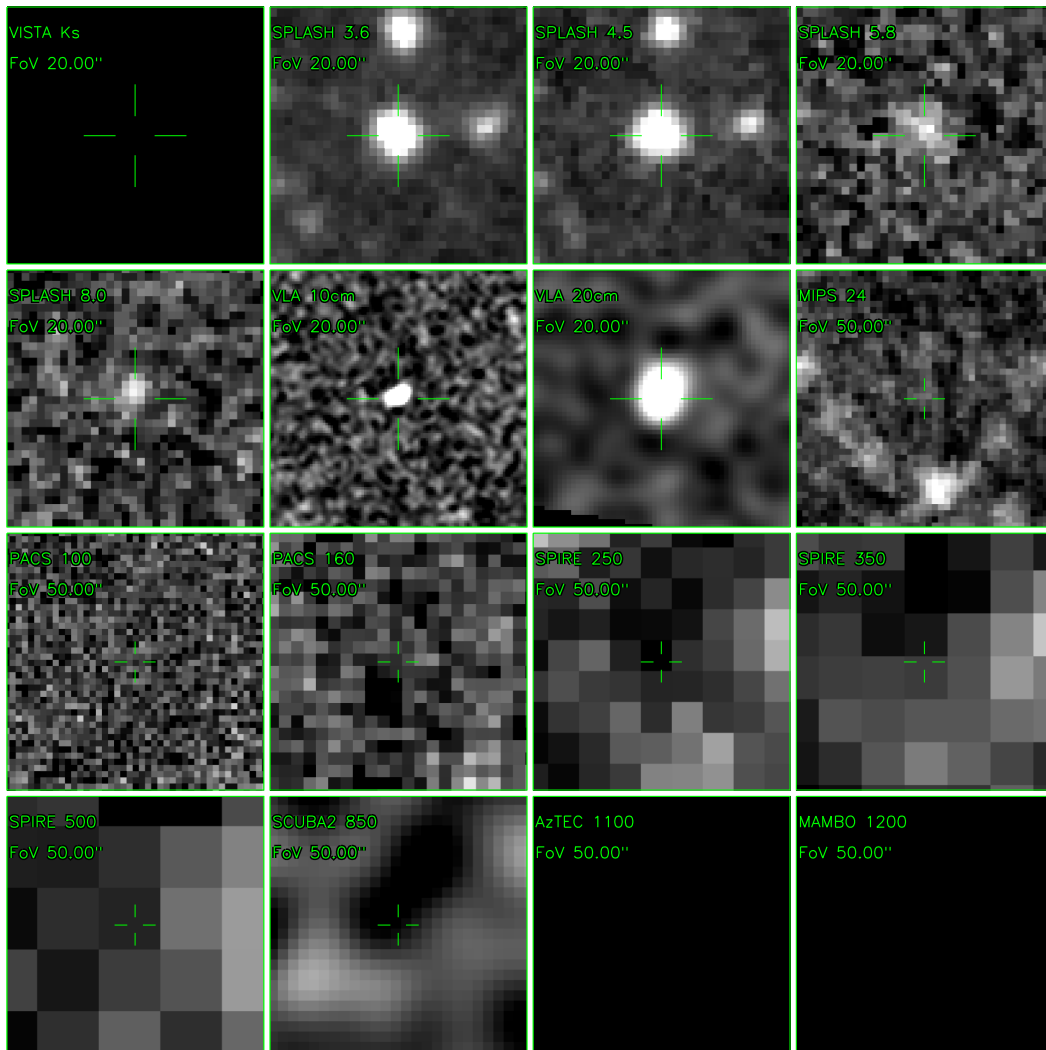
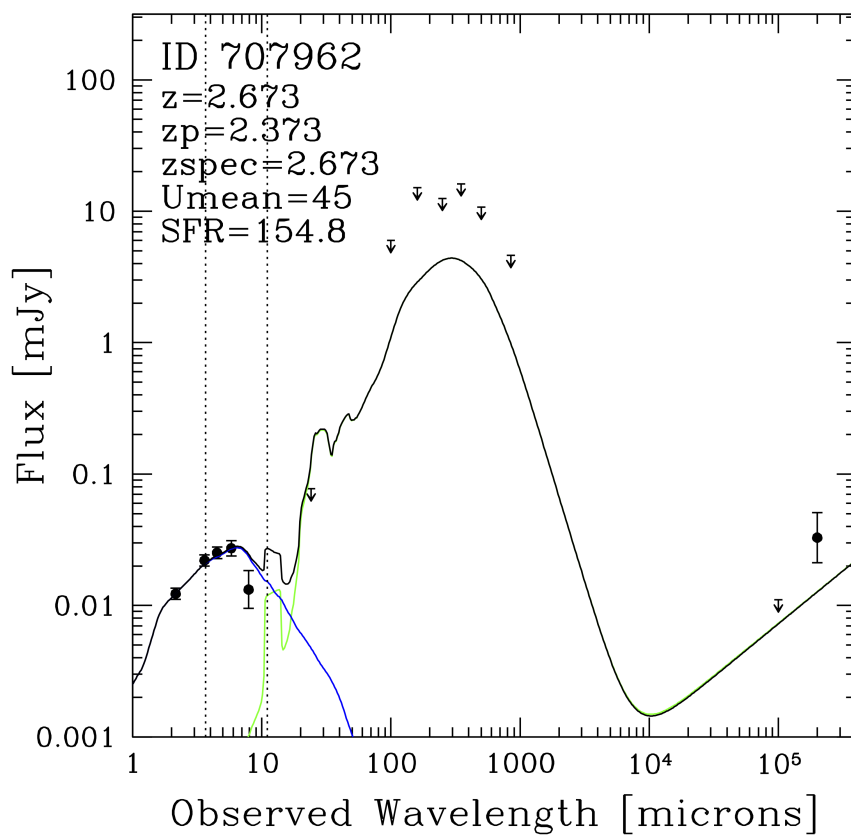
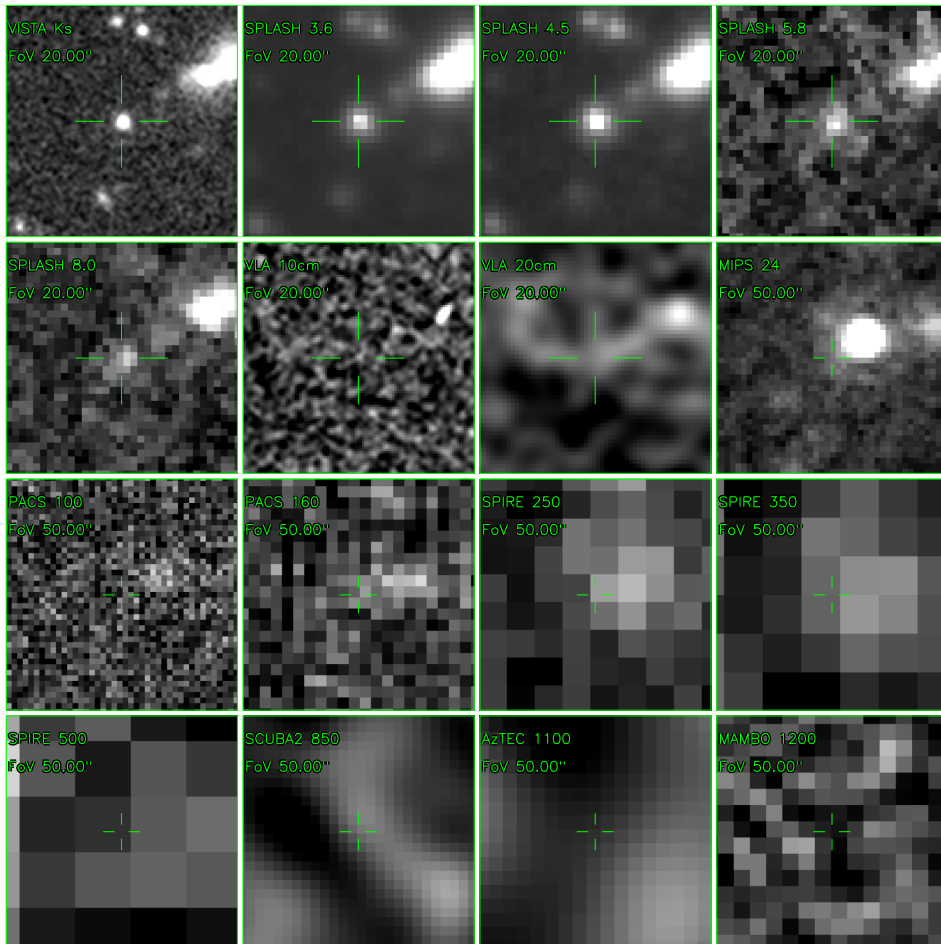
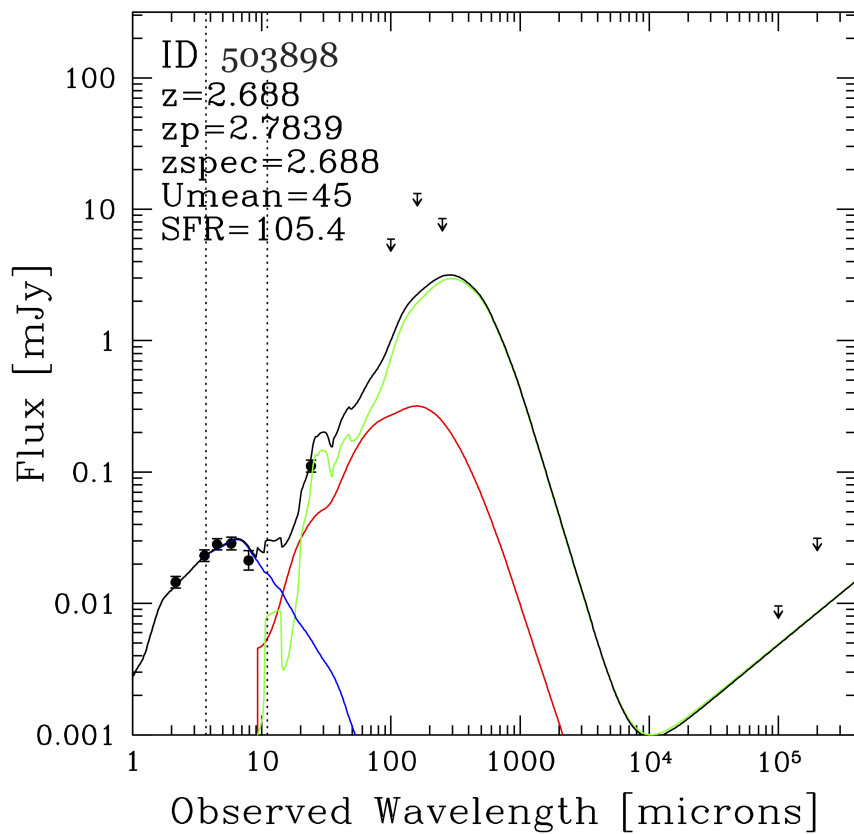
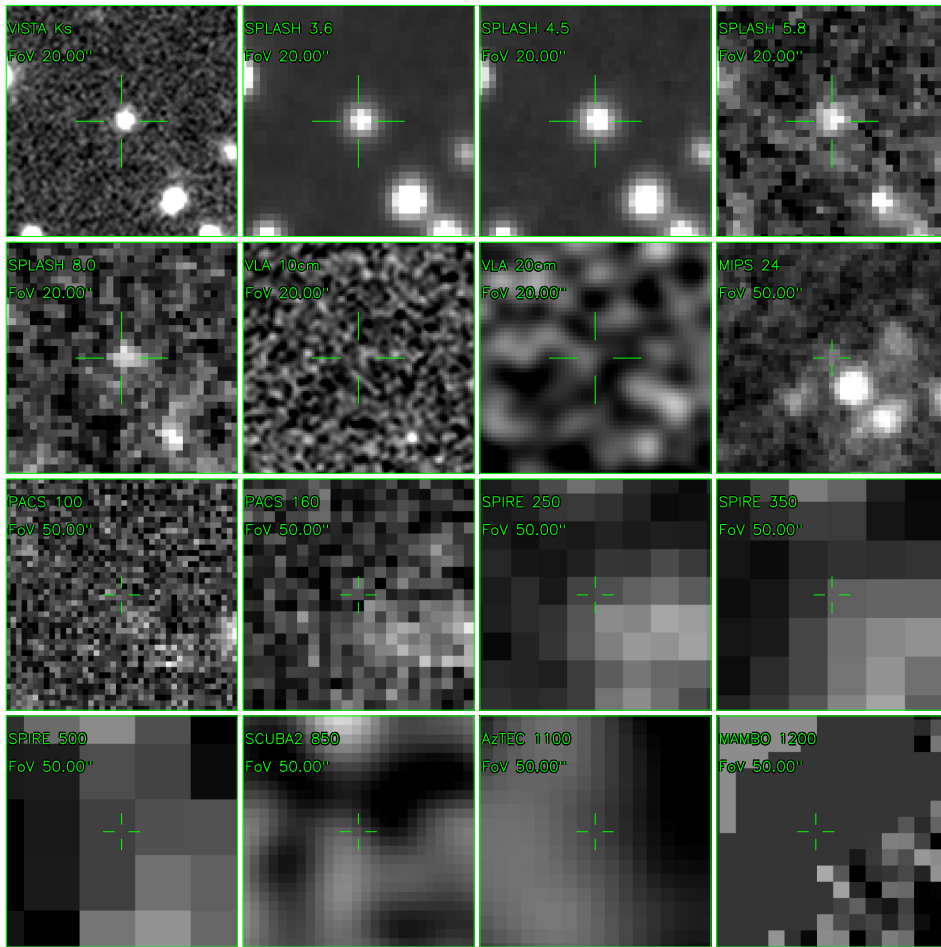


FIGURE A.1: ID135730





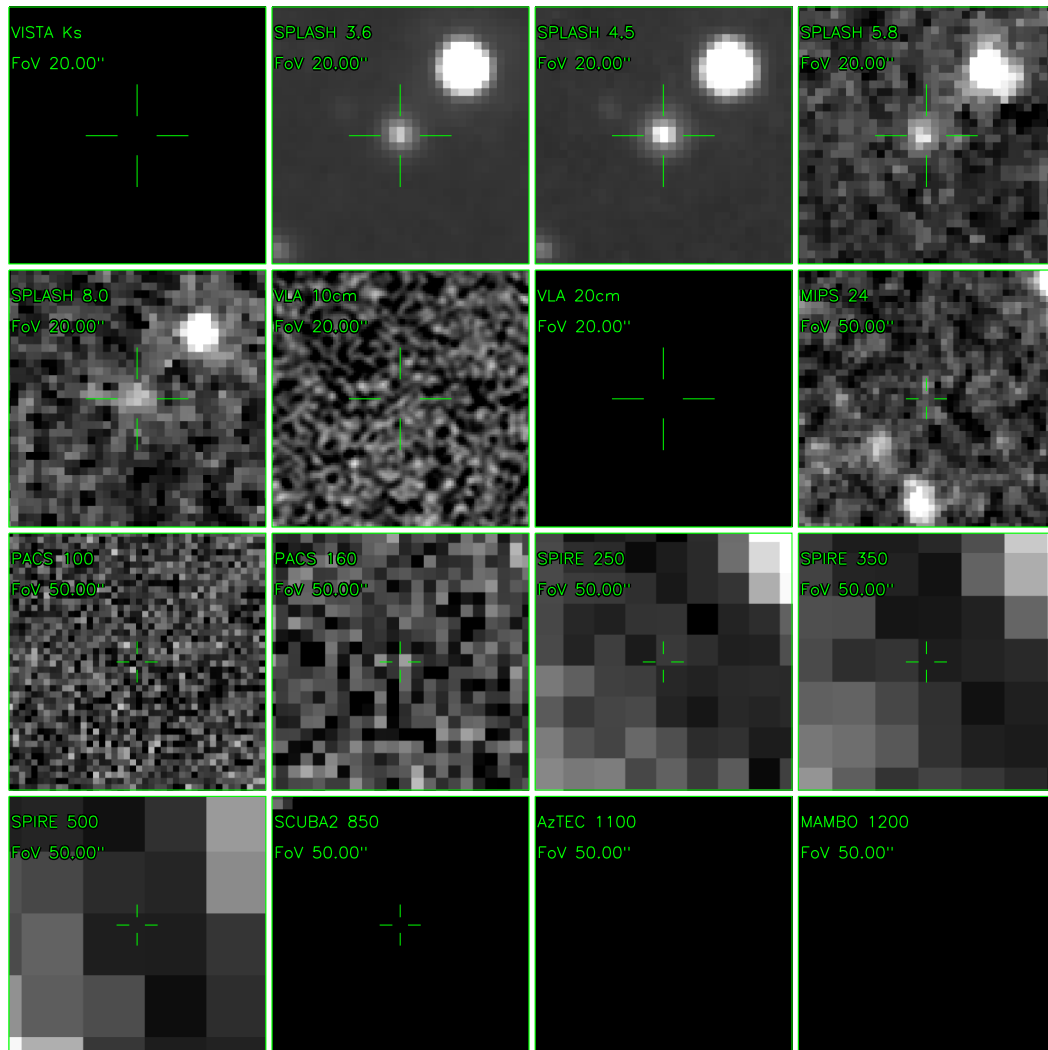
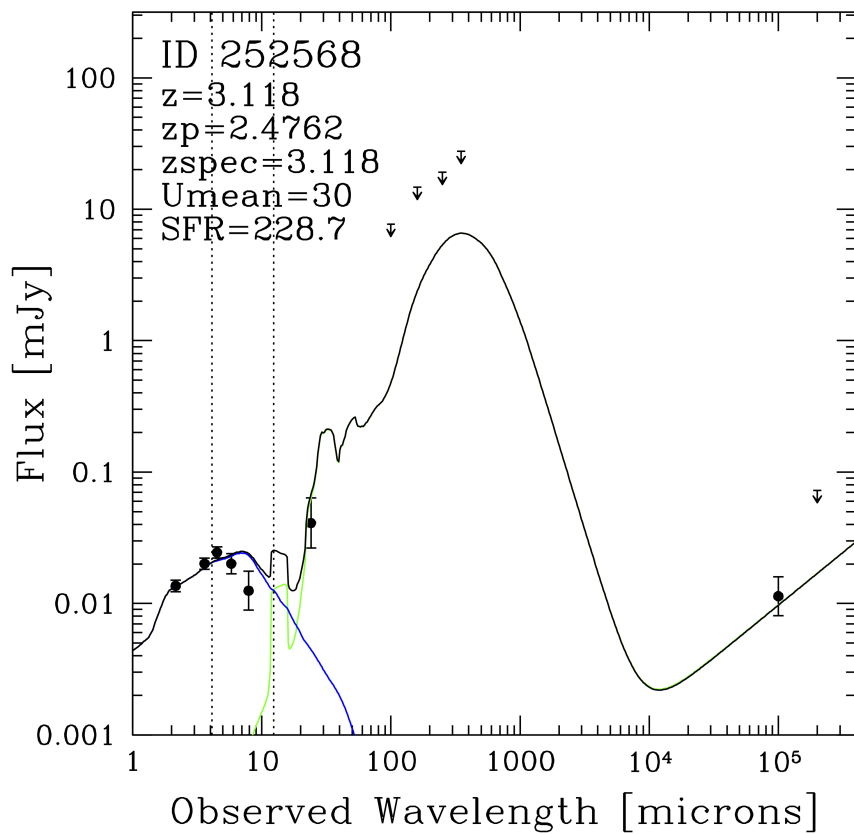
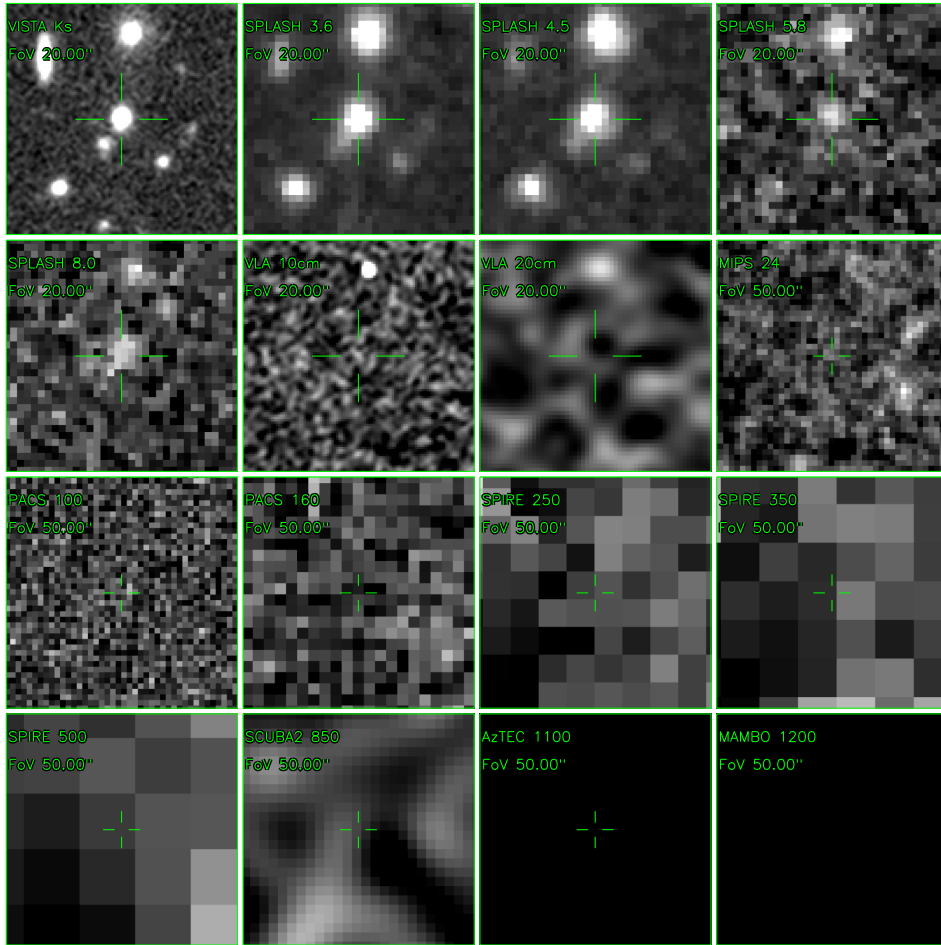
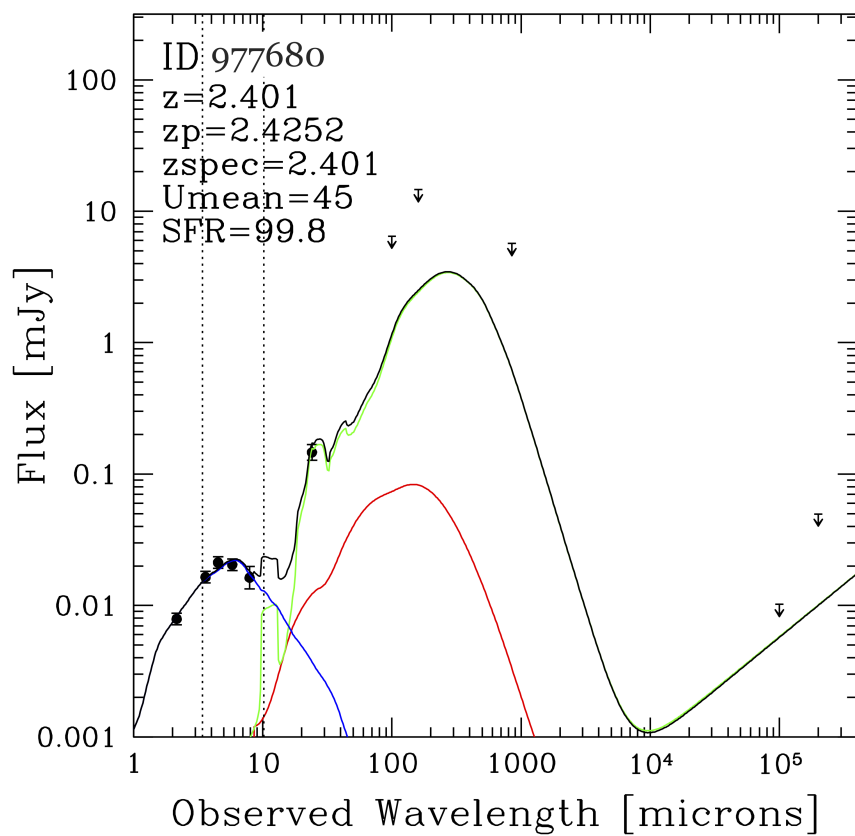
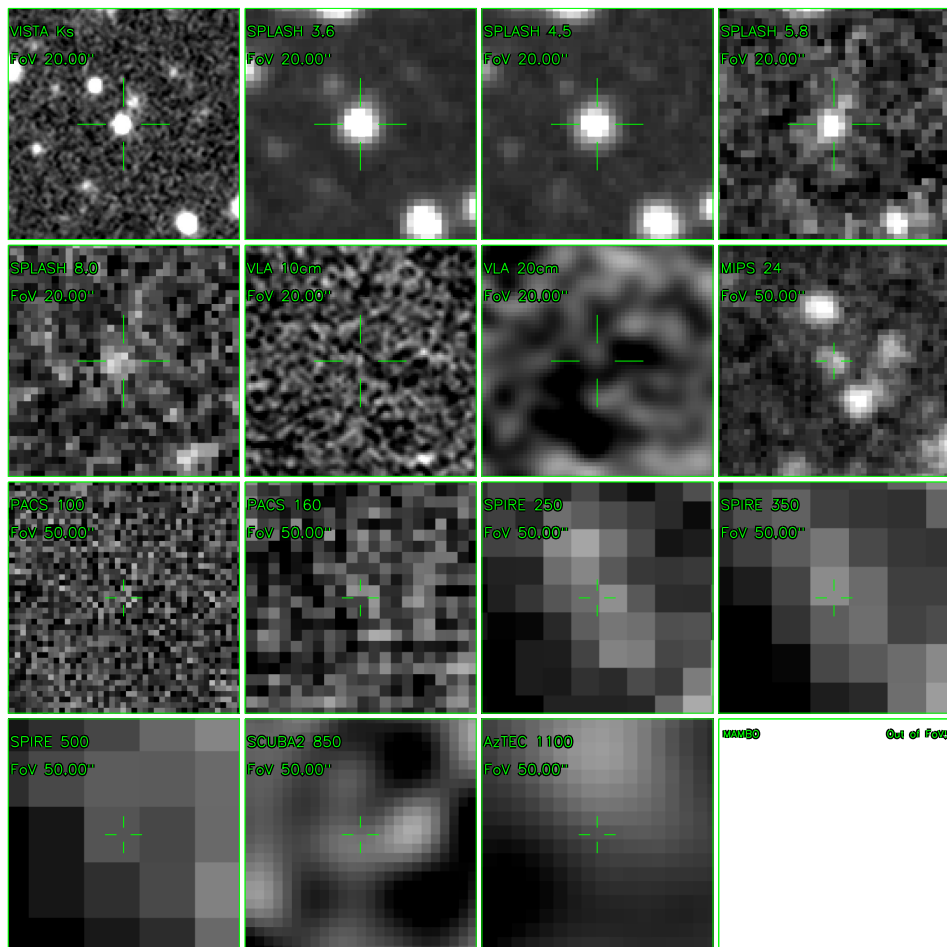
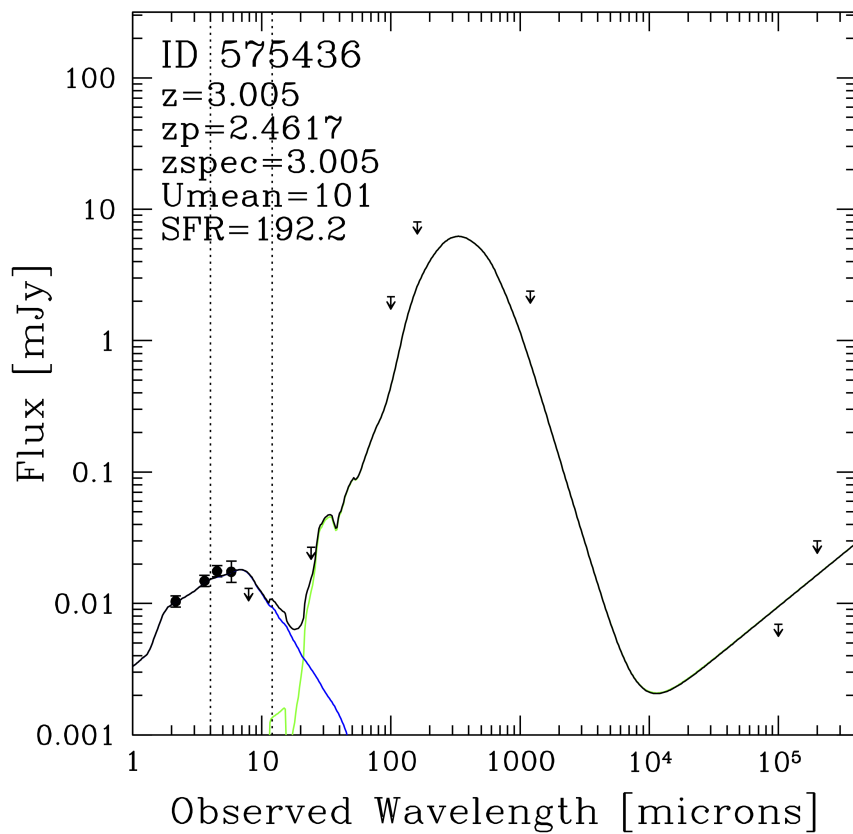
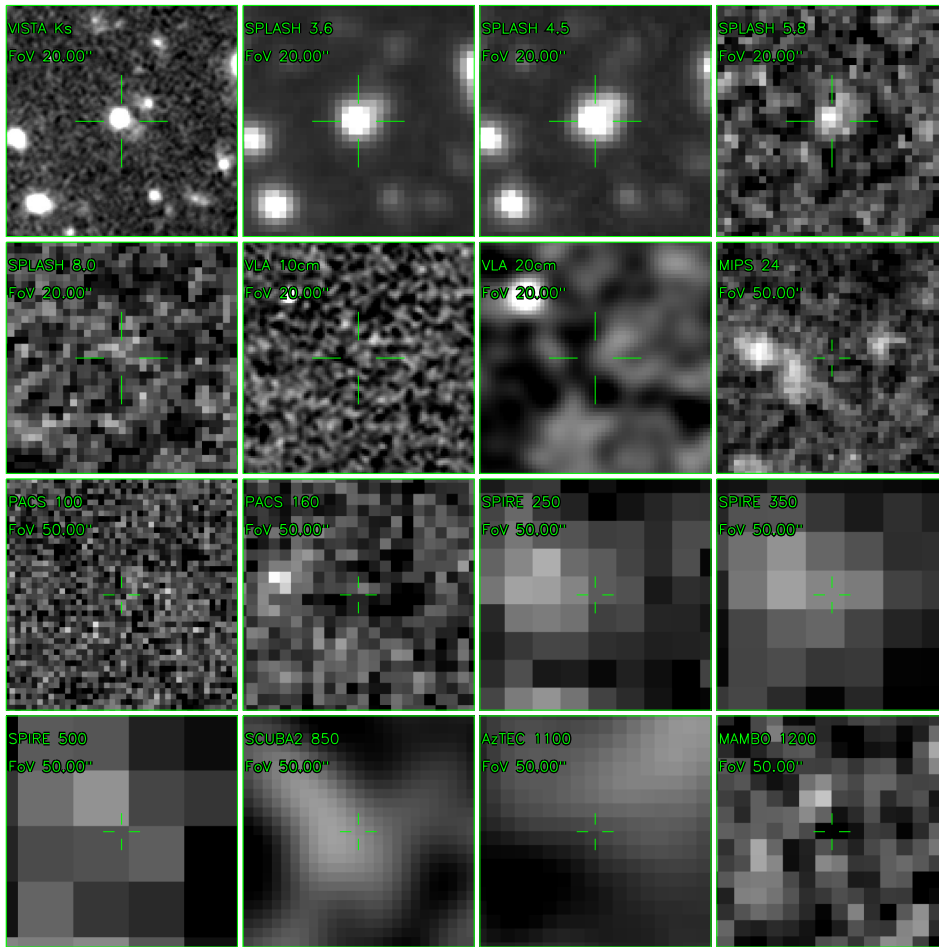
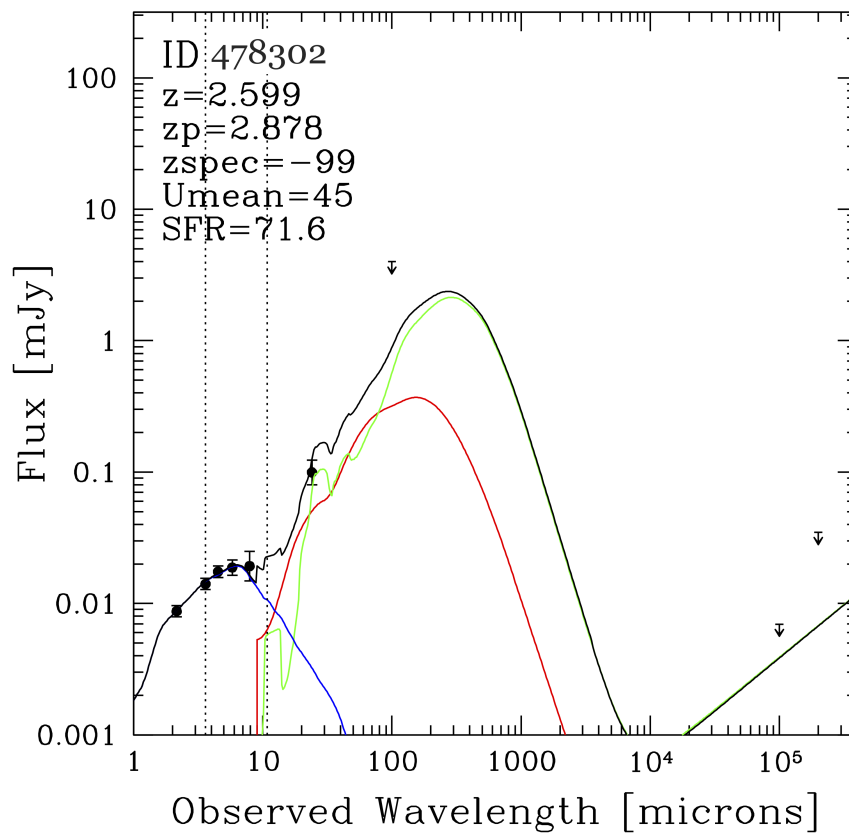
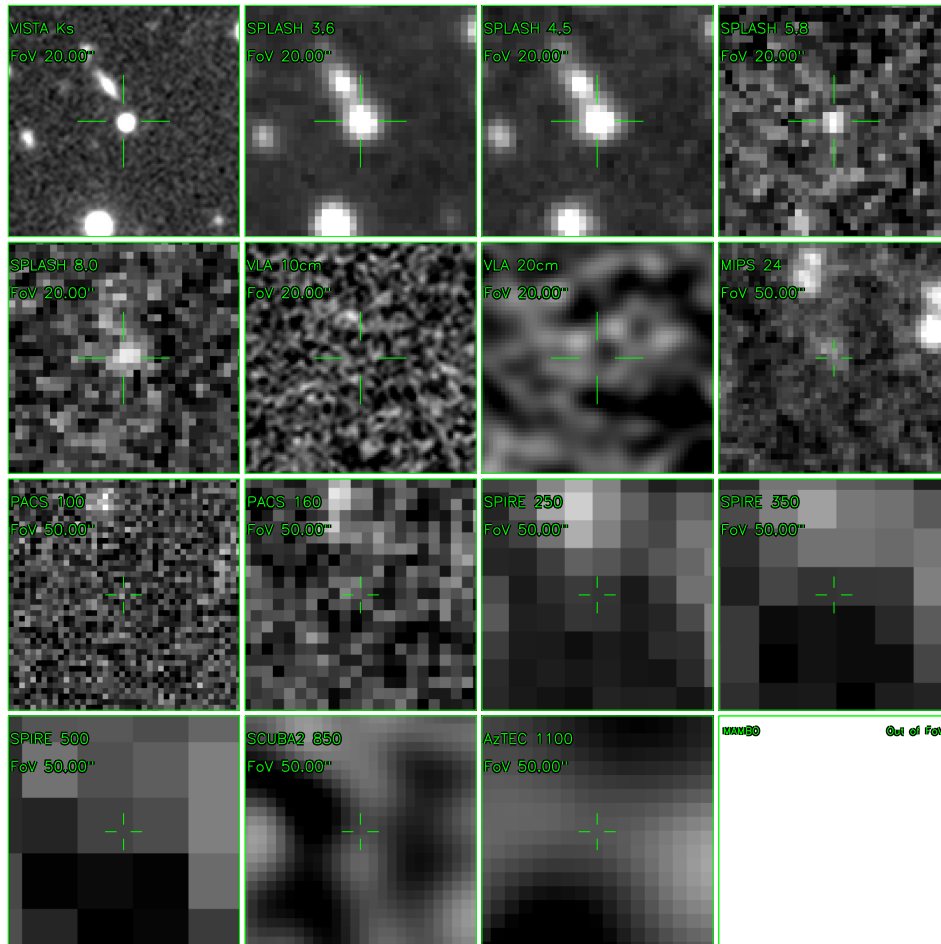


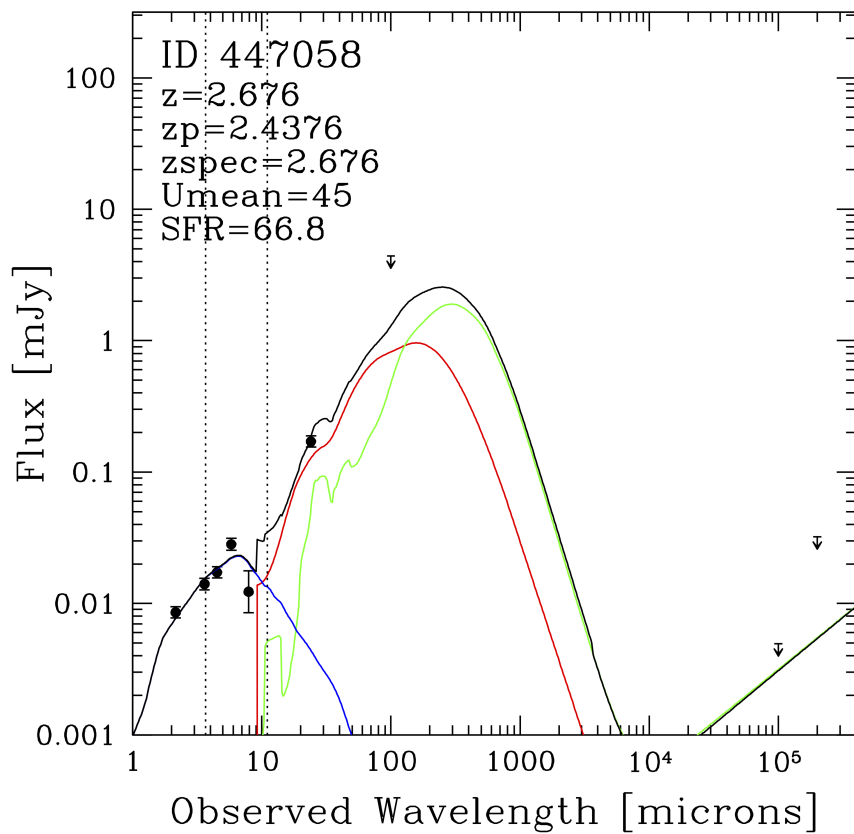
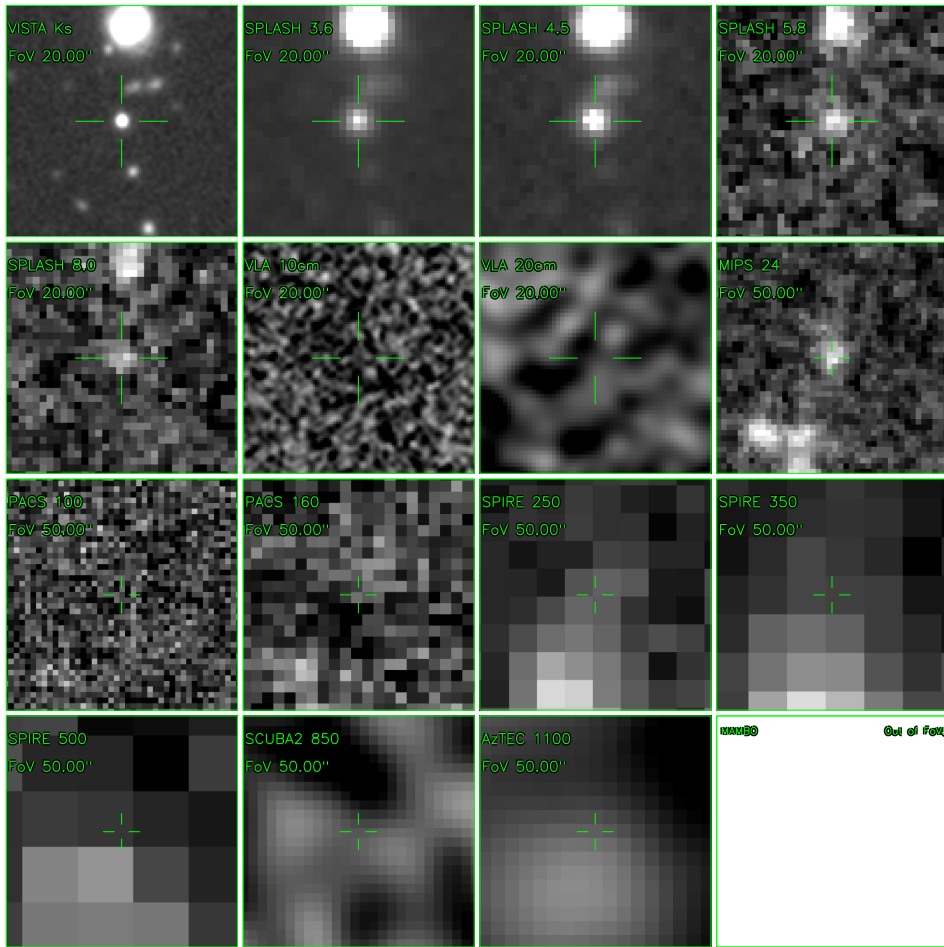
FIGURE A.1: ID137182

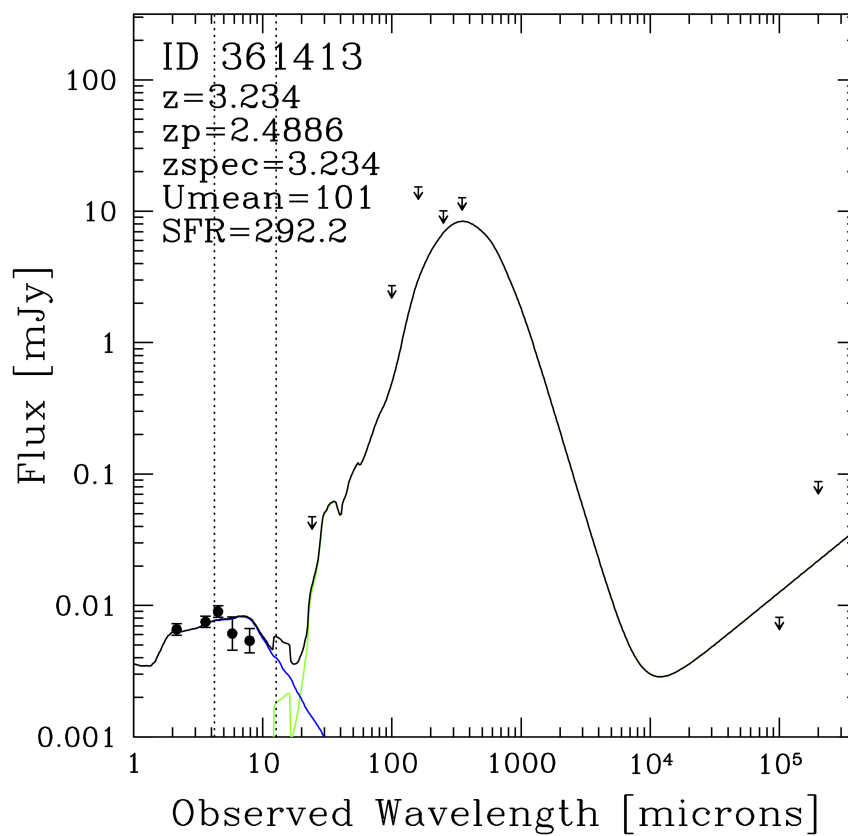
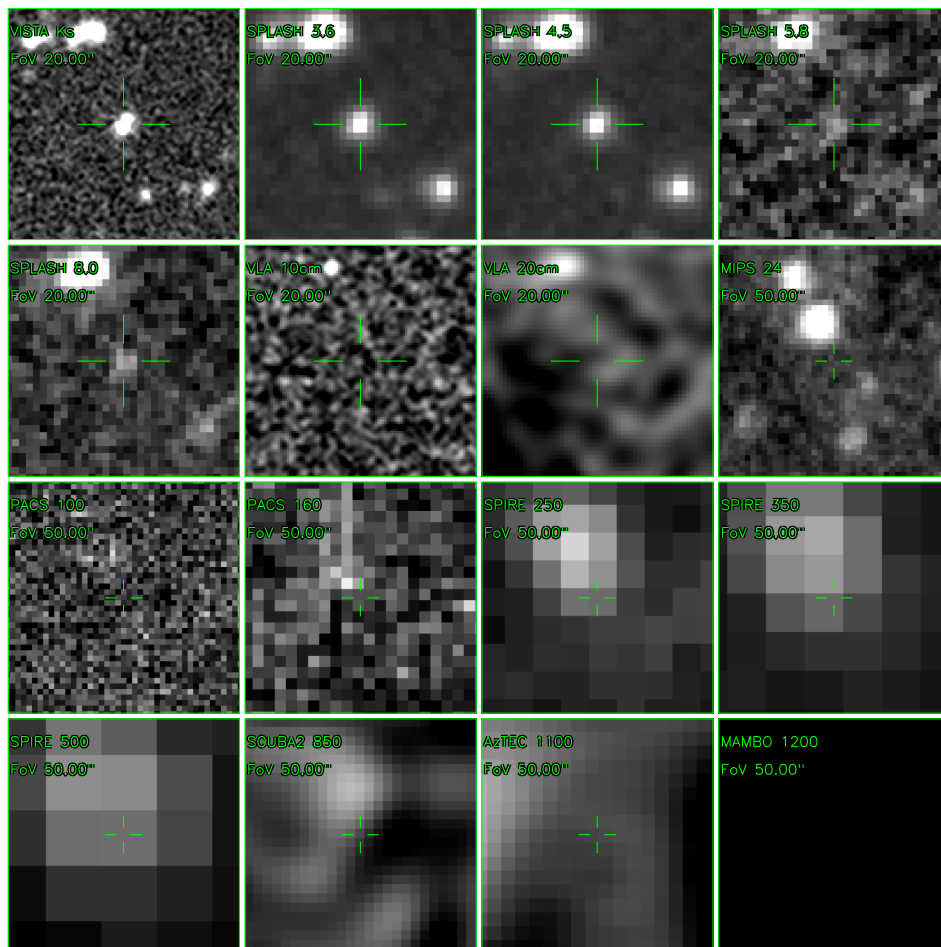












Appendix B

Contribution to other papers as co-author

During my PhD I contributed as a co-author to five papers and a letter, four published and two under revision. These works concern a range of topics, from intermediate redshift green valley galaxies and starbursts to high-redshift Ly α nebulae. For each of them I mostly participated to the interpretation and redaction of the manuscript. In some cases I contributed to the data analysis. The level of impact of my contribution varied depending on the subject and on type of the analysis. I summarize below the main conclusions of each paper starting from those where I directly worked on the data and then listing the papers where I mainly contributed to the redaction and discussion.

Lustig et al. 2021 performed a complementary analysis on the same sample introduced in this manuscript. They performed the morphological and structural analysis of the H-band imaging with GALFIT to extract the effective radii, sersic indices and axis ratios from the surface brightness profile of our targets. They conclude that our sample of massive ($\log(M_*/M_\odot) \approx 11.2$, Chabrier IMF) quiescent galaxies is largely composed by already bulge-dominated (median $n \approx 4.5$) compact ($R_e \approx 1.4$ kpc) systems in agreement with previous mass-size relations extrapolated at the highest masses and redshifts. Also, they provide an independent support on the fraction of post-starburst systems at $z \sim 3$ by replicating the sample selection on the Muzzin et al., 2013a catalog and measuring the fraction of candidates with UVJ colors consistent with the post-starburst area identified by Belli, Newman, and Ellis, 2019b. I contributed to this work through discussions and providing the spectroscopic redshifts together with an improved reduced imaging data set carried out using a more recent version of *grizli* which fixed the issue of persistence mentioned in Sect.2.4.

mancini19 performed multi-wavelength bulge to disk decomposition of a sample of $0.45 < z < 1$ star-forming galaxies with reduced specific star formation rate, the so-called green valley galaxies (GV), in order to compare the star formation histories of the two components as inferred from deep Keck optical spectroscopy. They conclude that the maximally-old stellar ages of bulges are hinting at those galaxies being an example of rejuvenation. In particular, they argue for a population of quiescent systems not yet observed

at high- z in order to fill the mismatch between the number density of GV galaxies and the lower one of ETGs at $1 < z < 3$. I contributed to this work performing an independent estimate of the light-weighted ages of the dominant stellar components of bulges in their stacked spectrum using STARLIGHT (Cid Fernandes et al., 2005). Although this test did not eventually figure in the published paper, it served as an additional independent test in favor of their conclusions.

Gobat et al. 2020 developed a model description of the gas fraction evolution in QGs as a function of the derivative of the passive SMF. They reproduce the observed gas fractions from $z \sim 4$ tentative estimates down to local ETGs at fixed mass without making direct assumptions on the quenching mechanism. They argue that the observed evolution is mainly governed by recently quenched galaxies departing from the main sequence with gas fractions not higher than 10%, namely by progenitor bias. They also argue that the trend at $z < 1$ is due to steadier depletion of the ISM, coupled with a higher incidence of gas-exhaustive events. I provided the $z \sim 3$ data as well as feedback on the manuscript.

Calabrò et al. 2019b investigated the role of major mergers in the formation of stellar clumps often attributed, at high- z , to violent disk instabilities. They compared the clumpiness distribution of 109 main sequence and 79 Herschel-detected starburst galaxies at $0.5 < z < 0.9$. Assuming starbursts as a proxy for merger-induced systems, they find that the mergers significantly enhance clumpiness with respect to isolated disks and reaching up to 20% of the total galaxy emission. They performed novel hydrodynamical simulations which produce consistent results. Lastly, they found a mild anti-correlation between clumpiness and merger stage, decreasing towards final coalescence. I contributed to this work providing feedback on the manuscript.

Daddi et al. 2020 (under revision) discovered a 300 kpc-wide giant Ly α nebula centered on a massive galaxy group $z=2.91$ in COSMOS. Keck Cosmic Web Imager observations reveal three cold gas filaments converging into the center of the potential well of its dark matter halo. The group hosts enhanced star formation as probed by ALMA and NOEMA observations. The nebula is consistent with cold gas accretion as inferred from the morphological and kinematical analysis, revealing the prevalence of Ly α blueshifted components. The overall energetics of the system favor gravity as the primary cause powering Ly α emission, as opposed to AGN or star-formation related processes. Albeit a firm conclusion cannot be drawn due to the likely complex interplay between accretion, outflows and recombination, this systems represents one of the best laboratories to quantitatively test models of cold gas accretion. I contributed to this work through discussions and providing feedback on the manuscript.

Delvecchio et al. 2020 (under revision) revised the interpretation of the correlation between infrared and radio luminosity in star-forming galaxies, which was found to mildly decrease with redshift by previous studies.

They decomposed such a correlation at $0.1 < z < 4.5$ in a sample of more than 400,000 mass-selected star-forming galaxies in COSMOS, in terms of stellar mass and redshift simultaneously. They stacked the deepest available infrared/sub-mm and radio images at different bands accounting for clustering and removing AGN candidates. They find that the apparent redshift trend previously reported in the literature is mainly driven by a strong stellar mass dependence, which implies a bias of infrared or radio-selected samples against low-mass systems at high- z . Additionally, they argue that the stronger radio-to-IR emission observed in more massive galaxies could be possibly linked to increasing compactness of star formation. I contributed to this work providing feedback on the manuscript.

The full list of publications is reported below. It includes papers that are in still under revision.

- P. Lustig, V. Strazzullo, **C. D'Eugenio** et al. 2020, “Compact, bulge dominated structures of spectroscopically confirmed quiescent galaxies at $z \sim 3$ ”, MNRAS, 501, 2659;
- R. Gobat, G. Magdis, F. Valentino, **C. D'Eugenio** 2020, “On the gas fraction of passive galaxies and its evolution as a consequence of their creation rate”, ApJL, 644, L7;
- C. Mancini, E. Daddi, S. Juneau ..., **C. D'Eugenio**, ..., et al. 2019, “Rejuvenated galaxies with very old bulges at the origin of the bending of the main sequence and of the ‘green valley’ ”, MNRAS, 489, 1265;
- A. Calabró, E. Daddi, J. Fensch, ..., **C. D'Eugenio**, ..., et al. 2019, “Merger induced clump formation in distant infrared luminous starburst galaxies”, A&A, 632, A98;
- E. Daddi, F. Valentino, R. M. Rich, ..., **C. D'Eugenio**, ..., et al. 2020, “Three Lyman- emitting filaments converging to a massive galaxy group at $z=2.91$: discussing the case for cold gas infall”, A&A, arXiv:2006.11089;
- I. Delvecchio, E. Daddi, D. Elbaz, ..., **C. D'Eugenio**, ..., et al. 2020, “The infrared-radio correlation of star-forming galaxies is strongly M_* -dependent but nearly redshift-invariant since $z \sim 4$ ”, A&A, arXiv:2010.05510.

Appendix C

Accepted proposals

I insert here a NOEMA proposal that was accepted (B rated) but, to this date, not observed. It is based on the detection of dust continuum flux at 1.1mm to measure the dust mass for three of our HST targets by probing the Rayleigh-Jeans tail of the dust emission. By assuming a gas-to-dust conversion factor, as done for lower redshift quiescent galaxies, this would yield an estimate of the cold gas mass hosted by these systems. The requested sensitivities were set to probe whether the strong evolution observed for passive elliptical galaxies from $z=0$ to 1.76 continues, flattens, or actually inverts towards $z=3$, providing independent constraints with respect to the [OII]-derived value for the gas fraction inferred in this thesis work.

PROPOSAL FOR THE NOEMA INTERFEROMETER

Title: Play it back: rewinding the history of the ISM content in massive passive galaxies to the earliest epochs

PIs: Chiara D'Eugenio (FR)

CoIs: Emanuele Daddi (FR), Raphael Gobat (CL), Veronica Strazzullo (DE) (pending), Shuowen Jin (ES), Antonello Calabro' (FR), Annagrazia Puglisi (FR), Mark Dickinson (US), Andrea Cimatti (IT), Chiara Mancini (IT), Sophia Lianou (FR)

Proposal category: Standard

Scientific category: Galaxy structure & evolution

Total requested time: 30.0 (PolyFiX)

Abstract:

The formation of quiescent early-type galaxies, and their quenching mechanism(s), is still a subject of intense debate in galaxy evolution. An efficient way to get more clues on this matter is to study of the most distant passive objects known so far - closer and closer to their formation event - and in the understanding the evolution of their interstellar medium across cosmic time. We take advantage of a pilot sample of spectroscopically confirmed quiescent galaxies at $z=3$, obtained from HST grism spectroscopy, proposing the use of NOEMA to detect the dust continuum flux at 1.1mm of 2 of our targets, thus measuring M_{dust} and constraining M_{gas} . The requested sensitivities are set to clarify whether the extremely strong evolution observed for passive elliptical galaxies from $z=0$ to 1.76 continues, flattens, or actually inverts towards $z=3$, providing new constraints on their quenching mechanism.

Resubmission: W18DL

Proposal history:

This is a resubmission of a previous proposal, W18DL. Target 93434 was given a B-rating for 13h of telescope time (including overheads) but not yet observed. ID169603 was dropped from observations as it was flagged for being in the NIKA2/COSMOS field which is fenced against 1mm continuum observations. However, as shown in the PDF file, it falls outside of said field.

Sources:

Id	Epoch	RA	DEC	z (redshift)	Setups	
93434	J2000	09:57:48.592	01:39:57.661	3.124	1	edit/delete
21292	J2000	10:00:57.345	01:29:39.460	2.557	1	edit/delete
169603	J2000	10:02:00.972	01:50:24.128	3.23	1	edit/delete

Technical sheet "3 targets":

Summary

Point source detection with only continuum on 3 source(s).

Total observing time: 30.00 (10.00 * 3) hours

Track fractions: Any: 100.0 % from: C, D

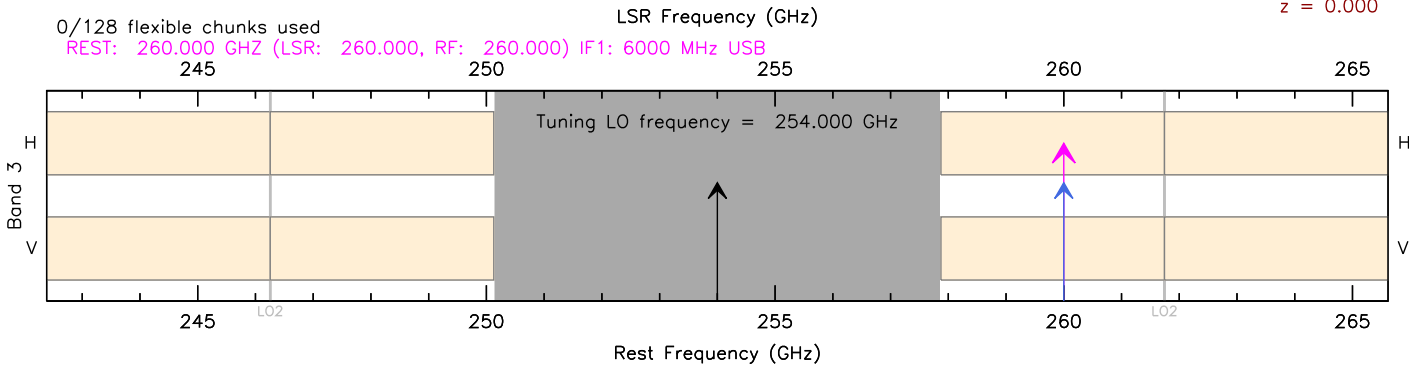
Instrumental tuning

Spectral windows:
 df = 2000.0 kHz

0/128 flexible chunks used

REST: 260.000 GHZ (LSR: 260.000, RF: 260.000) IF1: 6000 MHz USB

REDSHIFT
 $z = 0.000$



Half the most narrow SPW is equivalent to an offset of 2232.301 km/s in source LSR velocity

Source properties for continuum

Expected signal: 78.0 microJy/beam Sensitivity: 39.5 microJy/beam (15488.0 MHz x 2 polar) → SNR: 2

PI note:

This project is part of the PhD thesis of the PI, close to the end of the second year, which aims at shedding light on passive galaxies' formation and evolution.

Scientific context

Our goal is to probe the dust content of three passively evolving galaxies (PEGs) selected from a pilot sample of spectroscopically confirmed quiescent galaxies at $z \sim 3$, in order to get clues on the surprising rise of their dust fraction from $z \sim 0$ to $z \sim 1.76$ and on its evolution towards higher redshift.

In the local Universe, Early-Type Galaxies (ETGs) dominate the top-end of the galaxy stellar mass function, above $5 \times 10^{10} M_{\odot}$, thus enclosing the key of mass assembly. They are believed to have formed very rapidly at $z > 3 - 4$ and having evolved passively after a fast, yet obscure quenching phase. It is well known that today's ETGs show negligible traces of dust and star formation activity (Lianou et al. 2016) with respect to the star forming main sequence (MS) of galaxies. However, this is not the case at $z \geq 1.76$, roughly 10 Gyr ago, when they show 2 dex more dust than their local counterparts, $M_{dust}/M_{\star} \sim 8 \times 10^{-4}$ vs $\sim 10^{-6}$ at $z=0$, at a temperature that is on average 10 K lower than for MS galaxies with the same L_{IR} (Gobat et al. 2018). While this result constrains the average dust content of passive galaxies at $z = 1.76$, **it is unclear what happens before, closer to their formation epochs, e.g. $z \geq 3$** . If they follow the cosmological rise of the gas fraction in galaxies, a trend with redshift going as $(1+z)^{\alpha}$ might be expected (see Fig.1) with $\alpha \geq 4 - 5$ in case the fast trend between $z \sim 0$ and $z \sim 1.76$ were to continue implying a very rapid increase of M_{dust}/M_{\star} that would result in dust masses of ETGs at $z \sim 3$ at least a factor of 6 higher than at $z \sim 1.76$ at fixed stellar mass. This would indeed be highly surprising since ETGs would then contain dust (and gas) fractions comparable or higher than normal MS galaxies *while* still showing quiescent spectra (i.e. rest-frame 4000Å break). If instead they mimic the well-established behaviour of MS galaxies a milder rise of factors of 2-3 ($\alpha \sim 2.2$) could be expected. Alternatively, there might be a flattening of the relation due to the absence of evolution. All of these scenarios imply that the quenching mechanism(s) failed at removing all the gas while the leftover material is kept at low star formation efficiencies (Martig et al. 2009). Lastly, if the quenching mechanism effectively wiped out *all* the pre-existing gas, the dust content at $z \sim 1.76$ could be due to stellar evolution and maybe accretion of satellites. In this case sampling ETGs closer to their quenching epoch could reveal progressively less material as there would be less time for both stellar evolution and minor mergers to act.

To sketch the evolution of the total dust mass and of the cold gas fraction up to the highest redshifts one needs to study the most distant passive objects known so far. Given that $z \sim 3$ passive galaxies are indeed rare, and the nature of compact red objects often ambiguous, spectroscopic redshift confirmations are mandatory to verify their passiveness and reject interlopers. Until now the build up of statistically relevant samples of passive galaxies at high redshift has reached only as far as $z \sim 2.6$ via deep rest-frame optical or near-IR spectra (Daddi 2005, Cimatti 2008, Kriek 2009, Onodera 2015, Newman 2018). Recently, the search for passive objects extended to $z \sim 3$ mostly by finding individual galaxies: the $z=2.99$ ETG by Gobat et al. 2012 identified thanks to the presence of a prominent 4000 Å break at $1.6 \mu\text{m}$; and a massive ($\sim 1.7 \times 10^{11} M_{\odot}$) quenched galaxy at $z=3.717$ by Glazebrook et al. 2017. To this date, only Schreiber et al. 2018 provided a sizable sample of passive galaxies at $z \sim 3$ reporting rest-frame optical MOSFIRE spectra of 3 objects with Balmer breaks in addition to the Glazebrook's one.

The need for a wider sample of high-redshift ETGs lead us to design an on-going HST WFC3/G141 spectroscopic survey to observe 10 passive galaxy candidates at $2.5 < z < 3.5$. The selection as passives was performed on the basis of their observed BzK and rest-frame UVJ colors, the absence of a $24 \mu\text{m}$ detection and the lack of acceptable SED fits for dusty starburst solutions. The data were reduced and analyzed by means of the `grizli` software package¹ yielding at least 9 passive objects, 3 of which we ask for continuum data (see Tab. 1). The spectra of the proposed NOEMA targets, shown in Fig.2, show the presence of either a strong 4000Å break or a Balmer break indicative of quiescent evolution since at least 0.5 Gyr.

One way of **estimating M_{dust}** from the FIR flux is to take advantage of the optically thin Rayleigh-Jeans tail of thermal dust emission as in Magdis et al. 2011 and Scoville et al. 2013. This method is still applicable to high- z objects by moving at frequencies lower than 345 GHz to avoid sampling the peak of the SED, sensible to recent star formation (Scoville et al. 2014). In particular, for objects at $z \sim 3$ sampling the observed SED at 260 GHz would fit this constraint while still avoiding a sensible drop in flux. This

¹<https://github.com/gbrammer/grizli>

approach was applied to individual galaxies by Magdis et al. 2011 and Scoville et al. 2014 up to $z \sim 2$ and was later extended by Bethermin et al. 2015, via stacking, all the way up to $z \sim 4$. This will allow us to estimate M_{dust} by fitting the 260 GHz fluxes with templates of dust grain emission (Draine & Li 2007) by varying the mean intensity of the radiation field $\langle U \rangle$ and the dust temperature (T_{dust}) as in Bethermin et al. 2015; and to put a first constraint on M_{gas} by assuming a reasonable gas-to-dust ratio (G/D) conversion (Galametz et al. 2011, Magdis 2011, 2012a, Gobat et al. 2018) and a gas-metallicity phase close to the solar value given the high stellar masses of our sample (see Table 1). We stress here that we would adopt a similar G/D value as in Gobat et al. 2018 to infer M_{gas} since it can be considered a rather conservative choice given the uncertainties and the scatter of the relation between G/D and gas phase metallicity. Also, our sources remain undetected in Herschel/SCUBA-2/MAMBO photometry.

A robust derivation of M_{dust} requires the use of mm data as noted in Magdis et al. 2011 and Galametz et al. 2011, as it reduces the uncertainties on absolute value of M_{dust} by a factor of two. Moreover, the consistency in the prescriptions for the dust emission modeling adopted for the low-, intermediate- and the high- z ETGs, at comparable stellar masses, guarantees meaningful **relative measurements** among the massive tail of the passive population, i.e. the oldest, which are essentially the core of the project.

We recently stacked the spectra of the 9 galaxies classified as securely passive, detecting a 5σ [OII] emission line (see Fig. 3) which, adopting Kennicutt 1998 relation, yields a dereddened residual star formation rate of $SFR = 7.2 \pm 2 M_{\odot} yr^{-1}$, roughly 1/60 that of a coeval MS galaxy at the mean M_{\star} of our sample. Since the star formation efficiency $SFE = SFR/M_{gas}$ of ETGs appears to be suppressed by a factor of 2-3 with respect to MS galaxies both locally and at intermediate z (Gobat et al. 2018), thus not varying significantly over a 10 Gyr period, we adopted the same SFE of intermediate z ETGs, namely $5.01 \times 10^{10} yr^{-1}$, to tentatively infer the cold gas mass M_{mol} of our sample, obtaining $M_{mol} = 1.47 \pm 0.74 \times 10^{10} M_{\odot}$, hence a gas fraction of $\sim 8.7\%$ which is indeed similar to what found at $z \sim 1.8$. This seems to rule out the steep rise in gas fraction highlighted between more recent epochs. We stress that while the uncertainties related to the method proposed here would not discriminate precisely between the trends in Fig.1, a detection on the expected flux level for a mild-to-no evolution would help to independently strengthen the flattening highlighted by the [OII] emission line. A surprisingly high S/N detection, instead, even in three galaxies, would imply an even lower SFE and that our extrapolation would have to be reconsidered, which would be an intriguing outcome on its own. In conclusion, acquiring NOEMA data represents an invaluable piece of information as it will, *for the first time*, provide constraints on the dust and gas evolution on secure distant ETGs and an empirical/observative evidence of their evolution from $z \sim 0$ to $z \sim 1.76$. This will open the door for future investigations and, ultimately, will help in disentangling the elusive quenching mechanisms that led to the formation of such intriguing galaxies.

Planned observations

We ask for NOEMA observations of our $z \sim 3$ passive galaxies. Exploiting NOEMA improved sensitivity we would have the chance to investigate on the 3 possible paths from $z = 1.76$ to $z \sim 3$ described above:

- (1) *Further positive evolution of the ISM content*: (a) if indeed M_{dust}/M_{\star} rises at the pace extrapolated from $z=0$ to $z=1.76$ ($\alpha \geq 4-5$) we would detect galaxies even up to $S/N \sim 10-15$; (b) if instead $\alpha \sim 2.2$ we would detect galaxies with $S/N \sim 4-5$.
- (2) *No evolution*: in this conservative case we would detect all galaxies at a 2σ level;
- (3) *Negative evolution*: in this last case, stacking the 3 galaxies we could constrain the reduction in flux to be at least a factor of ~ 2 , which would already be a significant hint at the inversion of the trend reported in Gobat et al. 2018.

We set our observing time requirements to allow a $S/N = 2$ detection even in the case of no-evolution, namely 10h on source per galaxy. The availability of **accurate positions from HST** allow us to statistically use continuum measurements down to 2σ . We thus need to measure a continuum flux of $S_{260GHz} = 78 \mu Jy$ at 2σ , setting a target rms of $39.5 \mu Jy$. Being our sources very compact, we can accept any configuration that would deliver a synthesized beam between $0.9''$ and $1.4''$, hence either configuration C or D. ID169603 was flagged for being in the NIKA2/COSMOS field and hence discarded. However, comparing their positions (see Fig. 4), this target seems to fall outside of it.

Supporting material

References

- Lianou et al. 2016, MNRAS, 461, 2856
- Gobat et al. 2018, NatAstr, 2, 239
- Scoville et al. 2013, IAU proceedings, 292, 279
- Scoville et al. 2014, ApJ, 783, 84
- Magdis et al. 2011, ApJL, 740, L15
- Magdis et al. 2012a, ApJ, 760, 6
- Bethermin et al. 2015, A&A 573, A113
- Draine & Li 2007, ApJ, 657, 810-837
- Galametz et al. 2011, A&A 532, A56
- Daddi et al. 2005, ApJ, 631, L13L16
- Cimatti et al. 2008, A&A 482, 2142
- Kriek et al. 2009, ApJ, 700, 221231
- Onodera et al. 2015, ApJ, 808, 161
- Krogager et al. 2013, MNRAS, 433, 3091
- Glazebrook et al. 2017, Nat, Vol 544, pp. 71-74
- Simpson et al. 2017, ApJL, 844
- Bruzual G., Charlot S., 2003, MNRAS, 344, 1000
- Maraston C., Nieves Colmenárez L., Bender R., Thomas D., 2009, A&A, 493, 425

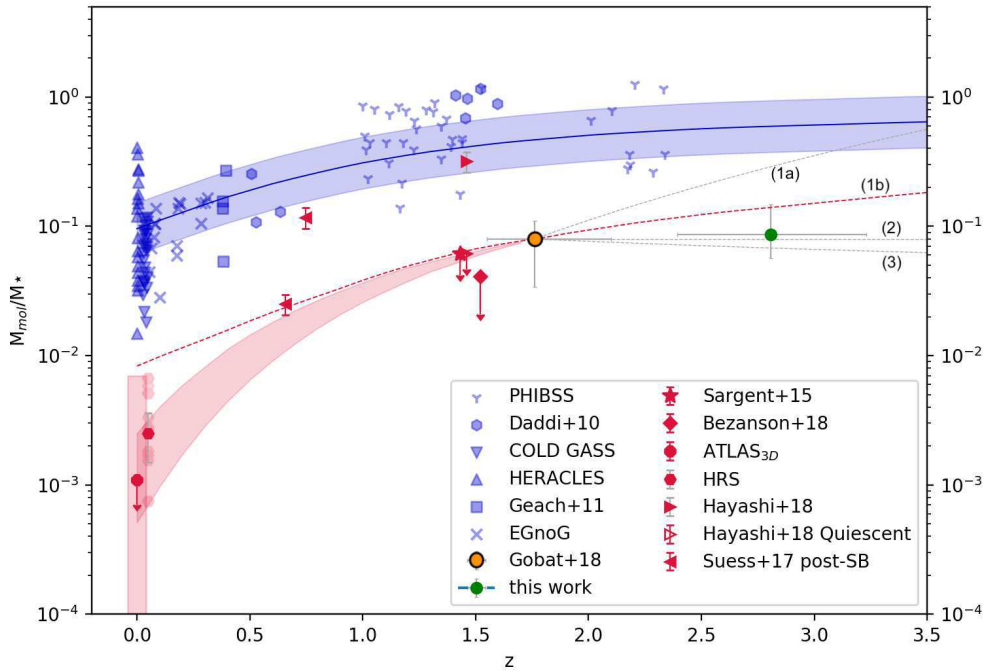


Figure 1: Evolution of molecular gas fraction M_{mol}/M_* as a function of redshift for main sequence and quiescent galaxies. The reference sample of 977 ETGs at $\langle z \rangle \sim 1.76$ is marked as an orange dot. The solid line shows the evolution of an average MS galaxy with stellar mass $5 \times 10^{10} M_\odot$. The red dashed curve shows the dust fraction evolution (traced by molecular gas) offset by a factor of 6 and for the median stellar mass of the Gobat+18 sample. Even when accounting for offsets in M_* between local and high- z samples there is an increase by more than two orders of magnitudes in M_{mol}/M_* which grows faster than what is happening in MS galaxies. The green dot shows an independent estimate derived from the $SFR_{[OII]}$ obtained from our passive sample's average spectrum, to be tested by NOEMA data.

ID	RA	DEC	z	$\log(M_*)$	t_{SSP} [Gyr]
21292	10 00 57.363	+01 29 39.263	2.557 ± 0.005	11.2	0.7
93434	09 57 48.592	+01 39 57.661	3.118 ± 0.002	11.0	0.5
169603	10 02 0.972	+01 50 24.128	3.234 ± 0.011	10.7	0.3

Table 1: Targets' characteristics and ages of the best fit Simple Stellar Populations (Bruzual & Charlot 2003, BC03). Stellar masses are derived using the Chabrier 2003 IMF. They were rescaled to the Salpeter IMF when computing the expected fluxes so to be consistent with the reference work of Gobat et al. 2018.

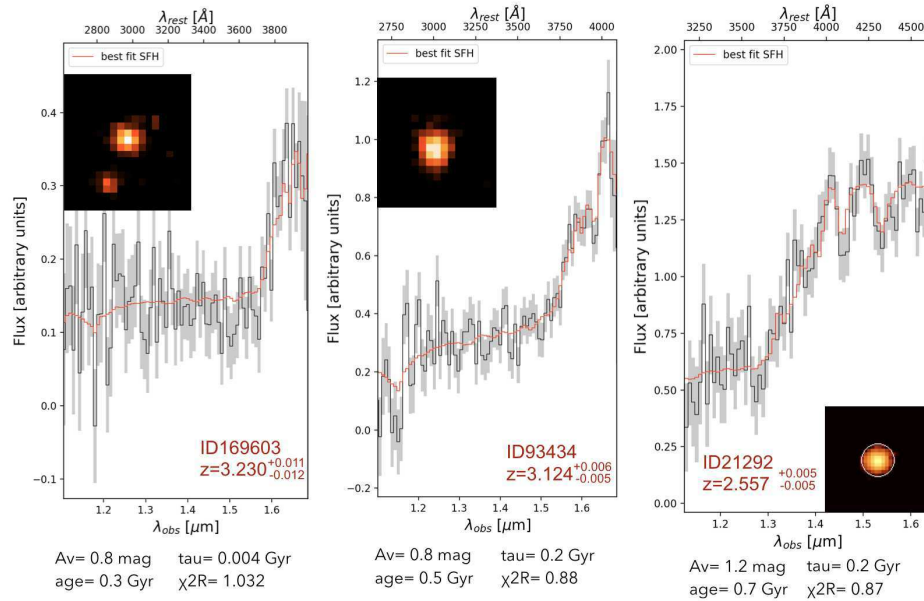


Figure 2: HST spectra are shown for the proposed objects. Red curves: best fit SSPs from BC03, ages are reported in Table 1. $Z = Z_{\odot}$ is assumed throughout. Cutouts from HST/WFC3 F160W imaging are reported. White circles: regions with a radius of $0.6''$.

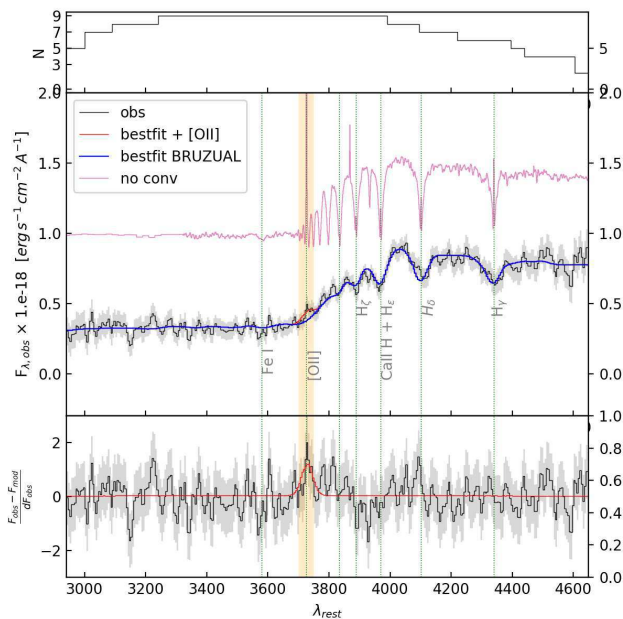


Figure 3: **Top:** Number of galaxies contributing at each spectral bin. **Middle:** Stacked spectrum of 9 quiescent galaxies. Blue curve: best-fit models from BC03. Red curve: gaussian fit to the residuals, added to the blue continuum. Green dotted lines: identified absorption features. The pink curve shows the best-fit BC03 template at its original resolution, shifted in flux for clarity. **Bottom:** Fit residuals normalized to the error spectrum.

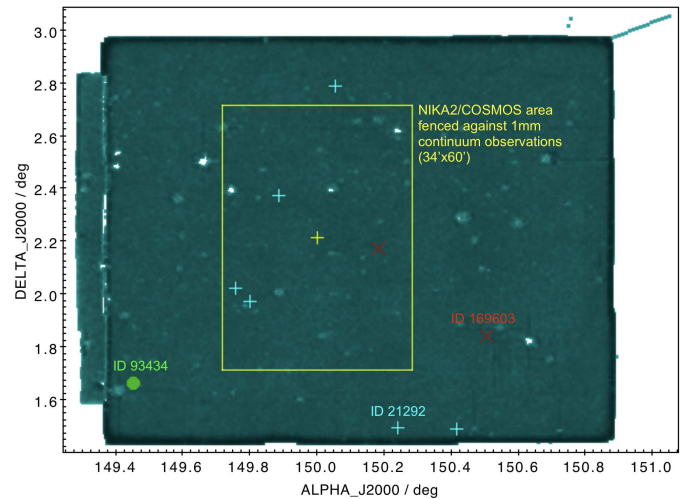


Figure 4: Position of the previously rejected ID169603 with respect to the NIKA2/COSMOS field. The target appears to be outside the protected area.

Appendix D

First author papers

I insert here the letter published on ApJ regarding the stacked spectrum and the direct measurement of post-starburst features in $z \sim 3$ quiescent galaxies. Afterwards, I add the paper on the detailed analysis of the full sample submitted to A&A. At the time of writing, this latter one is under revision and was uploaded on arXiv.



The Typical Massive Quiescent Galaxy at $z \sim 3$ is a Post-starburst

C. D'Eugenio¹, E. Daddi¹, R. Gobat², V. Strazzullo³, P. Lustig³, I. Delvecchio^{1,4}, S. Jin^{5,6}, A. Puglisi^{1,7,8},
A. Calabró⁹, C. Mancini¹⁰, M. Dickinson¹¹, A. Cimatti¹², and M. Onodera^{13,14}

¹CEA, IRFU, DAp, AIM, Université Paris-Saclay, Université Paris Diderot, Sorbonne Paris Cité, CNRS, F-91191 Gif-sur-Yvette, France; chiara.deugenio@cea.fr

²Instituto de Física, Pontificia Universidad Católica de Valparaíso, Casilla 4059, Valparaíso, Chile

³Faculty of Physics, Ludwig-Maximilians-Universität, Scheinerstr. 1, D-81679 Munich, Germany

⁴INAF—Osservatorio Astronomico di Brera, Via Brera 28, I-20121, Milano, Italy

⁵Instituto de Astrofísica de Canarias (IAC), E-38205 La Laguna, Tenerife, Spain

⁶Universidad de La Laguna, Dpto. Astrofísica, E-38206 La Laguna, Tenerife, Spain

⁷Center for Extragalactic Astronomy, Durham University, South Road, Durham DH1 3LE, UK

⁸INAF—Osservatorio Astronomico di Padova, Vicolo dell'Osservatorio, 5, I-35122 Padova, Italy

⁹INAF—Osservatorio Astronomico di Roma, via di Frascati 33, I-00078, Monte Porzio Catone, Italy

¹⁰Department of Physics and Astronomy, University of Padova, Vicolo dell'Osservatorio, 3, I-35122, Padova, Italy

¹¹National Optical Astronomy Observatories, 950 N Cherry Avenue, Tucson, AZ 85719, USA

¹²Università di Bologna, Dipartimento di Fisica e Astronomia, Via P. Gobetti 93/2, I-40129, Bologna, Italy

¹³Subaru Telescope, National Astronomical Observatory of Japan, National Institutes of Natural Sciences (NINS), 650 North A'ohoku Place, Hilo, HI 96720, USA

¹⁴Department of Astronomical Science, SOKENDAI (The Graduate University for Advanced Studies), 650 North A'ohoku Place, Hilo, HI 96720, USA

Received 2019 December 17; revised 2020 February 20; accepted 2020 February 27; published 2020 March 18

Abstract

We have obtained spectroscopic confirmation with *Hubble Space Telescope* WFC3/G141 of a first sizeable sample of nine quiescent galaxies at $2.4 < z < 3.3$. Their average near-UV/optical rest-frame spectrum is characterized by low attenuation ($A_V \sim 0.6$ mag) and a strong Balmer break, larger than the 4000 \AA break, corresponding to a fairly young age of ~ 300 Myr. This formally classifies a substantial fraction of classically selected quiescent galaxies at $z \sim 3$ as post-starbursts, marking their convergence to the quenching epoch. The rapid spectral evolution with respect to $z \sim 1.5$ quiescent galaxies is not matched by an increase of residual star formation, as judged from the weak detection of [O II] $\lambda 3727$ emission, pointing to a flattening of the steep increase in gas fractions previously seen from $z \sim 0$ to 1.8. However, radio 3 GHz stacked emission implies either much stronger dust-obscured star formation or substantial further evolution in radio-mode AGN activity with respect to $z \sim 1.5$.

Unified Astronomy Thesaurus concepts: Galaxy evolution (594); Galaxy quenching (2040); Quenched galaxies (2016)

1. Introduction

Timing the formation and quenching of the most massive ($M_* > 10^{11} M_\odot$) passively evolving galaxies (PEGs) is the subject of intense debate. Several studies kept unveiling their existence at progressively increasing lookback times, placing their formation at $z > 3-4$ (Gobat et al. 2012; Glazebrook et al. 2017; Forrest et al. 2020; Valentino et al. 2020). Reproducing the observed number density of such galaxies at all epochs is a compelling concern of current galaxy evolution models in cosmological simulations, as the relative importance of the quenching mechanisms is not yet clear (Man & Belli 2018). To this end, several photometric samples of high- z PEGs exist (Straatman et al. 2014; Merlin et al. 2018), yet spectroscopic confirmation is still needed to precisely assess their redshifts and the degree of contamination by star-forming interlopers, especially at epochs when PEGs might be just starting to emerge. At $z \sim 3$ the chances of collecting statistically meaningful samples of PEG spectra are hampered by their rarity and lack of prominent emission lines. Therefore, the assembly of sizeable samples of quiescent spectra is essential to improve upon the photometric age/dust-attenuation estimation for the bulk of their stellar populations, to draw relative comparisons of their spectral properties with respect to lower-redshift massive PEGs and to reveal any residual emission line that might be linked to star formation. The latter point provides useful information on the availability of unstable, cold molecular gas that is, itself, a poorly constrained quantity at

this epoch. In this Letter we report on the average stellar population properties in a sizeable sample of nine spectroscopically confirmed $2.4 < z < 3.3$ quiescent galaxies. We constrain their global residual star formation from the average [O II] emission, showing implications on their average gas fraction. We assume a Λ CDM cosmology with $H_0 = 70 \text{ km s}^{-1} \text{ Mpc}^{-1}$, $\Omega_M = 0.27$, $\Omega_\Lambda = 0.73$, and a Salpeter initial mass function (IMF). Magnitudes are given in the AB photometric system.

2. Sample Selection and Analysis

We selected galaxies from a parent sample of more than 50 reliable PEGs candidates with $K_{\text{tot}} < 22.5$ in the McCracken et al. (2010) catalog with photometric redshifts between $2.5 \leq z_{\text{phot}} \leq 3.5$ in the COSMOS field. A first selection was done using the BzK criterion (Daddi et al. 2004) selecting passive BzK galaxies plus objects formally classified as star-forming BzK but having a signal-to-noise ratio (S/N) < 5 in the B and z bands, to retain passive galaxies as they become fainter in such bands with increasing redshift and decreasing mass. We then selected from this sample *UVJ* quiescent galaxies (Williams et al. 2009), exploiting photometric redshifts calibrated for high- z PEGs (Onodera et al. 2012; Strazzullo et al. 2015). To minimize contamination from dusty star-forming galaxies, objects in McCracken et al. (2010) with Spitzer/MIPS $24 \mu\text{m}$ S/N > 4 were discarded, except for galaxies with high-confidence passive spectral energy distributions (SEDs). Objects having SED fits to optical–NIR

Table 1
Main Properties of our Sample Derived from the Stacked Spectrum (See the Text)

$\langle z \rangle$	M_* ($10^{11} M_\odot$)	t_{50} (Gyr)	A_V (mag)	D_n4000	D_B	$EW_{[O II]}$ (Å)	$F_{[O II]}$ ($\text{erg s}^{-1} \text{cm}^{-2}$)	SFR ($M_\odot \text{yr}^{-1}$)
2.808	1.8 ± 0.8	$0.30_{-0.05}^{+0.20}$	$0.9_{-0.5}^{+0.4}$	1.28 ± 0.05	1.88 ± 0.07	2.1 ± 0.6	$3.1 \pm 0.7 \times 10^{-18}$	7 ± 3

Note. Solar metallicity and a Salpeter IMF were assumed throughout.

broadband photometry consistent with dusty star-forming solutions and contaminated photometry in all images were also discarded. Among the most massive bona fide passive candidates, 10 galaxies were targeted for *Hubble Space Telescope* (*HST*) WFC3/IR G141 near-IR¹⁵ observations: 9 with $H_{AB} < 22$ ($M_* > 1.1 \times 10^{11} M_\odot$) plus 1 robust candidate with $H_{AB} = 22.9$ ($M_* = 8 \times 10^{10} M_\odot$) among the highest- z objects. Scheduling from 1 to 3 orbits (17 in total) according to each source’s flux provided low-resolution spectra ($R = 130$) with a mean S/N ~ 4.5 per resolution element for each target and ancillary F160W imaging (*HST* GO 15229 program). The data were reduced and decontaminated from neighboring sources’ overlapping spectra by means of the `grizli` software package (Brammer 2018).¹⁶ For each target a 2D spectrum was produced and drizzled to a scale of 0.8 times the native pixel size. The 1D spectra were then optimally extracted (Horne 1986) and fitted from 11000 to 16900 Å with Bruzual & Charlot (2003, hereafter BC03) composite stellar populations derived using different star formation histories (SFHs): allowing for a constant, exponentially declining, delayed exponentially declining, and a truncated SFH, where the star formation rate (SFR) drops to 0 after a timescale between $\tau = 0.001 - 1.0$ Gyr. Ages were allowed to vary between $t = 100$ Myr and 10 Gyr, from redshift 5 to 0. The Calzetti et al. (2000) extinction law was adopted with A_V varying between 0 and 8 mag. BC03 templates were broadened to the grism resolution using a Gaussian kernel whose FWHM was derived via a Gaussian fit of the 2D light profile of each source.

The broadband photometry (Laigle et al. 2016) for each galaxy was also fitted imposing the grism-derived redshifts. The addition of the photometric information mostly leads to narrowing down the range of dust extinction values at any confidence level. The detailed analysis of individual galaxies will be presented in a forthcoming paper.

2.1. Quiescence of Individual Targets

We tested the quiescent/dusty star-forming nature of each galaxy adding the χ^2 matrices of fits to spectra and photometry and comparing the goodness-of-fit of the best-fitting constant star-forming (CSF) template with that of a solution defined as passive by constraining the best-fitting SFH as follows: $t_{50} \geq 0.3$ Gyr, $A_V < 0.8$ mag, and $t_{50}/\tau \geq 10$, where t_{50} is the lookback time at which the galaxy formed 50% of its stellar mass. To reject a solution (i.e., to classify it as inconsistent with respect to the other one *and* with the data) its probability had to be < 0.01 , as inferred from their χ^2 difference. Star-forming solutions were rejected for all sources except for one, whose redshift was not properly constrained by our data. If this galaxy were in our selected range in redshift, its quiescence would be rejected with 80% confidence, hence we excluded it. We were

thus left with nine galaxies classified as passive with a median redshift of $z_m = 2.808$ and a median stellar mass of $M_\odot 1.8 \times 10^{11}$.

3. Stacked Spectrum

To fully exploit the sample size we created an average spectrum. We scaled the wavelength vector of each galaxy to z_m and interpolated their fluxes and error spectra on a 5 Å rest-frame grid, increasing the error in each new pixel by the square root of the width ratio between the old and the new spectral bin, to account for the introduced noise correlation. Each error spectrum was interpolated in quadrature. Each spectrum was normalized to its average flux between $\lambda_{\text{rest}} = 3800$ and 3900 Å in order to select a wavelength range covered for all galaxies. We then created a stacked spectrum as the inverse variance weighted mean of the individual fluxes in each wavelength bin. The final error spectrum was computed as the error on the flux-weighted mean in each pixel. A jackknife resampling provides consistent results. The median z_{spec} uncertainty from our individual galaxies is $dz \sim 0.006$ at 68% confidence. This does not affect the final spectral resolution, being three times smaller than the broadening from galaxy sizes. The average spectrum was rescaled to match the average broadband photometry of the sample at $\lambda_{\text{rest}} = 3800\text{--}3900$ Å, in turn obtained by stacking the individual galaxy best-fit SEDs (as done for the spectra). Figure 1 shows the average spectrum with clear Balmer absorption lines from $H\eta$ to $H\gamma$, the [O II] (unresolved) doublet at 3727 Å, and the Fe I absorption line. With a mean S/N ~ 13 per pixel at 4000 Å this is, to date, one of the highest S/N spectra available for high- z PEGs and the first spanning a large spectral range around key spectral breaks.

We analyzed the stacked spectrum as in Section 2, this time limiting the age grid to the age of the universe at $z_m = 2.808$ (2.3 Gyr) and using the average FWHM derived for the individual targets as spectral broadening.¹⁷ The mean properties of our sample result in $t_{50} = 0.30_{-0.05}^{+0.20}$ Gyr and $A_V = 0.6_{-0.4}^{+0.6}$ mag at fixed solar metallicity given the high $\langle M_* \rangle$ of our sample (Mancini et al. 2019; see Table 1). The 1σ uncertainties were estimated marginalizing over these two quantities, taking into account the simple parameterizations used for the SFHs.

We then measured the $H_{\delta A}$, D_n4000 , and D_B spectral indices (Worthey & Ottaviani 1997; Balogh et al. 1999; Kriek et al. 2006). Since our spectral resolution is worse than in the original Lick system, the $H_{\delta A}$ was measured on the best-fit BC03 model smoothed to the Lick resolution and adding the broadening due to a 200 km s^{-1} stellar velocity dispersion corresponding to our $\langle M_* \rangle$. The D_n4000 and D_B instead are not affected much by resolution. The indices result in $D_n4000 = 1.28 \pm 0.05$, $D_B = 1.88 \pm 0.07$, and $H_{\delta A} = 10.1_{-0.6}^{+0.0}$ Å. The error on $H_{\delta A}$ was computed measuring the

¹⁵ Rest-frame near-UV/optical.

¹⁶ <https://github.com/gbrammer/grizli>

¹⁷ This analysis does not include the information from the stacked photometry.

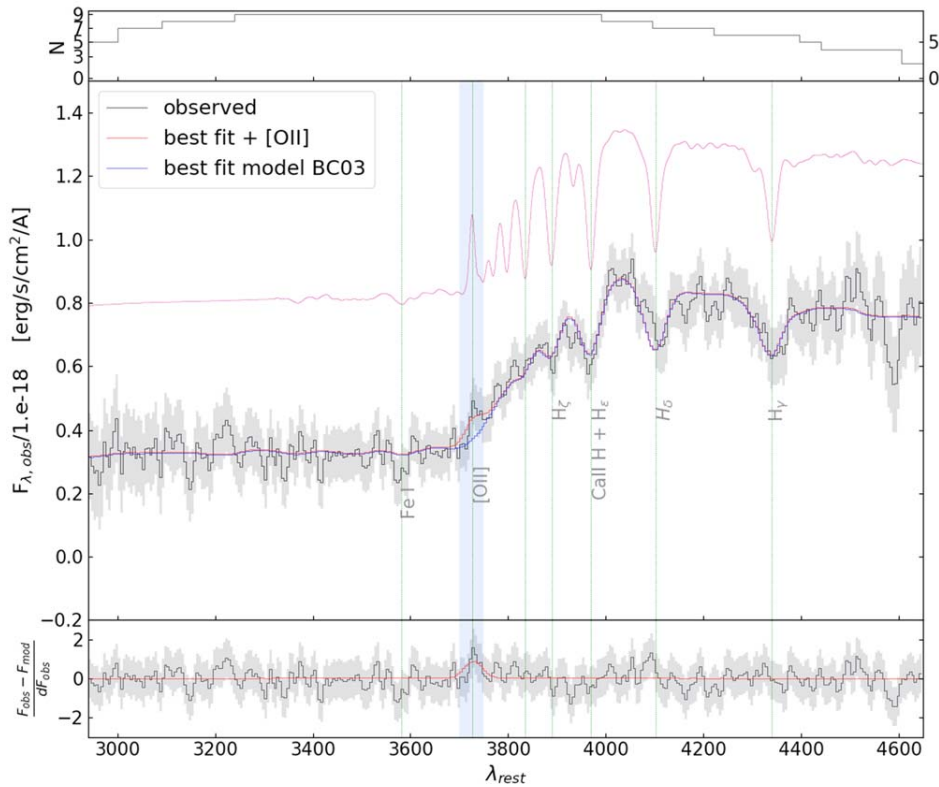


Figure 1. Top: number of galaxies contributing to each spectral bin. Middle: stack of nine quiescent galaxies’ spectra. Blue curve: best-fit model from the BC03 library. Red curve: gaussian fit to the residual, added to the blue continuum. Pink curve: best-fit BC03 template smoothed for a $\sigma_v \sim 200$ km s^{-1} , shifted in flux for clarity. Vertical dotted lines mark the identified absorption features. Bottom: fit residuals normalized to the error spectrum.

index maximum variation on the templates within the uncertainties on t_{50} and A_V , accounting for the negative correlation between these two. The weakness of the D_n4000 compared the strength of the Balmer break (D_B) and of $H_{\delta A}$ classifies the spectrum as post-starburst dominated by A-type stars. We show the indices in Figure 2, where we also show $H_{\delta A}$ measured directly on the stacked spectrum to display the effect of low resolution. We checked whether our spectroscopic sample is representative of the parent photometric sample and quantified the impact of the selection bias introduced by the H-band selection at $2.5 \leq z \leq 3.5$. A Kolmogorov–Smirnov test reveals that the probability of being drawn from the same M/L distribution is only 3%, confirming the selection bias. However, removing 30% of the highest M/L objects from the parent sample yields $p = 0.5$, leaving our *HST* sample consistent with the remaining 70%. The median M/L ratios of the two samples become identical once the highest M/L objects, 40% of the parent sample, are removed. The lowest M/L that a non-post-starburst galaxy (defined here as a stellar population characterized by $D_B/D_n4000 < 1$) would have relative to that of our average galaxy implies a cut ($M/L_{old} \geq M/L_{HST} + \Delta M/L$) that includes at most 30% of the unobserved sample. We thus conservatively conclude that at least 60%–70% of passive galaxies at $z \sim 3$ are post-starburst, as the remaining “redder” galaxies could be as well post-starbursts with higher dust extinction, but also redshift interlopers, star-forming interlopers, or AGN (our single failed confirmation from spectroscopy is among the reddest and lowest M/L galaxies in the parent sample). Hence, the typical passive galaxy at $z \sim 3$ is a post-starburst. This conclusion is corroborated by the global fast rise of the passive stellar mass function over

$2.5 < z < 4$ (Muzzin et al. 2013; Davidzon et al. 2017) consistent with a ~ 1 dex increase of the number density, implying that a large proportion of the massive passive population in place at $z \sim 3$ must have been very young and recently formed. In addition, from Figure 3 and from the strong Balmer lines in the published spectra, it appears that all $z \geq 3$ spectroscopically confirmed passive galaxies from the literature are sharing our global spectral properties. Further efforts need to be taken to spectroscopically identify truly old and passive galaxies (non-post-starburst) at high redshift, if they exist.

4. Residual Star Formation

Given the tight anticorrelation between the age of a stellar population and the specific SFR (sSFR = SFR/M_*) of its host galaxy, expected in the case of a smooth intrinsic SFH (as opposed to a simple stellar population (SSP), or a complex SFH), we investigated whether the age decrease at fixed M_* from $z \sim 1.5$ to $z \sim 2.8$ translates into a higher sSFR.

We used MPFIT to model the residuals of the fit using a single Gaussian centered and fixed at 3727 \AA with a width matched to the data spectral resolution, measuring $F_{[O II]} = (3.1 \pm 0.7) \times 10^{-18} \text{ erg s}^{-1} \text{ cm}^{-2}$. The observed [O II] flux was dereddened adopting the best-fit dust attenuation ($A_V = 0.6 \text{ mag}$) using a value of $f = 0.83$ for the ratio between stellar and nebular extinction (Kashino et al. 2013) as in Gobat et al. (2017) in order to perform a consistent relative comparison. Following Kennicutt (1998) we then obtained an $SFR = 7 \pm 3 M_{\odot} \text{ yr}^{-1}$, which is a factor of ~ 60 below the main-sequence level at $2.5 < z < 3.5$ (Schreiber et al. 2015). This is in agreement with estimates for intermediate redshift quiescent galaxies from

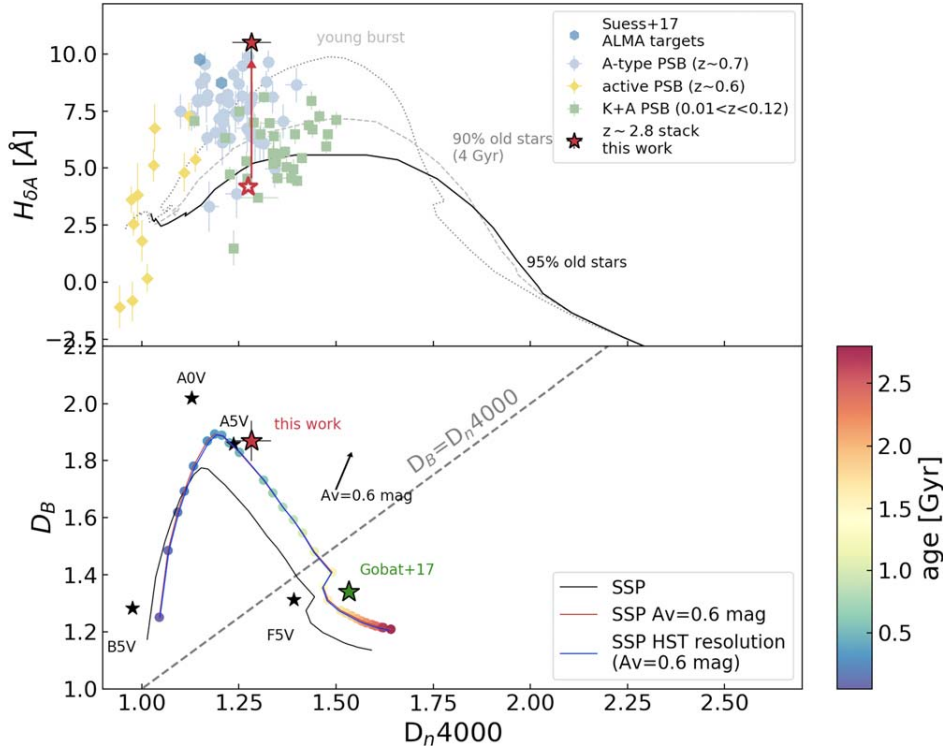


Figure 2. Top: comparison between our average D_n4000 and $H_{\delta A}$ and $z \sim 0.7$ A-type post-starburst galaxies (light blue dots) from Suess et al. (2017). Green squares and yellow diamonds: K+A local post-starbursts and $z \sim 0.6$ active post-starbursts, from French et al. (2015) and Sell et al. (2014), respectively. Open star: $H_{\delta A}$ computed on the stacked spectrum, as a lower limit due to resolution. Tracks with different amounts of old stars (age > 4 Gyr) from Suess et al. (2017) are shown, going from no old stars (dotted line) to 95% of old stars (solid line). Bottom: strength of the Balmer and 4000 Å break indices as a function of the SSP age. Red and green stars represent the indices measured on our stack spectrum and on Gobat et al. (2017) spectrum, respectively. Black stars mark the indices computed on theoretical stellar spectra smoothed to *HST* resolution (Rodríguez-Merino et al. 2005).

dereddened [O II] luminosity ($\text{SFR}_{[\text{O II}]} = 4.5 M_{\odot} \text{yr}^{-1}$; Gobat et al. 2017), which is in turn consistent with their FIR luminosity ($\text{SFR}_{\text{IR}} = 4.8^{+1.8}_{-1.3} M_{\odot} \text{yr}^{-1}$; Gobat et al. 2018, hereafter G18). Therefore, the age evolution implied by the continuum appears to occur at constant sSFR. This is also suggested by the equivalent width (EW) of the line that is 2.1 ± 0.6 Å rest-frame. This value is almost half that obtained by Gobat et al. (2017) due to a higher UV continuum produced by ~ 1 Gyr younger stars. Assuming that the [O II] flux arises from a 100 Myr old stellar population, forming stars at a constant rate and with $A_V = 0.6$ mag, we subtracted the associated continuum component from the stacked spectrum to explore the effect on the age determination, deriving $t_{50} = 0.30^{+0.20}_{-0.05}$ Gyr and $A_V = 0.9^{+0.4}_{-0.5}$ mag. Letting the age and extinction of the star-forming component vary (100–300 Myr and 0.6–1.5 mag, respectively) leaves t_{50} unchanged while increasing A_V up to 1.0 mag. The flux at $\lambda > 4400$ Å varies around the 95% of the original flux, suggesting that the CSF component does not account for more than 1%–2% of $\langle M_{\star} \rangle$ as also confirmed by the mass produced in a $\Delta t \sim 300$ Myr at a constant SFR of $10 M_{\odot} \text{yr}^{-1}$, namely, the upper limit inferred here. We thus conclude that the presence of the youngest stellar population does not impact our results significantly. The sSFR of our sample, $(4.35 \pm 2.47) \times 10^{-11} \text{yr}^{-1}$, is consistent with the available estimates at $z \sim 1.5$ –1.8 (Sargent et al. 2015; Bezanson et al. 2019) and with the sSFR for the four quiescent galaxies with a spectral break in Schreiber et al. (2018) for which $\text{sSFR}_{[\text{O II}]}$ is available. However, the best-fit t_{50} obtained here implies a formation redshift $z_{\text{form}} \gtrsim 3.2$, meaning that at $z \sim 4$ our galaxies would

be actively forming stars. To check that the average spectrum is not dominated by emission from unobscured AGN, we removed from the stack the two X-ray detected sources ($L_{X_{2-10 \text{ keV}}} = 10^{44.3}$ and $10^{43.7} \text{ erg s}^{-1}$), getting $F_{[\text{O II}]_{\text{noX}}} = (3.53 \pm 0.90) \times 10^{-18} \text{ erg s}^{-1} \text{ cm}^{-2}$ consistent within the uncertainties. Stacking the available X-ray data in COSMOS for the undetected sources results in $L_{X_{2-10 \text{ keV}}} < 10^{43.1} \text{ erg s}^{-1}$. If part of the [O II] luminosity were caused by low AGN activity or shocks, the intrinsic SFR would be even lower, strengthening the conclusion that the young spectral age does not directly map into a higher sSFR. Using the UV-extended Maraston et al. (2009) models the best-fitting template yields a similar $t_{50} \sim 0.3$ Gyr but produces a slightly worse χ^2 and a less solid [O II] detection, with a flux that is 60% of the one measured with BC03 templates, at 2.9σ confidence.

5. Discussion

It is interesting to place our $z \sim 3$ results in the overall evolutionary context of passive galaxies. In order to be able to compare to the available literature we express, for convenience, the SFR constraints in terms of the available gas fraction through the relation $f_{\text{mol}} = \text{sSFR}/\text{SFE}$, where SFE is the star formation efficiency. We caution that this is just an alternative way to look at the SFR result, as we are using the same single constraint: we use both quantities interchangeably in the following and notably in Figure 4. We assume the same SFE derived in G18 ($5 \times 10^{-10} \text{ yr}^{-1}$), which is lower by $\times 2$ –3 than that of typical star-forming galaxies, noticing that such reduced SFE is also typical of post-starburst galaxies (Suess et al. 2017). Our SFR thus converts

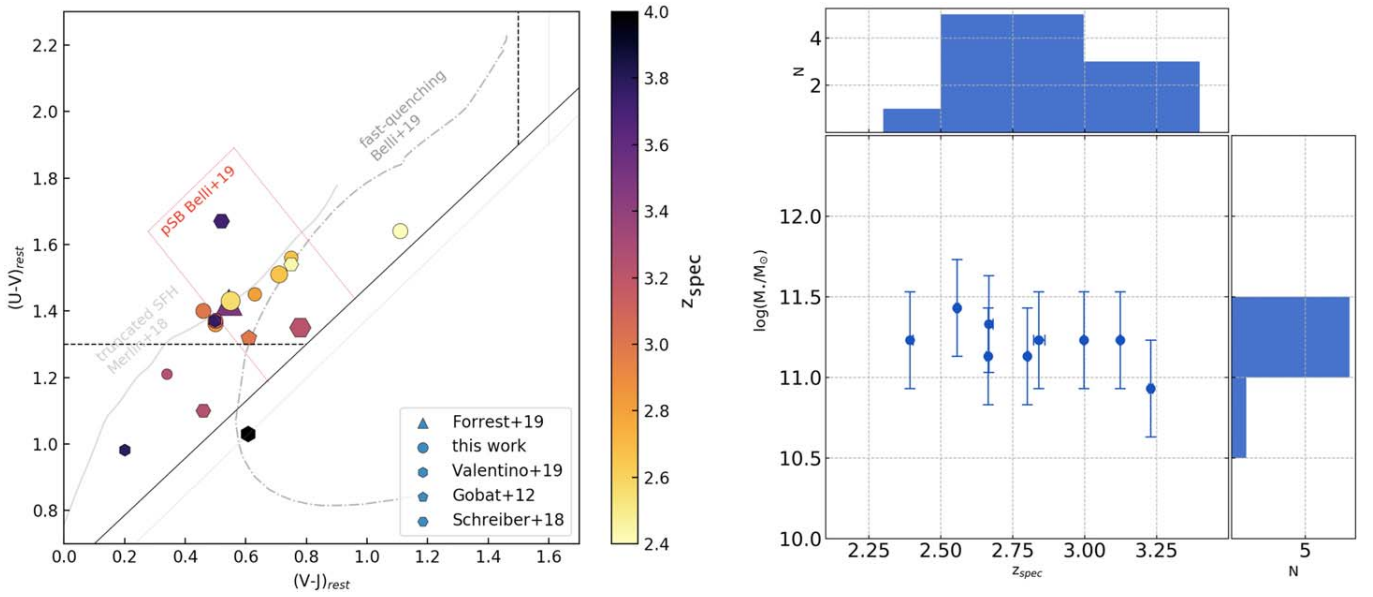


Figure 3. Left: UVJ colors of high-redshift ($z > 2.5$) quiescent galaxies color coded for their spectroscopic redshift. Solid and dotted–dashed tracks show the color evolution for fast-evolving SFHs, from Merlin et al. (2018) and Belli et al. (2019), respectively. The red box shows the post-starburst region as defined in Belli et al. (2019). Marker sizes are proportional to stellar mass. Right: stellar mass and redshift distributions of the sample.

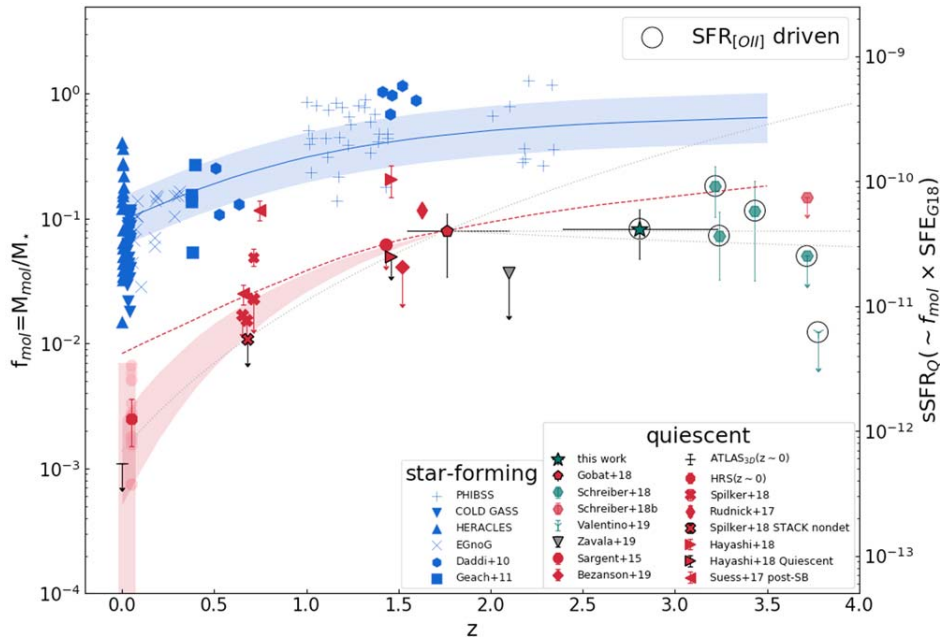


Figure 4. Evolution of f_{mol} or, equivalently (see Section 5), the $sSFR$ of quiescent galaxies ($sSFR_Q$) with redshift, adapted from Gobat et al. (2018). Red symbols mark quiescent galaxies, old and post-starbursts, with CO or dust-continuum measures, whereas circled green symbols mark estimates from $SFR_{[O III]}$ alone, converted to f_{mol} adopting G18 SFE. Black contours mark stacked samples, where horizontal error bars show the spread in redshift of individual targets. Blue symbols mark the gas fraction of low-, intermediate-, and high- z ($z > 1$) MS galaxies. The blue curve and shaded area mark the evolution of an average $5 \times 10^{10} M_\odot$ MS galaxy and its 0.2 dex scatter (Sargent et al. 2014). The red dotted curve shows the same relation, offset by a factor of 6 and for a stellar mass of $\log(M^*(z) + \Delta M)$, where ΔM is the offset between the median mass of G18 sample and the M^* of the passive stellar mass function at $\langle z \rangle \sim 1.8$. The pink shaded area shows the trend derived in G18. Gray lines are extrapolations of the low-redshift trend assuming a gas fraction rise as $(1 + z)^\alpha$, with $\alpha \sim 4-5$, as fast as in G18; $\alpha = 2.2$ as for MS galaxies; $\alpha = 0$ for no evolution; and $\alpha = -0.5$ representative of a negative evolution.

into $M_{mol} = (1.5 \pm 0.6) \times 10^{10} M_\odot$, hence $f_{mol} \sim 9 \pm 4\%$. We compare it to CO or dust-continuum-based gas fractions and upper limits (converted to Salpeter) for quiescent and post-starburst galaxies: Davis et al. (2014) and Saintonge et al. (2011) for local massive PEGs; Sargent et al. (2015), Bezanson et al. (2019),

Spilker et al. (2018), Zavala et al. (2019), Rudnick et al. (2017), Suess et al. (2017), Spilker et al. (2018), Hayashi et al. (2018), and Gobat et al. (2018) for intermediate- z quiescent galaxies; Schreiber et al. (2018) and Valentino et al. (2020) for $z \sim 3-4$ galaxies. Despite the uncertainties, our data at $z \sim 3$ seem to disfavor the

steep $(1+z)^{4-5}$ trend inferred from $z = 0$ to 1.5–2, suggesting a flattening in the M_{mol}/M_* evolution (or, equivalently, of the sSFR).

The published $\text{SFR}_{[\text{O II}]}$ for $z > 3$ galaxies with a clear spectral break in Schreiber et al. (2018) and Valentino et al. (2020) also seem to support this trend.

Our data thus suggest that a substantial fraction of the massive quiescent population at $z \sim 3$ is approaching the quenching epoch, becoming intrinsically young and with spectra of post-starburst galaxies, but with a more or less constant f_{mol} (or, equivalently, sSFR) over $1.5 < z < 3-4$. Various processes could be simultaneously acting: cosmological cold flows, AGN feedback, dust grain growth in the interstellar medium, satellite accretion or dust destruction by sputtering with a hot X-ray halo. It is beyond the scope of this Letter to investigate this further.

One could wonder if highly obscured star formation could be present and go unrecognized, given that their post-starburst nature might suggest that a highly obscured starburst might have been previously present. Stacking at 3 GHz (excluding two clear radio AGN detections at $S_{3\text{ GHz}} = 0.58 \pm 0.03$ mJy and 14 ± 4 μ Jy) results in a 3σ signal with $S_{3\text{ GHz}} = 2.72 \pm 0.93$ μ Jy, which translates into a rest-frame $L(1.4\text{ GHz}) \sim 2 \times 10^{23}$ W Hz⁻¹, 4 times higher than in Gobat et al. (2018). This is probably just suggesting a higher radio AGN activity at fixed stellar mass closer to the quenching epoch, continuing the rapid evolution seen from $z = 0$ to 1.5–2. On the other hand, such a detection would also be formally consistent with 40–50 $M_{\odot} \text{ yr}^{-1}$ of obscured star formation (assuming the IR–radio correlation at $z = 3$; Delhaize et al. 2017). This would still place the typical object 8 times below the MS. While we tend to interpret strong Balmer absorption lines plus weak [O II] emission as a sign of post-starburst galaxies with residual unobscured star formation, we cannot fully rule out stronger obscured star formation, which could be analogous to what seen locally for $e(a)$ galaxies (Poggianti & Wu 2000). Only future Atacama Large Millimeter/submillimeter Array observations of several of these targets could conclusively solve this issue.

We thank the anonymous referee for their constructive report and Gabriel Brammer for his help with `grizli`. A.C. acknowledges grants PRIN MIUR 2015, PRIN 2017 (20173ML3WW_001), and ASI n.I/023/12/0. S.J. acknowledges MICIU grant AYA2017-84061-P, co-financed by FEDER. I.D. is supported by Marie Skłodowska-Curie grant agreement No. 788679.

ORCID iDs

C. D'Eugenio  <https://orcid.org/0000-0001-7344-3126>
 E. Daddi  <https://orcid.org/0000-0002-3331-9590>
 R. Gobat  <https://orcid.org/0000-0003-0121-6113>
 V. Strazzullo  <https://orcid.org/0000-0001-7975-2894>
 P. Lustig  <https://orcid.org/0000-0002-7241-8866>

I. Delvecchio  <https://orcid.org/0000-0001-8706-2252>
 S. Jin  <https://orcid.org/0000-0002-8412-7951>
 A. Puglisi  <https://orcid.org/0000-0001-9369-1805>
 A. Calabró  <https://orcid.org/0000-0003-2536-1614>
 C. Mancini  <https://orcid.org/0000-0002-4297-0561>
 M. Dickinson  <https://orcid.org/0000-0001-5414-5131>
 A. Cimatti  <https://orcid.org/0000-0002-4409-5633>
 M. Onodera  <https://orcid.org/0000-0003-3228-7264>

References

- Balogh, M. L., Morris, S. L., Yee, H. K. C., et al. 1999, *ApJ*, 527, 54
 Behroozi, P. S., Conroy, C., & Wechsler, R. H. 2010, *ApJ*, 717, 379
 Belli, S., Newman, A. B., & Ellis, R. S. 2019, *ApJ*, 874, 17
 Bezanson, R., Spilker, J., Williams, C. C., et al. 2019, *ApJL*, 873, L19
 Brammer, G. 2018, `gbrammer/grizli`: Preliminary Release, Zenodo, doi:10.5281/ZENODO.1146904
 Bruzual, G., & Charlot, S. 2003, *MNRAS*, 344, 1000
 Calzetti, D., Armus, L., Bohlin, R. C., et al. 2000, *ApJ*, 533, 682
 Cimatti, A., Daddi, E., Renzini, A., et al. 2004, *Natur*, 430, 184
 Daddi, E., Cimatti, A., Renzini, A., et al. 2004, *ApJ*, 617, 746
 Davidzon, I., Ilbert, O., Laigle, C., et al. 2017, *A&A*, 605, A70
 Davis, T. A., Young, L. M., Crocker, A. F., et al. 2014, *MNRAS*, 444, 3427
 Dekel, A., & Birnboim, Y. 2006, *MNRAS*, 368, 2
 Delhaize, J., Smolčić, V., Delvecchio, I., et al. 2017, *A&A*, 602, A4
 Forrest, B., Annunziatella, M., Wilson, G., et al. 2020, *ApJL*, 890, L1
 French, K. D., Yang, Y., Zabludoff, A., et al. 2015, *ApJ*, 801, 1
 Glazebrook, K., Schreiber, C., Labbé, I., et al. 2017, *Natur*, 544, 71
 Gobat, R., Daddi, E., Magdis, G., et al. 2018, *NatAs*, 2, 239
 Gobat, R., Daddi, E., Strazzullo, V., et al. 2017, *A&A*, 599, A95
 Gobat, R., Strazzullo, V., Daddi, E., et al. 2012, *ApJL*, 759, L44
 Hayashi, M., Tadaki, K.-ichi, Kodama, T., et al. 2018, *ApJ*, 856, 118
 Horne, K. 1986, *PASP*, 98, 609
 Kashino, D., Silverman, J. D., Rodighiero, G., et al. 2013, *ApJL*, 777, L8
 Kennicutt, R. C. 1998, *ARAA*, 36, 189
 Kriek, M., van Dokkum, P. G., Franx, M., et al. 2006, *ApJ*, 645, 44
 Laigle, C., McCracken, H. J., Ilbert, O., et al. 2016, *ApJ*, 224, 24
 Man, A., & Belli, S. 2018, *NatAs*, 2, 695
 Mancini, C., Daddi, E., Juneau, S., et al. 2019, *MNRAS*, 489, 1265
 Maraston, C., Nieves Colmenáez, L., Bender, R., et al. 2009, *A&A*, 493, 425
 McCracken, H. J., Capak, P., Salvato, M., et al. 2010, *ApJ*, 708, 202
 Merlin, A., Fontana, A., Castellano, M., et al. 2018, *MNRAS*, 473, 2098
 Muzzin, A., Marchesini, D., Stefanon, M., et al. 2013, *ApJ*, 777, 18
 Onodera, M., Renzini, A., Carollo, M., et al. 2012, *ApJ*, 755, 26
 Poggianti, B. M., & Wu, H. 2000, *ApJ*, 529, 157
 Rodríguez-Merino, L. H., Chavez, M., Bertone, E., et al. 2005, *ApJ*, 626, 411
 Rudnick, G., Hodge, J., Walter, F., et al. 2017, *ApJ*, 849, 27
 Saintonge, A., Kauffmann, G., Kramer, C., et al. 2011, *MNRAS*, 415, 32
 Sargent, M. T., Daddi, E., Béthermin, M., et al. 2014, *ApJ*, 793, 19
 Sargent, M. T., Daddi, E., Bournaud, F., et al. 2015, *ApJL*, 806, L20
 Schreiber, C., Glazebrook, K., Nanayakkara, T., et al. 2018, *A&A*, 618, A85
 Schreiber, C., Pannella, M., Elbaz, D., et al. 2015, *A&A*, 575, A74
 Sell, P. H., Tremonti, C. A., Hickox, R. C., et al. 2014, *MNRAS*, 441, 3417
 Spilker, J., Bezanson, R., Barišić, I., et al. 2018, *ApJ*, 860, 103
 Straatman, C. M. S., Labbé, I., Spitler, L. R., et al. 2014, *ApJL*, 783, L14
 Strazzullo, V., Daddi, E., Gobat, R., et al. 2015, *A&A*, 576, L6
 Suess, K. A., Bezanson, R., Spilker, J. S., et al. 2017, *ApJL*, 846, L14
 Valentino, F., Tanaka, M., Davidzon, I., et al. 2020, *ApJ*, 889, 93
 Williams, R. J., Quadri, R. F., Franx, M., et al. 2009, *ApJ*, 691, 1879
 Worthey, G., & Ottaviani, D. L. 1997, *ApJ*, 111, 377
 Zavala, J. A., Casey, C. M., Scoville, N., et al. 2019, *ApJ*, 887, 183

HST grism spectroscopy of $z \sim 3$ massive quiescent galaxies

Approaching the metamorphosis

C. D'Eugenio¹, E. Daddi¹, R. Gobat², V. Strazzullo^{3,4,5,6}, P. Lustig⁴, I. Delvecchio^{1,5}, S. Jin^{7,8}, A. Cimatti^{9,10}, and M. Onodera^{11,12}

¹ CEA, Irfu, DAp, AIM, Université Paris-Saclay, Université de Paris, CNRS, F-91191 Gif-sur-Yvette, France

² Instituto de Física, Pontificia Universidad Católica de Valparaíso, Casilla 4059, Valparaíso, Chile

³ Faculty of Physics, Ludwig-Maximilians-Universität, Scheinerstr. 1, 81679 Munich, Germany

⁴ University of Trieste, Piazzale Europa, 1, 34127 Trieste TS, Italy

⁵ INAF - Osservatorio Astronomico di Brera, via Brera 28, I-20121, Milano, Italy & via Bianchi 46, I-23807, Merate, Italy

⁶ INAF - Osservatorio Astronomico di Trieste, via Tiepolo 11, I-34131, Trieste, Italy

⁷ Instituto de Astrofísica de Canarias (IAC), E-38205 La Laguna, Tenerife, Spain

⁸ Universidad de La Laguna, Dpto. Astrofísica, E-38206 La Laguna, Tenerife, Spain

⁹ Università di Bologna, Dipartimento di Fisica e Astronomia, Via Gobetti 93/2, I-40129, Bologna, Italy

¹⁰ INAF - Osservatorio Astrofisico di Arcetri, Largo E. Fermi 5, I-50125, Firenze, Italy

¹¹ Subaru Telescope, National Astronomical Observatory of Japan, National Institutes of Natural Sciences, 650 North A'ohoku Place, Hilo, HI 96720, USA

¹² Department of Astronomical Science, SOKENDAI (The Graduate University for Advanced Studies), 650 North A'ohoku Place, Hilo, HI, 96720, USA

December 4, 2020

ABSTRACT

Tracing the emergence of the massive quiescent galaxy (QG) population requires the build-up of reliable quenched samples, disentangling these systems from red, dusty star-forming sources. We present *Hubble Space Telescope* WFC3/G141 grism spectra of 10 quiescent galaxy candidates selected at $2.5 < z < 3.5$ in the COSMOS field. Spectroscopic confirmation for the whole sample is obtained within 1-3 orbits thanks to the presence of strong spectral breaks and Balmer absorption lines. Combining their spectra with optical to near-infrared (near-IR) photometry, star-forming solutions are formally rejected for the entire sample. Broad spectral indices are consistent with the presence of young A-type stars flagging the last major episode of star formation to have taken place no earlier than ~ 300 -800 Myr prior to observation, confirming clues from their post-starburst UVJ colors. Marginalizing over three different slopes of the dust attenuation curve, we obtain short mass-weighted ages and an average peak star formation rate of $\text{SFR} \sim 10^3 M_{\odot} \text{yr}^{-1}$ at $z_{\text{formation}} \sim 3.5$. Despite mid- and far-IR data being too shallow to determine the obscured SFR on a galaxy-by-galaxy basis, median stack emission from 3GHz data constrains the level of residual obscured SFR to be globally below $50 M_{\odot} \text{yr}^{-1}$, hence three times below the scatter of the coeval main sequence. Alternatively, the very same radio detection suggests a widespread radio-mode feedback by active galactic nuclei (AGN) four times stronger than in $z \sim 1.8$ massive QGs. This is accompanied by a 30% fraction of X-ray luminous AGN with a black hole accretion rate per unit SFR enhanced by a factor of ~ 30 with respect to similarly massive QGs at lower redshift. The average compact, bulge-dominated morphologies, coupled with the young mass-weighted ages, suggest that the mechanisms responsible for structural transformation might be concomitant with (or preceding) the ones causing quenching.

Key words. Quiescent galaxies – Galaxy evolution – Quenching

1. Introduction

The formation channels that lead to the build up of the red sequence of massive, quiescent galaxies (QGs) that we observe in the local universe are still to be fully understood. In the present-day Universe 75% of the total stellar mass budget is locked into spheroids, either spiral bulges or elliptical galaxies. These are several Gyr-old, pressure-supported stellar systems which are unable to host significant amount of star-formation (Renzini 2006). The majority of massive galaxies ($\log(M_{\star}/M_{\odot}) > 10.5$) in the local Universe appear to be quenched, with QGs outnumbering star-forming galaxies by a factor of 10 at $\log(M_{\star}/M_{\odot}) > 11.5$

(Baldry et al. 2004). Fossil records studies have established that the most massive galaxies are the ones where the oldest stellar populations are found, implying an anti-correlation between their stellar mass and the duration of their main star-formation episode (Gallazzi et al. 2005; Thomas et al. 2005; Citro et al. 2016). Such results have then been reinforced by the first identifications of QGs at increasing redshifts (Dunlop et al. 1996; Franx et al. 2003; Cimatti et al. 2004; Daddi et al. 2005) granted by near-infrared (NIR) sensitive detectors which sample the rest-frame optical at $z \geq 1.5$. These advances were essential to show that the assembly and quenching of massive systems took place at $z > 1.5$ with little evolution thereafter of the high-mass end of the luminosity/stellar mass functions, especially compared to the progressive rise of the low-mass end (Fontana et al. 2004;

Send offprint requests to: C. D'Eugenio, e-mail: chiara.deugenio@cea.fr

Cimatti et al. 2006; Arnouts et al. 2007; Drory et al. 2009; Pozzetti et al. 2010; van Dokkum et al. 2014; Gargiulo et al. 2016; Davidzon et al. 2017; Kawinwanichakij et al. 2020). The growth of the lower-mass end of the red sequence can be thought of as the result of the generalized progressive decline of the global star formation rate density through gas consumption, cluster related processes and cosmic starvation affecting the star-forming population mostly at $z < 1.5$ (e.g. Emsellem et al. 2011; Saracco et al. 2011; Carollo et al. 2013; Madau & Dickinson 2014; Sargent et al. 2014; Schreiber et al. 2015; Wild et al. 2016; Maltby et al. 2018; Matharu et al. 2019; Kawinwanichakij et al. 2020). On the other hand, understanding how massive galaxies quenched in an epoch when galaxies were generally gas rich and prodigiously star-forming ($2 < z < 4$, Daddi et al. 2010; Tacconi et al. 2010; Genzel et al. 2010; Madau & Dickinson 2014) is itself non trivial.

Historically, the progressive discovery of populations of massive QGs already in place at high- z (Dunlop et al. 1996; Franx et al. 2003; Cimatti et al. 2004; Daddi et al. 2005; Kriek et al. 2009; Gobat et al. 2012; Glazebrook et al. 2017) posed challenges to hierarchical models of structure formation (e.g. Cimatti et al. 2006; Steinhardt et al. 2016). Hydrodynamical simulations and semi-analytical models (SAM) have struggled to reproduce the comoving number densities of massive, passively evolving galaxies at $z > 2-3$, falling short by roughly an order of magnitude (Wellons et al. 2015; Nelson et al. 2015; Steinhardt et al. 2016; Davé et al. 2016; Cecchi et al. 2019; Schreiber et al. 2018). In recent years, however, confirmations of quiescent galaxies extended up to $z \sim 4$ (Glazebrook et al. 2017; Schreiber et al. 2018; Valentino et al. 2020; Forrest et al. 2020a,b) while cosmological simulations progressively increased in volume, spatial and mass resolution, as well as in improvements of feedback schemes and subgrid physics regulating star formation (Vogelsberger et al. Illustris: 2014a,b; Genel et al. Illustris: 2014; Nelson et al. Illustris: 2015; Pillepich et al. Illustris TNG: 2018; Nelson et al. Illustris TNG: 2019; Schaye et al. EAGLE: 2015; Davé et al. SIMBA: 2019). The most recent estimates of the number density of QGs, either from observational samples or from state-of-the-art cosmological simulations, appear to broadly agree on the number density of quiescent galaxies up to $z \sim 4$ but it is unclear whether a population of passive objects exists as early as $z \sim 5$ in significant numbers (Merlin et al. 2019; Valentino et al. 2020). Additionally, the degree to which such an agreement is robust against systematics, like for example the exact details of sample selection, is not firmly established (Merlin et al. 2019).

Despite the major progress accomplished so far in this field, it remains unclear whether there is a dominant process that causes quenching (Man & Belli 2018). The extreme stellar densities suggested by compact quiescent systems at $z \sim 2$ (Franx et al. 2003; Daddi et al. 2005; van Dokkum et al. 2008; Newman et al. 2012) point at them being remnants of an intense burst of star formation triggered by the rapid collapse of a large amount of gas that occurred at $z > 4$. This could be resulting e.g. from starbursts plunging down into quiescence after dissipative gas-rich mergers (Cimatti et al. 2008; Elbaz et al. 2018; Gómez-Guijarro et al. 2018, 2019; Puglisi et al. 2019) or more “secular-like” evolution through disk instabilities in high-redshift dusty star-forming galaxies, quickly accreting and consuming gas, leaving compact passive remnants (e.g. Dekel et al. (2009); Barro et al. (2013); Toft et al. (2014); Zolotov et al. (2015)). Increased consensus among SAMs and hydrodynamical simulations has been reached when it comes to ascribe the shut down of star formation in massive galaxies to AGN feedback (De Lucia & Blaizot 2007; Henriques et al. 2017; Girelli et al. 2020). Major mergers or vio-

lent disk instabilities can compress the gas into massive compact cores and trigger starburst events which rapidly consume the gas of the system (Dekel & Silk 1986; Murray et al. 2005). Quasar activity is ignited by these processes, launching powerful outflows into the CGM and depleting the host galaxy from its reservoirs (Sanders et al. 1988; Di Matteo et al. 2005; Hopkins et al. 2006; McCarthy et al. 2011). However, AGN feedback is not the only process that can halt or reduce star formation in high- z galaxies. Cosmological starvation (Feldmann & Mayer 2015) and/or the development of a stable virial shock in sufficiently massive haloes (Dekel & Birnboim 2006; Cattaneo et al. 2006) could play a role, followed by maintenance processes such as radio-mode feedback from radiatively inefficient accretion onto a SMBH (Best et al. 2005; Croton et al. 2006), gravitational heating of the diffuse medium from infalling satellites (Dekel & Birnboim 2006; Khochfar & Ostriker 2008; Johansson et al. 2009, 2012) or morphological quenching (Martig et al. 2009). Therefore the detailed study of large, statistically relevant samples of massive quiescent galaxies is crucial to discern among these mechanisms. Robust samples of quiescent galaxies however are challenging to build up: the spectra necessary to reject low redshift interlopers or star forming contaminants become increasingly more difficult to obtain at $z > 1.4$ since it requires either long integrations in 8-10m class ground-based telescopes or space-based observations. Moreover, the rapid drop in number density of massive quenched objects at $z > 1.5$ requires large areas covered by deep observations. On a positive note, on the other hand, one can leverage the boundedness of the age of the Universe to investigate the demographics of the quiescent population across cosmic time as it keeps emerging. In fact, as the population becomes younger and younger at increasing redshift, the discerning power of rest-frame optical spectra at mapping the early star formation of massive QGs surpasses the one at low redshift. This is because around $z \gtrsim 2$ the Universe starts to be young enough to make stellar age differences of ~ 1 Gyr, down to few hundred Myr, visible thanks to the rapid appearance of Balmer absorption lines in stellar populations of ages < 1 Gyr, when A-type stars enter the Turn-Off (therefore increasingly dominating the integrated stellar spectra). Relatively large samples of QGs have been constructed up to $z \sim 2.5$ in COSMOS and the CANDELS fields exploiting large telescopes (e.g. Bezanson et al. (2013); Belli et al. (2015); Onodera et al. (2015); Belli et al. (2019); Kriek et al. (2016); Stockmann et al. (2020)) or HST in combination with strong lensing (Whitaker et al. 2012, 2013; Newman et al. 2018). These studies have been tracing the progressive youngening of $\log(M_*/M_\odot) > 11$ QGs with look-back time, revealing an increasing spread in stellar age and dust extinction with bulk values around 1–2 Gyr and $A_V = 0-1.0$ mag at $z \sim 2$, respectively. This is apparently happening while keeping high metallicities and velocity dispersions ($\sigma = 300-500$ km s^{-1}), consistent with local scaling relations (Toft et al. 2012; Onodera et al. 2012; van de Sande et al. 2013; Belli et al. 2015; Kriek et al. 2016; Belli et al. 2017; Estrada-Carpenter et al. 2019, 2020; Stockmann et al. 2020). The progressive appearance of the quenched population can be therefore quantified through the relative fraction of young versus old systems once an age threshold is defined (e.g. age > 1 Gyr, Whitaker et al. 2013). At even higher redshifts, the color selections generally applied to photometric samples already point at a substantial migration of QGs towards bluer colors (Whitaker et al. 2011; Muzzin et al. 2013), accompanied by the drop by roughly one order of magnitude of their number densities (Straatman et al. 2014; Davidzon et al. 2017). Spectroscopic follow-ups have the advantage of refining such picture by testing the colors of selected galaxies against

photometric errors, star forming interlopers or AGN interfering with their spectral energy distribution (SED). Here we present one of the largest samples of spectroscopically confirmed QGs at $2.4 < z < 3.3$ obtained with HST dedicated observations. In section 2 we describe the sample selection. In section 3 we give details on the observational strategy and data reduction. In section 4 we present the spectral analysis and the spectroscopic confirmation of our targets. Section 5 presents their formal classification, the impact of adding COSMOS2015 photometry with or without calibration of zero-points, as well as the use of marginalizing over multiple attenuation laws. In section 7 we constrain their recent star formation history (SFH) comparing the relative strength of the Balmer and 4000Å breaks. In section 8 we investigate the incidence of AGN in our sample. In section 9 we discuss our results in the context of the current literature. Finally, in section 10 we summarize our results and conclusions. We assume a Λ CDM cosmology with $H_0 = 70 \text{ km s}^{-1} \text{ Mpc}^{-1}$, $\Omega_M = 0.27$, $\Omega_\Lambda = 0.73$ and a Salpeter (1955) Initial Mass Function (IMF) unless otherwise specified. Magnitudes are given in the AB photometric system.

2. Sample selection

Given the expected low number density of high- z massive quiescent galaxies, large fields with deep photometric coverage are required for identification and robust assessment of their SEDs. For this reason, we identified a parent sample of more than 50 reliable passively evolving candidates in the 2deg^2 COSMOS field. Sources with $K_{tot} < 22.5$ were extracted from the McCracken et al. (2010) catalog, limiting the selection to those satisfying the observed-frame BzK color criterion for passive systems (Daddi et al. 2004). Targets formally classified as star-forming BzK with signal-to-noise ratio $S/N < 5$ in the B and z bands were retained, as these photometric candidates are degenerate with quiescent galaxies becoming fainter in such bands with increasing redshift and decreasing mass. Photometric redshifts specifically calibrated for high- z QGs were derived with EAZY (Brammer et al. 2008) as in Onodera et al. (2012) and Strazzullo et al. (2015), adopting the sample of 34 spectroscopically confirmed passive galaxies at $1.3 < z_{spec} < 2.1$ observed with VLT/VIMOS which later appeared in Gobat et al. (2017) and the sample of 18 passive galaxies at $1.4 < z_{spec} < 1.9$ of Onodera et al. (2012) observed with Subaru/MOIRCS as calibration samples. Such calibrated z_{phot} were used to select galaxies within $2.5 \leq z_{phot} \leq 3.5$ and to remove objects with UVJ rest-frame colors inconsistent with passive evolution (Pozzetti & Mannucci 2000; Labbé et al. 2005; Williams et al. 2009). SED fitting was performed using FAST (Kriek et al. 2009) allowing for constant and delayed exponentially declining SFHs. Optical dust attenuation was left free to vary up to $A_V = 5$ mag assuming a Calzetti et al. (2000) attenuation law. Fits were repeated adopting purely quiescent templates only. All sources with optical-NIR broadband photometry consistent with star-forming solutions were rejected. Contamination from dusty star-forming galaxies was further minimized removing objects with Spitzer/MIPS $24\mu\text{m}$ $S/N \geq 4$ detections in Le Floch et al. (2009) catalog, except for galaxies with high-confidence passive SEDs, indicative of mid-IR emission caused by a central dusty AGN torus. Among the most massive bona fide passive candidates, 10 galaxies were targeted for HST WFC3/IR G141 near-IR¹ observations: 9 with $H_{AB} < 22$ ($M_\star > 1.1 \times 10^{11} M_\odot$) plus 1 robust candidate with $H_{AB} = 22.9$ ($M_\star = 8 \times 10^{10} M_\odot$) as the highest- z candidate.

3. HST WFC3 F160W imaging and G141 grism spectroscopy

Ground-based observations have already confirmed the existence of quiescent galaxies at $z \sim 4$ (Schreiber et al. 2018; Valentino et al. 2020; Forrest et al. 2020a,b). However, in the framework of high- z galaxy evolution, their statistical power is mostly modulated by the time-expensiveness of such campaigns. Also, OH sky emission lines and related background notoriously affect the quality of the spectra, sometimes effectively cutting them in correspondence of spectral regions crucial to estimate stellar ages. Space-based observations, instead, ensure extended and continuous spectral coverage. In our specific case, HST WFC3 G141 slitless spectrograph has a spectral coverage from 1.1 to $1.7 \mu\text{m}$ reaching maximum transmission at $1.45 \mu\text{m}$. This allows access to the Balmer/4000 Å break region for all sources lying in our selected redshift range. In addition, relatively good mean $S/N \sim 15$ over 100 \AA at $1.6 \mu\text{m}$ is reached with a relatively low number of orbits for sources brighter than $H_{AB} < 22$. These two aspects allow the build up of statistically relevant samples of spectroscopically confirmed $z \sim 3$ quiescent galaxies in a relatively fast way. The G141 dispersion in the first spectral order is $46.5 \text{ \AA pixel}^{-1}$ and $R \sim 130$ for unresolved sources and/or compact objects like those considered in this paper. For resolved sources, the spectral resolution is determined by their morphology, namely their size along the dispersion axis. For these reasons, the selected sources were targeted for HST WFC3 observations including imaging and grism spectroscopy. As this paper focuses mostly on the spectroscopic analysis, we refer to Lustig et al. (2020) for a thorough analysis of their morphology.

3.1. Observing strategy

Observations for program GO 15229 took place from January 11th 2018 to December 2nd 2018. Each pointing was observed from 1 to 3 orbits according to each target H_{AB} magnitude, for a total of 17 orbits (see Table 1). For each target the first orbit was split into a direct F160W exposure (for a total of 984 s) and a grism G141 exposure (for a total of 1498 s) adopting the WFC3-IR-DITHER-LINE-3PT dither pattern. For targets with 2 orbits, the second orbit was also split in two, with total exposure 73 s in F160W and 2496 s in G141 adopting WFC3-IR-DITHER-BLOB dither pattern. The third orbit for ID 4 was a repetition of the second one. The ORIENT was carefully chosen for each target in order to avoid any contamination from neighboring sources.

3.2. Data reduction

The data reduction of direct F160W and grism G141 exposures was performed adopting the pipeline *grizli*, version number *0.7.0-34-g91c9412*². After relative alignment between each direct and grism exposures, absolute astrometric registration was performed providing the pipeline with COSMOS ACS I-band reference catalogs of RA/DEC positions of sources brighter than $I_{AB} < 27$ mag within a radius of $5'$ from each target. Grism sky background subtraction is performed by *grizli* by means of the Master sky images from Brammer et al. (2015) applying a grey correction using the F160W flat-field for the G141 grism. Their residuals are generally of the order of 0.5-1% of the overall background level and are further subtracted removing the column-average of the sky pixels in the grism exposures. During this

¹ Rest-frame near-UV/optical.

² <https://github.com/gbrammer/grizli>

Table 1: Coordinates and orbit details for the targeted galaxies.

ID	ID _{Laigle}	RA	DEC	N _{orbits}	total int. time (s)	
					F160W	G141
1	135730	10:01:39.9790	+01:29:34.49	1	983.8	1497.7
2	137182	10:00:57.3452	+01:29:39.46	1	983.8	1497.7
3	252568	09:57:48.5727	+01:39:57.82	2	1056.7	3993.9
4	361413	10:02:09.9700	+01:50:24.30	3	1129.7	6490.1
5	447058	09:59:11.7700	+01:58:32.96	2	1056.7	3993.9
6	478302	09:59:1.3123	+02:01:34.15	2	1056.7	3993.9
7	503898	10:01:31.8594	+02:03:58.79	1	983.8	1497.7
8	575436	10:00:43.7668	+02:10:28.71	2	1056.7	3993.9
9	707962	09:59:32.5170	+02:22:21.99	1	983.8	1497.7
10	977680	10:00:12.6549	+02:47:23.47	2	1056.7	3993.9

phase the pipeline also runs Astrodrizzle to reject cosmic rays, persistence and other artifacts. The final drizzling parameters were kept as default. A segmentation map is produced out of the drizzled and combined direct exposure. This is later used to identify and model the spectral trace of each object on each of the grism exposures and to generate model contaminants to be subtracted from the target’s cutout. The reduced and decontaminated 2D spectra of our targets are presented in Fig. 1 together with their relative F160W cutouts. At this stage, the detector’s FOV is parsed and modelled assuming simple linear continua for all objects in the field (brighter than 25 mag). Grizli then refines the modelling of the brightest objects ([16, 24] mag) with a second order polynomial fit, fitting spectra directly after subtracting off the model for contaminants. The 1D spectra were eventually optimally extracted propagating the background coefficients into the beam dimensions in order to remove any further background residuals. The final adopted scale of the extracted 1D spectra is 0.8 in units of the native dispersion of the G141 spectrograph. The field of view (FOV) of the WFC3-IR channel is 136" x 123", effectively enabling the search for serendipitous spectral breaks. Several of them were found in our grism exposures and will be addressed in a future work.

4. Spectroscopic confirmation

In the following sections we give a detailed description of the method used to measure the redshifts, as well as the criteria adopted to establish the nature of our sources. In brief, we first fitted the spectra alone to extract z_{spec} and check the quality of the z_{phot} calibration. Secondly, we added COSMOS2015 photometry from Laigle et al. (2016) to the analysis adopting the newly derived z_{spec} for SED fitting. We tested the performance of the combined fits when dropping the Zero Points (ZP) corrections proposed in Laigle et al. (2016) and when using different dust attenuation laws. Once the best configuration was identified, we tested the quiescence of individual targets on the basis of their rest-frame UV-to-NIR emission. As dust-obscured star formation manifests itself in emission at longer wavelengths, we searched for further constraints from the mid-infrared (MIR), far-infrared (FIR) and radio emission. Lastly, using the combined information from both spectroscopy and photometry, we characterized our targets in terms of mass-weighted age and dust extinction. We attempted also a direct estimation of the relative light-weighted strength of the Balmer and 4000 Å breaks, so as

to check the post-starburst nature of individual sources suggested by their UVJ colors, despite lacking high spectral resolution.

4.1. Fitting setup

The optimally-extracted spectra were fitted with a custom IDL routine that compares the 1D spectra with composite stellar population templates by χ^2 -minimization. Such templates were generated on the fly by combining a grid of Bruzual & Charlot (2003) (hereafter BC03) simple stellar population (SSP) models with a set of parametric SFHs: a constant, an exponentially declining, a delayed exponentially declining and truncated SFH. In the latter, the initial SFR drops to zero after a cutoff time τ_{tr} from the onset of star formation. In standard τ -models however, τ is the e-folding timescale of the SFH. The ratios of t/τ and t/τ_{tr} , when above unity, approximate the description of an SSP. Due to an apparent systematic excessive broadening when adopting the imaging cutouts to estimate the line spread function, the adopted templates were smoothed to the G141 resolution adopting a FWHM computed fitting the stacked absorption lines of each galaxy with the IRAF task *splot*, resulting in relatively good agreement after visual inspection. The variety in SFHs was chosen in order to allow for both passive and dusty star-forming solutions. The routine fits the observed spectra simultaneously with a set of emission lines complexes using standard line ratios (Anders & Fritze-v. Alvensleben 2003) and the SFR– $H\alpha$ calibration of Kennicutt 1998 where the SFR is taken from the model grid (see Gobat et al. 2012 for further details). In Table 2 we list the grid of parameters used for the fit. For redshift identification, the Calzetti et al. (2000) attenuation law was adopted and the stellar metallicity was left free to vary from 0.4 Z_{\odot} to 2.5 Z_{\odot} . The age of templates was constrained to be lower than the age of the Universe at a limiting redshift as described in the following: in order to reduce the computational cost, we fitted the observed spectra through a first pass done from $z=0.01$ to $z=5.0$ with a low resolution redshift grid ($dz=0.01$). The probability of a given redshift was computed comparing the χ^2 difference between the best fitting solution and all other solutions following Avni (1976) to determine the 1σ confidence range. Once the most probable peaks were identified, we narrowed down the redshift grid around the 1σ peaks, allowing for an interval of $\Delta z \sim 0.2$ spanned at $dz=0.001$. This time we limited the template library to the age of the Universe at the lowest most probable redshift. This approach led to the redshift probability distributions showed in the upper panels of Fig. 2.

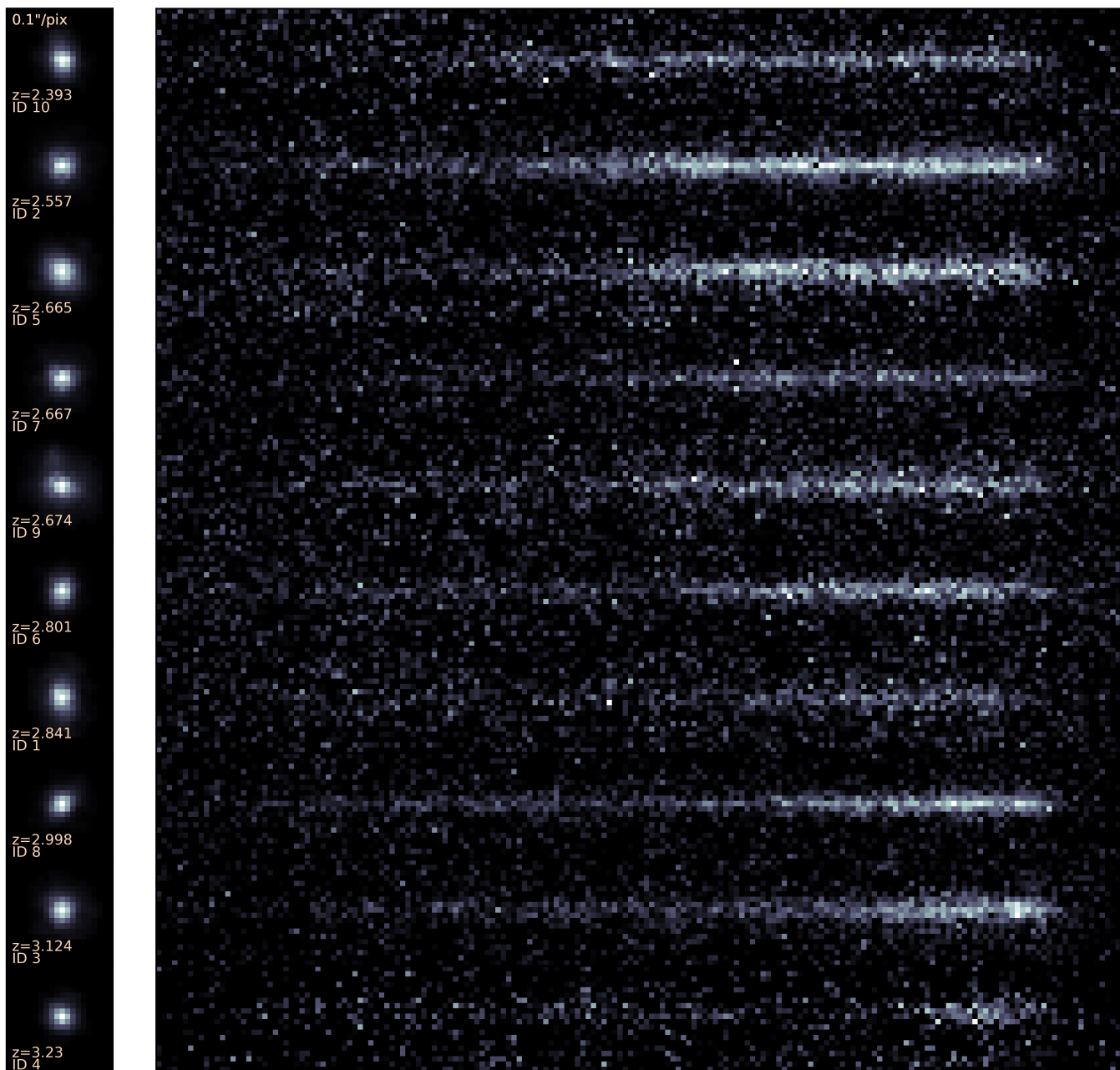


Fig. 1: F160W imaging cutouts (left) and 2D G141 spectra (right) at the native WFC3 pixel scale. Redshift increases from top to bottom. The color scale is in linear scale.

4.2. Redshift identification

Seven of our sources showed unambiguous redshift solutions at a 3σ confidence already during the low resolution pass ($dz=0.01$). Two show a secondary peak within the same confidence level and one (ID 7) lacks a marked spectral break. Nine galaxies out of ten are consistent with single solutions at 1σ . Despite the low resolution of G141 spectroscopy, redshift identification is made possible thanks to the presence of prominent spectral breaks and strong absorption lines for most of the targets (see Fig. 2). For the highest redshift sources, namely ID 3, 4 and 8, MgI and MgII 2640 – 2850 Å absorption lines also enter the spectrograph, albeit with relatively low S/N. Notably, ID 7 lacks absorption features as strong as for the rest of the sample.

This makes the spectrum formally consistent with multiple redshift solutions ($0.4 < z < 3.5$) within 1σ confidence. We checked the consistency of the lowest redshift solutions with the available COSMOS2015 photometry placing $z > 1.5$ as a lower-limit, confirmed by its SED which rises in flux from J to H band. The final spectroscopic confirmation of this source was obtained performing the combined fit of its photometry and grism spectrum across the $1 < z < 3.5$ redshift range at high-resolution ($dz=0.001$). This test confirms the previously derived best fit solution and reduces the error bars on z_{spec} at all confidence levels. At 1σ it yields $z = 2.674^{+0.005}_{-0.009}$, whereas at 3σ it yields $z = 2.674^{+0.021}_{-0.026}$ showing the stability of the best fit solution compared to the information derived from spectroscopy only (see Fig. 2). In the rest of the analysis we will refer to the

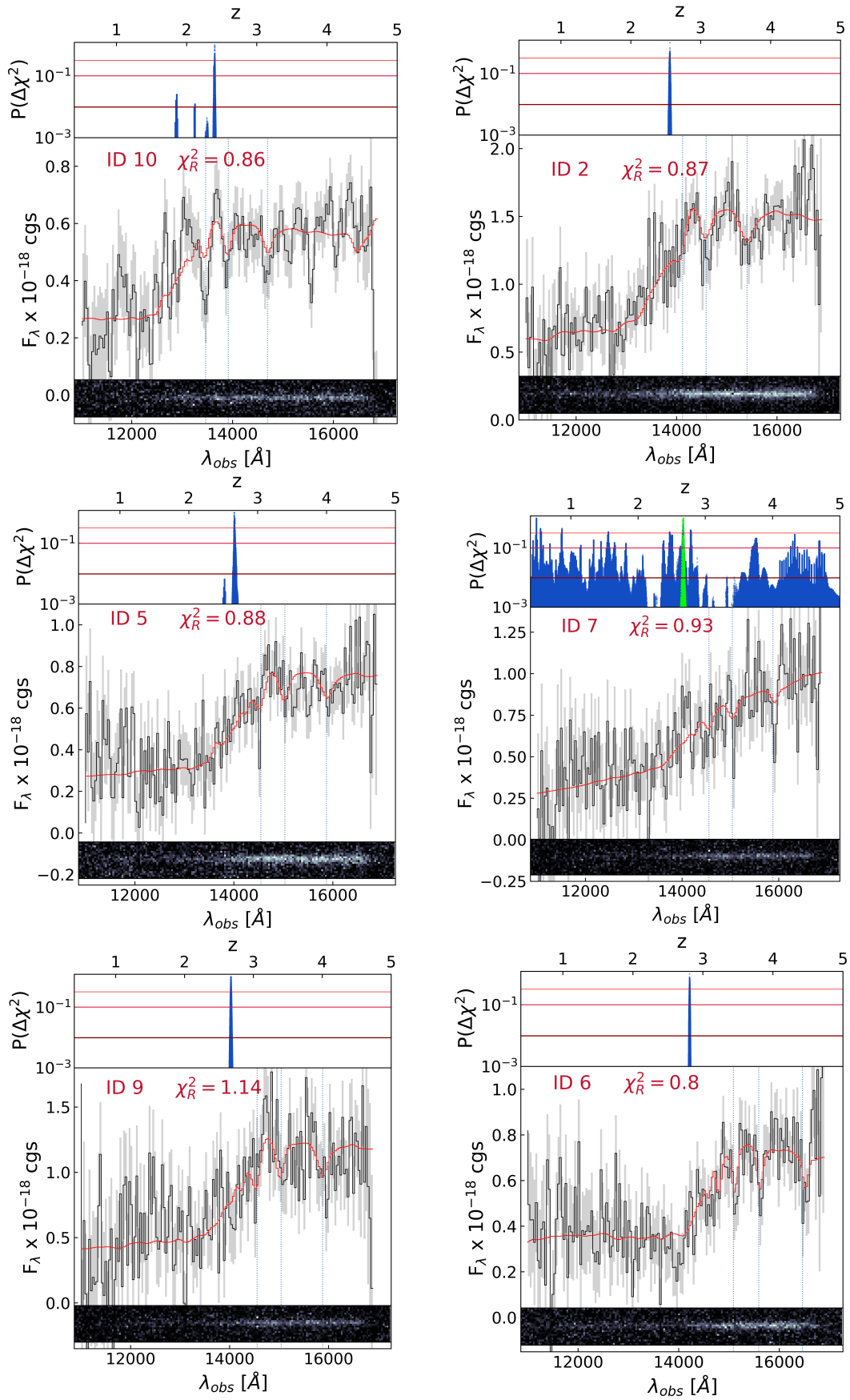


Fig. 2: Upper panels: redshift probability distribution for each target. Solid lines from light- to dark-red mark 1-, 2-, 3- σ confidence levels respectively. Green points for ID7 mark the redshift solutions obtained combining spectroscopy and photometry as described in Sect. 4.2. Middle panels: optimally extracted 1D grism spectra (black) and best-fitting solutions (red) of our targets. The noise vector is showed in grey in each panel. Bottom panels: corresponding 2D G141 spectra. The color scale is in linear scale. Galaxies are shown in order of increasing redshift.

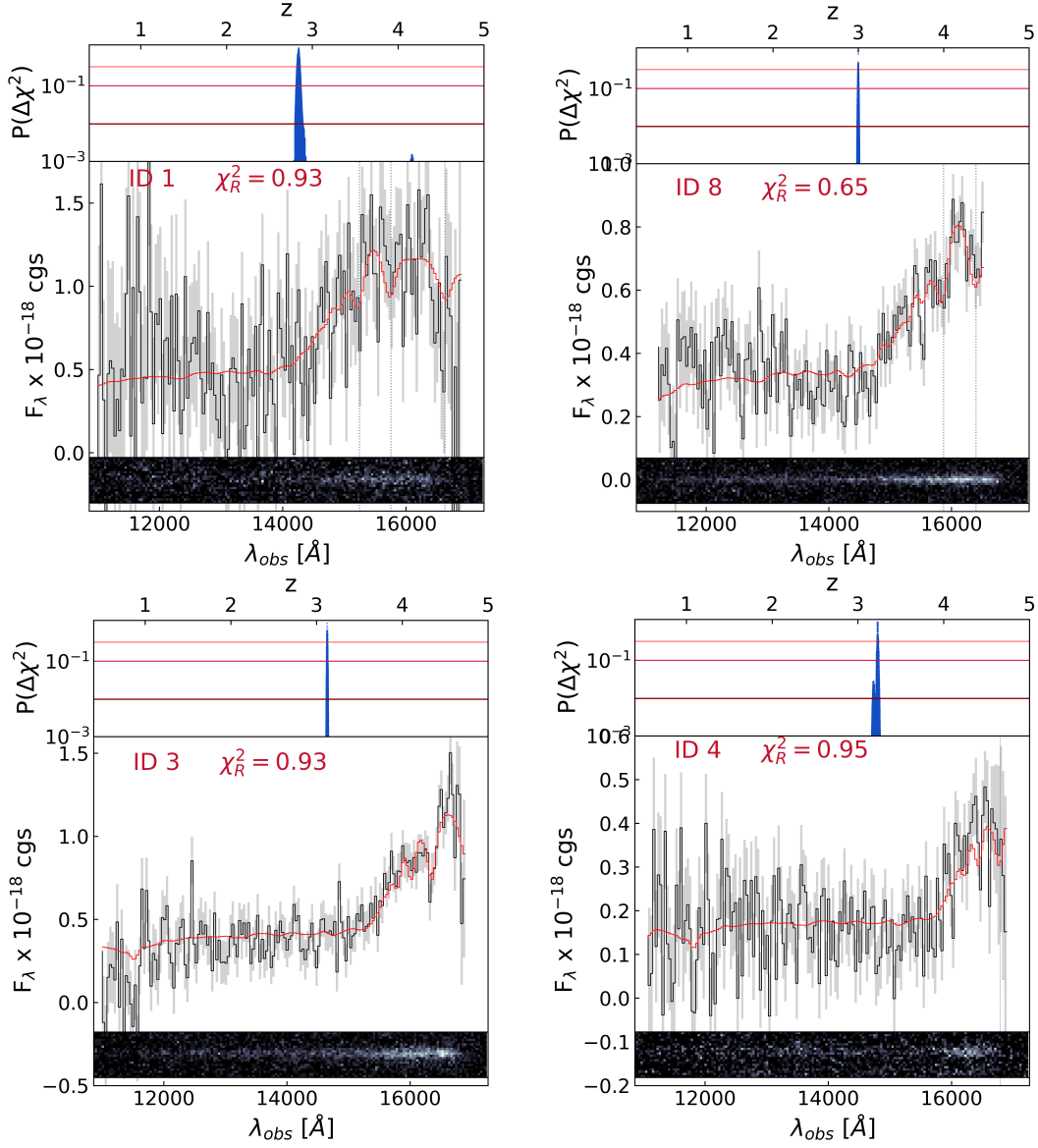


Fig. 2: Continued

Table 2: Grid of parameters used for the spectral fit and the optical-to-NIR SED modeling.

parameter [units]	min	max	step
z	0.01	5	0.01 (then 0.001)
age [Gyr]	0.1	$\text{age}_H(z)$	0.1
τ [Gyr]	0.001	1	0.1
A_V [mag]	0	8	0.1
Z/Z_\odot		0.4, 1, 2.5	
δ attenuation curve (Noll et al. 2009)		-0.7, -0.4, 0 (Calzetti)	
IMF		Salpeter 1955	
Stellar population templates		Bruzual & Charlot 2003	

former confidence level as done for the rest of the sources.

ID 10 shows excess flux at 11870 \AA . The secondary peak in the redshift probability distribution is placed at $z=2.3$, where the fitting routine is attempting at reproducing the two most promi-

nent absorption lines with H δ and H γ instead of H ϵ and H δ favored by the best fitting template. This redshift is not low enough to explain the excess flux with a [OII] $\lambda 3727$ emission line. Such line would have to be placed at $z=2.18$ yet it would not match with any of the absorption features present in the spectrum. We therefore interpret it as a spurious noise-driven feature.

4.3. Performance of photometric redshifts

We compared the resulting z_{spec} with the calibrated photometric redshifts used for the sample selection to assess the quality of the latter (Fig. 3). The quoted normalized median absolute deviation of the adopted photo- z ³ was $\sigma_{\text{NMAD}} = 0.025$ estimated on the spectroscopically confirmed sample at $z \sim 1.5$, reducing to 0.018 once galaxies with less reliable z_{spec} were excluded. As clarified in Strazzullo et al. 2015, the accuracy is maximum for bright objects (such as those used for spectroscopic confirmation) and decreases for fainter ones (either less massive sources or at higher z). In order to take this into account, in Fig. 3 we show the er-

³ $\sigma_{\text{NMAD}} = 1.48 \cdot \text{median}(|z_{\text{phot}} - z_{\text{spec}}| / (1 + z_{\text{spec}}))$, Hoaglin et al. 1983

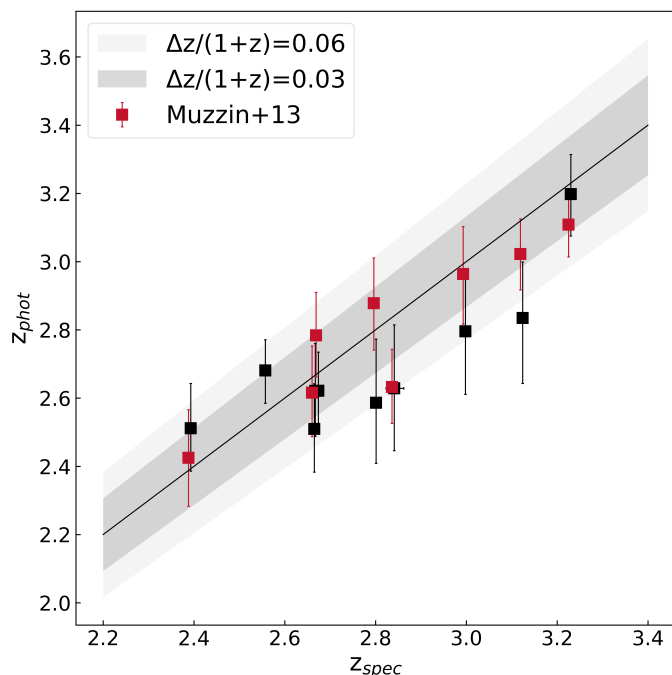


Fig. 3: Comparison between calibrated z_{phot} s and spectroscopic redshifts. Black squares mark the original calibrated z_{phot} s used for the selection. Red squares mark z_{phot} s from Muzzin et al. 2013. The black solid line and relative shaded area mark the 1:1 relation and the nominal dispersions between the original calibrated z_{phot} s and the newly derived z_{spec} (see text). Redshifts from Muzzin et al. 2013 have been shifted horizontally by -0.005 for clarity.

ror bars computed using the z_{phot} accuracy estimated by the authors for faint objects, as a function of the K band magnitude in McCracken et al. 2010. For objects between $K=[20.8, 22]$ - such as in our case - the expected uncertainty is $\sim 0.040(1+z)$. The z_{phot} used for the selection of our sample largely agree with the z_{spec} derived here, with a small systematic underestimation of 0.04%. We included the performance of photometric redshifts from Muzzin et al. 2013 as well. Note that ID 1 and ID 2 are outside the UltraVISTA area and therefore not present in this latter catalog. The nominal σ_{NMAD} we derived here by comparison with our spectroscopic sample are 0.057 and 0.033 respectively for the two catalogs. Applying the same calibration to the Muzzin et al. 2013 photometry at $z \sim 1.5$ (instead of McCracken et al. 2010), the accuracy improved to $\Delta z / (1+z) = 0.015$, especially at $z \geq 1.8$, comparable to that obtained in Muzzin et al. 2013, as can be expected given the deeper photometry in the Muzzin et al. 2013 with respect to McCracken et al. 2010 catalogs (see Strazzullo et al. 2015).

5. Quiescence test: joint spectroscopy and photometry

In order to characterize the physical properties of the targets, the HST grism spectroscopy was combined with COSMOS2015 broadband photometry from CFHT/u* to IRAC/5.8 μm ⁴ (Laigle et al. 2016). A lower limit of 0.05 mag was used for the photometric errors in all the bands. The two data sets were fit

⁴ IRAC/8 μm was excluded from the fit due to higher chances of AGN contamination

separately and later combined by adding the χ^2 matrices of the two fits. This procedure allows to find the solution that best fits both data sets minimizing the impact of residual mismatches in normalization between the spectrum and the photometric SED. The same range of model parameters that was used for the spectral fitting is used in Fig. 4 except for the redshift grid which was fixed to the 1σ range around the best fitting z_{spec} . At this stage, the metallicity was fixed to the solar value according to the normalization and scatter of the local ETG mass-metallicity relation (Thomas et al. 2010). Recent clues from HST/G102 grism spectra of $1 < z < 1.8$ QGs as part of the CLEAR survey seem to support the idea that massive quenched galaxies were enriched to approximately solar metallicity already at $z \sim 3$ (Estrada-Carpenter et al. 2019). As will be mentioned in Sect. 5.3, the results obtained were tested against the choice of template metallicities.

5.1. Photometric zero-point calibrations

When comparing the mass-weighted ages and dust extinction values obtained from the modeling of the grism data alone versus the grism data combined with broad-band photometry (see Sect. 5), we find them being inconsistent at more than 3σ in most cases. Our SED fits to total fluxes resulted in relatively high reduced χ^2 (χ_R^2), as can be seen in Fig. 5. Specifically, the probability associated with the total χ^2 is $\sim 0.5\%$, given the total degrees of freedom of the photometric fit of the whole sample. Changing the IMF or leaving the metallicity of templates free did not improve the χ_R^2 distribution.

As shown in Fig. 6, the means of the distributions of the normalized residuals in each band appear to suffer from systematic shifts, namely B , V , i^+ , z^{++} (marginally), J , H , IRAC/3.6 μm , IRAC/4.5 μm . As noted in Capozzi et al. (2016), the procedure of re-calibrating photometric zero-points (ZPs) to optimize photometric redshift retrieval (commonly performed when building photometric catalogs) can impact the results of SED fitting. These tweaks can introduce systematics in several bands, since the re-calibrations are often based on specific samples at a specific redshift. In the case of COSMOS2015 these were tailored on various samples of spectroscopically confirmed QGs at $z < 2.5$ (Onodera et al. 2012; Krogager et al. 2014; Stockmann et al. 2020), among a much larger number of star-forming galaxies. In addition to this, the templates used to derive such adjustments can also have a role in introducing systematics. In particular, the ones used in COSMOS2015 are: two BC03 templates with an exponentially declining SFH with a timescale $\tau = 0.3$ Gyr and extinction-free templates as in Ilbert et al. (2013); a set of 31 templates including spiral and elliptical galaxies from Polletta et al. (2007) and 12 BC03 templates of young blue star-forming galaxies.

The offsets that we find in our data suggest that model fluxes tend to overestimate observed fluxes when COSMOS2015 ZP corrections subtract flux to the observed signal and viceversa (see Fig. 7). Dropping ZP corrections reduces most of the wavelength-dependent systematics, producing a better agreement between models and the originally observed fluxes. In both Figs. 6 and 5, it can be seen that dropping ZP offsets has the largest effect compared to changing grid parameters at reducing the median of the χ_R^2 distribution. With this choice the probability associated with the resulting total χ^2 is 9%. A high χ_R^2 could be also flagging systematically low photometric errors. A common practice in such a case is to rescale photometric errors to

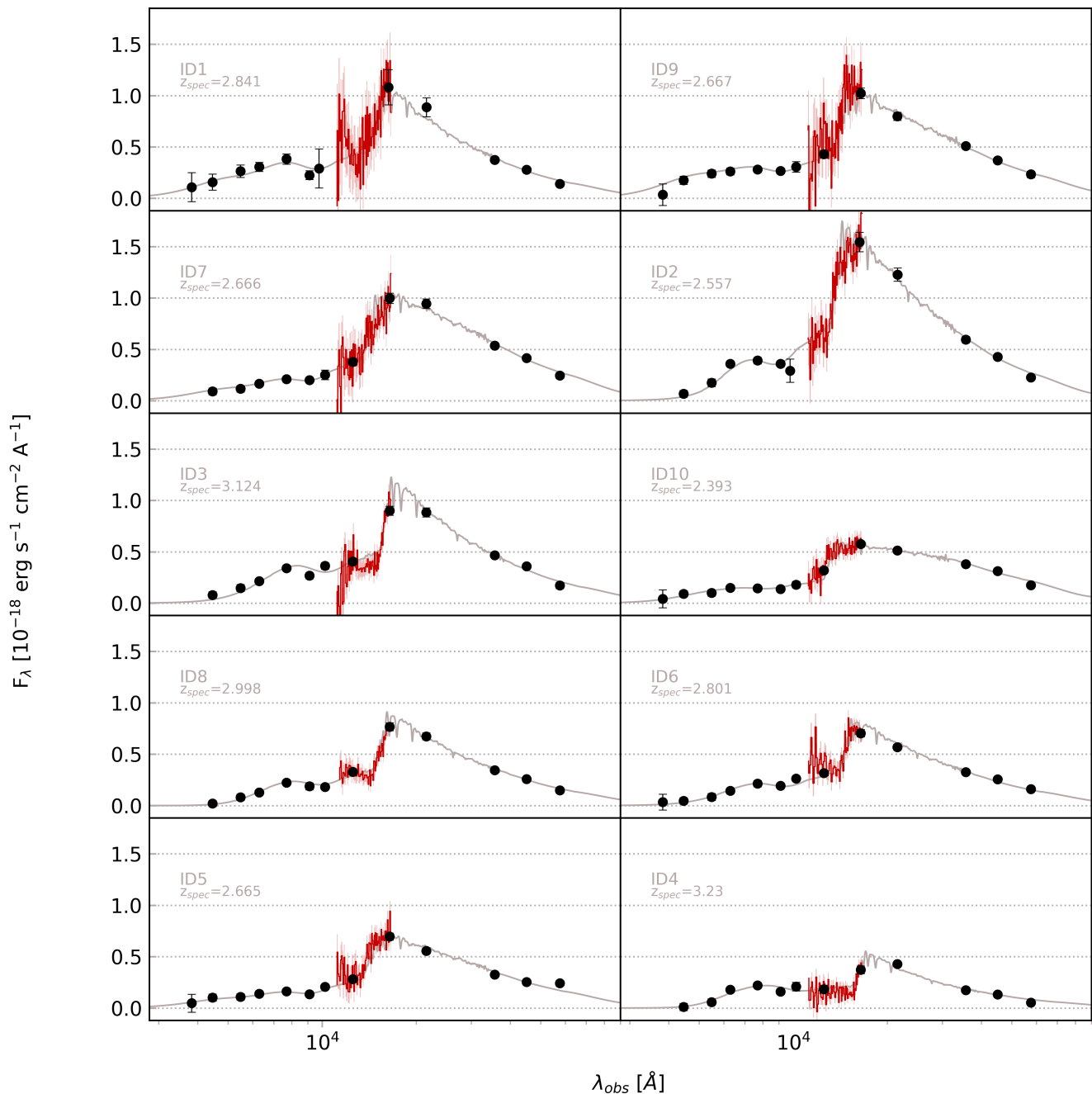


Fig. 4: Photometry from Laigle et al. (2016) catalog (black dots). Grey curves show the best fitting templates smoothed to the G141 resolution. The observed-frame grism spectra are superimposed, rebinned for clarity.

reach a $\chi_R^2 \sim 1$. However, given the behaviour highlighted in Fig. 6 and Fig. 5 such rescaling appears unnecessary. In fact, without using rescaled ZP offsets the median χ_R^2 is very close to 1. Lastly, a high χ_R^2 could be caused by broad residual distributions produced, for example, by the presence of some outliers in the sample. Visual inspections of imaging cutouts relative to each object in each band does not reveal peculiarities. We thus conclude that use of the ZP re-calibrations derived in Laigle et al. (2016) increase the inconsistencies between our spectroscopic and photometric data. For these reasons, the rest of the analysis

has been performed on the original COSMOS2015 photometry, namely without making use of any ZP correction.

5.2. Dust attenuation laws

Once the impact of photometric recalibrations has been reduced, we explored whether any inconsistency in terms of $\Delta\chi^2$ between the best fit spectroscopic solution and the combined one could be ascribed, for example, to an unsuitable attenuation law or to a SFH too smooth to reproduce simultaneously the NUV emission from young stellar populations and the NIR emission arising

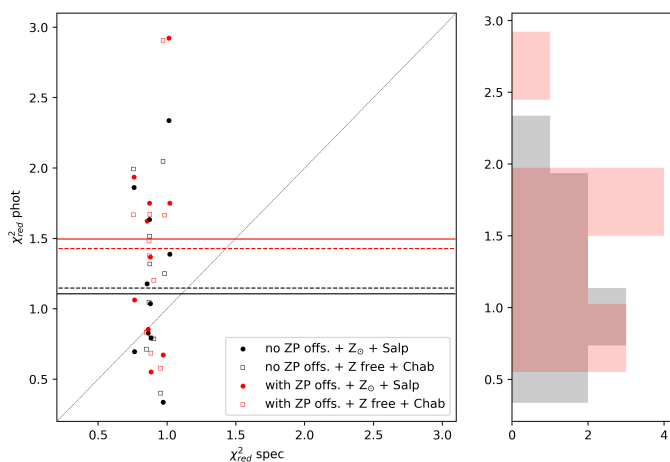


Fig. 5: Distributions of photometric reduced χ^2 before (red dots) and after removing the ZPs re-calibration (black dots). Median values are marked by red and black solid lines respectively. χ^2_{R} values obtained adopting a Chabrier IMF and leaving the metallicity free to vary are shown as empty squares. Their corresponding medians are shown as dashed lines.

ing from the bulk of the stellar mass. The use of attenuation laws steeper than Calzetti has been suggested to depend on the SSFRs of galaxies (Kriek & Conroy 2013; Salim et al. 2018). The slope of the curve is generally dependent on the grain size distribution and geometry, with steeper curves associated to differential attenuation according to the age of stellar populations. To test the role of dust attenuation recipes, we included in the fitting library alternative attenuation curves in addition to Calzetti et al. (2000). We adopted the methodology proposed in Salim et al. 2018, following from Noll et al. 2009, where the Calzetti curve is multiplied by a power-law term with exponent δ which sets the slope of the curve itself. Negative δ values imply a steeper slope in A_{λ}/A_V than in the Calzetti law at rest-frame $\lambda < 5500\text{\AA}$. In this formalism, the Calzetti law has $\delta=0$ by definition, whereas $\delta=-0.4$ is similar to the SMC curve. The curve is further modified by introducing the so-called 2175\AA bump (Fitzpatrick & Massa 1986), modeled as a Drude profile D_{λ} , with fixed central wavelength and width (FWHM=350 \AA) and varying amplitude. As we linked the bump strength to δ according to the linear relation found by Kriek & Conroy 2013 (see their eq. 3), the law was constrained mainly by one parameter, its slope, which we let vary between 0, -0.4 and -0.7. This latter value was introduced to test the expected behavior of local quiescent galaxies as shown in Salim et al. 2018. One in particular, the curve with $\delta = -0.4$, appears to reduce the dispersion of the χ^2_{R} distribution for the photometry and maximizes the consistency of the combined solution with the spectroscopic one. In fact, it systematically yields the lowest $\Delta\chi^2$ (median $\Delta\chi^2=3.1$) between the best fit spectroscopic and combined solutions which makes the two data sets consistent within 2σ , as can be seen in Fig. 8. When testing the overall goodness of fit in terms of the slope, $\delta = -0.4$ is the best fit solution preferred by the majority of the targets. Five galaxies out of nine tend to reject $\delta = -0.7$ at a 5% level (but not at 1%). Given the overall similar goodness of fit (especially between Calzetti and $\delta = -0.4$) it was not possible to reject one of them consistently for the entire sample. Therefore, during the rest of the analysis, we let δ vary, marginalizing over it when deriving physical parameters.

5.3. Quiescence of individual targets

We tested the quiescent/dusty star-forming nature of each galaxy by comparing the goodness-of-fit of the best fitting Constant Star-Forming (CSF) template with a free dust extinction parameter, with that of a solution defined as passive by constraining the best fitting SFH as follows: $t_{50} \geq 0.3$ Gyr, $A_V < 0.8$ mag and $t/\tau \geq 3$ where t_{50} is the lookback time at which the galaxy formed half of its stellar mass (our mass-weighted ages), t is the lookback time at the onset of star formation and τ is the timescale of the SFH. Such ratio corresponds to a drop in SFR of about a factor of 20 with respect to the initial value for an exponentially declining SFH. To classify a galaxy as quiescent, the consistency of the CSF solution has to show a probability of < 0.01 , as inferred from their χ^2 difference. This simple parameterization is able to discern to a zero-order level the consistency of both the spectrum and the photometry with a heavily dust attenuated star forming component, whether it fits better than the passive solution and the confidence level of its consistency. The test was performed fixing the redshift to z_{spec} . We first tested the spectra alone and then combined the photometric information by summing the χ^2 matrices of the two fits. In Fig. 9 we show the results of the test. We verified that letting z_{spec} vary within its 1σ confidence range does not impact the probabilities significantly. Letting the metallicity of the templates vary (adopting 0.4, 1 and $2.5 Z_{\odot}$) has a similarly negligible effect. Once the redshift of the target can be constrained to a sufficient accuracy, the addition of the photometry, with its wide wavelength coverage and overall quality, can help rejecting a SFH in those cases where spectroscopy alone is not able to robustly distinguish between the two. The test on ID 7 was performed letting z_{spec} vary within its 3σ confidence level of the combined fit. Given the lack of prominent (emission or absorption) lines, the spectrum alone is not able to reject star forming solutions. The combined fit, however, rejects such solutions ($P=0$, $\Delta\chi^2=183$, $\chi^2_{\text{R,SF}}=2.0$, $\chi^2_{\text{R,PASS}}=0.9$), even when adopting tighter constraints on the passive solution (e.g. $t/\tau > 10$ and $t > 0.5$). The second object showing the largest consistency with a star forming template is ID 10. Despite the addition of photometry rejecting star forming solutions, it should be noted that this object lies in a region of the UVJ diagram where contamination is expected to be more frequent (see Lustig et al. 2020). Moreover, its best fitting combined mass-weighted age and A_V are still pointing towards a very young and dust reddened stellar content ($t_{50} = 0.3^{+0.3}_{-0.1}$ and $A_V = 1.6^{+0.1}_{-0.3}$, respectively). We discuss very young sources with MIPS and Chandra detections in the following sections. We anticipate here that we consider ID 10 in particular an AGN host and likely an object close to its quenching phase. Given the arguments presented above, we conclude with reasonable confidence that all of our galaxies can be classified as passive on the basis of their UV-to-NIR emission.

6. SFR constraints from multiwavelength data sets

Here we take advantage of the recently released IR to (sub)millimeter Super-deblended catalog of Jin et al. 2018 (hereafter J18) and of the Chandra COSMOS-Legacy Survey catalog of Civano et al. 2016 to estimate the level of obscured star formation or nuclear AGN activity in our targets. First, we convert the flux densities of $24\mu\text{m}$ detections into the SFRs expected from $z \sim 3$ similarly massive MS galaxies and compare them to FIR constraints. Afterwards, we convert the very same flux densities into hard X-ray luminosities to check whether or not they are consistent with being AGN powered. Finally, we derive individual 3σ upper limits on the obscured SFR from VLA 3GHz flux

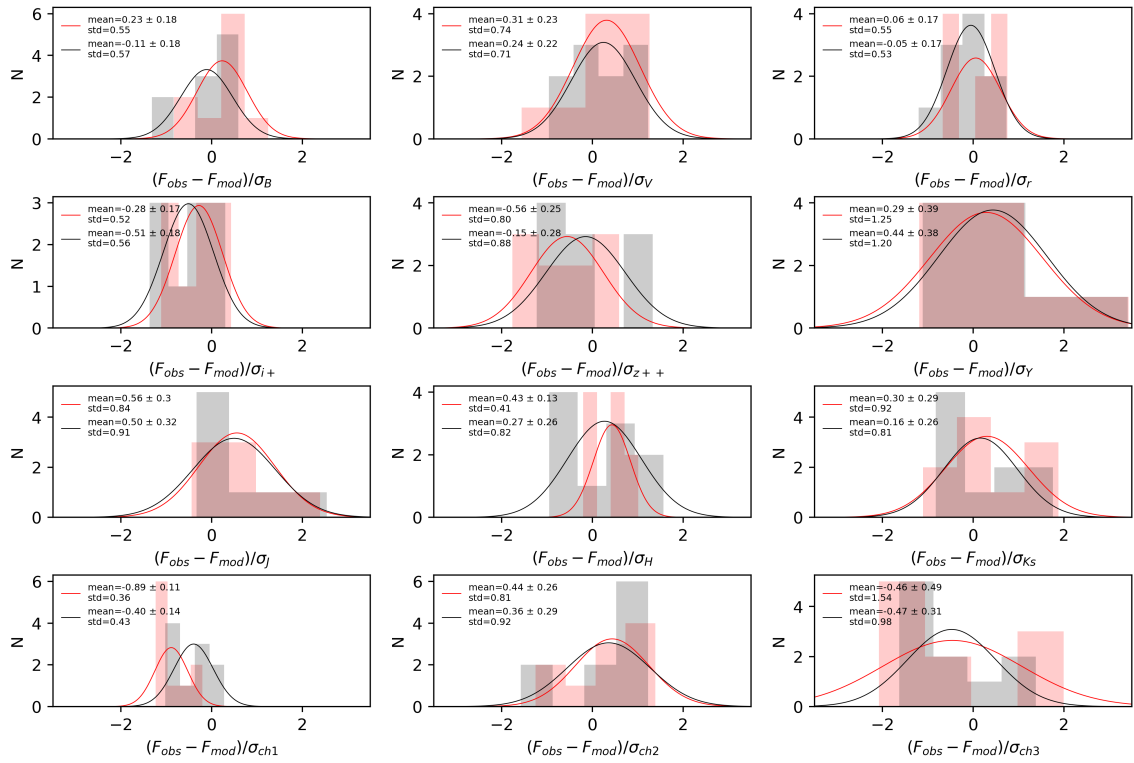


Fig. 6: Normalized residuals distribution of target galaxies in each photometric band. Red and black histograms show residuals adopting re-calibrated and original photometric zero points, respectively. Solid red and black curves show gaussian fits to such distributions. Their means, standard mean errors and standard deviations are listed in each panel.

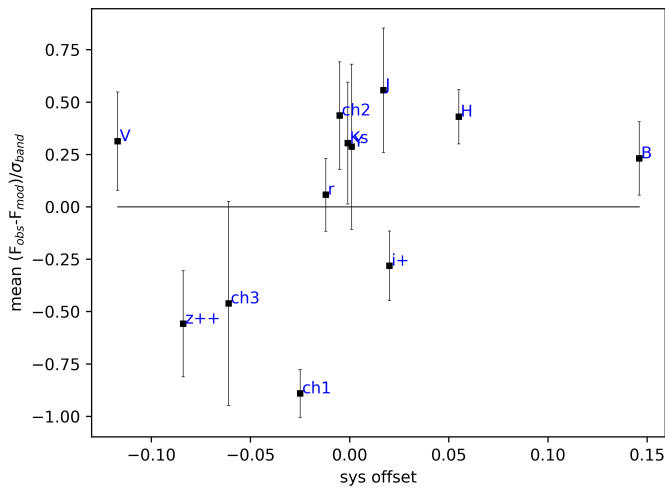


Fig. 7: Mean residuals of photometric bands as a function of the systematic offset to be applied to correct photometric ZPs. A correlation seems to be present, with increasing residuals for increasing corrections. Error bars mark the standard error on the mean shown in Fig. 6.

densities.

The prior-extraction method used in J18 fits the PSF of MIPS 24 μm , VLA 1.4 and 3GHz images (Smolčić et al. 2017) at the positions of known K_S -selected (plus radio 3GHz selected) sources. This procedure improves faint sources identification with respect to blindly-extracted catalogs such as in Le Floc'h et al. 2009 by

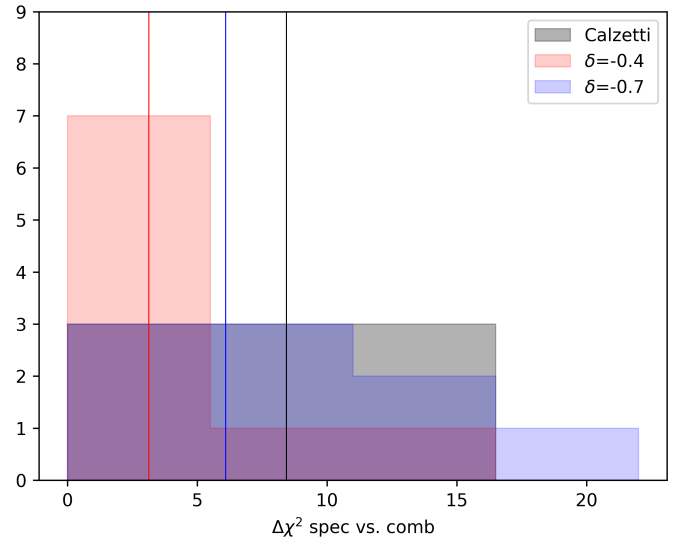


Fig. 8: Chi square difference between the best fitting spectroscopic solution and the best fitting combined solution selected from the spectral χ^2 matrix. Black, red and blue histograms show the distribution of such differences when varying extinction law. Vertical lines mark median values of the distributions. It can be seen that $\delta = -0.4$ is the one that reduces the median offset, bringing the solutions of the two fits consistent within 2σ .

significantly reducing flux errors (by roughly a factor of two) while also improving source deblending. This allows us to in-

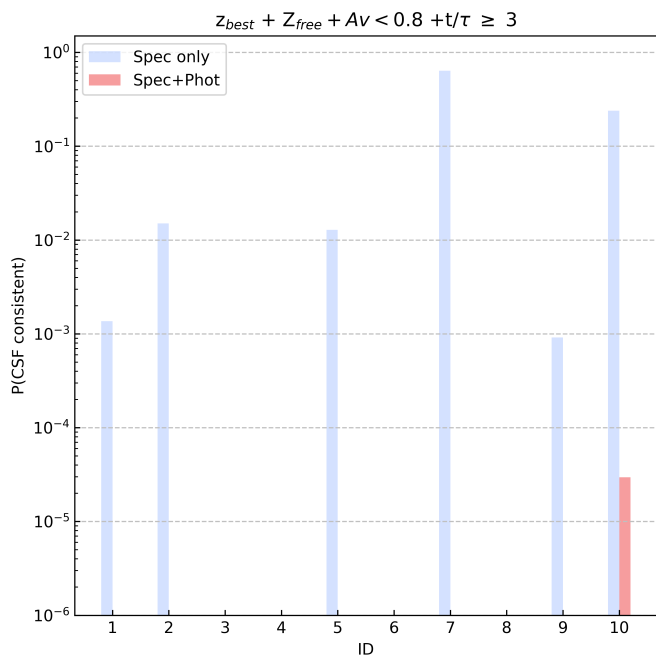


Fig. 9: Probability of constant star forming solutions relative to that of passive solutions. Blue bars mark the results from spectroscopy only. Red bars show the probabilities from the combined fit.

investigate in more detail individual mid- or far-IR detections that could have been missed by previous catalogs or judged of low significance. In particular, we recall here that our sample selection allowed for objects with Spitzer/MIPS $24\mu\text{m}$ detections ($S/N \geq 4$) from the Le Floch et al. 2009 catalog, or of higher S/N in case of SEDs with no acceptable star-forming solutions suggestive of an AGN driven MIR flux.

6.1. IR

The Super-deblended catalog marks five of our galaxies as detections in the MIPS $24\mu\text{m}$ band (ID 1, 5, 6, 7 and 10, see Table 3). None of them is significantly detected in the FIR. Specifically, all of them have a $S/N_{\text{FIR+mm}} < 5$, where $S/N_{\text{FIR+mm}}$ is the square root of the quadratic sum of the S/N computed in each band from $100\mu\text{m}$ to 1.2mm . ID 1 formally counts multiple detections in Spitzer/MIPS and *Herschel*/PACS bands but it is flagged as unreliable since it lies in a region of COSMOS affected by incomplete prior coverage and underestimated flux uncertainties. Visual inspection of its MIR and FIR cutouts did not reveal any detection at the source position (see Appendix A). We thus consider the IR detections of ID 1 as unreliable and exclude it from the following test.

At the mean redshift of this sample, observed-frame $24\mu\text{m}$ emission corresponds approximately to $6\mu\text{m}$ rest-frame. Emission at such wavelengths can arise from a range of processes: star-formation (Polycyclic Aromatic Hydrocarbons (PAH) emission lines and/or warm dust continuum); a dusty torus obscuring a central AGN; warm diffuse cirrus clouds heated by old stellar populations or circumstellar dust around Asymptotic Giant Branch (AGB) stars (Draine & Li 2007; Béthermin et al. 2015; Fumagalli et al. 2014). The $\sim 6''$ FWHM of Spitzer/MIPS PSF is larger than the typical optical projected size of our galaxies ($< 1''$ at 5000 \AA rest-frame) and prevents us from distinguishing

whether the emission is extended or centrally concentrated.

We computed the individual SFRs expected from the remainder four $24\mu\text{m}$ detections under the hypothesis that their emission is powered by star formation at the MS level emitting at the observed flux density. We corrected the flux densities by a factor of 1.7, as recommended in J18 and adopted conversions from Magdis et al. 2012. These conversions were driven from template SEDs of MS galaxies whose variation as a function of redshift is mainly driven by the strength of the mean radiation field $\langle U \rangle$, which maps the sSFR evolution. Such templates assume a fraction of dust mass into PAH of $q_{\text{PAH}} = 2.5\%$ for $z > 1.5$ MS galaxies.

The results can be found in Table 3 where we also report individual 3σ upper limits for undetected sources. The $24\mu\text{m}$ -derived SFRs range between ≈ 300 and $900 M_{\odot} \text{ yr}^{-1}$. This is the same order of magnitude of $z \sim 3 \log(M_{\star}/M_{\odot}) \sim 11$ MS galaxies albeit somewhat higher, inconsistent with FIR non-detections. Such MS galaxies, in fact, typically show FIR *Herschel* flux densities around a few to 10 mJy (Schreiber et al. 2015; Liu et al. 2018; Jin et al. 2018) which would be detected in *Herschel*/SPIRE. ID 10, 6 and 5 appear to tentatively show SPIRE/250- and $350 \mu\text{m}$ signal at the source position as revealed by visual inspection. For the latter two, the contamination by nearby projected FIR bright sources due to poor spatial resolution is evident. For ID 10 the J18 catalog formally provides non-detections at 100 and $160\mu\text{m}$ and no deblending at longer wavelengths. In postage stamps, the SPIRE/250 μm signal appears to show emission centered on the source position in the middle between two other $24\mu\text{m}$ bright sources. J18 attribute the 250- and $350\mu\text{m}$ signal to the severe blending of these two sources within the SPIRE large PSF, larger than the distance of these sources from our target ($\approx 10''$). As for the sources that remain individually undetected at $24\mu\text{m}$, the 3σ upper limits are too shallow to reject milder (but substantial) SFRs. Stacking the rest of the sample at $24\mu\text{m}$ results in $0.036 \pm 0.018 \text{ mJy}$ which translates into a shallow upper limit of $< 200 M_{\odot} \text{ yr}^{-1}$. We caution that the available 3σ depth of the Super-deblended data from Spitzer/MIPS, *Herschel*/SPIRE, *Herschel*/PACS in COSMOS is not sufficient to securely reject *sub-MS* levels of obscured star-formation on a galaxy-by-galaxy basis.

6.2. X-rays

ID 10, ID 6 and ID 7 have counterparts in the hard X-ray domain with rest-frame luminosities of the order of $\log(L_{X,2-10\text{keV}} [\text{erg s}^{-1}]) \sim 43.7, 44.3$ and 44.3 respectively, assuming a photon index $\Gamma = 1.4$ (e.g. Gilli et al. 2007). We tested whether their $24\mu\text{m}$ emission is consistent with being powered by an accreting black hole converting the observed-frame $24\mu\text{m}$ flux densities to unobscured rest-frame X-ray (2-10keV) luminosities, adopting the relation of Fiore et al. (2009) (see their eq. 1). This relation assumes that the 2–10 keV luminosity, computed directly from the observed fluxes without any correction for intervening absorption, can be considered representative of the intrinsic X-ray luminosity. The relation has a scatter of 0.2 dex and outliers in the case of significant X-ray absorption. For these three sources, their expected $L(2-10\text{keV})_{24\mu\text{m}}$ are in agreement with the observed ones within the uncertainties (see Table 3). Therefore, although we cannot reject the scenario in which some level of star formation would contribute to the rest-frame $6\mu\text{m}$ emission, we conclude that our data are fully explained by an AGN obscured by a dusty absorber.

Lastly, ID 5 shows a 0.1 mJy $24\mu\text{m}$ detection at 10σ significance which is not matched by an X-ray detection. Given that its spec-

trum and photometry are both pointing towards a passive nature, we tend to favour the hypothesis for which strong obscuration might be playing a role in hiding X-ray photons from the central engine.

6.3. Radio

We derived individual 3σ upper limits on the obscured SFR from the Super-deblended VLA 3GHz flux densities using the FIR-Radio correlation of Delvecchio et al. 2020 assuming that radio emission is given by star formation only. One galaxy is detected at 3GHz at 19σ (ID 1). Given the unphysically high SFR estimated for it ($\sim 10^4 M_{\odot} \text{ yr}^{-1}$, see Table 3), the origin of its radio emission is to be ascribed to AGN radio jets. Otherwise, the inferred upper limits result in $<120\text{-}190 M_{\odot} \text{ yr}^{-1}$, which do not conclusively rule out the presence of sub-MS levels of star formation on a galaxy-by-galaxy basis. Finally, as derived in D'Eugenio et al. 2020, the peak flux density of $S_{3\text{GHz}}=2.72\pm 0.93 \mu\text{Jy}$ obtained by mean-stacking 3GHz-undetected sources, translates into an upper limit on the global obscured SFR of $\sim 40\text{-}50 M_{\odot} \text{ yr}^{-1}$, a level of star-formation a factor of 6 lower than the coeval MS.

In summary, the average obscured SFR of our sample has been constrained to be below $\sim 40\text{-}50 M_{\odot} \text{ yr}^{-1}$ by a mean-stack detection at 3 GHz. However, individual 3 GHz radio upper limits to the obscured SFR are $<120\text{-}190 M_{\odot} \text{ yr}^{-1}$, therefore not sufficient to reject, on a galaxy-by-galaxy basis, star formation at 1σ below the estimated value for the MS at $z\sim 2.8$ corresponding to our stellar masses. Our sample contains four secure MIPS $24\mu\text{m}$ detections ($f_{24\mu\text{m}} \sim 0.1\text{-}0.2\text{mJy}$) with no FIR counterparts given also the shallow upper limits at these redshifts. Three of these detections are consistent with being AGN-powered given their luminous X-ray counterparts. The combined passive stellar emission for the remaining MIPS source points toward such galaxy being a likely obscured AGN host. The lack of individual strong constraints on the residual obscured SFR at these redshifts, combined with very young mass-weighted ages and high dust extinction values for some of our targets, renders the classification on a galaxy-by-galaxy basis somewhat ambiguous. We argue that extended spectral coverage (e.g. covering $H\alpha$ and [NII]) could be of help on this matter and that conclusive evidence on the nature of such high- z QGs can be obtained only with targeted deep mm observations.

7. Age determination

7.1. Spectral fit

Recent works suggest that, when it comes to estimating age and optical dust extinction, relatively simple parameterisations of the SFH perform similarly as more flexible ones and, all in all, behave in a relatively stable way at high redshift (Belli et al. 2019; Valentino et al. 2020). We conservatively marginalize over the different SFHs adopted here as to render the best fitting values and their uncertainties more robust. Fig.10 shows the resulting t_{50} and A_V extracted from the grism spectra (blue points) compared to those derived including COSMOS2015 photometry (red points). Light to dark shading marks 3-,2- and 1σ level confidence values respectively, obtained following Avni (1976) with two interesting parameters. The degeneracy between t_{50} and A_V appears to be strongly mitigated by the addition of the photometry once the redshift is constrained with sufficient accuracy to the

spectroscopic value. The bulk of our targets are consistent with having formed half of their stellar mass relatively recently, systematically having t_{50} below 1 Gyr. In some cases, such as for ID 10 and ID 6, the best fitting combination suggests the presence of dust enshrouded young stellar populations. Intriguingly these two galaxies are also detected in X-rays and $24 \mu\text{m}$, as discussed in Sects. 6.1 and 6.2, and might be galaxies which just entered into their quiescent phase or with residual SF below the levels probed our FIR data.

7.2. Relative strength of spectral breaks

The choice of SFH to infer evolutionary parameters intrinsically carries a degeneracy with the functional form adopted. A more direct approach is to quantify the light-weighted contribution of recent star-formation by measuring the relative contribution to the integrated stellar spectrum of short-lived massive stars with respect to long-lived lower-mass stars. Balmer absorption lines reach their maximum strength in A-type stars with a spectral break at 3646 \AA . Stars of lower mass and lower effective temperature produce metal absorption lines (Ca H & K, Fe, Mg) which result in a sharp spectral break at 4000 \AA . Moreover, the underlying continuum changes shape with time, progressively losing emission in the NUV/blue spectral range while flattening in the NIR. The different evolutionary rates of the stars producing the lines and their fractional contribution to the optical light at fixed mass, make it possible to trace the evolutionary stage of a galaxy. In Fig 11 (upper panels) we show the evolution of the spectral break measured through the D_B definition (Kriek et al. 2006) and the D_n4000 definition (Balogh et al. 1999) respectively, as well as the relative strength (the ratio) between the two (lower left panel). Lighter shaded curves show the variation with increasing duration of star-formation. The ratio is shown as a function of age of composite templates built with a short truncated SFH. The ratio is only mildly dependent on dust reddening since the two indices share a similar wavelength range. Also, the two indices are fairly robust against low resolution. As can be seen, the ratio varies strongly during the first 1 Gyr or so, reaching its maximum around 0.3-0.5 Gyr. Eventually, it drops below 1 once the light-weighted contribution from A-type stars fades away. Constant star-formation results instead in a ratio of ~ 1.1 rather constant with time. Varying the metallicity of the input templates has the effect of anticipating the transition to $D_B/D_n4000 > 1$. This effect is strongest when adopting supersolar metallicity ($2.5Z_{\odot}$) when the transition is reached at 0.9 Gyr. We suggest that such ratio could be used to spot post-starburst galaxies with high dust attenuation along and across the UVJ diagram when high-resolution spectra are unavailable.

In Fig. 11 (upper right) we show the two indices computed on our targets. The grey dashed line highlights the transition where the post-starburst ratio equals 1. The mean error in each side band was divided by the square root of the number of pixel within it. For ID 4, whose rest-frame spectrum does not cover the entire wavelength range required to compute the D_n4000 red side-band, the average flux density was taken as the mean of the best-fitting template in the same range. The error was computed as the mean of the noise spectrum taken on the last 10 spectral bins. We flagged this galaxy with a red diamond. The red star marks the values obtained on the average spectrum in D'Eugenio et al. (2020). Despite the large uncertainties driven by the S/N of our spectra, the indices all lie well above the 1:1 relation, thus marking the presence of young stellar populations in all of our targets. This supports the results of the spectral modeling, highlighting

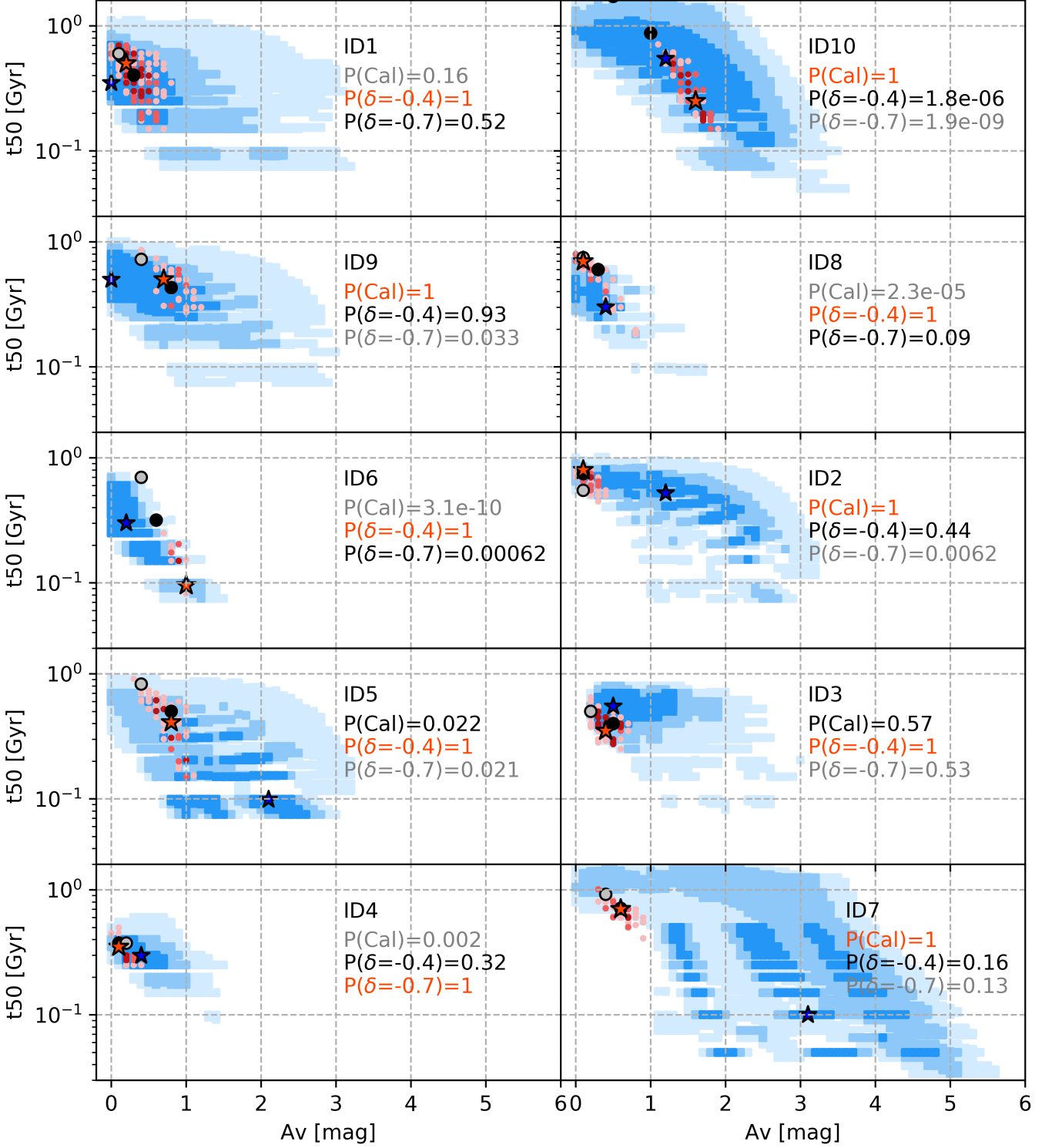


Fig. 10: Mass-weighted ages and dust extinction values for our targets. Blue squares mark the confidence regions (3 to 1 σ going from light to dark points) extracted from the spectra only. Red points show the solutions of the combined fit. Blue and red stars in each panel mark the best fit solution from the spectroscopic fit and the combined fit respectively. The probability of consistency of each extinction law with respect to the best fitting one are reported for each galaxy. As a reference, we report the best fitting combined solution at fixed extinction law as black and grey dots, their color coding follows that of the aforementioned probabilities.

how some of the most massive high- z QGs appear to be only recently quenched (Stockmann et al. 2020; Valentino et al. 2020; Forrest et al. 2020b). An overview of the physical parameters derived for our target galaxies can be found in Table 3.

8. Tracing AGN activity

Here we investigate the incidence and strength of BH activity on newly quiescent galaxies, in the framework of SMBH-galaxy

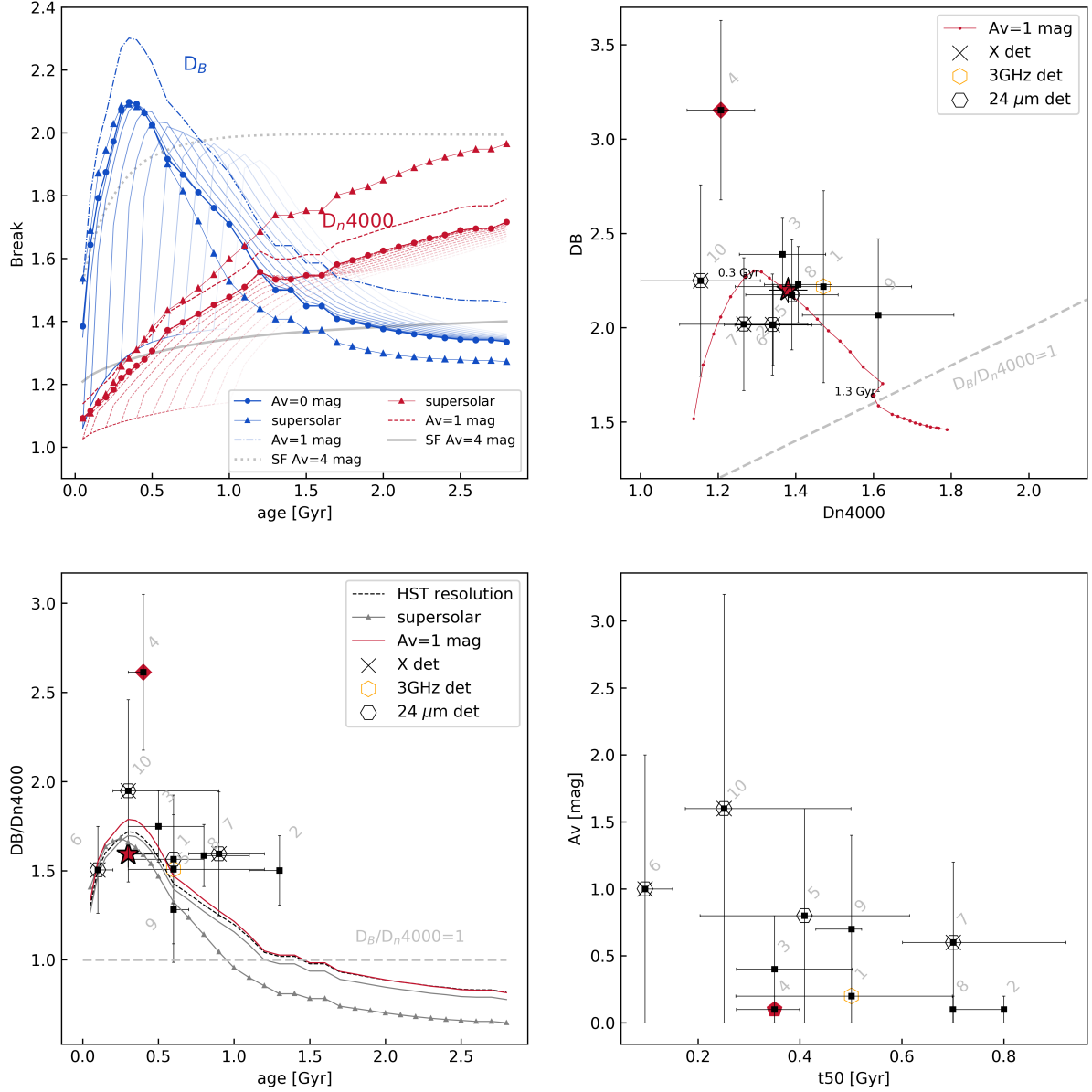


Fig. 11: *Upper left:* variation of the Balmer and 4000 Å breaks for CSPs as a function of their age using BC03 templates at solar metallicity. Lighter curves mark the evolution for a truncated SFH with increasing duration of star formation. The effect of adopting templates of different metallicity is displayed for the values that produce the largest variation, i.e. $2.5Z_{\odot}$ (triangles). Dotted and solid gray curves show the behavior of a constant SFH for the two breaks respectively. *Upper right:* individual values of D_B and D_n4000 for our targets. The red track shows their evolution with age and is attenuated by 1 mag. The gray dashed line marks the 1:1 relation. *Lower left:* variation of the index ratio as a function of age for an SSP-like template. The effect of smoothing templates to the HST resolution is shown by a black dashed curve. The effect of a $A_V = 1$ mag attenuation is shown instead by a red curve. The full transition between a Balmer-dominated and a 4000 Å -dominated spectrum is flagged when $D_B/D_n4000 = 1$ (grey dashed line), which happens around 1.3 Gyr of passive evolution. Dark grey triangles mark the evolution for $2.5Z_{\odot}$ templates. *Lower right:* best-fit values for the dust attenuation and mass-weighted age from the combined fit. Chandra X-ray, VLA 3GHz and Spitzer/MIPS 24 μ m detections are marked by black crosses, yellow and black hexagons respectively.

coevolution. In particular we can assess the level of mechanical feedback on our galaxies by studying the rest-frame 1.4 GHz luminosity averaged over the entire sample; and the incidence of radiatively efficient accretion by constraining the fraction of X-ray detected galaxies and their rest-frame hard X-ray luminosity respectively.

8.1. Radio

As mentioned, one galaxy (ID 1) is securely detected at 3GHz. Given the unphysically high SFR estimated for it ($\sim 10^4 M_{\odot} \text{ yr}^{-1}$), we ascribe the origin of its radio emission to AGN radio jets. Stacking the radio-undetected sources, in D'Eugenio et al. (2020) we obtained a peak flux density of $S_{3\text{GHz}} = 2.72 \pm 0.93 \mu\text{Jy}$.

This translates into a K-corrected rest-frame luminosity of $L(1.4 \text{ GHz}) = (2.0 \pm 0.7) \cdot 10^{23} \text{ W/Hz}$, which we interpret in this section as arising from low-luminosity AGN activity. Under the assumption that $z \sim 2.8$ quiescent galaxies share a FIR-to-radio SED similar to that of $z \sim 1.8$ analogs, we rescaled the best-fit model to the stacked SED of Gobat et al. 2018 (hereafter G18) to our median stellar mass and computed the 1.4 GHz luminosity expected from residual star formation according to the FIR-radio correlation ($L_{\text{mod}} = 1.2 \cdot 10^{22} \text{ W/Hz}$). Our observed $L(1.4 \text{ GHz})$ is 18 times higher, implying an excess signal of $L_{\text{mod}} = 1.8 \cdot 10^{23} \text{ W/Hz}$. This, in turn, is a factor of 3-4 higher than the excess found in $z \sim 1.8$ similarly massive QGs (G18). The low statistics implied by our sample size prevents us from making meaningful considerations on the overall duty cycle of AGN activity. It is worth mentioning, however, that the 0.66 duty cycle estimated in G18 from $z=1.4$ to $z=2.5$ implied a burst duration of 1.2 Gyr which is 1.6 times larger than our observational window (the cosmic time spanned by our sample is 0.72 Gyr). This, together with the ensemble radio detection, might imply that we are sampling an epoch when low-level AGN activity is almost always on in newly quiescent galaxies, with a stronger radio AGN activity with respect to what inferred for lower- z massive analogs.

8.2. X-ray

L_X can be viewed as a tracer of the typical rate of black hole growth in a given galaxy sample. Recent stacked analysis of quiescent galaxies in COSMOS constrains the average level of rest-frame hard X-ray emission to be $L_X = 2 \cdot 10^{43} \text{ erg s}^{-1}$ (Carraro et al. 2020, hereafter C20)⁵. While our non-detections are consistent with C20, our mean rest-frame $L(2-10)\text{keV}$ obtained as

$$L(2-10)\text{keV} = \frac{L_{X,\text{uplim}} \times N_{\text{nondet}} + \sum_{i=1}^{N_{\text{det}}} L_{X,i}}{N_{\text{nondet}} + N_{\text{det}}}$$

is higher by a factor of 2–3 at face value (see Fig. 12). The error bar on the average is computed as the error on the weighted mean.

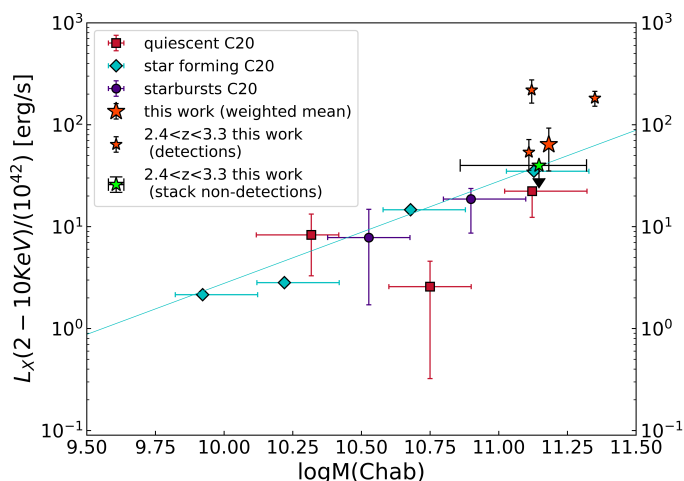


Fig. 12: X-ray luminosity in the 2-10 keV band as a function of stellar mass for quiescent (red squares), star forming (cyan diamonds) and starburst galaxies (violet circles) at $2.25 < z < 3.50$. Adapted from Carraro et al. 2020.

⁵ Our stellar masses were converted to a Chabrier IMF for consistency

Assuming the Lusso et al. (2012) bolometric corrections and a $M_{\text{BH}} = M_*/500$ conversion as in Häring & Rix (2004), we computed Eddington ratios for each target, defined as the bolometric X-ray luminosity (or its 3σ upper limit) divided by the Eddington luminosity expected at the stellar mass of the galaxy. We obtain Eddington ratios of $\lambda_{\text{EDD}} \sim 2 - 11\%$ for detected sources and 3σ upper limits lower than 1% for all the undetected ones. When repeating the test using $24\mu\text{m}$ -derived $L(2-10)\text{keV}$, we obtain λ_{EDD} which are a factor of 2 higher on average. Such λ_{EDD} translate into Black Hole Accretion Rates (BHAR)⁶ which are largely in agreement with C20 at $z \sim 3$. Dividing the mean $\langle \text{BHAR} \rangle$ by the average $\langle \text{SFR}_{[\text{OII}]}\rangle$ estimated in D’Eugenio et al. (2020) we obtain an increase by a factor of ~ 30 with respect to $1.3 < z < 2.25$ QGs at the same mass (see Fig. 13), consistent with the lower limit for massive $2.3 < z < 3.5$ QGs inferred from the same paper. Our mean L_X is marginally consistent with that star-forming galaxies in the same mass and redshift range, whereas the [OII]-derived dereddened SFR lies around ~ 60 times below the MS. This translates into $\langle \text{BHAR} \rangle / \langle \text{SFR} \rangle$ being a factor of ~ 60 higher than the high-mass end of the MS at $z \sim 3$. This supports the idea that, while the stellar mass growth of the host galaxy has already come to an end, the BH mass growth in high- z QGs takes longer to fade away, as already pointed out in C20, and might have had a role in quenching.

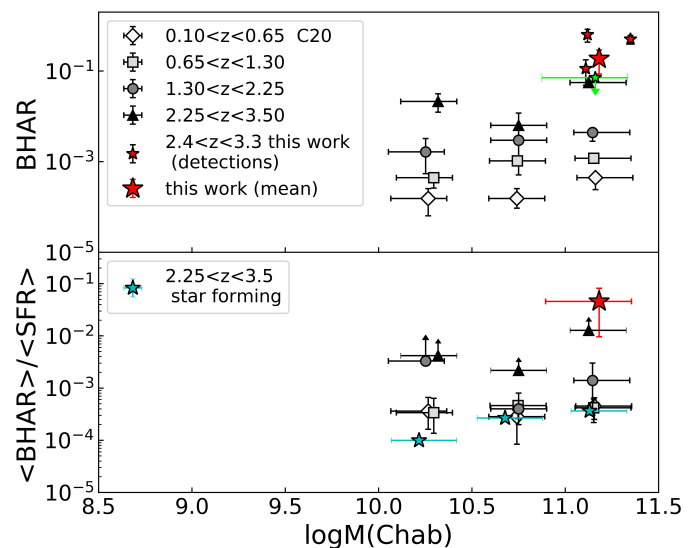


Fig. 13: BHAR (top) and BHAR per unit star formation rate (bottom) as a function of stellar mass for quiescent galaxies in COSMOS. Different symbols mark different redshift bins. Cyan stars mark main sequence galaxies in the same redshift range studied in this work. Error bars on the average BHAR reflect the dispersion of the weighted mean on the rest frame $L(2-10\text{keV})$ of the sample. The average $\text{SFR}_{[\text{OII}]}$ was converted to a Chabrier IMF. Adapted from Carraro et al. (2020).

The stochastic nature of detectable AGN activity implies that it is usually only observed in a small fraction of galaxies at a given time. Aird et al. (2019) report that high- z massive QGs exhibit enhanced AGN fractions compared to low- z SF galaxies hosting an equivalent SFR, suggesting that AGN activity in QGs

⁶ $\text{BHAR}(M_*, z) = (1 - \epsilon) \cdot L_{2-10\text{keV}} \cdot \text{kbol}(M_*, z) / (\epsilon c^2) = \lambda_{\text{EDD}} \cdot L_{\text{EDD}} \cdot 10^{-45.8} M_{\odot} \text{ yr}^{-1}$, where the efficiency of mass conversion is $\epsilon = 0.1$

might be fuelled and sustained by stellar-mass loss rather than the availability of cold gas. Their fraction of highly-accreting quiescent galaxies ($\lambda_{\text{SBHAR}} > 0.1$, i.e. at more than 10% the Eddington limit) reaches 2-3% around $z \sim 3$. The fraction of normally accreting AGN ($\lambda_{\text{SBHAR}} > 0.01$) reaches 20-30% in the quiescent population with SFRs of order of $0.5\text{-}1 M_{\odot} \text{ yr}^{-1}$.

Schreiber et al. (2018) find 18% of X-ray detections among $3.2 < z < 3.7$ massive UVJ-quiescent galaxies, plus an additional 30% in the young-quiescent (lower-left) region of the UVJ diagram. Several of their young-quiescent SEDs show similarities with our ID 5 and 6 in terms of SED shape and possibly young age. Olsen et al. (2013) report a $19\% \pm 9\%$ luminous AGN fraction in a mass-complete sample of massive UVJ selected quiescent galaxies at $1.5 < z < 2.5$, with a total low-luminosity AGN fraction up to 70%-100%, advocating in favor of episodic AGN activity to maintain low SFRs in quiescent galaxies. Including a possibly Compton thick source, our sample likely contains a 40% fraction of luminous AGN. We currently do not know in which direction the incompleteness due to the sample selection will affect the AGN fraction, since we are focusing on high-mass quiescent galaxies while excluding the strongest $24\mu\text{m}$ detections.

As noted in Aird et al. (2019), stellar mass-loss and AGN feedback tend to be disfavored mechanisms to cause relatively high-accretion rates and high AGN fractions in sub-MS and quiescent galaxies. The former could sustain the accretion onto the central BH by providing a relatively stable supply of low-angular momentum gas but is expected to result in relatively low accretion rates. Moreover, stellar mass loss is most efficient soon after star formation (2-5 Myr) and declines exponentially afterwards, making its contribution likely not sufficient to explain the highest λ_{EDD} measured for some of our objects (unless non-negligible SF is occurring). Instead, AGN feedback assumes that the gas supply, once used by the galaxy to sustain SF, is accreted by the central SMBH. However, even the shortest ages shown by our stellar populations would imply a stability of the radiatively efficient AGN feedback of order of hundreds of Myr, whereas radiatively efficient accretion is expected to be stable on time-scales of 0.1 Myr. One other mechanism proposed by Aird et al. 2019 could be the build-up of a compact bulge, which would increase the stellar density of the host galaxy, hence increasing the rate at which the AGN is triggered by infalling gas, as also supported by observations Barro et al. (2013). Fig. 14 shows that our likely-AGN hosts are among the most compact ones in the sample however they also show the lowest Sersic indices ($n=1.6\text{-}2.6$) implying that no clear-cut connection between radiative AGN feedback and central stellar density can be established with the present sample. However, despite no significant correlation being found between morphology (either R_e or n) and t_{50} , the very young mass weighted ages found for the sample as a whole and the average bulge dominated morphology suggest that structural transformation precedes or, at least, goes hand-in-hand with star formation rate suppression. The 30-40% fraction of AGN tentatively associated with young objects (seen also young quiescent galaxies in Schreiber et al. (2018)) might suggest that episodic AGN feedback might be triggered before a completely passive stellar core is settled.

9. Discussion

In the present paper we have characterized one of the largest representative samples of 10 high- z quiescent galaxies in terms of spectroscopic confirmation and age-estimation. We showed how HST observations are able to probe the (H-band) brightest end

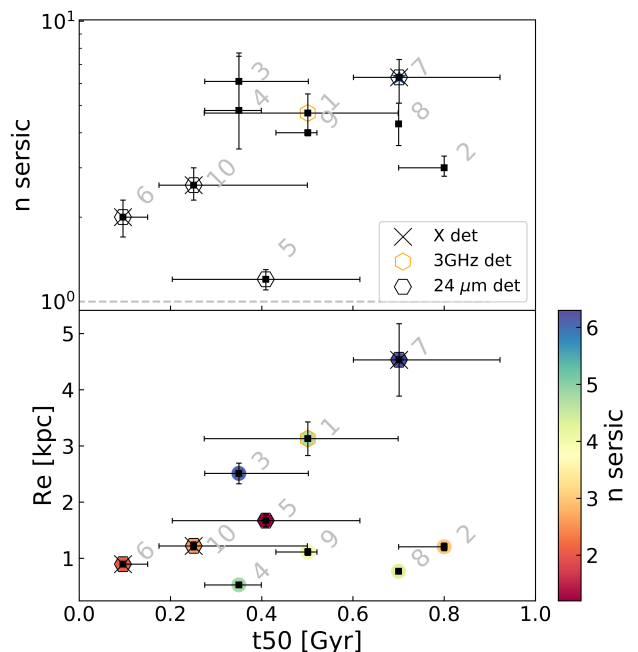


Fig. 14: Comparison between our mass-weighted ages and the morphological parameters derived in Lustig et al. (2020), namely Sersic index n and effective radius R_e at 5000 \AA rest-frame.

of the massive QG population providing access to clear spectral breaks in the majority of the objects. Such breaks can be used to quantitatively compare the amplitude of the Balmer absorption lines with respect to metal lines, hence quantifying the light-weighted contribution of young versus old stars at fixed stellar mass in early QGs. In other words, with relatively few HST orbits it is possible to both perform spectroscopic confirmation of QGs up to $z \sim 3.2$ and start quantifying the incidence of newly-quenched objects within the population. The particular configuration of spectral breaks characterising our sample (strong D_B and weak D_n4000) is due to the presence of luminous A-type stars. These often flag a relatively recent shut down of star formation, yet they have been also linked to galaxies hosting substantial amounts of obscured star formation contaminating the rest-frame colors commonly used when selecting high- z quiescent galaxies (Poggianti & Wu 2000; Lemaux et al. 2017). The quiescence of our targets was first tested and confirmed through their combined spectral (rest-frame NUV/optical) and photometric (rest-frame UV-to-NIR) emission, rejecting the presence of catastrophic photometric errors or prominent emission lines. They are however consistent with very young mass-weighted ages, which makes their final interpretation less clear. Given the shallow upper-limits on the obscured SFR placed by the current Spitzer/MIPS and Herschel/PACS and SPIRE data, we relied on the mean-stacked shallow detection at 3 GHz to constrain the potential obscured SFR to be on average below $50 M_{\odot} \text{ yr}^{-1}$ (D'Eugenio et al. 2020), hence 6 times lower the coeval MS, at most. The individual $24\mu\text{m}$ flux densities of three $5\text{-}10\sigma$ detections in the J18 super-deblended catalog were converted to hard X-ray luminosities, compared to Chandra COSMOS Legacy X-ray detections and judged being consistent with being AGN-powered. Converting individual 3 GHz 3σ upper-limits into SFRs results in $<120\text{-}190 M_{\odot} \text{ yr}^{-1}$, which are not conclusive to exclude substantial obscured star formation on a galaxy-by-galaxy basis. We also note that the origin of the mid-

IR emission is in principle unclear since it can arise from multiple phenomena such as a dusty AGN torus, star-formation, hot circumstellar dust around AGB stars and/or the presence of diffuse cirrus clouds heated by hot stellar populations (Fumagalli et al. 2014) or a combination thereof. From the broad agreement between the prominent Balmer breaks and the mass weighted ages of our galaxies we conclude that they have quenched relatively recently prior to observation. However, dedicated mm observations are required for 40% of our objects to conclusively assess the level of residual star formation. These, in fact, could potentially represent examples of rapidly transitioning galaxies which underwent a sharp truncation of their star formation, possibly through AGN feedback.

9.1. The emergence of massive quiescent galaxies at high- z

Despite the overall stability of the spectral fitting mentioned above, one should keep in mind that age estimates still rely upon the spectral fitting scheme adopted, on the assumptions made in the choice of template libraries and ultimately on the shape of the SFH used. Keeping such caveats in mind, we can start making meaningful statements on the ages of our QGs through relative comparisons of the mass-weighted ages within our sample. The bulk of our targets is consistent with having suppressed their star-formation very recently, between 300-800 Myr prior to observation. The median value being 0.5 Gyr with a dispersion of 0.2 Gyr. Two outliers are present, ID 6 and ID 10, showing younger ages than the bulk of the sample, 0.1 and 0.25 Gyr respectively. Despite the fact that for ID 10 the D_B/D_n4000 ratio appears to be the strongest (hence pointing at the highest contribution of A-type stars with respect to the underlying stellar population), the S/N of our spectra prevents us from identifying significant differences among our galaxies. Moreover, the downward trend of the D_B/D_n4000 ratio at $t_{50} \leq 0.1$ Gyr precludes the possibility of testing the age inferred from the spectral fit, such as for ID 6. Assuming an exponentially declining SFH and our best-fit t_{50} , our galaxies are consistent with having been forming half of their stellar mass around $z_{\text{form}} \sim 3.5$ at $\text{SFR} \sim 1800\text{-}3000 M_{\odot} \text{ yr}^{-1}$, similarly to what reported in Valentino et al. (2020) but shifted at a later epoch. We caution, however, that such simple representations of SFHs are unlikely to be representative of the *peak* SFR if the true SFH was more complex, such as in the case of multiple phases in the SFR (Barro et al. 2016) or mergers (which imply a degeneracy with mass assembly, hence in lower SFRs split between the progenitors). Interestingly, the common selection of high- z QGs preferentially selects bright blue UVJ quiescent objects where "dust-poor" PSBs often lie. In some cases, it extends to a bluer region outside the standard quiescent boundaries (either in the UVJ or in the NUVrJ selection) where compact transitioning galaxies are thought to lie along their fast drop in SFR (Belli et al. 2019; Schreiber et al. 2018; Valentino et al. 2020; Forrest et al. 2020a). This implies that high- z quiescent galaxies are selected more or less in the same evolutionary phase, namely after O and B stars exited the Turn Off and before the same happens for A-type stars. This appears to be manifesting through similar distributions of (mass-weighted) ages among the highest- z samples (perhaps unsurprisingly, see Fig. 15). This also means that the magnitude cut necessary for spectral acquisition is biasing the selection of high- z QGs against dusty PSBs or galaxies more slowly transitioning into quiescence (Belli et al. 2019). Moreover, considering the cosmic time between $z=2.8$ and $z=1.8$, the mass-weighted ages inferred for our targets appear to be broadly consistent with passive evolution into old QGs at intermediate redshifts (Whitaker et al. 2013). This is not the

case for higher- z massive QGs, confirming that the high- z selection is directly probing the continuous injection of new compact quiescent galaxies into the passive population.

The enhanced fraction of PSBs (60%-70%, D'Eugenio et al. 2020; Lustig et al. 2020) among photometrically selected $\log(M_{\star}/M_{\odot}) \geq 11$ QGs at $z \sim 3$, is linked to the progressive migration of the red-sequence towards bluer colors with increasing redshift. PSBs represent an increasing fraction of the whole QGs population with redshift (Wild et al. 2016). Particularly so also because the transition from Balmer to CaII absorption lines is fast compared to the overall lifetime of a galaxy at low redshift (at the epochs spanned in this work, instead, such a phase naturally represents a much larger fraction of a galaxy lifetime). When considering the growth of the red sequence, the observed fraction of PSBs among massive QGs remains low <1-3% from $z=0$ to $z \sim 0.5$ (Tran et al. 2003) and fastens between $z \sim 1-2$ to $\sim 20\%$ - 50% , with percentage variations mirroring different selection criteria (Le Borgne et al. 2006; Whitaker et al. 2013; Wild et al. 2016). The mounting fraction of massive QGs with evidence of recent quenching already accounts for half of the population at $z \sim 2$, when their number densities start to match (Whitaker et al. 2012). This is further supported by the growth rate of $\log(M_{\star}/M_{\odot}) \geq 10.8$ PSBs of less than 1 Gyr at $z \sim 2$ which accounts for half that of the whole quiescent population (Belli et al. 2019). The decrease in cosmic time allows to study the width of the distribution in quenching times of QGs: the emerging picture is one in which a continuous injection of objects into the quenched population manifests into the fast increase in the number density of young quiescent galaxies starting at $z \sim 1.5-2$ (Whitaker et al. 2011, 2013) with a reversal of their relative contribution to the red sequence with respect to old galaxies by $z \sim 3$. This trend appears to continue towards higher redshifts where relatively old quiescent galaxies appear to be still unobserved (Forrest et al. 2020b; Marsan et al. 2020). The latest spectroscopic constraints at $z \sim 3.5$ appear to find quasars or star forming redshift interlopers among the reddest objects in the passive UVJ region, however the long integrations required limit both the number and the quality of such spectra (Forrest et al. 2020b). At the time being, the question of whether or not PSBs scatter also into the reddest area of the passive UVJ region⁷ due to photometric errors or intrinsic properties such as dust or metallicity (which can also be read as *is the $z \sim 3$ population missing the descendants of any $z \sim 4-5$ massive quiescent galaxies?*) can be addressed only with very expensive targeted observations. The enhanced sensitivity of JWST will be able to map the full distribution of PSBs on the UVJ diagram to the highest redshifts. Establishing a detailed demographics of $z \sim 3$ (or higher) QGs to the faintest magnitudes will help clarifying the distribution of dust attenuation among spectroscopically confirmed extremely red-objects and in turn provide insights on the global star formation history of high- z QGs.

10. Summary and conclusions

We have obtained HST WFC3/G141 grism spectra for one of the first representative samples of ten $\log(M_{\star}/M_{\odot}) > 10.8$ quiescent galaxies at high redshift ($2.4 < z < 3.2$). HST observations efficiently provided us with the largest sample of QGs with a full continuous coverage along the Balmer/4000 Å spectral region at these redshifts. This allowed us to perform spectroscopic confirmation of QGs up to $z \sim 3.2$ and, thanks to widespread prominent Balmer Breaks, we were able to start quantifying the inci-

⁷ E.g. (U-V)+(V-J)>2.8

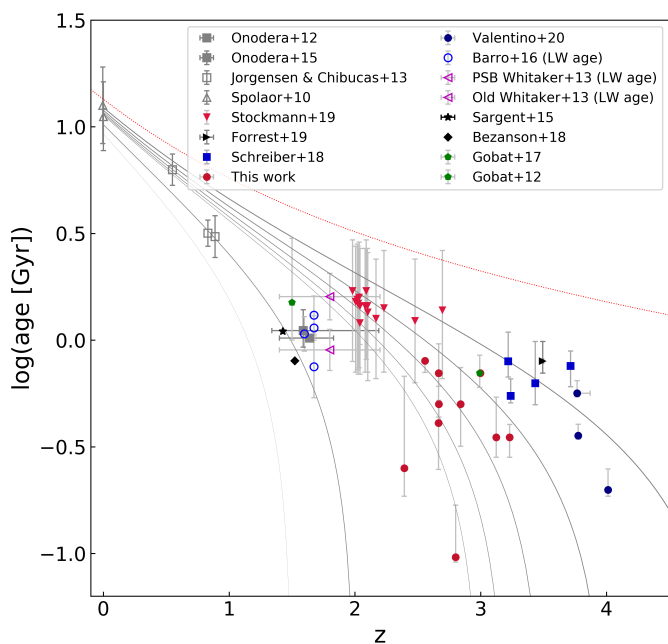


Fig. 15: Age evolution with redshift in $\log(M_*/M_\odot) > 10.5$ quiescent galaxies. Adapted from Onodera et al. (2015). For $z > 2.5$ QGs we show their mass-weighted ages (t_{50} s). The four targets selected from Schreiber et al. (2018) correspond to those recently followed up by Esdaile et al. (2020). Gray solid lines show, from thin to thick, the age of simple stellar populations made at a z_{form} from 1.5 to 5. The red dotted line marks the age of the Universe as a function of redshift.

dence of newly-quenched objects within the massive quenched population against contamination by lower redshift interlopers. The quiescence of our targets was tested by means of the combined information of our newly acquired rest-frame NUV/optical spectra and COSMOS2015 UV-to-NIR photometry. In addition, we also considered mid-IR, far-IR and radio detections from recently released super-deblended photometry (Jin et al. 2018).

Our main conclusions can be summarized as follows:

- successful spectroscopic confirmation was achieved for the full sample, confirming the quality of the original photometric selection;
- the joint analysis of our newly acquired rest-frame NUV/optical spectra and COSMOS2015 broad-band UV-to-NIR photometry confirms the quiescent nature of all our targets;
- although IR-based constraints on the obscured SFRs of our individual targets are weak with the available data ($< 120\text{-}190 M_\odot \text{ yr}^{-1}$), the quiescent nature inferred from grism spectra and optical/NIR SEDs is globally supported from the 3GHz stack of the sample yielding an obscured SFR $< 50 M_\odot \text{ yr}^{-1}$ (D'Eugenio et al. 2020);
- the use of photometric Zero Points re-calibrations proposed in Laigle et al. (2016) appears to be disfavored by our data. Such corrections were derived on a set of spectroscopically confirmed quiescent among a much larger number of star forming galaxies at intermediate redshifts and might not be necessary when it comes to extract the SEDs of QGs at high- z ;
- an attenuation curve steeper than Calzetti tends to reduce tensions between age and dust extinction values between photometry and spectroscopy. Nonetheless, our data do not allow

to securely discriminate among attenuation curves of different slopes;

- marginalizing the spectro-photometric fit over different attenuation curves and SFHs, the typical mass-weighted ages inferred for our objects range from 300-800 Myr, pointing at a recent rapid suppression of their SFR. Their global strength was quantified and compared to the one of the 4000 Å break by means of the D_B/D_n4000 ratio which is systematically higher than 1. This spectroscopically confirms on a galaxy-by-galaxy basis the post-SB nature of massive bright QGs, already pointed out by means of stacking (D'Eugenio et al. 2020) and by individual high-resolution spectra (Forrest et al. 2020b). More observational efforts are required to explore to which extent strong Balmer absorption lines are spread among lower mass-to-light ratio objects;
- interpreting our mid-IR and X-ray individual detections and the radio-stack shallow detection as a signature of AGN activity, our results are consistent with: a widespread radio AGN activity a factor of 4 stronger than in similarly massive QGs at intermediate redshifts, and a 30-40% incidence of luminous AGN in which the BH mass growth is substantially enhanced with respect both to $z \sim 2$ quiescent analogs ($\times 30$) and to coeval star forming galaxies at the same stellar mass ($\times 60$). This is in agreement with the recent results of Carraro et al. (2020) on the stacked emission of photometrically selected populations of QGs at $2.25 < z < 3.50$;
- our galaxies are globally characterized by a bulge-dominated, compact morphology (Lustig et al. 2020). Despite no clear trend between mass-weighted ages and R_e or Sersic indices could be found within the sample, the young ages yielded by their grism spectra and broad-band photometry suggest that structural transformation may precede or be concomitant with quenching.

The fast evolutionary phase probed by the magnitude-limited color selection seems the one in which the majority of $z > 2.5$ QGs are caught, systematically selecting newly quenched(-ing) objects which enter the quiescent population. We expect the number density of spectroscopically confirmed post-SBs (which was already matching the one of old systems at $z \sim 2$ based on photometric selections (Whitaker et al. 2013) to fully dominate the QGs mass-function at $z \sim 3$. JWST and ALMA will be crucial to trace the full demographics the quiescent population in an effort to map the distribution in quenching times and dust/molecular gas content, i.e. to get further insights on the global SFH of the emerging massive quenched systems.

Acknowledgements. We are grateful to G. Brammer for assistance with the data reduction, to C. Vignali for providing X-ray spectra and M. Salvato for additional redshift constraints and helpful discussions. C.D. is grateful to C. Gomez-Guijarro for helpful discussions. V.S. acknowledges support from the ERC-StG ClustersXCosmo grant agreement 716762. I.D. acknowledges the European Union's Horizon 2020 research and innovation program under the Marie Skłodowska-Curie grant agreement No 788679. A.C. acknowledges the support from the grants PRIN-MIUR 2017 and ASI n.2018-23-HH.0. Based on data products from observations made with ESO Telescopes at the La Silla Paranal Observatory under ESO programme ID 179.A-2005 and on data products produced by TERAPIX and the Cambridge Astronomy Survey Unit on behalf of the UltraVISTA consortium (Laigle cat.).

ID	Z_{spec}	$\log(M_*/M_{\odot})$	t_{50} [Gyr]	A_V [mag]	δ	$D_{r,4000}$	$f_{24\mu\text{m}}$ [mJy]	$\log L_X$ obs.	$\log L_X$ 24 μm	$S_{3\text{GHz}}$ [mJy]	$\text{SFR}_{24\mu\text{m}}$ [$M_{\odot}\text{yr}^{-1}$]	$\text{SFR}_{3\text{GHz}}$ [$M_{\odot}\text{yr}^{-1}$]
1	$2.841^{+0.021}_{-0.018}$	11.37	$0.5^{+0.2}_{-0.2}$	$0.2^{+0.3}_{-0.1}$	[-0.7,0]	1.47 ± 0.23	-	< 43.6	-	0.576 ± 0.03	867	~ 12930
2	$2.557^{+0.005}_{-0.005}$	11.50	$0.8^{+0.1}_{-0.1}$	$0.1^{+0.1}_{-0.0}$	[-0.4,0]	1.34 ± 0.10	-	< 43.16	-	-	-	-
3	$3.124^{+0.003}_{-0.003}$	11.55	$0.4^{+0.2}_{-0.1}$	$0.4^{+0.2}_{-0.2}$	[-0.7,0]	1.37 ± 0.11	0.041 ± 0.018	< 43.6	43.73	0.011 ± 0.004	< 540	< 307
4	$3.230^{+0.007}_{-0.006}$	10.98	$0.4^{+0.1}_{-0.1}$	$0.1^{+0.1}_{-0.0}$	[-0.7,-0.4]	1.21 ± 0.09	0.000 ± 0.024	< 43.6	43.60	0.003 ± 0.003	< 967	< 242
5	$2.665^{+0.003}_{-0.007}$	11.34	$0.4^{+0.2}_{-0.2}$	$0.8^{+0.2}_{-0.2}$	[-0.4]	1.39 ± 0.12	0.171 ± 0.017	< 43.6	44.02	0.000 ± 0.002	644	< 122
6	$2.801^{+0.005}_{-0.002}$	11.36	$0.1^{+0.1}_{-0.1}$	$1.0^{+0.0}_{-0.1}$	[-0.4]	1.34 ± 0.12	0.100 ± 0.021	44.34 ± 0.32	43.91	0.002 ± 0.003	508	< 197
7	$2.674^{+0.005a}_{-0.009}$	11.55	$0.7^{+0.2}_{-0.1}$	$0.6^{+0.1}_{-0.2}$	[-0.7,0]	1.27 ± 0.17	0.111 ± 0.011	44.26 ± 0.36	43.89	0.004 ± 0.003	419	< 183
8	$2.998^{+0.002}_{-0.003}$	11.40	$0.7^{+0.0}_{-0.0}$	$0.1^{+0.0}_{-0.0}$	[-0.7,-0.4]	1.41 ± 0.09	0.000 ± 0.018	< 43.6	43.42	0.002 ± 0.002	< 394	< 144
9	$2.667^{+0.015}_{-0.002}$	11.53	$0.5^{+0.1}_{-0.1}$	$0.7^{+0.1}_{-0.0}$	[-0.4,0]	1.61 ± 0.20	0.032 ± 0.023	< 43.6	43.50	0.005 ± 0.003	< 261	< 183
10	$2.393^{+0.011}_{-0.000}$	11.33	$0.3^{+0.3}_{-0.1}$	$1.6^{+0.1}_{-0.3}$	[0]	1.15 ± 0.15	0.146 ± 0.020	43.73 ± 0.29	43.87	0.005 ± 0.003	289	< 155

^a Obtained with the addition of NUV-to-NIR broad-band photometry as described in Sect. 4.2.

Table 3: Best fit values and their 1σ uncertainties. Observed 24 μm and 3GHz flux densities. Upper limits are given at 3σ . Those for the observed bolometric X-ray luminosities were derived median-stacking all undetected sources. Stellar masses are taken from Lustig et al. 2020 and converted to a Salpeter IMF. ID 2 is absent from the J18 catalog due to the absence of K_s and VLA 3 GHz priors.

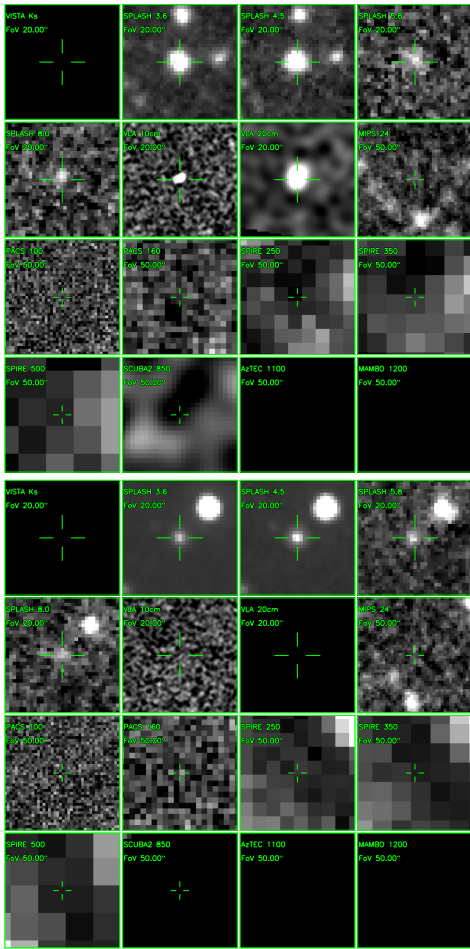
References

- Aird, J., Coil, A. L., & Georgakakis, A. 2019, MNRAS, 484, 4360
Anders, P. & Fritze-v. Alvensleben, U. 2003, A&A, 401, 1063
Arnouts, S., Walcher, C. J., Le Fèvre, O., et al. 2007, A&A, 476, 137
Avni, Y. 1976, ApJ, 210, 642
Baldry, I. K., Glazebrook, K., Brinkmann, J., et al. 2004, ApJ, 600, 681
Balogh, M. L., Morris, S. L., Yee, H. K. C., Carlberg, R. G., & Ellingson, E. 1999, ApJ, 527, 54
Barro, G., Faber, S. M., Dekel, A., et al. 2016, ApJ, 820, 120
Barro, G., Faber, S. M., Pérez-González, P. G., et al. 2013, ApJ, 765, 104
Belli, S., Newman, A. B., & Ellis, R. S. 2015, ApJ, 799, 206
Belli, S., Newman, A. B., & Ellis, R. S. 2017, ApJ, 834, 18
Belli, S., Newman, A. B., & Ellis, R. S. 2019, ApJ, 874, 17
Best, P. N., Kauffmann, G., Heckman, T. M., et al. 2005, MNRAS, 362, 25
Béthermin, M., Daddi, E., Magdis, G., et al. 2015, A&A, 573, A113
Bezanson, R., van Dokkum, P., van de Sande, J., Franx, M., & Kriek, M. 2013, ApJ, 764, L8
Brammer, G., Ryan, R., & Pirzkal, N. 2015, Source-dependent master sky images for the WFC3/IR grisms, Space Telescope WFC Instrument Science Report
Brammer, G. B., van Dokkum, P. G., & Coppi, P. 2008, ApJ, 686, 1503
Bruzual, G. & Charlot, S. 2003, MNRAS, 344, 1000
Calzetti, D., Armus, L., Bohlin, R. C., et al. 2000, ApJ, 533, 682
Capozzi, D., Maraston, C., Daddi, E., et al. 2016, MNRAS, 456, 790
Carollo, C. M., Bschorr, T. J., Renzini, A., et al. 2013, ApJ, 773, 112
Carraro, R., Rodighiero, G., Cassata, P., et al. 2020, arXiv e-prints, arXiv:2007.11002
Cattaneo, A., Dekel, A., Devriendt, J., Guiderdoni, B., & Blaizot, J. 2006, MNRAS, 370, 1651
Cecchi, R., Bolzonella, M., Cimatti, A., & Girelli, G. 2019, ApJ, 880, L14
Cimatti, A., Cassata, P., Pozzetti, L., et al. 2008, A&A, 482, 21
Cimatti, A., Daddi, E., & Renzini, A. 2006, A&A, 453, L29
Cimatti, A., Daddi, E., Renzini, A., et al. 2004, Nature, 430, 184
Citro, A., Pozzetti, L., Moresco, M., & Cimatti, A. 2016, A&A, 592, A19
Civano, F., Marchesi, S., Comastri, A., et al. 2016, ApJ, 819, 62
Croton, D. J., Springel, V., White, S. D. M., et al. 2006, MNRAS, 365, 11
Daddi, E., Bournaud, F., Walter, F., et al. 2010, ApJ, 713, 686
Daddi, E., Cimatti, A., Renzini, A., et al. 2004, ApJ, 617, 746
Daddi, E., Renzini, A., Pirzkal, N., et al. 2005, ApJ, 626, 680
Davé, R., Anglés-Alcázar, D., Narayanan, D., et al. 2019, MNRAS, 486, 2827
Davé, R., Thompson, R., & Hopkins, P. F. 2016, MNRAS, 462, 3265
Davidzon, I., Ilbert, O., Laigle, C., et al. 2017, A&A, 605, A70
De Lucia, G. & Blaizot, J. 2007, MNRAS, 375, 2
Dekel, A. & Birnboim, Y. 2006, MNRAS, 368, 2
Dekel, A., Sari, R., & Ceverino, D. 2009, ApJ, 703, 785
Dekel, A. & Silk, J. 1986, ApJ, 303, 39
Delhaize, J., Smolčić, V., Delvecchio, I., et al. 2017, A&A, 602, A4
Delvecchio, I., Daddi, E., Sargent, M. T., et al. 2020, arXiv e-prints, arXiv:2010.05510
D'Eugenio, C., Daddi, E., Gobat, R., et al. 2020, ApJ, 892, L2
Di Matteo, T., Springel, V., & Hernquist, L. 2005, Nature, 433, 604
Draine, B. T. & Li, A. 2007, ApJ, 657, 810
Drory, N., Bundy, K., Leauthaud, A., et al. 2009, ApJ, 707, 1595
Dunlop, J., Peacock, J., Spinrad, H., et al. 1996, Nature, 381, 581
Elbaz, D., Leiton, R., Nagar, N., et al. 2018, A&A, 616, A110
Emsellem, E., Cappellari, M., Krajnović, D., et al. 2011, MNRAS, 414, 888
Esdaile, J., Glazebrook, K., Labbe, I., et al. 2020, arXiv e-prints, arXiv:2010.09738
Estrada-Carpenter, V., Papovich, C., Momcheva, I., et al. 2019, ApJ, 870, 133
Estrada-Carpenter, V., Papovich, C., Momcheva, I., et al. 2020, ApJ, 898, 171
Feldmann, R. & Mayer, L. 2015, MNRAS, 446, 1939
Fiore, F., Puccetti, S., Brusa, M., et al. 2009, ApJ, 693, 447
Fitzpatrick, E. L. & Massa, D. 1986, ApJ, 307, 286
Fontana, A., Pozzetti, L., Donnarumma, I., et al. 2004, A&A, 424, 23
Forrest, B., Annunziatella, M., Wilson, G., et al. 2020a, ApJ, 890, L1
Forrest, B., Marsan, Z. C., Annunziatella, M., et al. 2020b, arXiv e-prints, arXiv:2009.07281
Franx, M., Labbé, I., Rudnick, G., et al. 2003, ApJ, 587, L79
Fumagalli, M., Labbé, I., Patel, S. G., et al. 2014, ApJ, 796, 35
Gallazzi, A., Charlot, S., Brinchmann, J., White, S. D. M., & Tremonti, C. A. 2005, MNRAS, 362, 41
Gargiulo, A., Saracco, P., Tamburri, S., Lonoce, I., & Ciocca, F. 2016, A&A, 592, A132
Genel, S., Vogelsberger, M., Springel, V., et al. 2014, MNRAS, 445, 175
Genzel, R., Tacconi, L. J., Gracia-Carpio, J., et al. 2010, MNRAS, 407, 2091
Gilli, R., Comastri, A., & Hasinger, G. 2007, A&A, 463, 79
Girelli, G., Pozzetti, L., Bolzonella, M., et al. 2020, A&A, 634, A135
Glazebrook, K., Schreiber, C., Labbé, I., et al. 2017, Nature, 544, 71
Gobat, R., Daddi, E., Magdis, G., et al. 2018, Nature Astronomy, 2, 239
Gobat, R., Daddi, E., Strazzullo, V., et al. 2017, A&A, 599, A95

- Gobat, R., Strazzullo, V., Daddi, E., et al. 2012, *ApJ*, 759, L44
 Gómez-Guijarro, C., Magdis, G. E., Valentino, F., et al. 2019, *ApJ*, 886, 88
 Gómez-Guijarro, C., Toft, S., Karim, A., et al. 2018, *ApJ*, 856, L21
 Häring, N. & Rix, H.-W. 2004, *ApJ*, 604, L89
 Henriques, B. M. B., White, S. D. M., Thomas, P. A., et al. 2017, *MNRAS*, 469, 2626
 Hopkins, P. F., Hernquist, L., Cox, T. J., et al. 2006, *ApJS*, 163, 1
 Ilbert, O., McCracken, H. J., Le Fèvre, O., et al. 2013, *A&A*, 556, A55
 Jin, S., Daddi, E., Liu, D., et al. 2018, *ApJ*, 864, 56
 Johansson, P. H., Naab, T., & Ostriker, J. P. 2009, *ApJ*, 697, L38
 Johansson, P. H., Naab, T., & Ostriker, J. P. 2012, *ApJ*, 754, 115
 Kawinwanichakij, L., Papovich, C., Ciardullo, R., et al. 2020, *ApJ*, 892, 7
 Kennicutt, Robert C., J. 1998, *ARA&A*, 36, 189
 Khochfar, S. & Ostriker, J. P. 2008, *ApJ*, 680, 54
 Kriek, M. & Conroy, C. 2013, *ApJ*, 775, L16
 Kriek, M., Conroy, C., van Dokkum, P. G., et al. 2016, *Nature*, 540, 248
 Kriek, M., van Dokkum, P. G., Franx, M., et al. 2006, *ApJ*, 645, 44
 Kriek, M., van Dokkum, P. G., Labbé, I., et al. 2009, *ApJ*, 700, 221
 Krogager, J. K., Zirm, A. W., Toft, S., Man, A., & Brammer, G. 2014, *ApJ*, 797, 17
 Labbé, I., Huang, J., Franx, M., et al. 2005, *ApJ*, 624, L81
 Laigle, C., McCracken, H. J., Ilbert, O., et al. 2016, *ApJS*, 224, 24
 Le Borgne, D., Abraham, R., Daniel, K., et al. 2006, *ApJ*, 642, 48
 Le Floch, E., Aussel, H., Ilbert, O., et al. 2009, *ApJ*, 703, 222
 Lemaux, B. C., Le Floch, E., Le Fèvre, O., et al. 2017, *A&A*, 597, C1
 Liu, D., Daddi, E., Dickinson, M., et al. 2018, *ApJ*, 853, 172
 Lusso, E., Comastri, A., Simmons, B. D., et al. 2012, *MNRAS*, 425, 623
 Lustig, P., Strazzullo, V., DEugenio, C., et al. 2020, *MNRAS*
 Madau, P. & Dickinson, M. 2014, *ARA&A*, 52, 415
 Magdis, G. E., Daddi, E., Béthermin, M., et al. 2012, *ApJ*, 760, 6
 Magnelli, B., Ivison, R. J., Lutz, D., et al. 2015, *A&A*, 573, A45
 Maltby, D. T., Almaini, O., Wild, V., et al. 2018, *MNRAS*, 480, 381
 Man, A. & Belli, S. 2018, *Nature Astronomy*, 2, 695
 Marsan, Z. C., Muzzin, A., Marchesini, D., et al. 2020, arXiv e-prints, arXiv:2010.04725
 Martig, M., Bournaud, F., Teyssier, R., & Dekel, A. 2009, *ApJ*, 707, 250
 Matharu, J., Muzzin, A., Brammer, G. B., et al. 2019, *MNRAS*, 484, 595
 McCarthy, I. G., Schaye, J., Bower, R. G., et al. 2011, *MNRAS*, 412, 1965
 McCracken, H. J., Capak, P., Salvato, M., et al. 2010, *ApJ*, 708, 202
 Merlin, E., Fortuni, F., Torelli, M., et al. 2019, *MNRAS*, 490, 3309
 Mullaney, J. R., Alexander, D. M., Goulding, A. D., & Hickox, R. C. 2011, *MNRAS*, 414, 1082
 Murray, N., Quataert, E., & Thompson, T. A. 2005, *ApJ*, 618, 569
 Muzzin, A., Marchesini, D., Stefanon, M., et al. 2013, *ApJ*, 777, 18
 Nelson, D., Genel, S., Vogelsberger, M., et al. 2015, *MNRAS*, 448, 59
 Nelson, D., Springel, V., Pillepich, A., et al. 2019, *Computational Astrophysics and Cosmology*, 6, 2
 Newman, A. B., Belli, S., Ellis, R. S., & Patel, S. G. 2018, *ApJ*, 862, 125
 Newman, A. B., Ellis, R. S., Bundy, K., & Treu, T. 2012, *ApJ*, 746, 162
 Noll, S., Burgarella, D., Giovannoli, E., et al. 2009, *A&A*, 507, 1793
 Olsen, K. P., Rasmussen, J., Toft, S., & Zirm, A. W. 2013, *ApJ*, 764, 4
 Onodera, M., Carollo, C. M., Renzini, A., et al. 2015, *ApJ*, 808, 161
 Onodera, M., Renzini, A., Carollo, M., et al. 2012, *ApJ*, 755, 26
 Pillepich, A., Springel, V., Nelson, D., et al. 2018, *MNRAS*, 473, 4077
 Poggianti, B. M. & Wu, H. 2000, *ApJ*, 529, 157
 Pozzetti, L., Bolzonella, M., Zucca, E., et al. 2010, *A&A*, 523, A13
 Pozzetti, L. & Mannucci, F. 2000, *MNRAS*, 317, L17
 Puglisi, A., Daddi, E., Liu, D., et al. 2019, *ApJ*, 877, L23
 Renzini, A. 2006, *ARA&A*, 44, 141
 Salim, S., Boquien, M., & Lee, J. C. 2018, *ApJ*, 859, 11
 Salpeter, E. E. 1955, *ApJ*, 121, 161
 Sanders, D. B., Soifer, B. T., Elias, J. H., et al. 1988, *ApJ*, 325, 74
 Saracco, P., Longhetti, M., & Gargiulo, A. 2011, *MNRAS*, 412, 2707
 Sargent, M. T., Daddi, E., Béthermin, M., et al. 2014, *ApJ*, 793, 19
 Schaye, J., Crain, R. A., Bower, R. G., et al. 2015, *MNRAS*, 446, 521
 Schreiber, C., Glazebrook, K., Nanayakkara, T., et al. 2018, *A&A*, 618, A85
 Schreiber, C., Pannella, M., Elbaz, D., et al. 2015, *A&A*, 575, A74
 Smolčić, V., Novak, M., Bondi, M., et al. 2017, *A&A*, 602, A1
 Steinhardt, C. L., Capak, P., Masters, D., & Speagle, J. S. 2016, *ApJ*, 824, 21
 Stockmann, M., Toft, S., Gallazzi, A., et al. 2020, *ApJ*, 888, 4
 Straatman, C. M. S., Labbé, I., Spitler, L. R., et al. 2014, *ApJ*, 783, L14
 Strazzullo, V., Daddi, E., Gobat, R., et al. 2015, *A&A*, 576, L6
 Tacconi, L. J., Genzel, R., Neri, R., et al. 2010, *Nature*, 463, 781
 Thomas, D., Maraston, C., Bender, R., & Mendes de Oliveira, C. 2005, *ApJ*, 621, 673
 Thomas, D., Maraston, C., Schawinski, K., Sarzi, M., & Silk, J. 2010, *MNRAS*, 404, 1775
 Toft, S., Gallazzi, A., Zirm, A., et al. 2012, *ApJ*, 754, 3
 Toft, S., Smolčić, V., Magnelli, B., et al. 2014, *ApJ*, 782, 68
 Tran, K.-V. H., Franx, M., Illingworth, G., Kelson, D. D., & van Dokkum, P. 2003, *ApJ*, 599, 865
 Valentino, F., Tanaka, M., Davidzon, I., et al. 2020, *ApJ*, 889, 93
 van de Sande, J., Kriek, M., Franx, M., et al. 2013, *ApJ*, 771, 85
 van Dokkum, P. G., Bezanson, R., van der Wel, A., et al. 2014, *ApJ*, 791, 45
 van Dokkum, P. G., Franx, M., Kriek, M., et al. 2008, *ApJ*, 677, L5
 Vogelsberger, M., Genel, S., Springel, V., et al. 2014a, *Nature*, 509, 177
 Vogelsberger, M., Genel, S., Springel, V., et al. 2014b, *MNRAS*, 444, 1518
 Wellons, S., Torrey, P., Ma, C.-P., et al. 2015, *MNRAS*, 449, 361
 Whitaker, K. E., Kriek, M., van Dokkum, P. G., et al. 2012, *ApJ*, 745, 179
 Whitaker, K. E., Labbé, I., van Dokkum, P. G., et al. 2011, *ApJ*, 735, 86
 Whitaker, K. E., van Dokkum, P. G., Brammer, G., et al. 2013, *ApJ*, 770, L39
 Wild, V., Almaini, O., Dunlop, J., et al. 2016, *MNRAS*, 463, 832
 Williams, R. J., Quadri, R. F., Franx, M., van Dokkum, P., & Labbé, I. 2009, *ApJ*, 691, 1879
 Zolotov, A., Dekel, A., Mandelker, N., et al. 2015, *MNRAS*, 450, 2327

Appendix A: Additional plots

We here insert the multi-wavelength cutouts (from K_s -band to 20 cm) of our sources, together with their SED fits when available. SEDs for IDs 1 and 2 are not present since ID1 lies in a region subjected to unreliable IR fluxes and uncertainties, while ID 2 is not present in the J18 catalog due to lack of UltraVISTA K_s and VLA 3 GHz radio priors. SED fitting was carried out fixing the redshift to the best fitting grism value of each galaxy and includes four components: a stellar component from BC03 templates (black curve); a mid-IR AGN torus from Mullaney et al. 2011 (red curve); a dust continuum component from Magdis et al. 2012 templates including Béthermin et al. 2015 L_{IR}/M_{dust} evolution with redshift (green curve); and a power-law radio continuum (Magnelli et al. 2015; Delhaize et al. 2017). The downward arrows show the 2σ upper limit at a given wavelength.



ID 1
zspec=2.841
NO SED

ID 2
zspec=2.557
NO SED

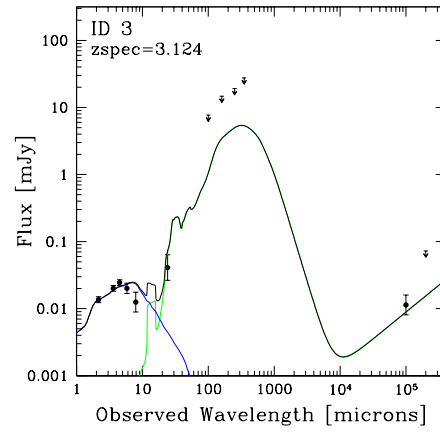
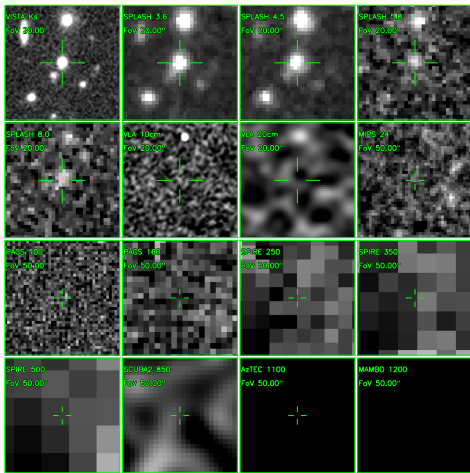
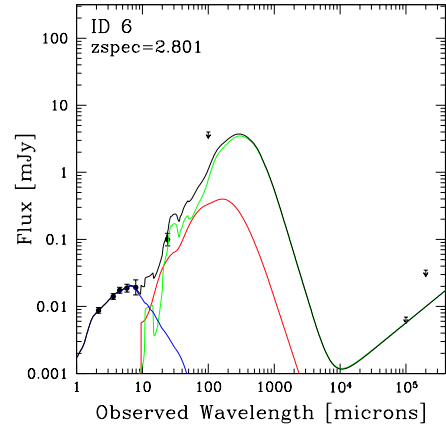
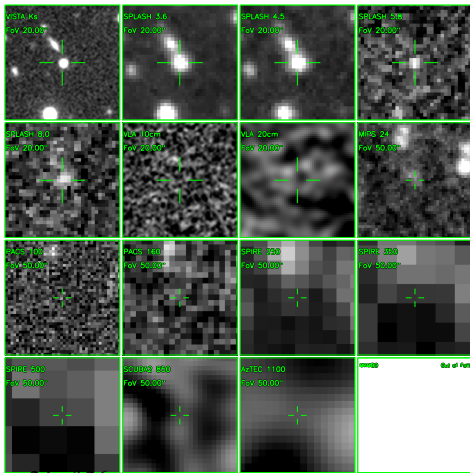
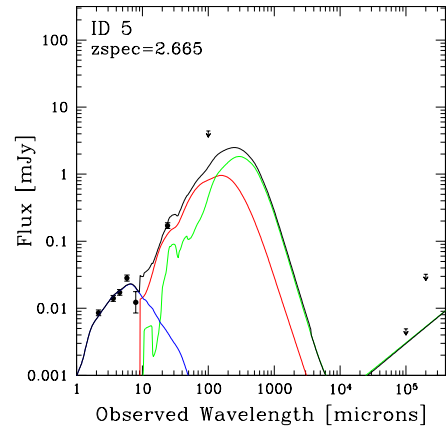
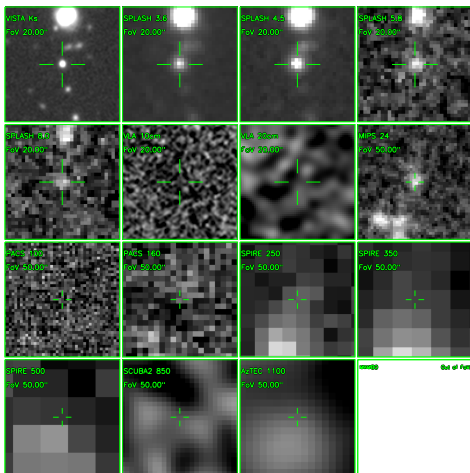
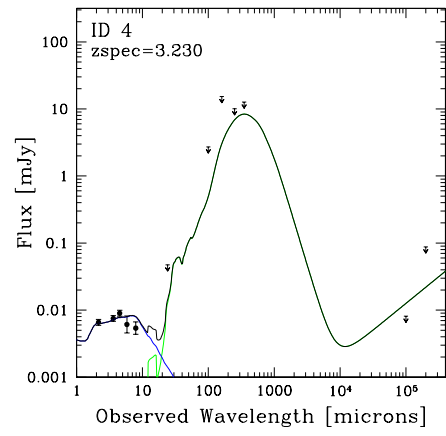
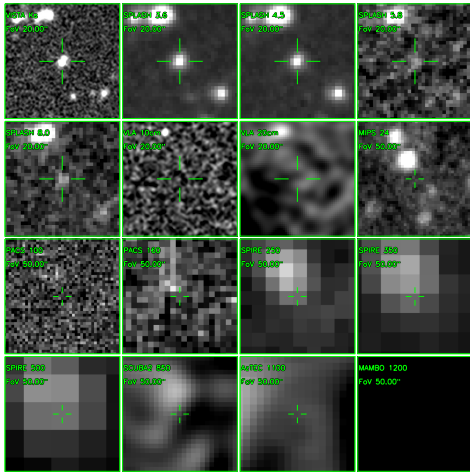
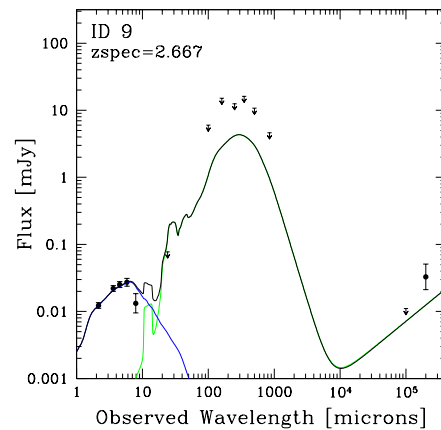
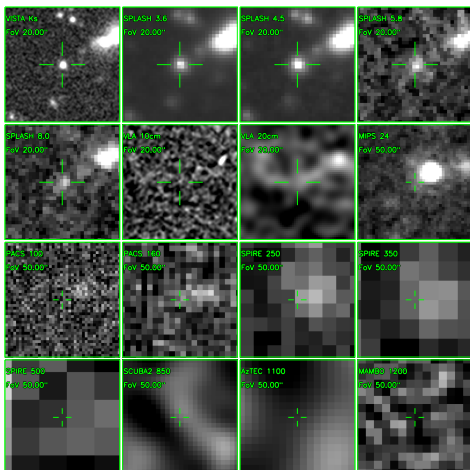
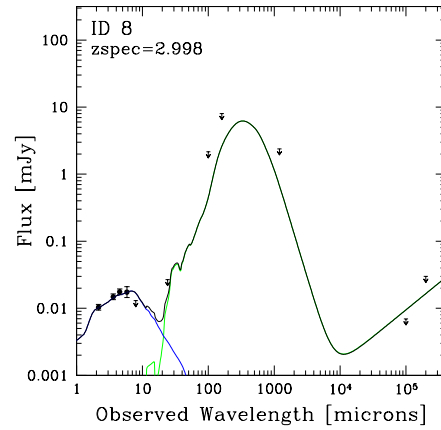
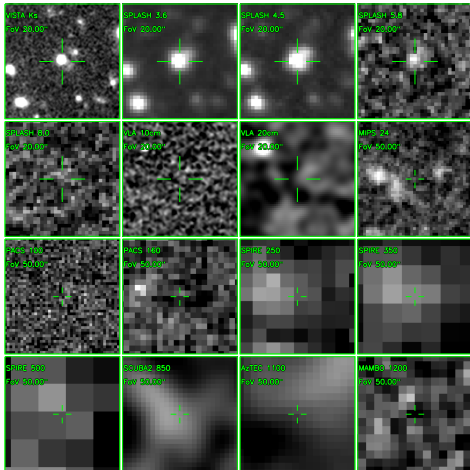
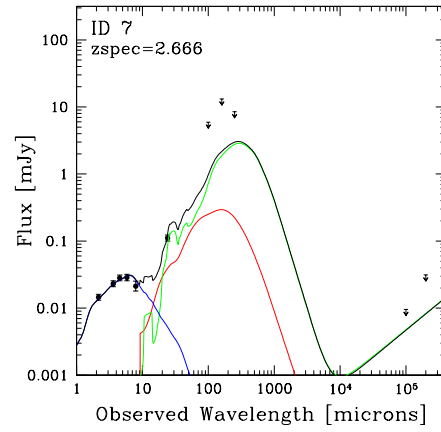
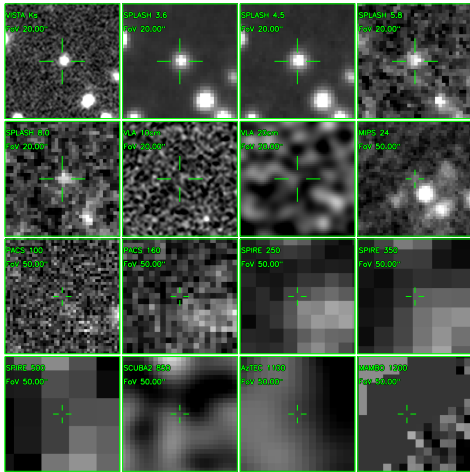


Fig. A.1: Left panel: multiband cutouts of our targets. The green text marks the instrument, the observed wavelength in units of μm and the size of the Field of View. Right panel: fits to the SEDs of our galaxies. The SEDs are fitted with a starburst-like dust continuum component (green curve Magdis et al. 2012), a stellar component (blue curve; Bruzual & Charlot 2003) and an AGN torus component (red curve Mullaney et al. 2011). The fits were fixed to the grism redshifts derived above. Upper limits are at 2σ .





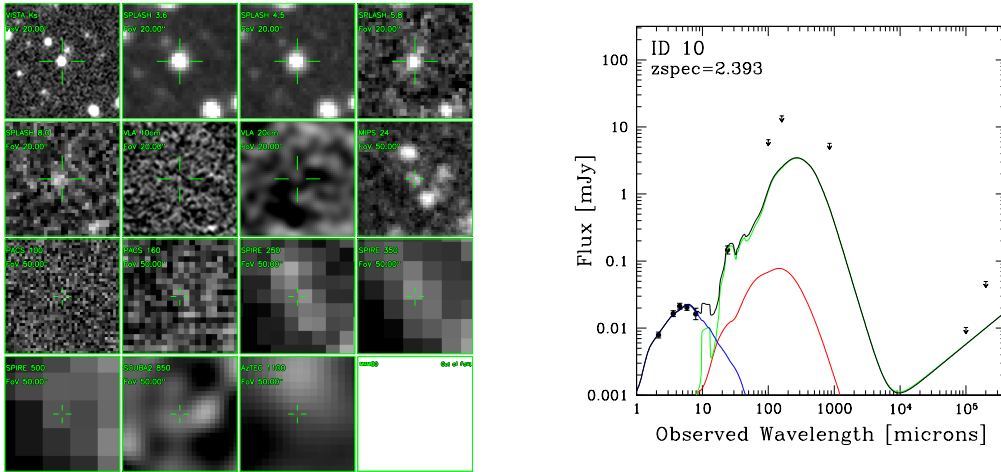


Fig. A.4: Continued.

Bibliography

In:

- Abbott, T. M. C. et al. (2018). "Dark Energy Survey Year 1 Results: A Precise H_0 Estimate from DES Y1, BAO, and D/H Data". In: 480.3, pp. 3879–3888.
- Abramson, Louis E. et al. (2014). "The Mass-independence of Specific Star Formation Rates in Galactic Disks". In: 785.2, L36, p. L36.
- Aird, J., A. L. Coil, and A. Georgakakis (2019). "X-rays across the galaxy population - III. The incidence of AGN as a function of star formation rate". In: 484.3, pp. 4360–4378.
- Alatalo, Katherine et al. (2014). "Catching Quenching Galaxies: The Nature of the WISE Infrared Transition Zone". In: 794.1, L13, p. L13.
- Anders, P. and U. Fritze-v. Alvensleben (2003). "Spectral and photometric evolution of young stellar populations: The impact of gaseous emission at various metallicities". In: 401, pp. 1063–1070.
- Arnouts, S. et al. (2007). "The SWIRE-VVDS-CFHTLS surveys: stellar mass assembly over the last 10 Gyr. Evidence for a major build up of the red sequence between $z = 2$ and $z = 1$ ". In: 476.1, pp. 137–150.
- Avni, Y. (1976). "Energy spectra of X-ray clusters of galaxies." In: 210, pp. 642–646.
- Baldry, Ivan K. et al. (2004). "Quantifying the Bimodal Color-Magnitude Distribution of Galaxies". In: 600.2, pp. 681–694.
- Balogh, Michael L. et al. (1999). "Differential Galaxy Evolution in Cluster and Field Galaxies at $z \sim 0.3$ ". In: 527.1, pp. 54–79.
- Barro, G. et al. (2014). "CANDELS+3D-HST: Compact SFGs at $z \sim 2-3$, the Progenitors of the First Quiescent Galaxies". In: 791.1, 52, p. 52.
- Barro, G. et al. (2016a). "Sub-kiloparsec ALMA Imaging of Compact Star-forming Galaxies at $z \sim 2.5$: Revealing the Formation of Dense Galactic Cores in the Progenitors of Compact Quiescent Galaxies". In: 827.2, L32, p. L32.
- Barro, Guillermo et al. (2013). "CANDELS: The Progenitors of Compact Quiescent Galaxies at $z \sim 2$ ". In: 765.2, 104, p. 104.
- Barro, Guillermo et al. (2016b). "Caught in the Act: Gas and Stellar Velocity Dispersions in a Fast Quenching Compact Star-Forming Galaxy at $z \sim 1.7$ ". In: 820.2, 120, p. 120.
- Baum, W. A. (1959). "Population Inferences from Star Counts, Surface Brightness and Colors". In: 71.419, pp. 106–117.
- Bell, Eric F. et al. (2004). "Nearly 5000 Distant Early-Type Galaxies in COMBO-17: A Red Sequence and Its Evolution since $z \sim 1$ ". In: 608.2, pp. 752–767.

- Belli, Sirio, Andrew B. Newman, and Richard S. Ellis (2015). “Stellar Populations from Spectroscopy of a Large Sample of Quiescent Galaxies at $Z \gtrsim 1$: Measuring the Contribution of Progenitor Bias to Early Size Growth”. In: 799.2, 206, p. 206.
- (2017). “MOSFIRE Spectroscopy of Quiescent Galaxies at $1.5 < z < 2.5$. I. Evolution of Structural and Dynamical Properties”. In: 834.1, 18, p. 18.
- (2019a). “MOSFIRE Spectroscopy of Quiescent Galaxies at $1.5 < z < 2.5$. II. Star Formation Histories and Galaxy Quenching”. In: 874.1, 17, p. 17.
- (2019b). “MOSFIRE Spectroscopy of Quiescent Galaxies at $1.5 \lesssim z \lesssim 2.5$. II. Star Formation Histories and Galaxy Quenching”. In: 874.1, 17, p. 17.
- Bertin, E. and S. Arnouts (1996). “SExtractor: Software for source extraction.” In: 117, pp. 393–404.
- Bertoldi, F. et al. (2007). “COSBO: The MAMBO 1.2 Millimeter Imaging Survey of the COSMOS Field”. In: 172.1, pp. 132–149.
- Best, P. N. et al. (2005). “The host galaxies of radio-loud active galactic nuclei: mass dependences, gas cooling and active galactic nuclei feedback”. In: 362.1, pp. 25–40.
- B  thermin, Matthieu et al. (2015). “Evolution of the dust emission of massive galaxies up to $z = 4$ and constraints on their dominant mode of star formation”. In: 573, A113, A113.
- Bezanson, Rachel et al. (2013). “Massive and Newly Dead: Discovery of a Significant Population of Galaxies with High-velocity Dispersions and Strong Balmer Lines at $z \sim 1.5$ from Deep Keck Spectra and HST/WFC3 Imaging”. In: 764.1, L8, p. L8.
- Bezanson, Rachel et al. (2019). “Extremely Low Molecular Gas Content in a Compact, Quiescent Galaxy at $z = 1.522$ ”. In: 873.2, L19, p. L19.
- Blumenthal, G. R. et al. (1984). “Formation of galaxies and large-scale structure with cold dark matter.” In: 311, pp. 517–525.
- Boquien, M. et al. (2019). “CIGALE: a python Code Investigating GALaxy Emission”. In: 622, A103, A103.
- Bournaud, Fr  d  ric et al. (2011). “Black Hole Growth and Active Galactic Nuclei Obscuration by Instability-driven Inflows in High-redshift Disk Galaxies Fed by Cold Streams”. In: 741.2, L33, p. L33.
- Bower, R. G. et al. (2006). “Breaking the hierarchy of galaxy formation”. In: 370.2, pp. 645–655.
- Brammer, G., R. Ryan, and N. Pirzkal (2015). *Source-dependent master sky images for the WFC3/IR grisms*. Space Telescope WFC Instrument Science Report.
- Brammer, G. B. et al. (2009). “The Dead Sequence: A Clear Bimodality in Galaxy Colors from $z = 0$ to $z = 2.5$ ”. In: 706.1, pp. L173–L177.
- Brammer, Gabriel B., Pieter G. van Dokkum, and Paolo Coppi (2008). “EAZY: A Fast, Public Photometric Redshift Code”. In: 686.2, pp. 1503–1513.
- Brinchmann, J. et al. (2004). “The physical properties of star-forming galaxies in the low-redshift Universe”. In: 351.4, pp. 1151–1179.

- Bruzual, G. and S. Charlot (2003). “Stellar population synthesis at the resolution of 2003”. In: 344.4, pp. 1000–1028.
- Calabrò, A. et al. (2019a). “Deciphering an evolutionary sequence of merger stages in infrared-luminous starburst galaxies at $z \sim 0.7$ ”. In: 623, A64, A64.
- Calabrò, Antonello et al. (2019b). “Merger induced clump formation in distant infrared luminous starburst galaxies”. In: 632, A98, A98.
- Calzetti, Daniela et al. (2000). “The Dust Content and Opacity of Actively Star-forming Galaxies”. In: 533.2, pp. 682–695.
- Capak, P. et al. (2007). “The First Release COSMOS Optical and Near-IR Data and Catalog”. In: 172.1, pp. 99–116.
- Capozzi, Diego et al. (2016). “Revisiting the role of the thermally pulsating asymptotic-giant-branch phase in high-redshift galaxies”. In: 456.1, pp. 790–830.
- Cappellari, Michele (2016). “Structure and Kinematics of Early-Type Galaxies from Integral Field Spectroscopy”. In: 54, pp. 597–665.
- (2017). “Improving the full spectrum fitting method: accurate convolution with Gauss-Hermite functions”. In: 466.1, pp. 798–811.
- Cappellari, Michele and Eric Emsellem (2004). “Parametric Recovery of Line-of-Sight Velocity Distributions from Absorption-Line Spectra of Galaxies via Penalized Likelihood”. In: 116.816, pp. 138–147.
- Cappelluti, N. et al. (2009). “The XMM-Newton wide-field survey in the COSMOS field. The point-like X-ray source catalogue”. In: 497.2, pp. 635–648.
- Carnall, A. C. et al. (2020). “Timing the earliest quenching events with a robust sample of massive quiescent galaxies at $2 < z < 5$ ”. In: 496.1, pp. 695–707.
- Carnall, Adam C. et al. (2019). “How to Measure Galaxy Star Formation Histories. I. Parametric Models”. In: 873.1, 44, p. 44.
- Carollo, C. M. et al. (2013). “Newly Quenched Galaxies as the Cause for the Apparent Evolution in Average Size of the Population”. In: 773.2, 112, p. 112.
- Carraro, R. et al. (2020). “Co-evolution of black hole accretion and star formation in galaxies up to $z=3.5$ ”. In: *arXiv e-prints*, arXiv:2007.11002, arXiv:2007.11002.
- Cassata, P. et al. (2010). “The Morphology of Passively Evolving Galaxies at $z \sim 2$ from Hubble Space Telescope/WFC3 Deep Imaging in the Hubble Ultra Deep Field”. In: 714.1, pp. L79–L83.
- Castignani, G. et al. (2014). “A New Method to Search for High-redshift Clusters Using Photometric Redshifts”. In: 792.2, 113, p. 113.
- Castignani, G. et al. (2019). “Molecular gas in radio galaxies in dense megaparsec-scale environments at $z = 0.4-2.6$ ”. In: 623, A48, A48.
- Cattaneo, A. et al. (2006). “Modelling the galaxy bimodality: shutdown above a critical halo mass”. In: 370.4, pp. 1651–1665.

- Cattaneo, A. et al. (2009). "The role of black holes in galaxy formation and evolution". In: 460.7252, pp. 213–219.
- Cecchi, Rachele et al. (2019). "Quiescent Galaxies at $z \gtrsim 2.5$: Observations versus Models". In: 880.1, L14, p. L14.
- Chevallard, Jacopo and Stéphane Charlot (2016). "Modelling and interpreting spectral energy distributions of galaxies with BEAGLE". In: 462.2, pp. 1415–1443.
- Cid Fernandes, Roberto et al. (2005). "Semi-empirical analysis of Sloan Digital Sky Survey galaxies - I. Spectral synthesis method". In: 358.2, pp. 363–378.
- Cimatti, A., E. Daddi, and A. Renzini (2006). "Mass downsizing and "top-down" assembly of early-type galaxies". In: 453.2, pp. L29–L33.
- Cimatti, A. et al. (2004). "Old galaxies in the young Universe". In: 430.6996, pp. 184–187.
- Cimatti, A. et al. (2008). "GMSS ultradeep spectroscopy of galaxies at $z \sim 2$. II. Superdense passive galaxies: how did they form and evolve?" In: 482.1, pp. 21–42.
- Citro, Annalisa et al. (2016). "Inferring the star-formation histories of the most massive and passive early-type galaxies at $z < 0.3$ ". In: 592, A19, A19.
- Civano, F. et al. (2016). "The Chandra Cosmos Legacy Survey: Overview and Point Source Catalog". In: 819.1, 62, p. 62.
- Conroy, Charlie (2013). "Modeling the Panchromatic Spectral Energy Distributions of Galaxies". In: 51.1, pp. 393–455.
- Cowie, L. L. et al. (2017). "A Submillimeter Perspective on the GOODS Fields (SUPER GOODS). I. An Ultradeep SCUBA-2 Survey of the GOODS-N". In: 837.2, 139, p. 139.
- Croton, Darren J. et al. (2006). "The many lives of active galactic nuclei: cooling flows, black holes and the luminosities and colours of galaxies". In: 365.1, pp. 11–28.
- da Cunha, Elisabete, Stéphane Charlot, and David Elbaz (2008). "A simple model to interpret the ultraviolet, optical and infrared emission from galaxies". In: 388.4, pp. 1595–1617.
- Daddi, E. et al. (2004). "A New Photometric Technique for the Joint Selection of Star-forming and Passive Galaxies at $1.4 < z < 2.5$ ". In: 617.2, pp. 746–764.
- Daddi, E. et al. (2005). "Passively Evolving Early-Type Galaxies at $1.4 < z < 2.5$ in the Hubble Ultra Deep Field". In: 626.2, pp. 680–697.
- Daddi, E. et al. (2007). "Multiwavelength Study of Massive Galaxies at $z \sim 2$. I. Star Formation and Galaxy Growth". In: 670.1, pp. 156–172.
- Daddi, E. et al. (2010). "Very High Gas Fractions and Extended Gas Reservoirs in $z = 1.5$ Disk Galaxies". In: 713.1, pp. 686–707.
- Daddi, E. et al. (2020). "Three Lyman-alpha emitting filaments converging to a massive galaxy group at $z=2.91$: a case for cold gas infall". In: *arXiv e-prints*, arXiv:2006.11089, arXiv:2006.11089.

- Davé, Romeel, Robert Thompson, and Philip F. Hopkins (2016). “MUFASA: galaxy formation simulations with meshless hydrodynamics”. In: 462.3, pp. 3265–3284.
- Davé, Romeel et al. (2017). “MUFASA: Galaxy star formation, gas, and metal properties across cosmic time”. In: 467.1, pp. 115–132.
- Davé, Romeel et al. (2019). “SIMBA: Cosmological simulations with black hole growth and feedback”. In: 486.2, pp. 2827–2849.
- Davidzon, I. et al. (2017). “The COSMOS2015 galaxy stellar mass function . Thirteen billion years of stellar mass assembly in ten snapshots”. In: 605, A70, A70.
- Davis, Timothy A. et al. (2014a). “The ATLAS^{3D} Project - XXVIII. Dynamically driven star formation suppression in early-type galaxies”. In: 444.4, pp. 3427–3445.
- (2014b). “The ATLAS^{3D} Project - XXVIII. Dynamically driven star formation suppression in early-type galaxies”. In: 444.4, pp. 3427–3445.
- De Lucia, Gabriella and Jérémy Blaizot (2007). “The hierarchical formation of the brightest cluster galaxies”. In: 375.1, pp. 2–14.
- De Lucia, Gabriella et al. (2006). “The formation history of elliptical galaxies”. In: 366.2, pp. 499–509.
- de Vaucouleurs, Gerard (1948). “Recherches sur les Nebuleuses Extragalactiques”. In: *Annales d’Astrophysique* 11, p. 247.
- (1961). “Integrated Colors of Bright Galaxies in the u, b, V System.” In: 5, p. 233.
- Dekel, A. and A. Burkert (2014). “Wet disc contraction to galactic blue nuggets and quenching to red nuggets”. In: 438.2, pp. 1870–1879.
- Dekel, A. and J. Silk (1986). “The Origin of Dwarf Galaxies, Cold Dark Matter, and Biased Galaxy Formation”. In: 303, p. 39.
- Dekel, Avishai and Yuval Birnboim (2006). “Galaxy bimodality due to cold flows and shock heating”. In: 368.1, pp. 2–20.
- Dekel, Avishai, Re’em Sari, and Daniel Ceverino (2009). “Formation of Massive Galaxies at High Redshift: Cold Streams, Clumpy Disks, and Compact Spheroids”. In: 703.1, pp. 785–801.
- Delvecchio, I. et al. (2020). “The infrared-radio correlation of star-forming galaxies is strongly M_* -dependent but nearly redshift-invariant since $z \sim 4$ ”. In: *arXiv e-prints*, arXiv:2010.05510, arXiv:2010.05510.
- D’Eugenio, C. et al. (2020). “The Typical Massive Quiescent Galaxy at $z \sim 3$ is a Post-starburst”. In: 892.1, L2, p. L2.
- Di Matteo, Tiziana, Volker Springel, and Lars Hernquist (2005). “Energy input from quasars regulates the growth and activity of black holes and their host galaxies”. In: 433.7026, pp. 604–607.
- Djorgovski, S. and Marc Davis (1987). “Fundamental Properties of Elliptical Galaxies”. In: 313, p. 59.
- Draine, B. T. and Aigen Li (2007). “Infrared Emission from Interstellar Dust. IV. The Silicate-Graphite-PAH Model in the Post-Spitzer Era”. In: 657.2, pp. 810–837.

- Dressler, A. and J. E. Gunn (1983). "Spectroscopy of galaxies in distant clusters. II. The population of the 3C 295 cluster." In: 270, pp. 7–19.
- Dressler, Alan et al. (1987). "Spectroscopy and Photometry of Elliptical Galaxies. I. New Distance Estimator". In: 313, p. 42.
- Dressler, Alan et al. (1999). "A Spectroscopic Catalog of 10 Distant Rich Clusters of Galaxies". In: 122.1, pp. 51–80.
- Drory, N. et al. (2009). "The Bimodal Galaxy Stellar Mass Function in the COSMOS Survey to $z \sim 1$: A Steep Faint End and a New Galaxy Dichotomy". In: 707.2, pp. 1595–1609.
- Dunlop, James et al. (1996). "A 3.5-Gyr-old galaxy at redshift 1.55". In: 381.6583, pp. 581–584.
- Elbaz, D. et al. (2007). "The reversal of the star formation-density relation in the distant universe". In: 468.1, pp. 33–48.
- Elbaz, D. et al. (2018). "Starbursts in and out of the star-formation main sequence". In: 616, A110, A110.
- Elvis, Martin et al. (2009). "The Chandra COSMOS Survey. I. Overview and Point Source Catalog". In: 184.1, pp. 158–171.
- Emsellem, Eric et al. (2011). "The ATLAS^{3D} project - III. A census of the stellar angular momentum within the effective radius of early-type galaxies: unveiling the distribution of fast and slow rotators". In: 414.2, pp. 888–912.
- Estrada-Carpenter, Vicente et al. (2019). "CLEAR. I. Ages and Metallicities of Quiescent Galaxies at $1.0 < z < 1.8$ Derived from Deep Hubble Space Telescope Grism Data". In: 870.2, 133, p. 133.
- Estrada-Carpenter, Vicente et al. (2020). "CLEAR. II. Evidence for Early Formation of the Most Compact Quiescent Galaxies at High Redshift". In: 898.2, 171, p. 171.
- Faber, S. M. and R. E. Jackson (1976). "Velocity dispersions and mass-to-light ratios for elliptical galaxies." In: 204, pp. 668–683.
- Feldmann, Robert and Lucio Mayer (2015). "The Argo simulation - I. Quenching of massive galaxies at high redshift as a result of cosmological starvation". In: 446.2, pp. 1939–1956.
- Fiore, F. et al. (2009). "Chasing Highly Obscured QSOs in the COSMOS Field". In: 693.1, pp. 447–462.
- Fitzpatrick, E. L. and D. Massa (1986). "An Analysis of the Shapes of Ultraviolet Extinction Curves. I. The 2175 Angstrom Bump". In: 307, p. 286.
- Fontana, A. et al. (2004). "The K20 survey. VI. The distribution of the stellar masses in galaxies up to $z \sim 2$ ". In: 424, pp. 23–42.
- Fontanot, Fabio et al. (2009). "The many manifestations of downsizing: hierarchical galaxy formation models confront observations". In: 397.4, pp. 1776–1790.
- Forrest, Ben et al. (2020a). "An Extremely Massive Quiescent Galaxy at $z = 3.493$: Evidence of Insufficiently Rapid Quenching Mechanisms in Theoretical Models". In: 890.1, L1, p. L1.

- Forrest, Ben et al. (2020b). “The Massive Ancient Galaxies At $z > 3$ NEar-infrared (MAGAZ3NE) Survey: Confirmation of Extremely Rapid Star-Formation and Quenching Timescales for Massive Galaxies in the Early Universe”. In: *arXiv e-prints*, arXiv:2009.07281, arXiv:2009.07281.
- Franco, M. et al. (2018). “GOODS-ALMA: 1.1 mm galaxy survey. I. Source catalog and optically dark galaxies”. In: 620, A152, A152.
- Franx, Marijn et al. (2003). “A Significant Population of Red, Near-Infrared-selected High-Redshift Galaxies”. In: 587.2, pp. L79–L82.
- Franzetti, P. et al. (2007). “The VIMOS-VLT deep survey. Color bimodality and the mix of galaxy populations up to $z \sim 2$ ”. In: 465.3, pp. 711–723.
- French, K. Decker et al. (2015). “Discovery of Large Molecular Gas Reservoirs in Post-starburst Galaxies”. In: 801.1, 1, p. 1.
- Fumagalli, Mattia et al. (2014). “How Dead are Dead Galaxies? Mid-infrared Fluxes of Quiescent Galaxies at Redshift $0.3 < z < 2.5$: Implications for Star Formation Rates and Dust Heating”. In: 796.1, 35, p. 35.
- Gabor, J. M. and R. Davé (2012). “The growth of red sequence galaxies in a cosmological hydrodynamic simulation”. In: 427.3, pp. 1816–1829.
- Gallazzi, Anna et al. (2005). “The ages and metallicities of galaxies in the local universe”. In: 362.1, pp. 41–58.
- Gargiulo, A. et al. (2016). “Ultramassive dense early-type galaxies: Velocity dispersions and number density evolution since $z = 1.6$ ”. In: 592, A132, A132.
- Geach, J. E. et al. (2017). “The SCUBA-2 Cosmology Legacy Survey: 850 μm maps, catalogues and number counts”. In: 465.2, pp. 1789–1806.
- Genel, Shy et al. (2014). “Introducing the Illustris project: the evolution of galaxy populations across cosmic time”. In: 445.1, pp. 175–200.
- Genzel, R. et al. (2010). “A study of the gas-star formation relation over cosmic time”. In: 407.4, pp. 2091–2108.
- Girelli, G. et al. (2020). “The stellar-to-halo mass relation over the past 12 Gyr. I. Standard ΛCDM model”. In: 634, A135, A135.
- Girelli, Giacomo, Micol Bolzonella, and Andrea Cimatti (2019). “Massive and old quiescent galaxies at high redshift”. In: 632, A80, A80.
- Glazebrook, Karl et al. (2017a). “A massive, quiescent galaxy at a redshift of 3.717”. In: 544.7648, pp. 71–74.
- (2017b). “A massive, quiescent galaxy at a redshift of 3.717”. In: 544.7648, pp. 71–74.
- Gobat, R. et al. (2012). “The Early Early Type: Discovery of a Passive Galaxy at $z_{\text{spec}} \sim 3$ ”. In: 759.2, L44, p. L44.
- Gobat, R. et al. (2017). “In and out star formation in $z \sim 1.5$ quiescent galaxies from rest-frame UV spectroscopy and the far-infrared”. In: 599, A95, A95.
- Gobat, R. et al. (2018). “The unexpectedly large dust and gas content of quiescent galaxies at $z > 1.4$ ”. In: *Nature Astronomy* 2, pp. 239–246.
- Gobat, R. et al. (2020). “The evolution of the gas fraction of quiescent galaxies modeled as a consequence of their creation rate”. In: 644, L7, p. L7.

- Gómez-Guijarro, C. et al. (2018). "Starburst to Quiescent from HST/ALMA: Stars and Dust Unveil Minor Mergers in Submillimeter Galaxies at $z \approx 4.5$ ". In: 856.2, 121, p. 121.
- Gómez-Guijarro, C. et al. (2019). "Compact Star-forming Galaxies as Old Starbursts Becoming Quiescent". In: 886.2, 88, p. 88.
- Goto, Tomotsugu (2007). "A catalogue of local E+A (post-starburst) galaxies selected from the Sloan Digital Sky Survey Data Release 5". In: 381.1, pp. 187–193.
- Goto, Tomotsugu et al. (2003). "H δ -Strong Galaxies in the Sloan Digital Sky Survey: I. The Catalog". In: 55, pp. 771–787.
- Goulding, A. D. et al. (2014). "Tracing the Evolution of Active Galactic Nuclei Host Galaxies over the Last 9 Gyr of Cosmic Time". In: 783.1, 40, p. 40.
- Granato, Gian Luigi et al. (2004). "A Physical Model for the Coevolution of QSOs and Their Spheroidal Hosts". In: 600.2, pp. 580–594.
- Griffin, M. J. et al. (2010). "The Herschel-SPIRE instrument and its in-flight performance". In: 518, L3, p. L3.
- Hammer, F. et al. (1997). "Canada-France Redshift Survey. XIV. Spectral Properties of Field Galaxies up to $z = 1$ ". In: 481.1, pp. 49–82.
- Häring, Nadine and Hans-Walter Rix (2004). "On the Black Hole Mass-Bulge Mass Relation". In: 604.2, pp. L89–L92.
- Hayashi, Masao et al. (2018). "Molecular Gas Reservoirs in Cluster Galaxies at $z = 1.46$ ". In: 856.2, 118, p. 118.
- Henriques, Bruno M. B. et al. (2017). "Galaxy formation in the Planck cosmology - IV. Mass and environmental quenching, conformity and clustering". In: 469.3, pp. 2626–2645.
- Hopkins, Philip F. et al. (2006). "A Unified, Merger-driven Model of the Origin of Starbursts, Quasars, the Cosmic X-Ray Background, Supermassive Black Holes, and Galaxy Spheroids". In: 163.1, pp. 1–49.
- Hopkins, Philip F. et al. (2008). "A Cosmological Framework for the Co-Evolution of Quasars, Supermassive Black Holes, and Elliptical Galaxies. II. Formation of Red Ellipticals". In: 175.2, pp. 390–422.
- Hopkins, Philip F. et al. (2009). "The effects of gas on morphological transformation in mergers: implications for bulge and disc demographics". In: 397.2, pp. 802–814.
- Horne, K. (1986). "An optimal extraction algorithm for CCD spectroscopy." In: 98, pp. 609–617.
- Hubble, E. P. (1926). "Extragalactic nebulae." In: 64, pp. 321–369.
- Jin, Shuowen et al. (2018). "'Super-deblended' Dust Emission in Galaxies. II. Far-IR to (Sub)millimeter Photometry and High-redshift Galaxy Candidates in the Full COSMOS Field". In: 864.1, 56, p. 56.
- Johansson, Peter H., Thorsten Naab, and Jeremiah P. Ostriker (2009). "Gravitational Heating Helps Make Massive Galaxies Red and Dead". In: 697.1, pp. L38–L43.
- (2012). "Forming Early-type Galaxies in Λ CDM Simulations. I. Assembly Histories". In: 754.2, 115, p. 115.

- Kashino, D. et al. (2013). "The FMOS-COSMOS Survey of Star-forming Galaxies at $z \sim 1.6$. I. $H\alpha$ -based Star Formation Rates and Dust Extinction". In: 777.1, L8, p. L8.
- Kaviraj, S. et al. (2007). "The UV properties of E+A galaxies: constraints on feedback-driven quenching of star formation". In: 382.3, pp. 960–970.
- Kawinwanichakij, Lalitwadee et al. (2020). "On the (Lack of) Evolution of the Stellar Mass Function of Massive Galaxies from $z = 1.5$ to 0.4 ". In: 892.1, 7, p. 7.
- Kennicutt Robert C., Jr. (1998). "Star Formation in Galaxies Along the Hubble Sequence". In: 36, pp. 189–232.
- Khochfar, Sadegh and Jeremiah P. Ostriker (2008). "Adding Environmental Gas Physics to the Semianalytic Method for Galaxy Formation: Gravitational Heating". In: 680.1, pp. 54–69.
- Kocevski, Dale D. et al. (2012). "CANDELS: Constraining the AGN-Merger Connection with Host Morphologies at $z \sim 2$ ". In: 744.2, 148, p. 148.
- Koekemoer, Anton M. et al. (2011). "CANDELS: The Cosmic Assembly Near-infrared Deep Extragalactic Legacy Survey—The Hubble Space Telescope Observations, Imaging Data Products, and Mosaics". In: 197.2, 36, p. 36.
- Kriek, Mariska and Charlie Conroy (2013). "The Dust Attenuation Law in Distant Galaxies: Evidence for Variation with Spectral Type". In: 775.1, L16, p. L16.
- Kriek, Mariska et al. (2006). "Direct Measurements of the Stellar Continuum and Balmer/4000 Å Breaks of Red $z > 2$ Galaxies: Redshifts and Improved Constraints on Stellar Populations1," in: 645.1, pp. 44–54.
- Kriek, Mariska et al. (2009). "An Ultra-Deep Near-Infrared Spectrum of a Compact Quiescent Galaxy at $z = 2.2$ ". In: 700.1, pp. 221–231.
- Kriek, Mariska et al. (2016). "A massive, quiescent, population II galaxy at a redshift of 2.1". In: 540.7632, pp. 248–251.
- Krogager, J. K. et al. (2014). "A Spectroscopic Sample of Massive, Quiescent $z \sim 2$ Galaxies: Implications for the Evolution of the Mass-Size Relation". In: 797.1, 17, p. 17.
- Labbé, Ivo et al. (2005). "IRAC Mid-Infrared Imaging of the Hubble Deep Field-South: Star Formation Histories and Stellar Masses of Red Galaxies at $z > 2$ ". In: 624.2, pp. L81–L84.
- Laigle, C. et al. (2016). "The COSMOS2015 Catalog: Exploring the 1 <math>z < 6</math> Universe with Half a Million Galaxies". In: 224.2, 24, p. 24.
- Le Borgne, Damien et al. (2006). "Gemini Deep Deep Survey. VI. Massive $H\delta$ -strong Galaxies at $z \sim 1$ ". In: 642.1, pp. 48–62.
- Le Floc'h, Emeric et al. (2009). "Deep Spitzer $24 \mu\text{m}$ COSMOS Imaging. I. The Evolution of Luminous Dusty Galaxies—Confronting the Models". In: 703.1, pp. 222–239.
- Leja, Joel et al. (2019). "How to Measure Galaxy Star Formation Histories. II. Nonparametric Models". In: 876.1, 3, p. 3.

- Lemaux, B. C. et al. (2017). "Hidden starbursts and active galactic nuclei at $0 < z < 4$ from the Herschel-VVDS-CFHTLS-D1 field: Inferences on coevolution and feedback (Corrigendum)". In: 597, C1, p. C1.
- Lin, Lihwai et al. (2017). "SDSS-IV MaNGA-resolved Star Formation and Molecular Gas Properties of Green Valley Galaxies: A First Look with ALMA and MaNGA". In: 851.1, 18, p. 18.
- Liu, Daizhong et al. (2018). "'Super-deblended' Dust Emission in Galaxies. I. The GOODS-North Catalog and the Cosmic Star Formation Rate Density out to Redshift 6". In: 853.2, 172, p. 172.
- Lusso, E. et al. (2012). "Bolometric luminosities and Eddington ratios of X-ray selected active galactic nuclei in the XMM-COSMOS survey". In: 425.1, pp. 623–640.
- Lustig, Peter et al. (2021). "Compact, bulge-dominated structures of spectroscopically confirmed quiescent galaxies at $z \approx 3$ ". In: 501.2, pp. 2659–2676.
- Lutz, D. et al. (2011). "PACS Evolutionary Probe (PEP) - A Herschel key program". In: 532, A90, A90.
- Madau, Piero and Mark Dickinson (2014). "Cosmic Star-Formation History". In: 52, pp. 415–486.
- Magdis, Georgios E. et al. (2012). "The Evolving Interstellar Medium of Star-forming Galaxies since $z = 2$ as Probed by Their Infrared Spectral Energy Distributions". In: 760.1, 6, p. 6.
- Maltby, David T. et al. (2018a). "The structure of post-starburst galaxies at $0.5 < z < 2$: evidence for two distinct quenching routes at different epochs". In: 480.1, pp. 381–401.
- (2018b). "The structure of post-starburst galaxies at $0.5 < z < 2$: evidence for two distinct quenching routes at different epochs". In: 480.1, pp. 381–401.
- Man, Allison and Sirio Belli (2018). "Star formation quenching in massive galaxies". In: *Nature Astronomy* 2, pp. 695–697.
- Mancini, Chiara et al. (2019). "Rejuvenated galaxies with very old bulges at the origin of the bending of the main sequence and of the 'green valley'". In: 489.1, pp. 1265–1290.
- Maraston, C. et al. (2009). "Absorption line indices in the UV. I. Empirical and theoretical stellar population models". In: 493.2, pp. 425–444.
- Marchesi, S. et al. (2016). "The Chandra COSMOS Legacy survey: optical/IR identifications". In: 817.1, 34, p. 34.
- Marsan, Z. Cemile et al. (2015). "Spectroscopic Confirmation of an Ultra Massive and Compact Galaxy at $z = 3.35$: a Detailed Look at an Early Progenitor of Local Giant Ellipticals". In: 801.2, 133, p. 133.
- Marsan, Z. Cemile et al. (2020). "The Number Densities and Stellar Populations of Massive Galaxies at $3 < z < 6$: A Diverse, Rapidly Forming Population in the Early Universe". In: *arXiv e-prints*, arXiv:2010.04725, arXiv:2010.04725.

- Martig, Marie et al. (2009). "Morphological Quenching of Star Formation: Making Early-Type Galaxies Red". In: 707.1, pp. 250–267.
- Martín-Navarro, Ignacio, Glenn van de Ven, and Akin Yıldırım (2019). "Star formation quenching imprinted on the internal structure of naked red nuggets". In: 487.4, pp. 4939–4950.
- Matharu, J. et al. (2019). "HST/WFC3 grism observations of $z \sim 1$ clusters: the cluster versus field stellar mass-size relation and evidence for size growth of quiescent galaxies from minor mergers". In: 484.1, pp. 595–617.
- McCarthy, I. G. et al. (2011). "Gas expulsion by quasar-driven winds as a solution to the overcooling problem in galaxy groups and clusters". In: 412.3, pp. 1965–1984.
- McCracken, H. J. et al. (2010). "The COSMOS-WIRCam Near-Infrared Imaging Survey. I. BzK-Selected Passive and Star-Forming Galaxy Candidates at $z_{\text{gsim}} 1.4$ ". In: 708.1, pp. 202–217.
- McCracken, H. J. et al. (2012). "UltraVISTA: a new ultra-deep near-infrared survey in COSMOS". In: 544, A156, A156.
- Merlin, E. et al. (2018). "Chasing passive galaxies in the early Universe: a critical analysis in CANDELS GOODS-South". In: 473.2, pp. 2098–2123.
- Merlin, E. et al. (2019). "Red and dead CANDELS: massive passive galaxies at the dawn of the Universe". In: 490.3, pp. 3309–3328.
- Momcheva, Ivelina G. et al. (2016). "The 3D-HST Survey: Hubble Space Telescope WFC3/G141 Grism Spectra, Redshifts, and Emission Line Measurements for $\sim 100,000$ Galaxies". In: 225.2, 27, p. 27.
- Morishita, T. et al. (2018). "Metal Deficiency in Two Massive Dead Galaxies at $z \sim 2$ ". In: 856.1, L4, p. L4.
- Moster, Benjamin P. et al. (2010). "Constraints on the Relationship between Stellar Mass and Halo Mass at Low and High Redshift". In: 710.2, pp. 903–923.
- Murray, Norman, Eliot Quataert, and Todd A. Thompson (2005). "On the Maximum Luminosity of Galaxies and Their Central Black Holes: Feedback from Momentum-driven Winds". In: 618.2, pp. 569–585.
- Muzzin, Adam et al. (2013a). "A Public K_s -selected Catalog in the COSMOS/ULTRAVISTA Field: Photometry, Photometric Redshifts, and Stellar Population Parameters". In: 206.1, 8, p. 8.
- Muzzin, Adam et al. (2013b). "The Evolution of the Stellar Mass Functions of Star-forming and Quiescent Galaxies to $z = 4$ from the COSMOS/UltraVISTA Survey". In: 777.1, 18, p. 18.
- Naab, Thorsten, Peter H. Johansson, and Jeremiah P. Ostriker (2009). "Minor Mergers and the Size Evolution of Elliptical Galaxies". In: 699.2, pp. L178–L182.
- Nelson, Dylan et al. (2015). "The impact of feedback on cosmological gas accretion". In: 448.1, pp. 59–74.
- Nelson, Dylan et al. (2019). "The IllustrisTNG simulations: public data release". In: *Computational Astrophysics and Cosmology* 6.1, 2, p. 2.

- Newman, Andrew B. et al. (2012). "Can Minor Merging Account for the Size Growth of Quiescent Galaxies? New Results from the CANDELS Survey". In: 746.2, 162, p. 162.
- Newman, Andrew B. et al. (2018). "Resolving Quiescent Galaxies at $z \gtrsim 2$. I. Search for Gravitationally Lensed Sources and Characterization of Their Structure, Stellar Populations, and Line Emission". In: 862.2, 125, p. 125.
- Noeske, K. G. et al. (2007). "Star Formation in AEGIS Field Galaxies since $z=1.1$: The Dominance of Gradually Declining Star Formation, and the Main Sequence of Star-forming Galaxies". In: 660.1, pp. L43–L46.
- Noll, S. et al. (2009). "Analysis of galaxy spectral energy distributions from far-UV to far-IR with CIGALE: studying a SINGS test sample". In: 507.3, pp. 1793–1813.
- Oliver, S. J. et al. (2012). "The Herschel Multi-tiered Extragalactic Survey: HerMES". In: 424.3, pp. 1614–1635.
- Olsen, Karen P. et al. (2013). "Evidence for Widespread Active Galactic Nucleus Activity among Massive Quiescent Galaxies at $z \sim 2$ ". In: 764.1, 4, p. 4.
- Onodera, M. et al. (2012). "Deep Near-infrared Spectroscopy of Passively Evolving Galaxies at $z \gtrsim 1.4$ ". In: 755.1, 26, p. 26.
- Onodera, M. et al. (2015). "The Ages, Metallicities, and Element Abundance Ratios of Massive Quenched Galaxies at $z \sim 1.6$ ". In: 808.2, 161, p. 161.
- Pawlik, M. M. et al. (2018). "The origins of post-starburst galaxies at $z < 0.05$ ". In: 477.2, pp. 1708–1743.
- Peebles, P. J. E. (1982). "Large-scale background temperature and mass fluctuations due to scale-invariant primeval perturbations". In: 263, pp. L1–L5.
- Peng, Ying-jie et al. (2010). "Mass and Environment as Drivers of Galaxy Evolution in SDSS and zCOSMOS and the Origin of the Schechter Function". In: 721.1, pp. 193–221.
- Pillepich, Annalisa et al. (2018). "Simulating galaxy formation with the IllustrisTNG model". In: 473.3, pp. 4077–4106.
- Planck Collaboration et al. (2020). "Planck 2018 results - VI. Cosmological parameters". In: *A&A* 641, A6.
- Poggianti, B. M. et al. (2013). "Superdense Galaxies and the Mass-Size Relation at Low Redshift". In: 762.2, 77, p. 77.
- Poggianti, Bianca M. and Hong Wu (2000). "Optical Spectral Signatures of Dusty Starburst Galaxies". In: 529.1, pp. 157–169.
- Poggianti, Bianca M. et al. (2009). "The Environments of Starburst and Post-Starburst Galaxies at $z = 0.4-0.8$ ". In: 693.1, pp. 112–131.
- Poglitsch, A. et al. (2010). "The Photodetector Array Camera and Spectrometer (PACS) on the Herschel Space Observatory". In: 518, L2, p. L2.
- Pozzetti, L. and F. Mannucci (2000). "Extremely red galaxies: age and dust degeneracy solved?" In: 317.1, pp. L17–L21.

- Pozzetti, L. et al. (2010). "zCOSMOS - 10k-bright spectroscopic sample. The bimodality in the galaxy stellar mass function: exploring its evolution with redshift". In: 523, A13, A13.
- Puglisi, A. et al. (2019). "The Main Sequence at $z \sim 1.3$ Contains a Sizable Fraction of Galaxies with Compact Star Formation Sizes: A New Population of Early Post-starbursts?" In: 877.2, L23, p. L23.
- Querejeta, M. et al. (2015). "Formation of S0 galaxies through mergers. Explaining angular momentum and concentration change from spirals to S0s". In: 579, L2, p. L2.
- Rasera, Y. and R. Teyssier (2006). "The history of the baryon budget. Cosmic logistics in a hierarchical universe". In: 445.1, pp. 1–27.
- Renzini, Alvio (2006). "Stellar Population Diagnostics of Elliptical Galaxy Formation". In: 44.1, pp. 141–192.
- Riess, Adam G. et al. (2019). "Large Magellanic Cloud Cepheid Standards Provide a 1% Foundation for the Determination of the Hubble Constant and Stronger Evidence for Physics beyond Λ CDM". In: 876.1, 85, p. 85.
- Rizzo, Francesca, Filippo Fraternali, and Giuliano Iorio (2018). "S0 galaxies are faded spirals: clues from their angular momentum content". In: 476.2, pp. 2137–2167.
- Robertson, J. G. (1986). "Optical extraction of single-object spectra from observations with two-dimensional detectors." In: 98, pp. 1220–1231.
- Rodríguez-Merino, L. H. et al. (2005). "UVBLUE: A New High-Resolution Theoretical Library of Ultraviolet Stellar Spectra". In: 626.1, pp. 411–424.
- Rudnick, Gregory et al. (2017). "Deep CO(1-0) Observations of $z = 1.62$ Cluster Galaxies with Substantial Molecular Gas Reservoirs and Normal Star Formation Efficiencies". In: 849.1, 27, p. 27.
- Saintonge, Amélie et al. (2011). "COLD GASS, an IRAM legacy survey of molecular gas in massive galaxies - I. Relations between H_2 , H I, stellar content and structural properties". In: 415.1, pp. 32–60.
- Salim, Samir, Médéric Boquien, and Janice C. Lee (2018). "Dust Attenuation Curves in the Local Universe: Demographics and New Laws for Star-forming Galaxies and High-redshift Analogs". In: 859.1, 11, p. 11.
- Salpeter, Edwin E. (1955). "The Luminosity Function and Stellar Evolution." In: 121, p. 161.
- Salvador-Rusiñol, Núria et al. (2019). "Sub one per cent mass fractions of young stars in red massive galaxies". In: *Nature Astronomy* 4, pp. 252–259.
- Sanders, D. B. et al. (1988). "Ultraluminous Infrared Galaxies and the Origin of Quasars". In: 325, p. 74.
- Sanders, D. B. et al. (2007). "S-COSMOS: The Spitzer Legacy Survey of the Hubble Space Telescope ACS 2 deg² COSMOS Field I: Survey Strategy and First Analysis". In: 172.1, pp. 86–98.
- Santini, P. et al. (2019). "Passive galaxies in the early Universe: ALMA confirmation of $z \sim 3-5$ candidates in the CANDELS GOODS-South field". In: 486.1, pp. 560–569.

- Santini, P. et al. (2020). "The emergence of passive galaxies in the early Universe". In: *arXiv e-prints*, arXiv:2011.10584, arXiv:2011.10584.
- Saracco, P., M. Longhetti, and A. Gargiulo (2011). "Constraining the star formation and the assembly histories of normal and compact early-type galaxies at $1 < z < 2$ ". In: 412.4, pp. 2707–2716.
- Saracco, Paolo et al. (2020). "The Rapid Buildup of Massive Early-type Galaxies: Supersolar Metallicity, High Velocity Dispersion, and Young Age for an Early-type Galaxy at $z = 3.35$ ". In: 905.1, 40, p. 40.
- Sargent, M. T. et al. (2014). "Regularity Underlying Complexity: A Redshift-independent Description of the Continuous Variation of Galaxy-scale Molecular Gas Properties in the Mass-star Formation Rate Plane". In: 793.1, 19, p. 19.
- Sargent, M. T. et al. (2015). "A Direct Constraint on the Gas Content of a Massive, Passively Evolving Elliptical Galaxy at $z = 1.43$ ". In: 806.1, L20, p. L20.
- Schawinski, Kevin et al. (2011). "HST WFC3/IR Observations of Active Galactic Nucleus Host Galaxies at $z \sim 2$: Supermassive Black Holes Grow in Disk Galaxies". In: 727.2, L31, p. L31.
- Schaye, Joop et al. (2015). "The EAGLE project: simulating the evolution and assembly of galaxies and their environments". In: 446.1, pp. 521–554.
- Schinnerer, E. et al. (2010). "The VLA-COSMOS Survey. IV. Deep Data and Joint Catalog". In: 188.2, pp. 384–404.
- Schmidt, Maarten (1959). "The Rate of Star Formation." In: 129, p. 243.
- Schreiber, C. et al. (2015). "The Herschel view of the dominant mode of galaxy growth from $z = 4$ to the present day". In: 575, A74, A74.
- Schreiber, C. et al. (2016). "Observational evidence of a slow downfall of star formation efficiency in massive galaxies during the past 10 Gyr". In: 589, A35, A35.
- Schreiber, C. et al. (2018a). "Jekyll & Hyde: quiescence and extreme obscuration in a pair of massive galaxies 1.5 Gyr after the Big Bang". In: 611, A22, A22.
- Schreiber, C. et al. (2018b). "Near infrared spectroscopy and star-formation histories of $3 \leq z \leq 4$ quiescent galaxies". In: 618, A85, A85.
- Sell, P. H. et al. (2014). "Massive compact galaxies with high-velocity outflows: morphological analysis and constraints on AGN activity". In: 441.4, pp. 3417–3443.
- Shen, Shiyin et al. (2003). "The size distribution of galaxies in the Sloan Digital Sky Survey". In: 343.3, pp. 978–994.
- Silk, Joseph and Martin J. Rees (1998). "Quasars and galaxy formation". In: 331, pp. L1–L4.
- Smolčić, V. et al. (2017). "The VLA-COSMOS 3 GHz Large Project: Continuum data and source catalog release". In: 602, A1, A1.
- Spilker, Justin et al. (2018). "Molecular Gas Contents and Scaling Relations for Massive, Passive Galaxies at Intermediate Redshifts from the LEGA-C Survey". In: 860.2, 103, p. 103.

- Steinhardt, Charles. L. et al. (2016). "The Impossibly Early Galaxy Problem". In: 824.1, 21, p. 21.
- Stockmann, Mikkel et al. (2020). "X-shooter Spectroscopy and HST Imaging of 15 Massive Quiescent Galaxies at $z \gtrsim 2$ ". In: 888.1, 4, p. 4.
- Straatman, Caroline M. S. et al. (2014). "A Substantial Population of Massive Quiescent Galaxies at $z \sim 4$ from ZFOURGE". In: 783.1, L14, p. L14.
- Strateva, Iskra et al. (2001). "Color Separation of Galaxy Types in the Sloan Digital Sky Survey Imaging Data". In: 122.4, pp. 1861–1874.
- Strazzullo, V. et al. (2015). "Passive galaxies as tracers of cluster environments at $z \sim 2$ ". In: 576, L6, p. L6.
- Suess, Katherine A. et al. (2017). "Massive Quenched Galaxies at $z \sim 0.7$ Retain Large Molecular Gas Reservoirs". In: 846.2, L14, p. L14.
- Tacchella, S. et al. (2015). "Evidence for mature bulges and an inside-out quenching phase 3 billion years after the Big Bang". In: *Science* 348.6232, pp. 314–317.
- Tacconi, L. J. et al. (2010). "High molecular gas fractions in normal massive star-forming galaxies in the young Universe". In: 463.7282, pp. 781–784.
- Taniguchi, Y. et al. (2007). "The Cosmic Evolution Survey (COSMOS): Subaru Observations of the HST Cosmos Field". In: 172.1, pp. 9–28.
- Taniguchi, Yoshiaki et al. (2015). "The Subaru COSMOS 20: Subaru optical imaging of the HST COSMOS field with 20 filters*". In: 67.6, 104, p. 104.
- Thomas, Daniel et al. (2005). "The Epochs of Early-Type Galaxy Formation as a Function of Environment". In: 621.2, pp. 673–694.
- Thomas, Daniel et al. (2010). "Environment and self-regulation in galaxy formation". In: 404.4, pp. 1775–1789.
- Tinsley, B. M. (1978). "Evolutionary synthesis of the stellar population in elliptical galaxies. II. Late M giants and composition effects." In: 222, pp. 14–22.
- (1980). "Evolution of the Stars and Gas in Galaxies". In: 5, pp. 287–388.
- Tinsley, Beatrice M. (1972). "Stellar Evolution in Elliptical Galaxies". In: 178, pp. 319–336.
- Toft, S. et al. (2012). "Deep Absorption Line Studies of Quiescent Galaxies at $z \sim 2$: The Dynamical-mass-Size Relation and First Constraints on the Fundamental Plane". In: 754.1, 3, p. 3.
- Toft, S. et al. (2014a). "Submillimeter Galaxies as Progenitors of Compact Quiescent Galaxies". In: 782.2, 68, p. 68.
- (2014b). "Submillimeter Galaxies as Progenitors of Compact Quiescent Galaxies". In: 782.2, 68, p. 68.
- Toft, Sune et al. (2017). "A massive, dead disk galaxy in the early Universe". In: 546.7659, pp. 510–513.
- Trager, S. C. et al. (2000). "The Stellar Population Histories of Early-Type Galaxies. II. Controlling Parameters of the Stellar Populations". In: 120.1, pp. 165–188.
- Tran, Kim-Vy H. et al. (2003). "The Nature of E+A Galaxies in Intermediate-Redshift Clusters". In: 599.2, pp. 865–885.

- Treister, E. et al. (2012). "Major Galaxy Mergers Only Trigger the Most Luminous Active Galactic Nuclei". In: 758.2, L39, p. L39.
- Tremonti, Christy A. et al. (2004). "The Origin of the Mass-Metallicity Relation: Insights from 53,000 Star-forming Galaxies in the Sloan Digital Sky Survey". In: 613.2, pp. 898–913.
- Trujillo, Ignacio et al. (2007). "Strong size evolution of the most massive galaxies since $z \sim 2$ ". In: 382.1, pp. 109–120.
- Trujillo, Ignacio et al. (2009). "Superdense Massive Galaxies in the Nearby Universe". In: 692.2, pp. L118–L122.
- Valentino, Francesco et al. (2020). "Quiescent Galaxies 1.5 Billion Years after the Big Bang and Their Progenitors". In: 889.2, 93, p. 93.
- Valentinuzzi, T. et al. (2010). "Superdense Massive Galaxies in Wings Local Clusters". In: 712.1, pp. 226–237.
- van de Sande, Jesse et al. (2013). "Stellar Kinematics of $z \sim 2$ Galaxies and the Inside-out Growth of Quiescent Galaxies". In: 771.2, 85, p. 85.
- van der Wel, A. et al. (2014). "3D-HST+CANDELS: The Evolution of the Galaxy Size-Mass Distribution since $z = 3$ ". In: 788.1, 28, p. 28.
- van Dokkum, Pieter G. et al. (2008). "Confirmation of the Remarkable Compactness of Massive Quiescent Galaxies at $z \sim 2.3$: Early-Type Galaxies Did not Form in a Simple Monolithic Collapse". In: 677.1, p. L5.
- van Dokkum, Pieter G. et al. (2014). "Dense Cores in Galaxies Out to $z = 2.5$ in SDSS, UltraVISTA, and the Five 3D-HST/CANDELS Fields". In: 791.1, 45, p. 45.
- Vergani, D. et al. (2010). "K+a galaxies in the zCOSMOS survey . Physical properties of systems in their post-starburst phase". In: 509, A42, A42.
- Vogelsberger, M. et al. (2014a). "Properties of galaxies reproduced by a hydrodynamic simulation". In: 509.7499, pp. 177–182.
- Vogelsberger, Mark et al. (2014b). "Introducing the Illustris Project: simulating the coevolution of dark and visible matter in the Universe". In: 444.2, pp. 1518–1547.
- Wellons, Sarah et al. (2015). "The formation of massive, compact galaxies at $z = 2$ in the Illustris simulation". In: 449.1, pp. 361–372.
- Whitaker, Katherine E. et al. (2010). "The Age Spread of Quiescent Galaxies with the NEWFIRM Medium-band Survey: Identification of the Oldest Galaxies Out to $z \sim 2$ ". In: 719.2, pp. 1715–1732.
- Whitaker, Katherine E. et al. (2011). "The NEWFIRM Medium-band Survey: Photometric Catalogs, Redshifts, and the Bimodal Color Distribution of Galaxies out to $z \sim 3$ ". In: 735.2, 86, p. 86.
- Whitaker, Katherine E. et al. (2012a). "A Large Population of Massive Compact Post-starburst Galaxies at $z > 1$: Implications for the Size Evolution and Quenching Mechanism of Quiescent Galaxies". In: 745.2, 179, p. 179.
- (2012b). "A Large Population of Massive Compact Post-starburst Galaxies at $z \geq 1$: Implications for the Size Evolution and Quenching Mechanism of Quiescent Galaxies". In: 745.2, 179, p. 179.

- Whitaker, Katherine E. et al. (2013). "Quiescent Galaxies in the 3D-HST Survey: Spectroscopic Confirmation of a Large Number of Galaxies with Relatively Old Stellar Populations at $z \sim 2$ ". In: 770.2, L39, p. L39.
- White, S. D. M. and M. J. Rees (1978). "Core condensation in heavy halos: a two-stage theory for galaxy formation and clustering." In: 183, pp. 341–358.
- Wild, Vivienne et al. (2007). "Bursty stellar populations and obscured active galactic nuclei in galaxy bulges". In: 381.2, pp. 543–572.
- Wild, Vivienne et al. (2009). "Post-starburst galaxies: more than just an interesting curiosity". In: 395.1, pp. 144–159.
- Wild, Vivienne et al. (2016). "The evolution of post-starburst galaxies from $z=2$ to 0.5". In: 463.1, pp. 832–844.
- Wild, Vivienne et al. (2020). "The star formation histories of $z \sim 1$ post-starburst galaxies". In: 494.1, pp. 529–548.
- Williams, Rik J. et al. (2009). "Detection of Quiescent Galaxies in a Bicolor Sequence from $Z = 0-2$ ". In: 691.2, pp. 1879–1895.
- Wong, Kenneth C. et al. (2020). "H0LiCOW XIII. A 2.4% measurement of H_0 from lensed quasars: 5.3σ tension between early and late-Universe probes". In:
- Worthey, Guy and D. L. Ottaviani (1997). " $H\gamma$ and $H\delta$ Absorption Features in Stars and Stellar Populations". In: 111.2, pp. 377–386.
- Wuyts, Stijn et al. (2007). "What Do We Learn from IRAC Observations of Galaxies at $2 < z < 3.5$?" In: 655.1, pp. 51–65.
- Yesuf, Hassen M. et al. (2014). "From Starburst to Quiescence: Testing Active Galactic Nucleus feedback in Rapidly Quenching Post-starburst Galaxies". In: 792.2, 84, p. 84.
- Zabludoff, Ann I. et al. (1996). "The Environment of "E+A" Galaxies". In: 466, p. 104.
- Zamojski, M. A. et al. (2007). "Deep GALEX Imaging of the COSMOS HST Field: A First Look at the Morphology of $z \sim 0.7$ Star-forming Galaxies". In: 172.1, pp. 468–493.
- Zavala, J. A. et al. (2019). "On the Gas Content, Star Formation Efficiency, and Environmental Quenching of Massive Galaxies in Protoclusters at $z \approx 2.0-2.5$ ". In: 887.2, 183, p. 183.
- Zhou, L. et al. (2020). "GOODS-ALMA: Optically dark ALMA galaxies shed light on a cluster in formation at $z = 3.5$ ". In: *arXiv e-prints*, arXiv:2008.08518, arXiv:2008.08518.
- Zolotov, Adi et al. (2015). "Compaction and quenching of high- z galaxies in cosmological simulations: blue and red nuggets". In: 450.3, pp. 2327–2353.